The UV spectrum of the Galactic Bulge

Dissertation
zur Erlangung des Doktorgrades
der Mathematisch-Naturwissenschaftlichen Fakultät
der Christian-Albrechts-Universität
zu Kiel

vorgelegt von
Giorgia Busso

Kiel
2006

Supervisors:

Dr. Sabine Moehler

European Southern Observatory

Pr. Giampaolo Piotto

Universitá di Padova

Diese Dissertationsschrift wurde in Form und Inhalt nur unter Zuhilfenahme der angegebenen Hilfsmittel unter Anleitung von Dr. S.Möhler angefertigt. Sie wurde noch nicht an anderer Stelle ganz oder zum Teil im Rahmen eines Prüfungsverfahrens vorgelegt oder zur Veröffentlichung eingereicht.

Kiel, den 15.Dezember 2006

Giorgia Busso

ABSTRACT

The UV excess that elliptical galaxies and bulge of spiral galaxies show in their spectra at $\lambda \lesssim 2300\text{Å}$ was one of the most puzzling discoveries in the last 30 years, since these stellar systems were believed to be old and metal rich, without young and massive stars emitting most of their flux at short wavelength. After a long controversy about which kind of stars could be responsible for this feature, it is now accepted that this UV emission is caused by evolved low mass stars, in particular Extreme Horizontal Branch stars (EHB), called also sdB stars from their spectral classification. These stars are faint in the optical wavelength range and until recently it was impossible to resolve them in the nearest galaxies. The closest stellar system (for age and metallicity) in which it is possible to resolve them is the bulge of our Galaxy. A sample of sdBs star candidates was observed in our bulge by Zoccali et al.[2003], by means of V and I photometry. To check their evolutionary status (since they could be indeed sdBs but also cooler stars affected by lower reddening), a follow-up spectroscopic analysis of these stars has been necessary and I obtained the observations at the Very Large Telescope (VLT) telescope during the programme 073.D-0168B. I reduced these data and I compared the obtained spectra with models of hot evolved stars. This analysis confirmed indeed that most of these stars are bulge sdBs, while some candidates turned out to be disk sdBs or cool stars. To be sure that the observed bulge region was not peculiar, I looked for other sdBs candidates in other bulge fields. With this aim I reduced ESO Imaging Survey (EIS) photometric data of bulge fields: sdB star candidates are present also in these fields.

Adopting the method of Santos et al.[1995], I finally constructed the integrated spectrum from the UV to the optical of the Galactic bulge, using both spectroscopic and photometric data and a spectral library (Pickles 1998 and Lejeune et al. 1997): the stars in the color-magnitude diagram (CMD) are associated to the library spectra, depending on their evolutionary status and temperature. The total integrated spectrum is obtained by the sum of the spectra associated to the CMD. I compared the integrated bulge spectrum with old single stellar population synthetic spectra calculated by Bruzual & Charlot [2003], obtaining for the bulge a range in age and metallicity in agreement with previous work. The bulge integrated spectrum shows only a very weak UV excess, but probably a too strict selection of the sample of the sdB star candidates in the CMD and the exclusion of post Asyntotic Giant Branch stars influenced the result.

To verify the procedure, I constructed the integrated spectrum also for the Galactic Globular Clusters NGC 6388 and NGC 6441, which show a

not expected population of EHB stars. Furthermore, the analysis of Hubble Space Telescope multiband photometry suggests the existence of more than one stellar population, with different Helium abundance, implying that in both clusters there have been at least two star formation episodes.

ABSTRACT

Der UV-Exzess, den elliptische Galaxien und der Bulge von Spiral-Galaxien in ihrem Spektrum bei $\lambda \lesssim 2300$ Å zeigen, ist eine der rätselhaftesten Entdeckungen der letzten 30 Jahre. Es wurde bisher angenommen, dass diese Sternpopulationen alt und metallreich seien, ohne junge, massereiche Sterne, die ihren höchsten Fluss bei kurzen Wellenlängen haben. Nach einer langen Kontroverse, welche Sterne denn für die oben genannte Tatsache verantwortlich sein könnten, wird nun angenommen, dass der UV-Exzess von entwickelten, massearmen Sternen stammt, wie den Extreme Horizontal Branch Stars (EHB), die gemäss ihrer Spektralklassifikation auch sdB Sterne genannt werden. Es handelt sich um Sterne, die im optischen Wellenlängenbereich schwach leuchten und bis vor kurzem war es unmöglich sie in benachbarten Galaxien zu beobachten. Ein Sternsystem das in Alter und Metallizität den elliptischen Galaxien nahe kommt und in dem diese Sternen aufgelöst werden können, ist der Bulge unserer Galaxie. Zoccali et al [2003] haben ein Sample von sdB-Kandidaten im Bulge unserer Galaxie mittels V- und I-Photometrie beobachtet. Um den Stand der Entwicklung dieser Sterne zu prüfen (es könnten in sdB Sterne sein, aber ebenso kühle Sterne mit einer nur geringen Rötung), war eine spektroskopische Follow-Up-Analyse dieser Sterne notwendig, für die ich Beobachtungen am Very Large Telescope (VLT) im Rahmen des Programms 073.D-0168B durchführte. Ich reduzierte diese Daten und verglich sie mit Modellspektren entwickelter, heisser Sterne. Diese Analyse bestätigte die Annahme, dass die meisten der Sterne sdB's im Bulge sind, während einige Kandidaten entweder kühlere Sterne beziehungsweise sdB-Sterne in der galaktischen Scheibe sind. Um sicher zu stellen, dass es sich bei der beobachteten Bulge-Region nicht um eine Region mit besonderen Eigenschaften handelt, suchte ich nach weiteren sdB-Kandidaten in anderen Bulge-Regionen. Zu diesem Zweck reduzierte ich ESO Imaging Survey (EIS) Daten dieser Felder: sdB-Kandidaten sind auch in diesen Feldern vorhanden. Zuletzt konstruierte ich das integrierte Spektrum vom UV bis in den optischen Wellenlängenbereich nach der Methode von Santos et al. [1995], wobei sowohl spektrokopische als auch photometrische Daten und eine Spektral-Bibliothek (Pickles und Lejeune et al. 1997) benutzt worden sind: Die Sterne im Farben-Helligkeits-Diagramm (CMD) werden mit den Bibliotheks-Spektren verknüpft, abhängig von ihren Temperaturen und ihrer jeweiligen Entwicklung. Das gesamte integrierte Spektrum ist die Summe der aller Bibliotheks-Spektren die einem der Sterne im beobachteten CMD zugeordnet sind. Ich habe das integrierte Bulge-Spektrum mit synthetischen Spektren [Bruzual & Charlot (2003)] für einzelne alte stellare Populationen verglichen und erhielt eine Bestätigung des Alters und der Metallizität des

Bulges. Das integrierte Spektrum zeigt nur einen sehr schwachen UV-Exzess, wobei anzumerken ist, dass die Selektion des Samples der sdB-Kandidaten im CMD sehr streng war und der Ausschluss von Post Asymptotic Giant Branch Sternen das Resultat wahrscheinlich beeinflusst hat.

Um meine bisherige Vorgehensweise zu Prüfen habe ich ein integriertes Spektrum auch für die Kugelsternhaufen NGC 6388 und NGC 6441 konstruiert, die eine nicht erwartete Population von EHB-Sternen zeigen. Weiterhin deutet die Analyse der Hubble Space Telescope Multiband Photometrie auf die Existenz von mehr als einer stellaren Population mit verschiedener Helium-Häufigkeit hin, was wiederum impliziert, dass in den beiden Haufen mindestens zwei Phasen der Sternentstehung statt gefunden haben müssen.

ABSTRACT

L'eccesso ultravioletto che le galassie ellittiche e i nuclei (*bulges*) delle galassie a spirali mostrano nel loro spettro, ad una lunghezza d'onda $\lambda \lesssim$ 2300 Å e' stato una delle scoperte più enigmatiche degli ultimi 30 anni, in quanto si pensava che questi sistemi stellari fossero vecchi e ricchi di metalli, senza le giovani stelle massicce che emettono la maggior parte del loro flusso a corte lunghezze d'onda. Dopo una lunga controversia su quali stelle possano essere responsabili di questo fenomeno, e` ora comunemente accettato che l'emissione UV e` causata da stelle evolute di piccola massa, in particolare stelle di Estremo Ramo Orizzontale, o subnane di tipo spettrale B. Questi oggetti sono deboli nella banda ottica e, fino a poco tempo fa, era impossibile risolverli nelle galassie più vicine. Il sistema stellare più simile (per età e metallicità) in cui è possibile risolvere queste stelle è il bulge della nostra Galassia. Un campione di candidate sdB è stato osservato nel nucleo da Zoccali et al.[2003], per mezzo di fotometria nelle bande V e I. Per controllare il loro stato evolutivo (poiché potrebbero essere appunto sdBs ma anche stelle più fredde affette da un minore arrossamento), è stata necessaria una analisi spettroscopica. Ho osservato questi oggetti al Very Large Telescope (VLT) nel corso del programma 073.D-0168B. Ho ridotto questi dati e ho confrontato gli spettri ottenuti con modelli di stelle evolute calde. Questa analisi ha confermato che la maggior parte di queste stelle sono sdBs appartenenti al bulge galattico, mentre altre candidate sono risultate essere sdBs appartenenti al disco o stelle fredde. La riduzione fotometrica di dati EIS (Eso Imaging Survey) del bulge ha mostrato che candidate sdBs sono presenti anche in questi campi.

Adottando il metodo di Santos et al[1995], ho finalmente costruito lo spettro integrato dall'UV all'ottico del nucleo galattico, usando sia i dati spettroscopici che quelli fotometrici ed anche una libreria di spettri (Pickles 1998 e Lejeune et al. 1997): le stelle nel diagramma colore-magnitudine (CMD) sono associate agli spettri della libreria, associazione che dipende dallo status evolutivo e dalla temperatura. Lo spettro integrato totale e' ottenuto come la somma degli spettri associati al CMD. Ho confrontato lo spettro integrato del nucleo con spettri sintetici di popolazioni stellari singole calcolati da Bruzual & Charlot [2003], ottenendo una conferma dell'etá e della metallicitá del bulge. Lo spettro integrato mostra un eccesso UV ma molto debole. Probabilmente una selezione troppo severa del campione di candidate sdBs e l'esclusione di stelle post-Ramo Asintotico hanno influenzato il risultato.

Per verificare la procedura, ho costruito lo spettro integrato anche per gli Ammassi Globulari Galattici NGC 6388 e NGC 6441, i quali mostrano una

inaspettata popolazione di stelle di EHB. Inoltre l'analisi di fotometria multibanda ottenuta da Hubble Space Telescope suggerisce l'esistenza di piú di una popolazione stellare, con diverse abbondanze di elio, ipotesi che implica che in entrambi gli ammassi ci sono stati almeno due episodi di formazione stellare.

Contents

Chapter 1

Introduction

One of the most puzzling discovery in the last 30 years was that some elliptical galaxies and bulges of spiral galaxies show in their spectra a sudden upturn in the UV range, at $\lambda < 2300$Å (see Fig. 1.1 and Sec.1.1). This was unexpected since these stellar systems were believed to be old and metal rich, without young and massive stars emitting most of their flux at short wavelength. After a long controversy about which kind of stars could be responsible for this feature, it is now accepted that this UV emission is caused by evolved low mass stars (see Sec.1.2). Since these stars are faint, until recently it was impossible to resolve them in the nearest galaxies. The closest stellar system (for age and metallicity) in which it is possible to resolve them is the bulge of our Galaxy (Sec.1.3). A sample of candidate evolved low mass stars was observed in our bulge by Zoccali et al. [2003], by means of V and I photometry. Because of their position in the color magnitude diagram (see Fig:1.2), their evolutionary status is uncertain: they could be indeed evolved old stars but also cooler stars affected by a lower reddening. A follow-up spectroscopic analysis of these stars has been therefore necessary and I obtained the observations at the Very Large Telescope (VLT) telescope during the program 073.D-0168B. I describe the reduction and the analysis of these data in Ch.2 and 3 respectively. To be sure that the observed bulge region was not peculiar, I looked for other evolved low mass stars candidates in other bulge fields. The ESO Imaging Survey (EIS) observed several galactic fields and its archive provide also images in the B,V,I filters of bulge fields, which I reduced (see Ch.4). Adopting the method of Santos et al. [1995a], I finally constructed the integrated spectrum of the Galactic bulge, using both spectroscopic and photometric data and a spectral library (see 5). I describe the method and the results in Ch.6. The evolved low mass stars I studied though are not the only one present in the Galactic bulge. Two Galactic Globular Clusters (GGCs), namely NGC 6388 and NGC 6441, show a not expected population of these stars. I discuss these two stellar systems in Ch.7.

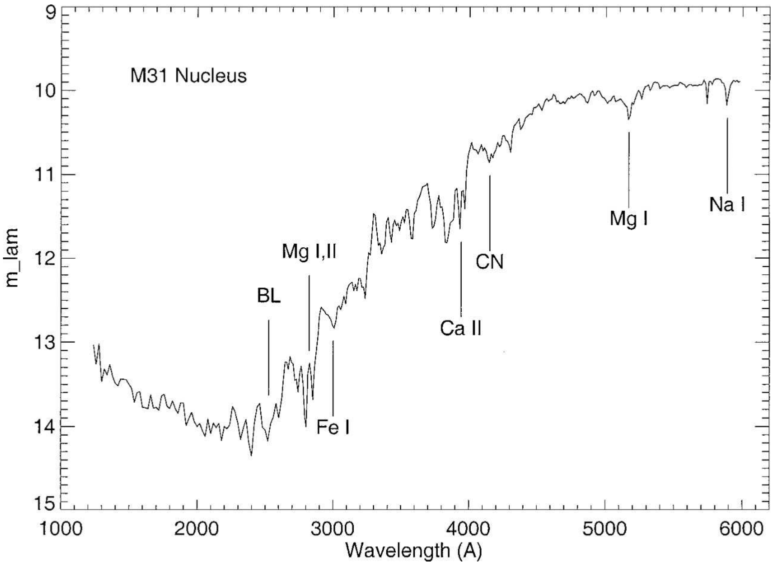

Figure 1.1: A composite UV-optical energy distribution for the bulge of the spiral galaxy M31 (From O'Connell [1999])

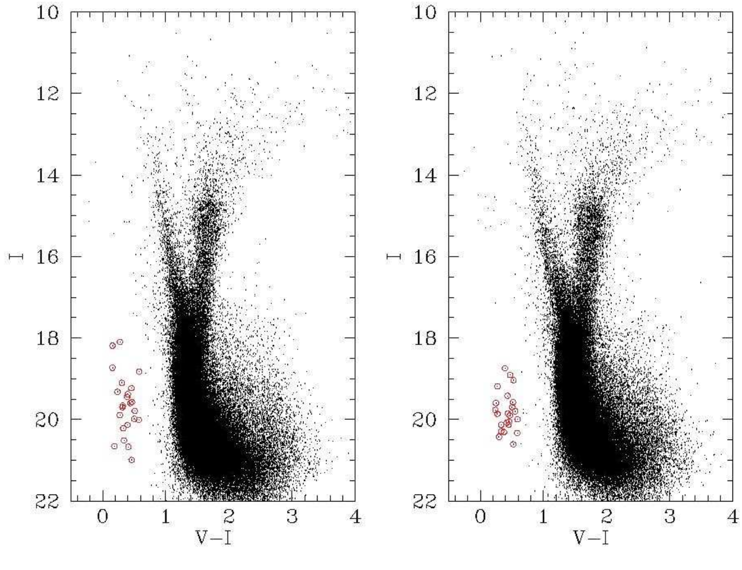

Figure 1.2: Color magnitude diagrams of two of the 8 chips of the Wide Field Imager(WFI) (from Zoccali et al. [2003]). The stars marked in red are the evolved low mass stars candidates.

1.1 The UV excess of the elliptical galaxies

1.1.1 The history

As already said, the UV excess (called also UV upturn or UVX) in the early-type systems (ellipticals galaxies and bulges of spiral galaxies) has been a puzzle for many years.

One of the first hypothesis suggested by Code [1969] to explain the phenomenon was that the UV emission was non thermal radiation from an active nucleus (AGN) or scattering of photons from hot massive stars by interstellar dust, implying that elliptical galaxies contain an appreciable young stellar population. Hills [1971] pointed out that the steep rise of the UV spectrum was incompatible with known non thermal sources but was closely matched by the Rayleigh-Jeans tail of a high temperature ($T_{eff} \gtrsim 20000$ K) thermal source and he proposed, as responsible of the feature, highly evolved, hot, low mass stars such as the central stars of planetary nebulae or their hot white dwarf descendants (see Sec.1.2). Tinsley [1971] argued that the UV light arose instead from young, massive, main sequence stars.

The spatial structure of the emission and the presence (or lack) of particular spectral features helped to clarify the several scenarios. An AGN is a concentrated point source, while a population of low mass stars should have a smooth distribution and young, massive stars populations have a clumpy structure, similar to the OB associations[1] found in spiral arms. Observations of bright early-type galaxies, taken with the International Ultraviolet Explorer (IUE) satellite, confirmed that the UV light profile is parallel to the smooth one of the visible light (Bertola et al. [1980], O'Connell et al. [1986]). High resolution UV imaging from the Hubble Space Telescope (HST) has confirmed the absence of massive stars in the centers of the two closest galaxies M31 and M32 (King et al. [1992], Lauer et al. [1998]) and in most UVX sources in the nuclei of 56 early-type galaxies in the survey of Maoz et al. [1996], validating the hypothesis that the far-UV light originates in a stellar component with dynamics characteristic of the bulk of the old stellar population. Also spectroscopic observations confirmed this result: the first IUE spectra (Bertola et al. [1980], Oke et al. [1981], Deharveng et al. [1982]) showed that the strong, broad emission lines characteristic of active nuclei were absent, excluding the AGN hypothesis, while Hopkins Ultraviolet Telescope (HUT) spectra (Ferguson et al. [1991], Brown et al. [1997]) revealed the lack of strong CIV absorption lines at λ =1548,1551 Å, typical of young massive stars. The spectra instead were well matched by the integrated light

---

[1] The term OB association is used to describe a large collection of gas and young massive stars (O-type and B-type).

expected from populations of evolved low mass stars, in particular the best fit (Brown et al. [1997]) was achieved considering a mixed population of post-Asyntotic Giant Branch (post-AGB) and Extreme Horizontal Branch stars (EHB, see Sec.1.2).

1.1.2 Correlations with other parameters

A correlation between the UV excess and independent measurable parameters can give clues to the source of the UVX but could also be exploited to gain insight into the evolution of the UVX as a function of look-back time. In fact, except in cases where the UV radiation is obscured by dust (e.g. in edge-on S0-Sb galaxies), the UV excess has been detected in all nearby early-type systems observed with an adequate signal-to-noise ratio.

One of the most interesting properties of the UV excess is its large variation from object to object. The "strength" of the UV excess is measured by the difference between the magnitude at 1500 Å and the V magnitude, indicated by the color (1500-V): the bluer the color is, the stronger is the UV flux. The amplitude of the UVX in the centers of bright ellipticals and Sb galaxies varies from ∼4.5 to ∼2, which is a factor of 10 in the ratio of far-UV to visible flux (O'Connell [1999]).

Dependance on metallicity

In the first studies on a possible correlation with other parameters, the UV excess appeared to be stronger in more metal-rich galaxies (Burstein et al. [1988]). The metallicity is measured by means of the spectral line index Mg_2, which measures the Mg I+MgH absorption features near 5170 Å, produced by the dominant old stellar population. Burstein et al. [1988] observed indeed that the UV colors became bluer as the metallicity index Mg_2 increased (see Fig. 1.3).

Recently though, Rich et al. [2005], using a bigger sample of data from the GALEX[2] satellite, found that there is no such correlation between metallicity and UV excess (see Fig. 1.4). The new sample contain objects more distant than those considered in Burstein et al. [1988], but nonetheless they are early-type galaxies in the relatively local universe (at redshift $z<0.2$).

Dependance on age

If the source of the UV excess is EHB stars, theoretical models (Yi et al. [1999]) expect a rapid decline of the UVX as a function of increasing redshift,

---

[2] Galaxy Evolution Explorer: http://www.galex.caltech.edu/

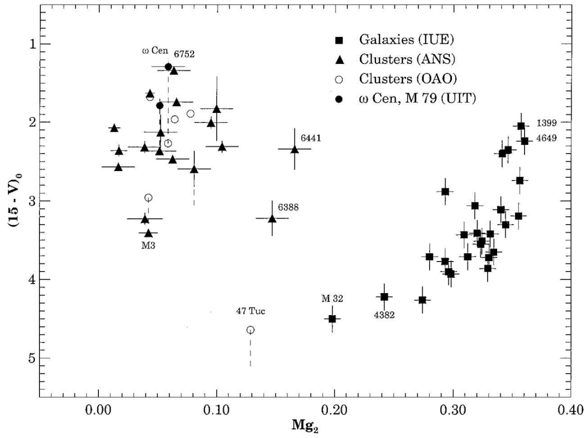

Figure 1.3: Amplitude of the UV excess in older stellar populations, measured by the color (1500-V), as function of the metallicity index Mg_2 (from Dorman et al. [1995]): at higher metallicity the UV excess of the galaxies (marked by triangles) is stronger.

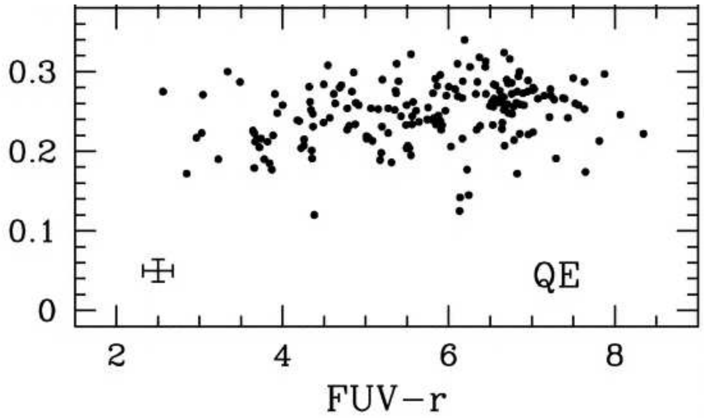

Figure 1.4: Relation between the metallicity index Mg_2 and the UV color (Rich et al. [2005]) for elliptical galaxies: there is not significant relation between metallicity and UVX.

since we are looking at younger elliptical galaxies (Greggio & Renzini [1990], Tantalo et al. [1996]). Furthermore only in the last few gigayears the masses of old turnoff stars have been low enough that the helium-burning progeny of red giant branch tip stars would have envelopes thin enough to make the stars UV-bright.

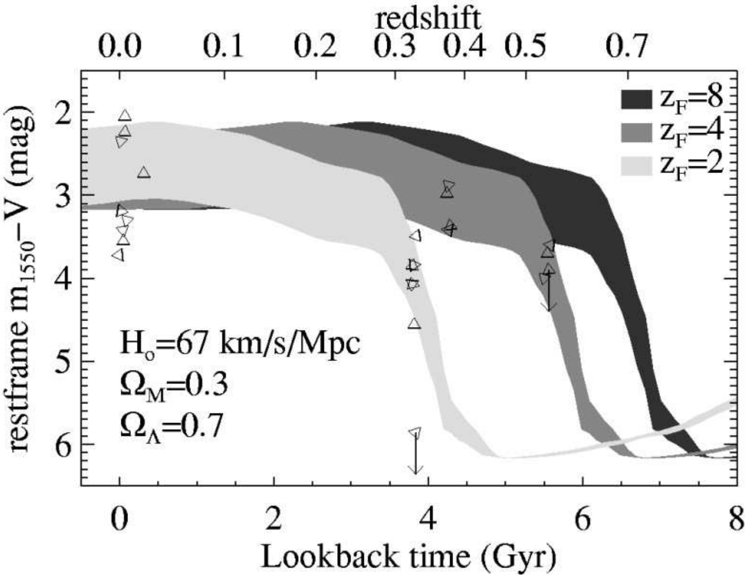

Figure 1.5: From Brown et al. 2003: the evolution of the UV upturn as a function of the redshift: the data are marked with triangles; the expected evolution of this emission in giant elliptical galaxies (Tantalo et al. 1996), assuming three different epoch of star formation, is also shown.

Brown et al. [2003] mapped the evolution of the UV upturn as a function of the redshift, with HST observations of galaxy clusters at $0.3<z<0.6$. Fig. 1.5 shows a comparison of their data with the expected evolution of the UV emission in elliptical galaxies. They found that at $z\sim0.3$ (corresponding to 3.9 Gyrs ago) the UVX is significantly weaker than it is in the current epoch, but also that increasing the lookback time the UVX evolution is flat. This could be explained with large variations in the formation epoch of giant elliptical galaxies in clusters (ruled out by Brown et al. 2003) or with a wide dispersion in the parameters that govern EHB formation or it might be that another source of UV radiation is becoming dominant at increasing redshift (e.g. residual star formation) as the EHB stars disappear.

More recently, Rich et al.[2005] found no correlation between UVX and redshift, but their sample is at $z<0.2$, therefore, as it is shown in Fig. 1.5, possibly the galaxies are not young enough.

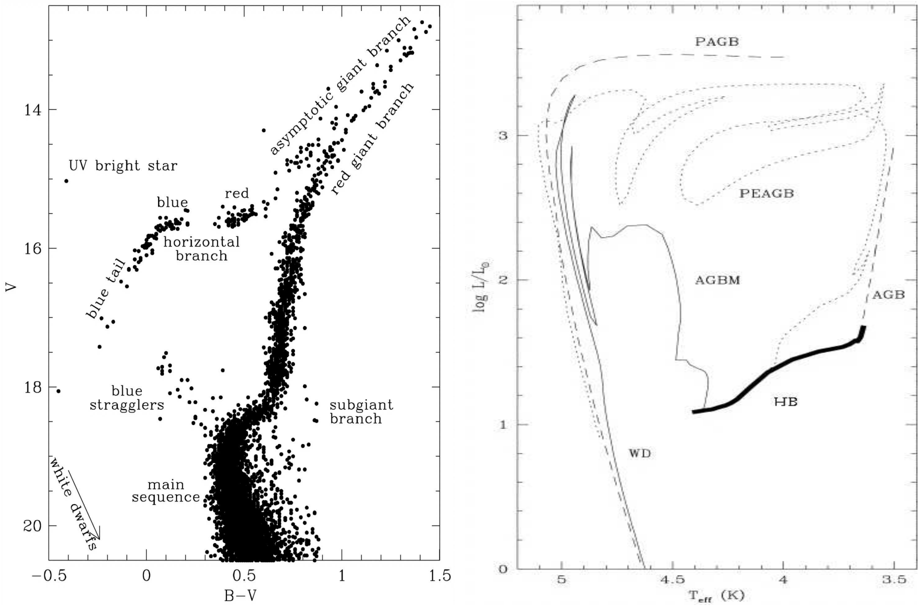

Figure 1.6: Left panel: Color magnitude diagram of the Globular cluster M3 with the marked evolutionary sequences (from Moehler [2001]); right panel: evolutionary paths after the HB phase (from Brown et al. [1997])

1.2 Evolution of a low mass star

Usually a low mass star is defined as a star with an initial mass $\lesssim$2.2 $M_\odot$. To better explain the different evolutionary phases, I refer to Fig. 1.6.

The star burns hydrogen (H) during the Main Sequence (MS) phase. After having finished burning hydrogen (H) in the core, the star burns H in a shell, while the core, now composed of helium (He), is degenerated. During this phase the star evolves along the Red Giant Branch (RGB), increasing the He-core mass. Once the He core reaches a critical mass ($\sim$0.5 $M_\odot$), a He-burning runaway is initiated in the core (He-flash), which continues until the electron degeneracy is removed. The He-flash occurs at the tip of the RGB and after it the star reaches the locus called Horizontal Branch (HB). In this phase the star burns He in its core and H in a outer shell, and it has a H-rich envelope, whose mass influences the position of the star on the HB: the more massive the envelope is and the cooler and redder the star appears, viceversa if the envelope is thin the star is hotter and bluer. In some cases the envelope is too thin to sustain H-shell burning: this is the case of the Extreme Horizontal Branch stars (see sec. 1.2.1). The other main factors determining the star position on the HB, i.e. the metallicity, the He abundance, the mass loss that the star experience on the RGB, the rotation, have a not negligible role.

After the HB, the evolution of the star depends on the H-envelope mass:

- if M_{env} >0.07 $M_{\odot}$, after the He in the core is exhausted, the star burns He in an inward shell and H in an outer shell, while the core of Carbon and Oxygen (C-O) is inert. This is the Asyntotic Giant Branch (AGB) phase. At some point, the H-shell becomes instable, experiencing the Termally Pulsing AGB (TP-AGB) phase, and after that the outer layers are expelled forming a Planetary Nebula (PN), while the remaining degenerate C-O core becomes a White Dwarf (WD).
- if 0.03 <M_{env} <0.07 $M_{\odot}$, the star reaches the AGB but it leaves the sequence earlier with respect to a normal AGB star (Early AGB (E-AGB) phase) and evolves like a WD.
- if M_{env} <0.03 $M_{\odot}$, the star does not even manage to reach the AGB (AGB-manqué, AGB-M) and evolves like a WD.

Example of spectra of these evolved stars are shown in Fig. 1.7.

1.2.1 sdB stars

When the star, during the HB phase, has a very thin envelope and reaches T_{eff} >20000 K, it is called Extreme Horizontal Branch (EHB) star, because on the color-magnitude diagram (CMD) of the Globular clusters its position is at the very end of the HB. These stars though are observed not only in the Globular clusters but also locally, in which case they are referred as subdwarfs B (sdBs) from their spectral classification. The main characteristic of a sdB star is then the very thin envelope on the HB, so that it does not manage to sustain the H-shell burning. A so thin envelope means that the star experienced strong mass loss during the RGB phase. The reasons why the star lost so much matter is not yet very clear. D'Cruz et al. [1996] argued that an enhanced stellar wind near the tip of the RGB can cause a strong mass loss and a consequent thin envelope on the HB phase. Sweigart [1997a] suggested that helium mixing driven by internal rotation may account for such enhanced mass loss. These channels produce sdB stars that are either single or in wide, not interacting binaries. But sdBs can also form through various binary channels (Han et al. [2003]):

1. the primary component, i.e. the initially more massive star of the binary, experiences dynamical mass transfer during the RGB phase, leading to a common envelope and a spiral-in phase, typically leaving

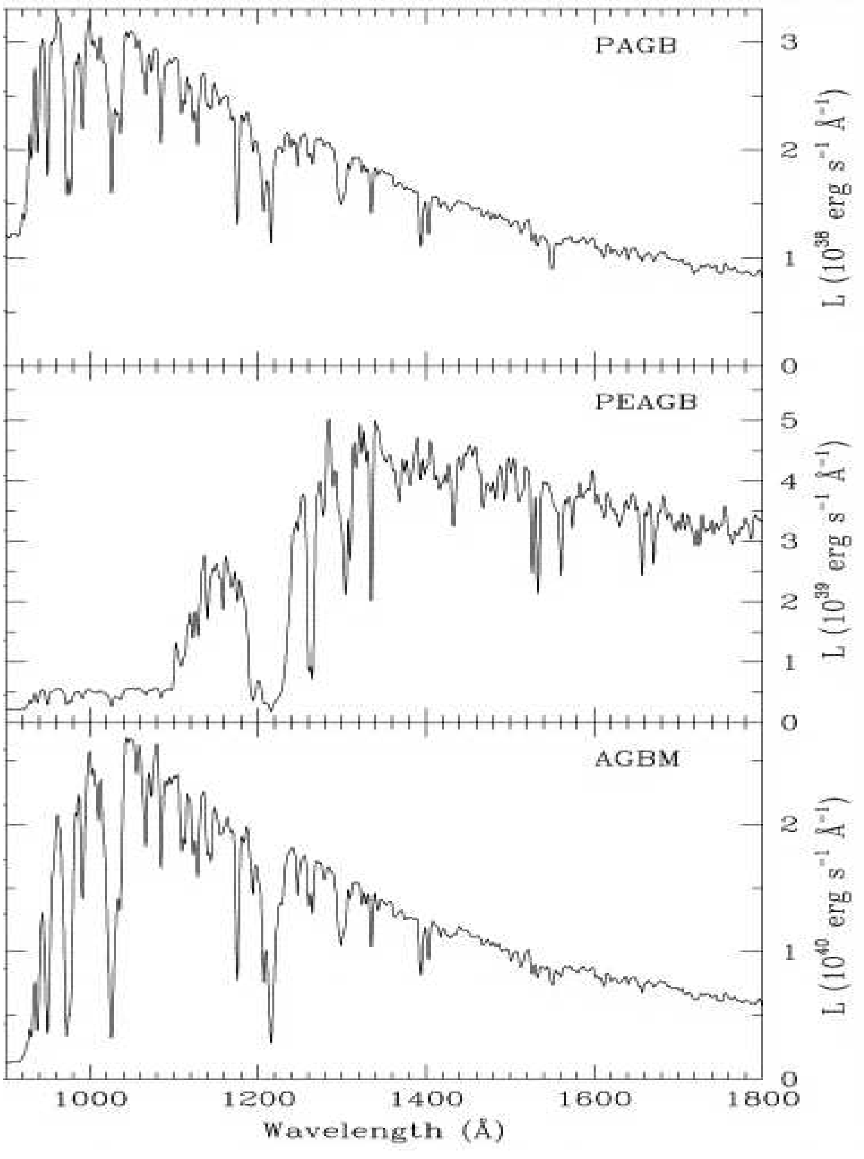

Figure 1.7: From top to bottom, the extreme UV spectra of a PostAGB, Post-Early AGB and AGB-manqué star respectively (from Brown et al. [1997]).

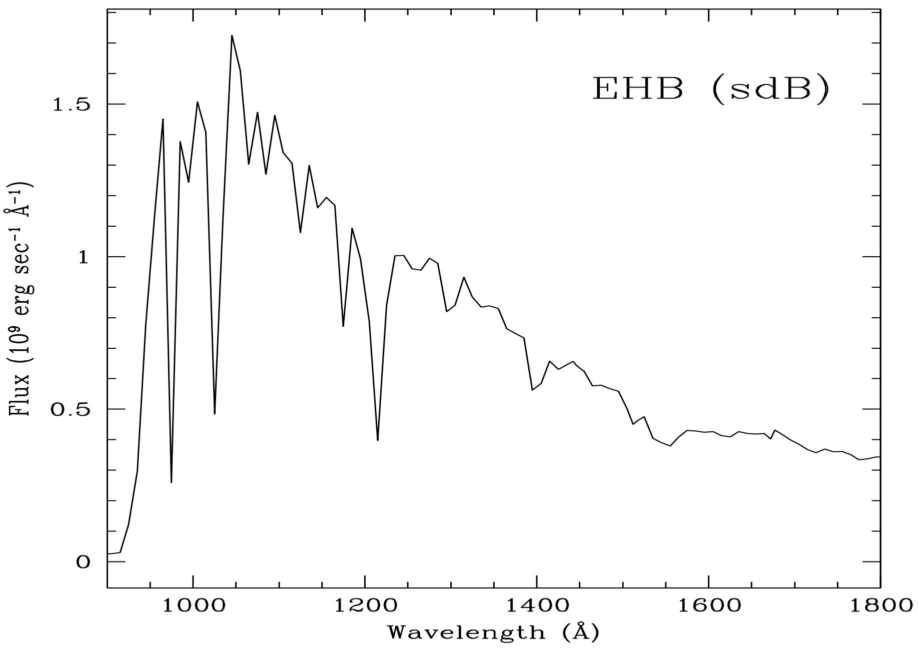

Figure 1.8: Example of extreme UV spectrum of a sdB star (spectrum obtained from the BaSel spectral library, see Ch.5).

a very close binary after the envelope has been ejected. If the core of the giant still ignites He, it forms a sdB star in a short-period binary with a Main Sequence (MS) companion;

2. if the first mass-transfer phase is stable, the primary will also lose most of its envelope producing a sdB star with a MS companion, but in this case in a wide orbit with orbital periods between ∼0.5 and 2000 days, depending on how angular momentum is lost during the transfer.

3. this case is very similar to the first case except that the companion is not a MS star but it is already a WD;

4. similar to the second case but the original mass of the giant is limited and the companion is a very massive WD;

5. if both binaries are helium WDs and their orbital period is sufficiently short, the two component may coalesce and if the merger product ignites He, this again leads to the formation of a single sdB star.

Han et al. [2003] investigated the importance of these evolutionary channels, finding that the most important are the channels 1, 2 and 5, but observational effects tend to increase the relative importance of channel 2 and 5.

Lisker et al. [2004] analyzed 77 sdBs spectra finding that 24 stars show evidence of a cool companion, while among the 53 single stars, 5 objects with relatively high luminosities show peculiar Hα profiles, possibly indicating strong stellar winds. These observations agree quite well with the calculation of Han et al. [2003].

An example of a theoretical spectrum of a sdB star is shown in Fig. 1.8.

1.3 The Galactic bulge

A problem that continues to baffle astronomers today is defining the structure of our star system, the Milky Way. Because we reside within our Galaxy, we cannot see the larger picture of what the Galaxy actually looks like, but so far it is well confirmed it is a spiral Galaxy, like for example M31 (see Fig. 1.9). Following the definition of Wyse et al. [1997], the bulge of a galaxy is *"a centrally concentrated stellar distribution with an amorphous -smooth- appearance"*.

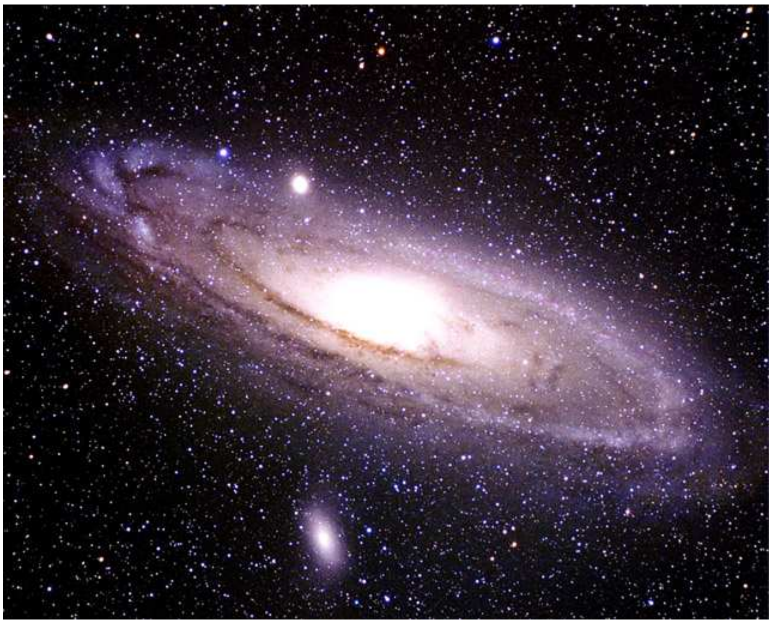

Figure 1.9: The close spiral galaxy M31 (picture taken from http://messier.obspm.fr)

Since the Sun is located on the Galactic plane, at a distance of about 8 Kpc from the center, interstellar dust clouds hamper a clear view of the nucleus of our Galaxy in the visual wavelength range. As a result, the nuclear region of the Milky Way and its surroundings is observed better at infrared and longer wavelengths, where interstellar reddening is negligible. Much of what is known about the Galactic bulge has been gained from such observations or by comparing it with the bulges of other galaxies as for example M31, where the central regions are observable without the hindrance of the interstellar dust. This assumption is supported by the similarity in the bulges of the Milky Way and of M31 of the radial distribution of surface brightness at λ=2.2 μm. Spectroscopic observations of M31 showed that the red giant stars of spectral types K and M are the source of the 2.2 μm radiation and this kind of stars are also found in large numbers in a few areas of the Milky Way where interstellar dust does not affect too much the observations (for example, the region called Baade's Window, at about 4 ° south of the Galactic center direction). In general the bulge is designated as the volume surrounding the Galactic center and extending outward to about 1.5 kpc, where it merges with the Galaxy's halo and the disk.

1.3.1 The formation of the bulge

The study of the Galactic bulge population is essential to understand the formation of our galaxy. The main hypothesis about the Milky Way formation is that in a lumpy, turbulent, protogalactic hydrogen and helium gas medium with some angular momentum, a density fluctuation became unstable against collapse under its own gravitation. In theory, if the kinetic energy generated by the collapse is radially dissipated, the collapse continues until stopped by rotation in a plane normal to the angular momentum vector while continuing in directions perpendicular to that plane. As the collapse proceeds, stars are first formed in a large centrally condensed spheroid (halo) and eventually in a galactic disk. As these stars evolve, heavier elements are built by nuclear reactions in their interiors and eventually ejected. Population II old stars are found in the galactic halo and were formed early in the collapse and reflect the space distribution, kinematics and metal poor chemical composition, as expected for the earlier stellar generations. Population I stars and the interstellar dust are younger metal rich objects confined to the disk.

It is not yet clear though how the bulge was formed, as several scenarios try to explain:

- the bulge was formed as central region of the halo. Like Wyse & Gilmore [1992] and Ibata & Gilmore [1995] observed, the angular momentum distribution of the bulge is very similar to that of the stellar halo and very different from that of the disk and the bulge stars does not show significant net rotation, suggesting the validity of the Eggen et al. [1962] scenario, where the bulge is the central region of the halo but formed with significantly more dissipation.

- the bulge was formed after the merge of the Galaxy with a larger companion. As suggested by Baugh et al. [1996] and Kauffmann [1996], the star formation occurs in the galaxy disks, which are destroyed during a merger with a significant larger companion. In such a merge, all the still existent disk stars are reassigned to the bulge, the cold gas present is assumed to be driven to the center and fuel a burst of star formation and a new disk is assumed to grow through accretion of intergalactic gas.

- the bulge was formed by accretion of dense stellar satellites. The central regions of galaxies are obvious repositories of accreted systems, as they are the bottom of the local potential well, therefore satellite galaxies could have contributed significantly to the bulge. Most of the population of the bulge was accreted in one or a few mergers of objects like the Magellanic Clouds (two irregular dwarf galaxies orbiting around the Milky Way) or the most luminous dwarf spheroidals (dSph, dwarf elliptical galaxies that are companions to the Milky Way), explaining the high metallicity of the bulge, while accretion of lower luminosity satellite galaxies could explain the metal-poor tail of the bulge abundance distribution (see Sec.1.3.3).

1.3.2 The shape of the bulge

The shape of the bulge can be inferred by integrated surface photometry (see Fig. 1.10). Binney et al. (1997), using near infrared data (in a wavelength range where luminosity comes almost entirely from stars and not dust) obtained from the COBE/DIRBE satellite, found that the shape of the bulge is a triaxial ellipsoid, which forms an angle $\phi \sim 20^\circ$ with the line of sight. Often this triaxial ellipsoid is called *bar*.

Further evidence that the Galaxy is barred comes from studies of individual stars, especially in those regions where the reddening effects are less, as in Baade's Window. One example is the Optical Gravitational Lensing Experiment (OGLE[3]) a project whose aim is monitoring the brightness of millions of stars in order to find one of the rare microlensing events, when

---

[3] http://bulge.astro.princeton.edu/ ogle/

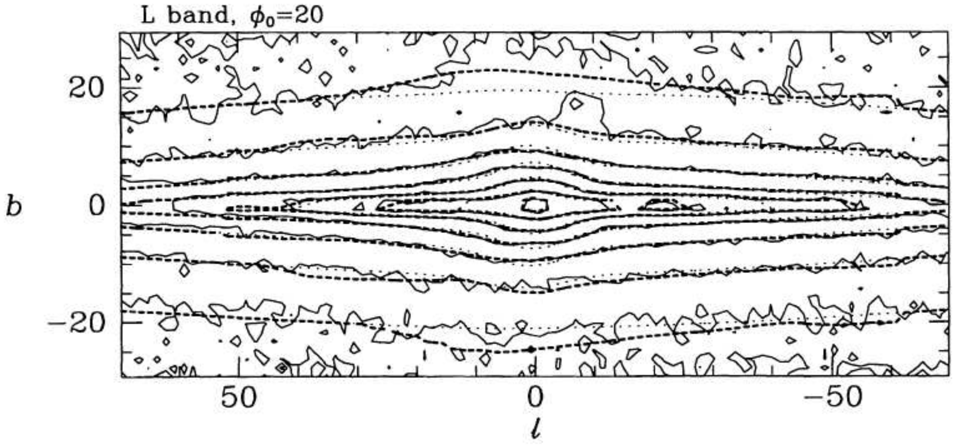

Figure 1.10: From Binney et al. [1997]: the brightness distribution of the Milky Way in the infrared, obtained from the COBE/DIRBE satellite; the brightness distribution obtained from a triaxial ellipsoid model (dashed lines), whose long axis form an angle $\phi \sim 20\,^\circ$ is also shown.

the light of a star is gravitationally lensed by a foreground star: the optical depth to microlensing τ (that is the probability that a source is affected by this phenomenon) predicted for a given light of sight increases with both the surface density Σ_b of bulge stars and the effective depth d_b of the bulge along that line of sight. Since τ depends on the shape of the considered system (Paczynski [1986b], Paczynski [1986a]), hence on the ratio q between the axies in the case of the bulge, measuring τ can then give an estimate of q: several OGLE observations (Udalski et al. [1994], Zhao et al. [1995]) give a value of τ compatible with a triaxial bulge, whose long axis forms an angle $\phi \sim 15\,^\circ$ with the Sun-center line. This result has been confirmed also by Stanek et al. [1994], with an independent method, that is the magnitude of the Horizontal Branch red clump[4], which is brighter for fields at same galactic latitude but different longitude.

While previous studies agree in saying that this triaxial bulge is actually a bar, more recent studies (López-Corredoira et al. [2001], López-Corredoira et al. [2005]), using newest 2MASS[5] data, seem to argue that there is a in-plane bar apart from the bulge: the bar is long and thin, and contains both young and older stars, whereas the triaxial bulge is shorter, far fatter and

---

[4] In a metal rich system, the Horizontal branch stars (see Sec.1.2) tend to cluster in to the cooler and redder part of the Horizontal Branch sequence, forming a feature called red clump.)

[5] Two Micron Sky Survey: http://www.ipac.caltech.edu/2mass/

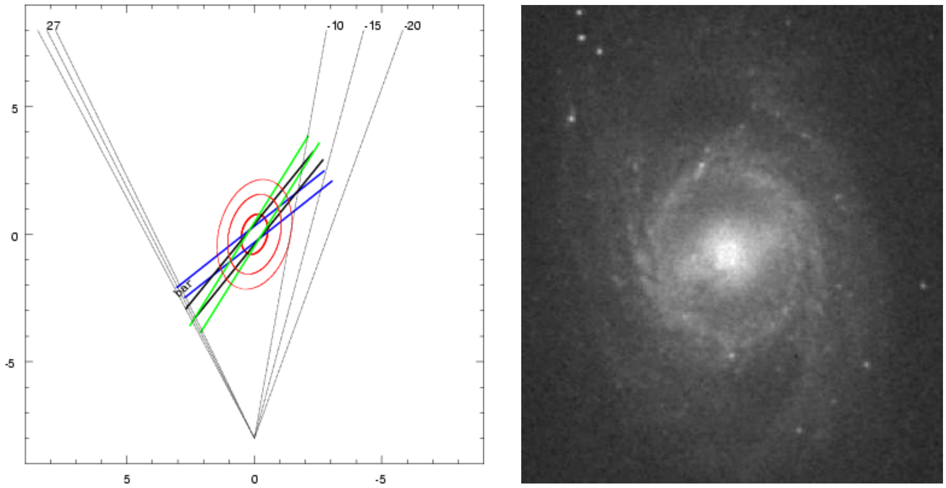

Figure 1.11: Left panel: a schematical representation of the proposed ”tri-axial bulge”(in red) + ”bar” structures in the inner Galaxy; the bar width is assumed to be 500 pc. Three possible bars (in blue, black and green) and the lines of sight at different longitudes are plotted (from López-Corredoira et al. [2001]). Right panel: a real example of this structure is the spiral galaxy M95 (NGC 3351) which show a bar apart from the prominent bulge in the centre (López-Corredoira et al. [2001]).

only contains old stars. Fig. 1.11 shows a schematical representation of the proposed configuration for the inner Galaxy and also how this structure is observed in other galaxies.

Moreover, another feature that showed up in the last years about the structure of our galaxy, is that it seems that disk and bulge do not merge continously but instead there is a hole between the two components: López-Corredoira et al. [2000], by means of stellar counts from 2MASS data, find the stellar density drops quickly with the distance from the center, in a region between 1.3 and 3 Kpc.

1.3.3 The bulge metallicity

The bulge population does not have only a single value of the metallicity, but it shows instead a metallicity distribution (MD), since the abundances range from metal poor to metal rich, reaching also supersolar values (see Fig. 1.13). It is essential then to obtain an estimate as precise as possible of the metallicity, since it can gives clues and provide constraints on the process of formation of the bulge, like for example in the case of the relative abundance of α–elements, produced by massive star Type II Supernovae

(SNe), and iron, produced by longer-timescale Type Ia SNe.

The first method to obtain the metallicity of the stars is to look at their spectra and obtain the abundances of the elements from the spectral lines. One of the first published study of the bulge metallicity distribution (MD) based on high resolution spectra is that by McWilliam & Rich [1994], who analysed a sample of 11 red giants in the Baade's Window and used this data to recalibrate a previous bulge MD based on low resolution spectra for 88 stars (Rich [1988]). The resulting MD is centered around [Fe/H]=-0.2, with the 34% of the stars above solar metallicity and no stars below [Fe/H]$\simeq -1.3$.

More recently Rich & Origlia [2005], by means of high resolution spectra taken at the Keck telescope, analysed a sample of M giants stars, finding that the iron abundance and composition of these stars are similar to those of the K giants, with a mean value [Fe/H]=-0.19. This study shows also that bulge stars are enhanced in α–elements at the level of $+0.3$ dex with respect to the solar composition stars. This α–enhancement was confirmed also by Fulbright et al. [2006], by means of high resolution Keck spectra of 27 K giants in the Baade Window, and by Zoccali et al. [2006], who measured Oxygen abundances in high resolution spectra (collected at FLAMES-UVES@VLT) of 50 K giants in four fields towards the Galactic bulge.

The bulge MD is confirmed by studies that measure the metallicity adopting a different approach, that is by using the color-magnitude diagram, where some features, like the Red Giant Branch (see Sec.1.2), depend on metallicity. In fact, at low metallicity, the opacity in the star atmospheres is lower causing the star to appear brighter and hotter; viceversa, at higher metallicity, the star is less luminous and cooler. In this way a metal rich population has a more sloped RGB with respect to a metal-poor population. Since the red giant star atmospheres are not very well known (because of the convection on the outer layers), also the more accurate models for this kind of stars are not the best to determine the metallicity, but nevertheless a photometric analysis permits to study a large sample of objects. Zoccali et al. [2003] adopted this approach to derivate a determination of the age and the metallicity of the bulge. Combining optical data (taken with WFI camera at the 2.2m@ESO telescope) with infrared observations (obtained from the 2MASS survey), they constructed a color magnitude diagram (Fig. 1.12), where the color (V-K) is very sensitive to metallicity, and compared it with fiducial RGB, obtained from globular clusters of known metallicity, used as templates (instead of not accurate models). The spread introduced by the distance and reddening dispersions is of the order of $\sim$0.1 dex in [M/H]. In Fig. 1.5 their obtained metallicity distribution compared with the one of previous works is shown: the MD has a peak at [M/H]~ -0.1, with a fairly sharp edge just above solar metallicity and a low metallicity tail, quite similar

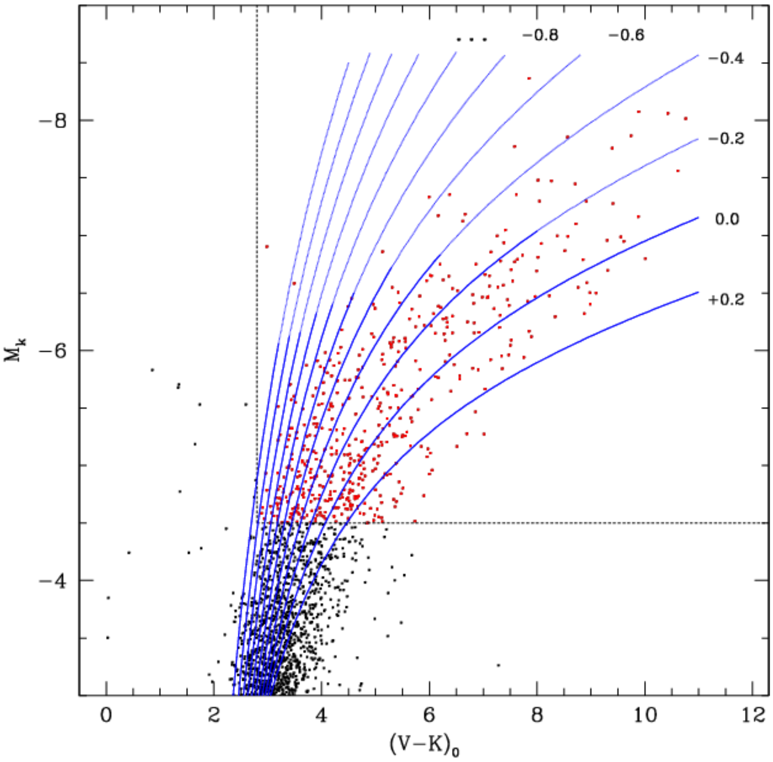

Figure 1.12: From Zoccali et al.[2003]: comparison between the photometry of bulge red giants and analytical red giant branches, at different metallicities, obtained from globular clusters of known metallicities.

to the spectroscopic results mentioned above, but relative to a much larger sample.

The metallicity distribution agrees with a closed box model (that is a star formation model without infall or outflow of gas), while the α–enhancement points to a bulge formed early and rapidly.

1.3.4 The bulge kinematics

As already said, to avoid the problem of the strong absorption due to the galactic disk dust, observations need to be obtained in the infrared. In order to determine the radial velocity, a convenient feature in the stellar spectra is the absorption band at 2.3μm caused by CO molecules (see Fig. 1.14): this band has a very sharp edge, called CO bandhead, at its red end, which can be accurately located in typical bulge spectra, as the one of red giants stars.

Blum et al. [1995], measuring indeed the CO bandhead in four bulge fields, determined the radial velocity dispersion σ_{los}, finding evidence that

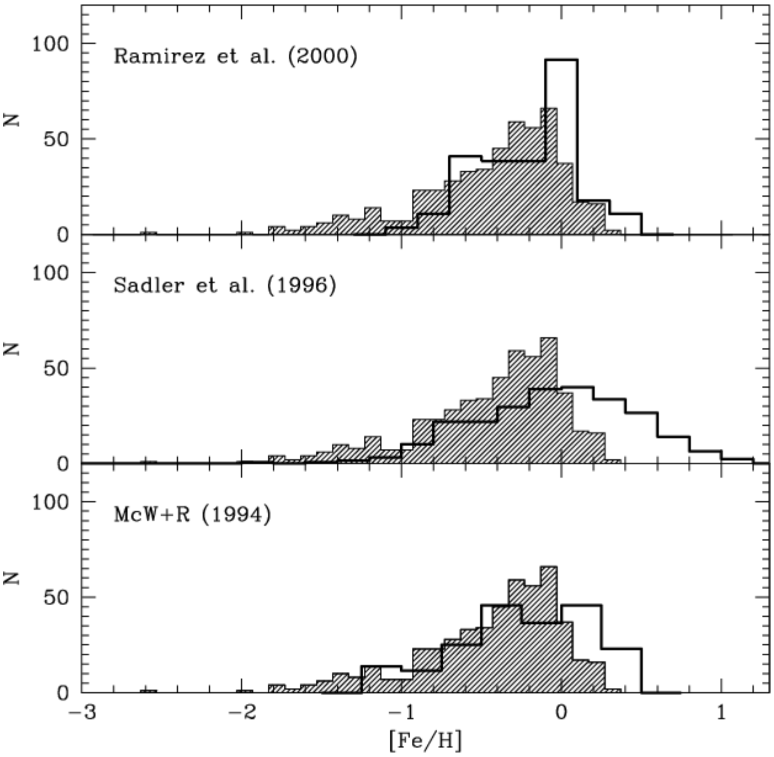

Figure 1.13: Comparison between the metallicity distribution found by Zoccali et al. [2003](shaded histogram) and previous works (as labeled).

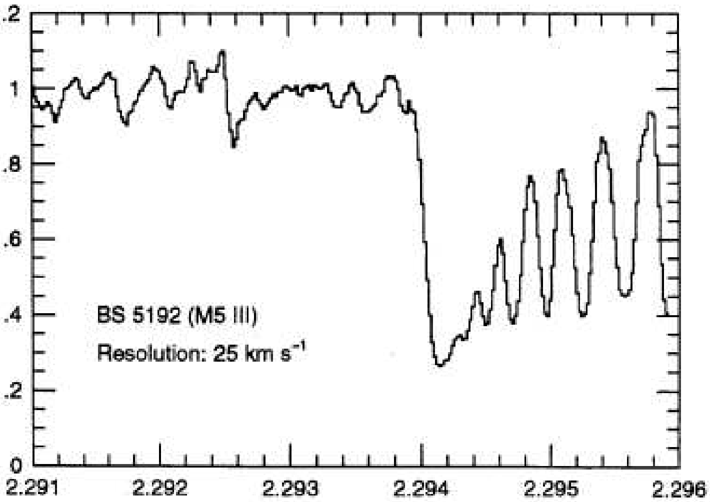

Figure 1.14: CO absorption band, at $\lambda \sim \mu$m (Blum et al. [1995]), used to determine radial velocity in the infrared.

σ_{los} increases toward the center, with a value in the innermost field of $\sigma_{los} = 153 \pm 17$km s^{-1}.

Minniti [1996], studying the kinematics of red giants in a field (at $l = +8$, $b = +7$) where there is a significant (∼30% of the sample) halo component, found that: (i) the bulge is rotating (54.4 ± 4.7 km s^{-1} is the mean Galactocentric velocity for the studied regions); (ii) the radial velocity dispersion σ_{los} decreases with increasing Galactocentric radius ($\sigma_{los} = 85 \pm 7$ km s^{-1}); (iii) there is a kinematic separation between metal rich bulge ([Fe/H]≥ -1) and metal-poor halo ([Fe/H]≤ -1) population, hinting to the fact that bulge and halo are two distinct Galaxy components. This was confirmed by Tiede & Terndrup [1999] who found similar results for a field at ($l = +8$, $b = -6$), symmetric with respect to the galactic plane to the one of Minniti [1996], meaning that the rotation is symmetric, at least in the outer regions of the bulge.

In general anyway the bulge kinematics is not very clear and its knowledge will hopefully improve in the future. Sumi et al. [2004] obtained a proper motion catalogue for 5 millions of stars in the direction of the bulge, using the OGLE photometry , but so far no extended study of this catalogue has been made.

1.3.5 The bulge age

Dating the bulge is complicated by several factors, such crowding, depth effects, variable reddening, metallicity dispersion and contamination by foreground disk. To reduce these factors, globular clusters, whose kinematics properties and metallicity distribution are not distinguishable from the ones of bulge stars, are often observed. Ortolani et al. [1995] studied NGC 6528 and NGC 6553, whose bulge membership is confirmed also by the proper motions: they found that the color magnitude diagrams of the clusters are basically identical, indicating same age and metallicity; also the difference of magnitude between the turnoff (TO) and the HB red clump in the CMD, indicating the age, is the same as that of an inner halo globular cluster NGC 104; and finally, the luminosity function (LF) of these clusters is identical to that of the stars in the Baade's Window. From all the evidence, Ortolani et al.(1995) concluded that the bulge underwent rapid chemical enrichment to solar abundance and beyond, very early in the evolution of the Galaxy, and the bulk of the stars formed nearly at the same time as the halo globular clusters and no more than 10% of the bulge population can have intermediate age.

Zoccali et al. [2003] estimate the bulge age comparing the luminosity difference between the HB clump and the Main Sequence turnoff of the bulge

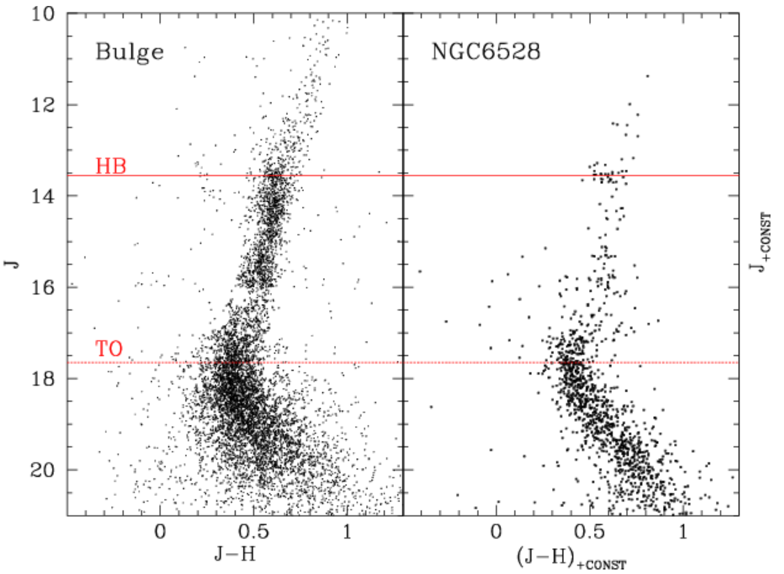

Figure 1.15: Comparison between the color-magnitude diagrams of a bulge field and NGC 6528 (Zoccali et al. 2003): the fact that turn-off (TO) and horizontal branch red clump have the same magnitude is a hint that the two pupulations are coeval.

to that of a globular cluster of similar metallicity, namely NGC 6558, whose metallicity is close to the average of the bulge. Fig. 1.15 shows this comparison and that the magnitude difference between the HB clump and the turnoff is virtually identical in the two diagrams: since $\delta age/age \simeq \delta(\Delta M_{TO}^{HB})$[6] (Renzini [1991]), the difference between the age of the cluster and the mean age of the bulge cannot be larger than $\sim 20\%$, reinforcing the conclusion of Ortolani et al. [1995] that the bulk of the bulge population is coeval to the two clusters NGC 6528 and NGC 6553. Moreover, the absence of an extension of the bulge main sequence beyond the turnoff rules out the presence of an intermediate-population.

---

[6] ΔM_{TO}^{HB} is the difference of magnitude between the Turn Off and the Horizontal Branch.

Chapter 2

Spectroscopic Data Reduction

I obtained the observations at the ESO Very Large Telescope with UT1 (Kueyen), equipped with the visual and near UV Focal Reducer and low dispersion Spectrograph (FORS2, Appenzeller et al. [1998]), on the nights June 22-23, 2004. FORS2 is an instrument designed for the wavelength range from 330 nm to 1100 nm, with a resolution $R = \lambda/\Delta\lambda = 260 - 2600$. The detector consists of a mosaic of two 2k×4k CCDs. The instrument field size is 6.8×6.8 arcmin with a scale of 0.20"/pixel.

In order to increase the number of spectra taken with one exposure, the Mask Exchange Unit (MXU), which can hold pre-prepared masks with slits for a large number of objects over the field of view, was used. Fig. 2.1 is an example of a mask applied to one of our fields.

As dispersing element I used the grism GRIS_600B, with a wavelength range of 330-621 nm and a dispersion of 50 $\AA/mm$. The adopted slit width and length are 0.7" and 20" respectively. Since the targets are distributed at different positions on the CCD, their spectra do not have the same wavelength range. The sdB star candidates are listed in Tab. 2.1.

In order to extract scientific data from the raw data, a number of data reduction steps have to be applied. These steps are described in the following sections.

2.1 Cosmic ray correction

Cosmic-ray hits cause defects in all astronomical images obtained with CCD detectors. The most usual approach to remove traces of cosmic rays from such images uses multiple frames of the same object and then combines them adopting an algorithm for rejecting the outlying data. But in many cases it is not possible to obtain multiple images of the same object, or the required

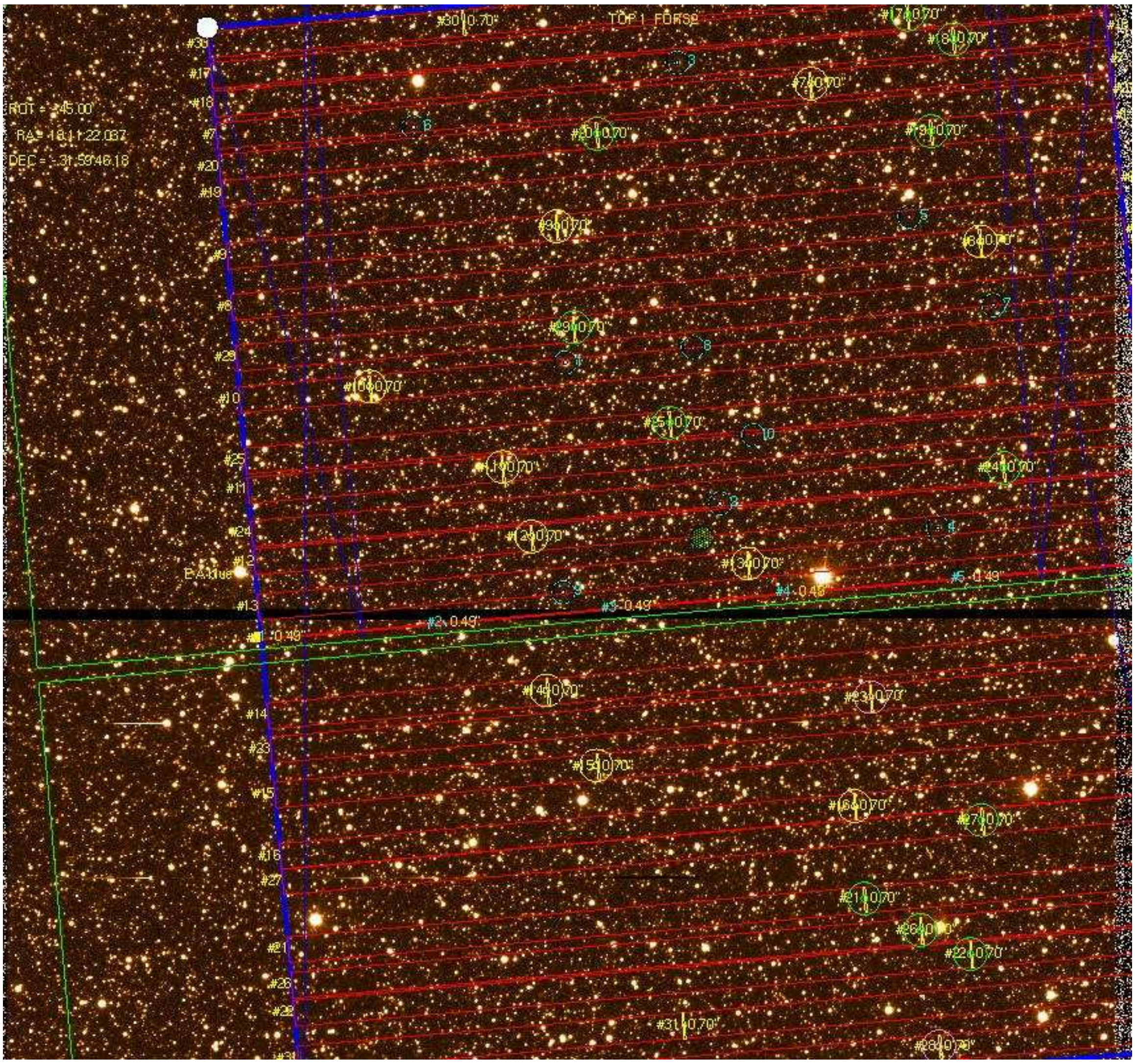

Figure 2.1: Example of MXU mask applied to one of the target bulge fields (this is a mosaic image, the two CCDs are shown). The details of two slits are shown in Fig.2.7.

target	α	δ	V	I
bulge1				
1001	18:11:20.48	-31:59:42.46	20.767	20.330
1002	18:11:25.99	-32:00:27.69	19.546	19.315
1003	18:11:28.01	-32:00:14.19	19.348	19.051
1004	18:11:21.42	-31:57:10.19	18.882	18.656
1005	18:11:28.39	-31:57:05.14	19.692	19.425
1006	18:11:13.30	-32:00:28.02	20.711	19.992
1007	18:11:20.03	-32:01:19.40	20.980	20.451
1008	18:11:32.63	-32:00:22.92	21.209	20.765
1009	18:11:31.46	-31:58:49.81	21.243	20.553
1010	18:11:22.64	-32:01:09.47	20.565	19.966
bulge2				
2001	18:09:22.15	-31:46:10.11	19.207	18.806
2002	18:09:24.66	-31:46:39.70	19.961	19.761
2003	18:09:31.40	-31:48:04.36	19.674	19.496
2004	18:09:31.28	-31:45:52.57	20.293	20.032
2005	18:09:15.96	-31:50:30.17	19.393	18.936
2006	18:09:09.43	-31:46:36.39	19.836	19.668
2007	18:09:15.29	-31:48:36.56	20.181	19.700
2008	18:09:14.15	-31:47:19.46	19.679	19.320
2009	18:09:17.07	-31:48:10.03	20.334	19.951
3010	18:09:15.29	-31:46:36.25	20.330	19.981
bulge3				
3001	18:09:08.50	-31:54:30.59	19.928	19.479
3002	18:09:14.16	-31:52:58.34	20.122	19.757
3003	18:09:13.91	-31:52:42.29	20.201	19.805
3004	18:08:58.64	-31:53:50.65	20.456	20.193
3005	18:09:03.79	-31:51:53.52	20.680	20.036
3006	18:08:58.87	-31:52:33.74	20.553	20.327
3007	18:08:55.81	-31:52:15.47	20.515	20.212
3008	18:09:17.33	-31:56:09.44	19.311	18.731
3009	18:09:16.04	-31:53:45.66	20.356	19.744

Table 2.1: Observed sdB star candidates. For each setup (bulge1, bulge2, bulge3), the target coordinates (2^{th} and 3^{th} columns) and V,I magnitudes (4^{th} and 5^{th} columns) are listed.

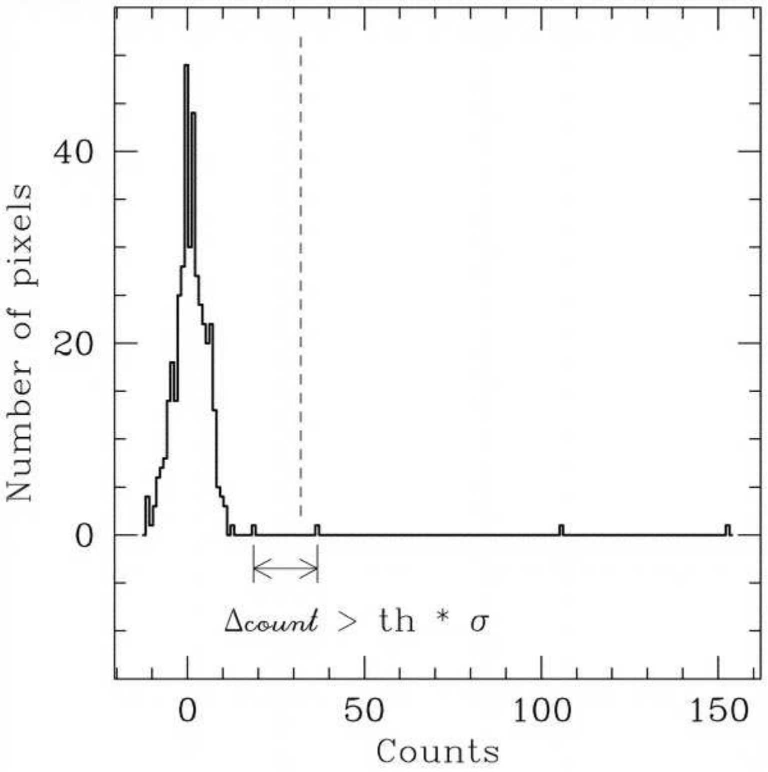

Figure 2.2: Histogram used in a typical application of the cosmic-ray detection algorithm. The vertical dashed line marks the lower limit of counts regarded as the cosmic rays. The arrows mark the first gap in the histogram with a width larger than the threshold (from Pych [2004]).

exposure time prevents from using multiple-image methods, as in our case, where the exposure times are very long.

Therefore I adopted the approach of Pych [2004], which is very effective when applied to the images with spectroscopic data. Their program *dcr* divides the whole frame in small overlapping frames. For each subframe it calculates the standard deviation of the distribution of counts. The standard deviation is then corrected for outlying pixels applying a σ-clipping step and will be used to define a threshold value.

In fact, after having constructed a histogram of the distribution of counts (see Fig.2.2) and having found its mode, there are some gaps in the histogram. If a gap wider than the threshold is found, the pixels above such a gap are assumed to be affected by cosmic rays and are substituted with the average of counts in the neighboring pixels. Since cosmic rays are often multiple-pixel events, the procedure of detection and cleaning runs iteratively. The threshold value I used is 3.5.

2.2 Bias and Flats

A bias current is routinely applied to CCD detectors in order to avoid negative values, which would confuse the analogic-digital conversion. This current has the effect that a non-zero count is recorded in all pixels. I obtained *bias frames* to estimate the effect. The average of the bias frames have been smoothed and the result subtracted from all other frames before using them in the reduction.

All CCDs have non-uniformities, i.e. even a uniformly illuminated CCD does not yield the same signal in each pixel. On small scale this is caused by slight differences in pixel sizes, on larger scale for example by small variations in the silicon thickness across the chip. To correct for this effect, flat images have been taken (an example is shown in Fig.2.3), illuminating the CCD with a lamp. These frames have been averaged, then the slits have been extracted, cutting the images on the borders of each slit, and each "slit flat image" has been normalized, dividing by the corresponding averaged smoothed flat image. Fig.2.4 shows a comparison between a not normalized and normalized flat image.

After Bias subtraction, the "data slit images" have been extracted by the frames from the frames containing the spectra. Finally, the flat field correction, was performed by dividing each data slit image by the corresponding normalized slit flat image.

2.3 Wavelength calibration and rebinning

The next step has been to convert the positions of the spectral lines from the coordinates in pixels to wavelength (Å). Using calibration frames, produced by illuminating the slits with a calibration lamp (in this case a He-Ne lamp), the lamp spectrum for each slit was obtained (see Fig.2.5). Since the slits have different positions in the CCD, each slit shows a different portion of the spectrum (Fig.2.5). Comparing the slit spectra with the template lamp spectrum provided by ESO (Fig.2.6), it is possible to find the slit wavelength range and the correspondence between pixel and Å for each slit.

The slit images have been rebinned two-dimensionally with a step size of 0.5 Å (the raw spectra have a step size of 1.5 Å) along the dispersion axis.

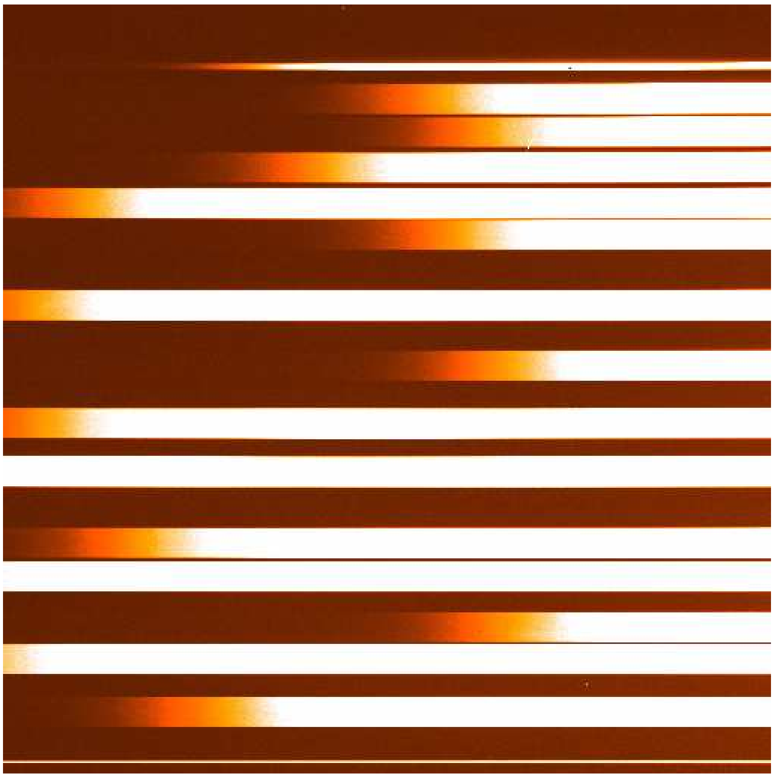

Figure 2.3: Example of a flat field image, with cuts=[0,10000].

Figure 2.4: Example of slit images extracted from the flat field frame; at the top the raw (not normalized) image is shown, with cuts=[0,10000], while at bottom the normalized image is shown, with cuts=[0.9,1.1]

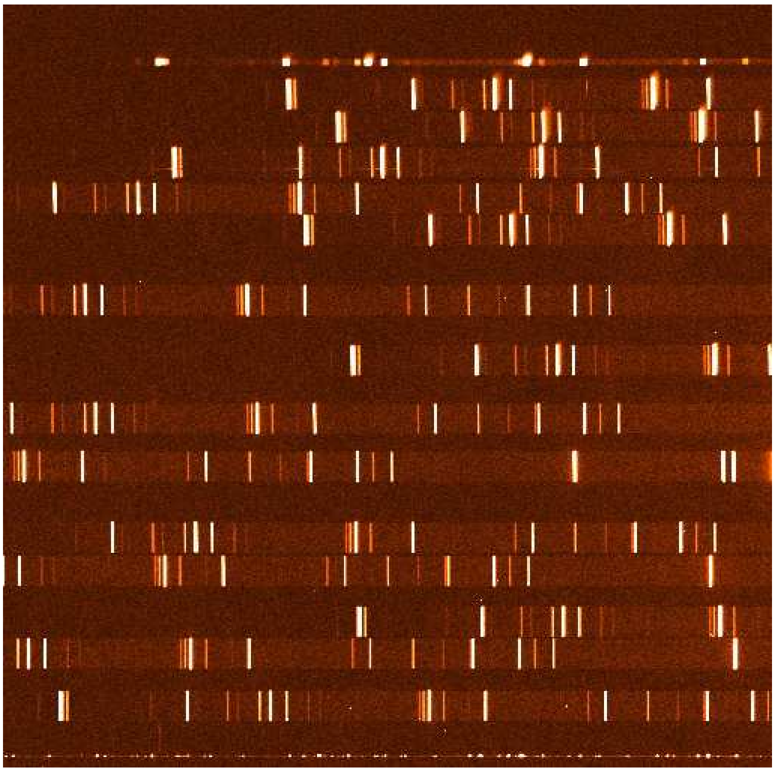

Figure 2.5: Example of one lamp image: the lines in the spectrum of the lamp are evident. The smallest spectra at the top and at the bottom of the CCD are those of the reference stars.

2.4 Sky correction and spectrum extraction

The observed field is quite crowded and some targets have other stars very close to them, causing some problems in the measure of the sky background. Two different methods were used, depending on the crowding of the target star.

If the star was isolated, meaning that if there were other stars in the slitlets (Fig.2.7, bottom), they were sufficiently separated from our target to identify regions uncontaminated by any stellar source, the spatial distribution of the sky background was approximated by a constant (see Fig.2.8).

If the slitlet showed severe crowding (an example is shown in Fig.2.7,top), meaning that the spectra were overlapping, each stellar profile was fitted with a Moffat function:

$$f(x;a,b,c,d) = a[1+((\frac{2(x-b)}{c})^2]^{-d} \tag{2.1}$$

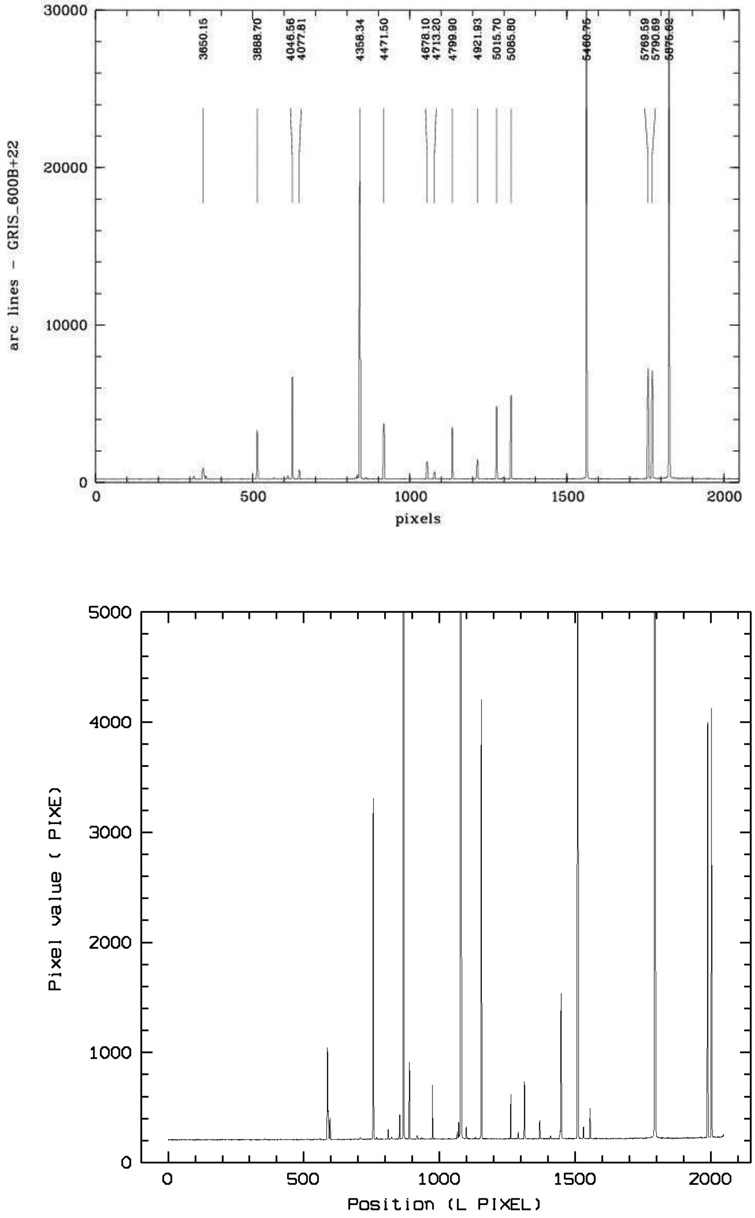

Figure 2.6: Top: Reference arc lamp frame provided by FORS2@ESO web page; bottom: example of 1-dimension calibration frame acquired during observations (for one slit). The wavelength calibration is obtained comparing the two plots.

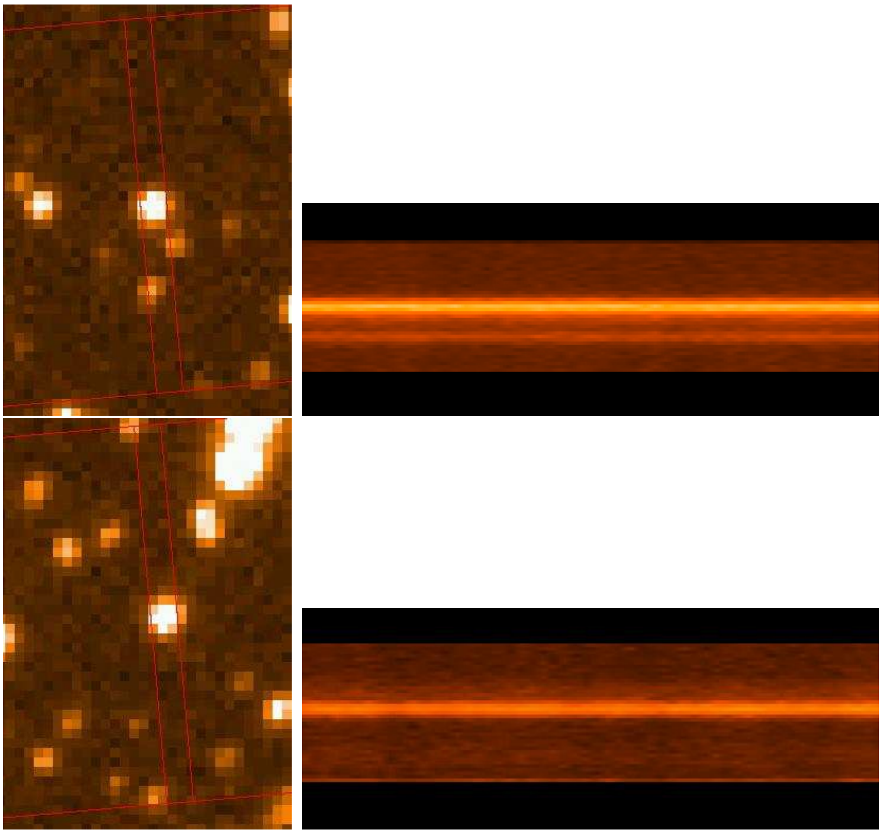

Figure 2.7: Examples of crowded (top) and isolated star (bottom), with the corresponding spectra.

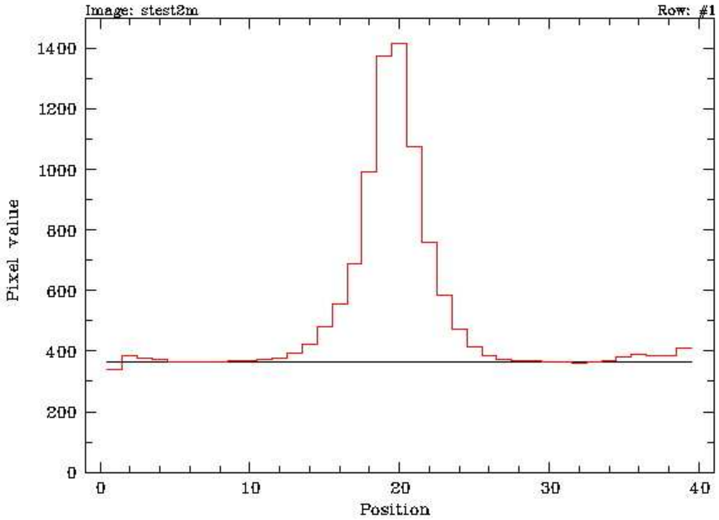

Figure 2.8: Example of sky subtraction in the case of an isolated star: the profile of the star spectrum is shown in red, while the sky backround is the black line.

where x is the spatial coordinate along the slit, a,b,c are the function parameters representing the function value at the profile peak, the profile center, the half width half maximum respectively. The exponent d is the parameter om which the spread of the profile wings depends, and it has been fixed to 1.

The whole spatial profile along the slit was reproduced by the sum of all the profiles; all the profiles but the one of the target were then subtracted (see Fig.2.9) as background. The target spectra were then extracted using the algorithm *extract/long* in MIDAS (Horne [1986]): the rows of the spectrum are added with weights which are determined by the S/N ratio. Remaining cosmic ray hits are removed by analyzing the profile perpendicular to the dispersion.

2.5 Corrections for the atmospheric extinction, detector response and radial velocity

The atmosphere influences the quality of the observations since it absorbs some of the radiation arriving on the Earth. The absorption depends on the wavelength of the incoming radiation following an extinction law. To correct

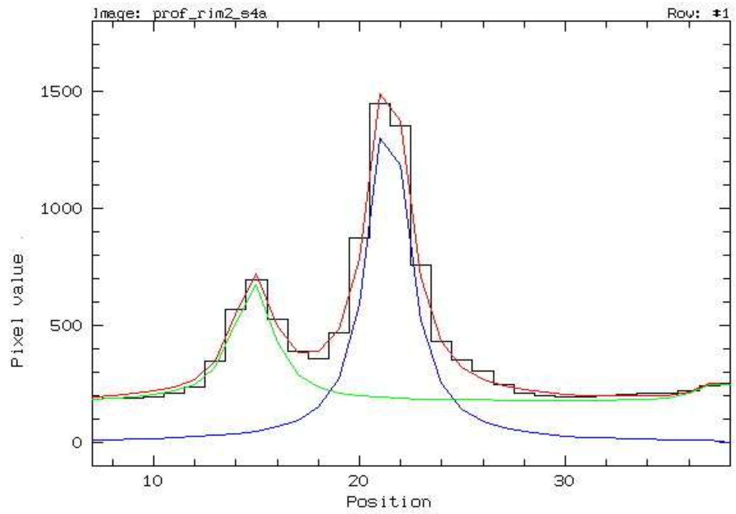

Figure 2.9: Example of sky subtraction in the case of a crowded slit: in blue the profile of the target star, in green the profile of the close star and the sky background, in red the sum of the two profiles.

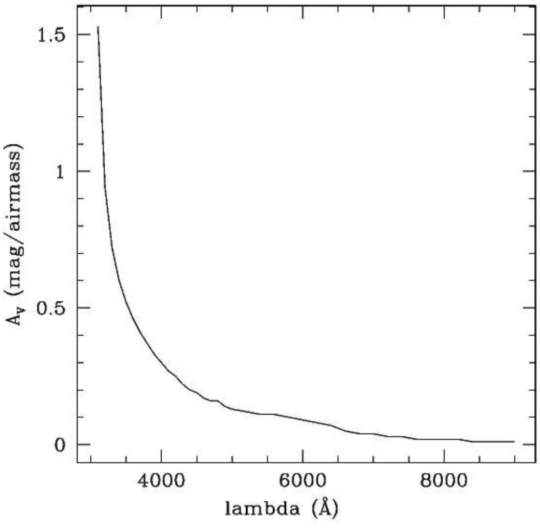

Figure 2.10: Extinction law for the LaSilla site (Tug [1977]), describing how the absorbtion due to the Earth atmosphere varies with the wavelength of the incoming radiation

this effect, the task *extinction/long* in MIDAS, which uses the extinction law described by Tug [1977] for the LaSilla site (shown in Fig.2.10) was used.

To account for the response of the complete system (seeing, optical sys-

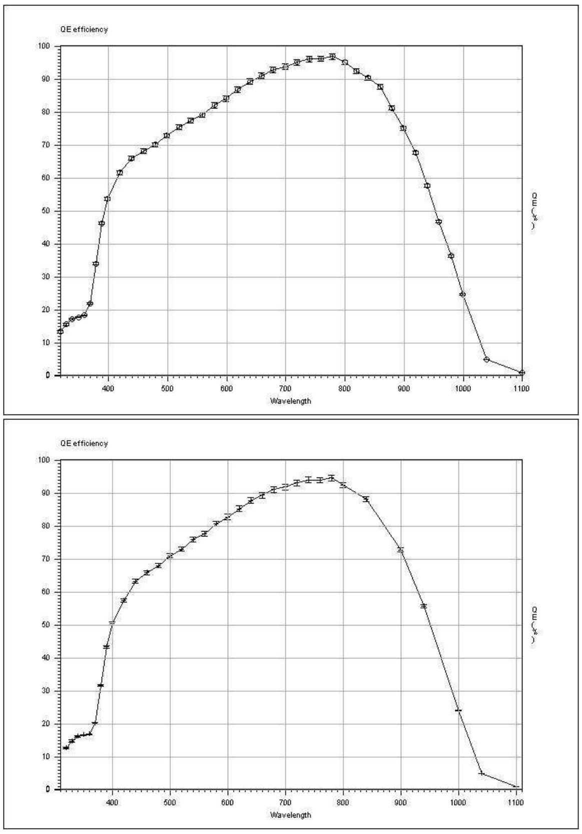

Figure 2.11: Quantum efficiency curves of the FORS2 CCDs, provided by ESO

tem, detectors, etc..), which could vary from night to night because of the weather and other factors, each spectrum was divided by the corresponding night response curve obtained from standard stars observations in the same nights.

2.5.1 Standard stars

As already mentioned, the targets spectra were corrected for the response of the system, dividing them by the system response curve, which has been calculated by means of standard stars observations. It is necessary to do that because the quantum efficiency (Q.E.) of the detector, the telescope response and the spectrograph efficiency vary with the wavelength. In Fig.2.11 the Q.E. curves[1], provided by ESO, for the two CCDs of FORS2 are shown.

---

[1] http://www.eso.org/projects/odt/Fors2/qeu.html

In theory the system response should be always the same (without the atmosphere effects), but in different nights it could be slightly different. Therefore spectrophotometric standard (see Tab. 2.2) stars[2] were observed each night, to obtain the night's response curve .

star	α_{2000}	δ_{2000}	Sp. Type	V	(B-V)
EG274	16h23m33.75s	−39°13'47.5"	DA	11.03	−0.14
G60-54	13h00m09.53s	+03°28'55.7"	DC	15.81	+0.64
LTT4816	12h38m50.94s	−49°47'58.8"	DA	13.79	+0.17
LTT9491	23h19m34.98s	−17°05'29.8"	DC	14.10	+0.03

Table 2.2: Spectrophotometric standard stars (from ESO website)

In order to obtain a better sampling of the whole CCD λ-range, each standard star was observed in different positions on the CCD. In this way the spectra start and end at different wavelengths and therefore have different λ-extensions.

Regarding the reduction of the spectra, the procedure is the same as before: the images have been corrected for bias, flat-fielded and rebinned, the spectra were extracted after the sky subtraction and corrected for atmospheric extinction. Since the standard stars have been observed at different times when the conditions were not perfect, the spectra have been normalized to the same flux at $\lambda = 5250$ Å to bring them to the same level. The differences between different spectra of the same standard star anyway were small (see Fig.2.12). Finally, comparing these spectra with the flux values provided by ESO (Oke [1990], Hamuy et al. [1995]), the response curves for each standard have been calculated and then fitted with splines.

In this way I have got several response curves, one for each standard star, which overlap in different ways, because they have different wavelength coverage. I grouped then the response curves with the same wavelength extension and for each group I calculated the median. The median curves overlap at the extremes, therefore to obtain an unique curve, I considered in the wavelength region where they overlap (for example between λ_1 and λ_2), a linear combination of the curves:

$$y = \frac{\lambda-\lambda_2}{\lambda_1-\lambda_2} y_1 + \frac{\lambda-\lambda_1}{\lambda_2-\lambda_1} y_2$$

In Fig.2.13 there is an example of the response curve obtained for one of the observing nights.

---

[2] www.eso.org/instruments/fors/tools/FORS_Std/FORS2_Std.html

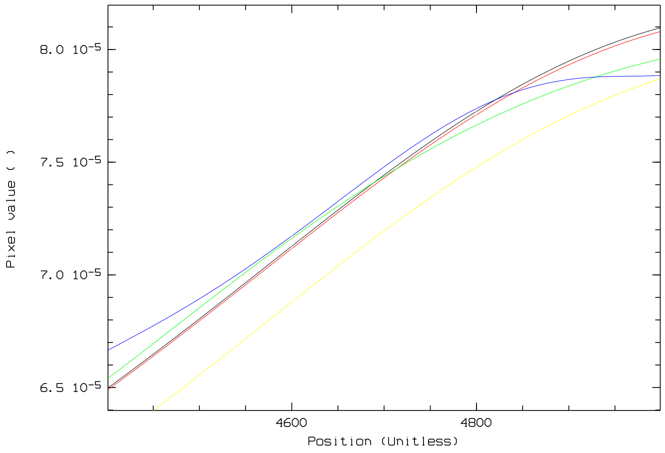

Figure 2.12: Example of different response curves for one standard star (in this case EG 274)

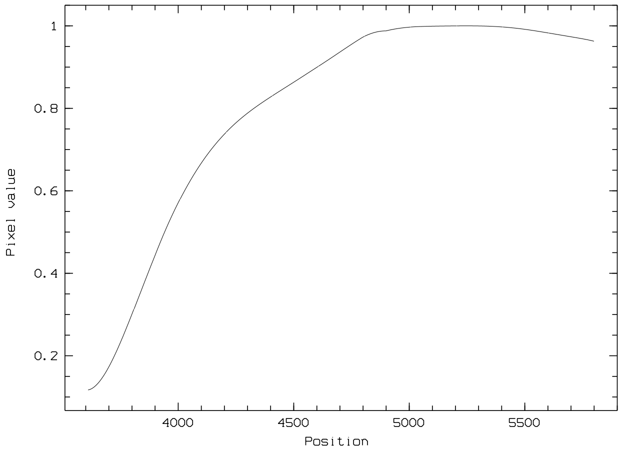

Figure 2.13: Response curve obtained for one of the observations nights (in this case for the 22 June 2004 night)

2.5.2 Radial velocity correction

Owing to the motion of the stars and the Earth, their spectra are shifted because of the Doppler effect:

$$\Delta\lambda/\lambda = (\lambda - \lambda_0)/\lambda = v_r/c \tag{2.2}$$

where λ is the observed wavelength, λ_0 is the laboratory wavelength, v_r is the radial velocity of the star and c is the light velocity.

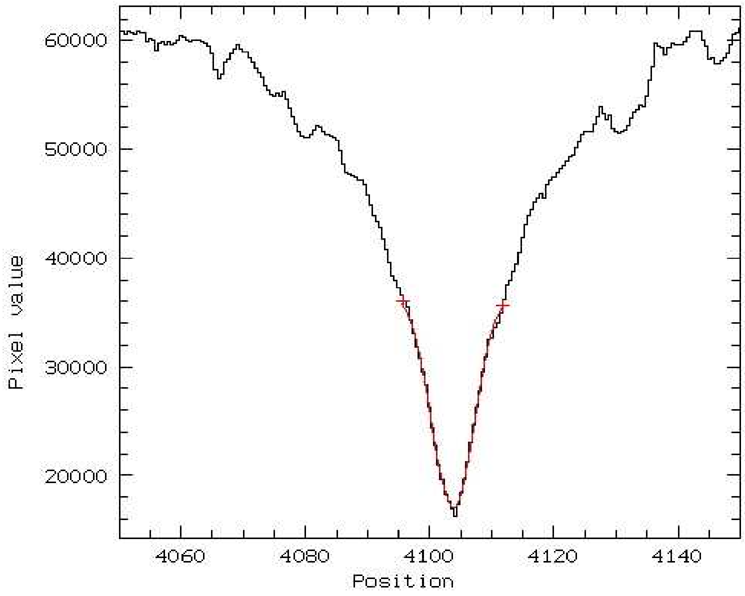

Figure 2.14: Example of core fit of one of the Balmer lines, in this case H_δ=4101.73 Å.

To find the shift in wavelength, the cores of the Balmer lines in each spectrum were fitted with a Gaussian (see example in Fig. 2.14). Comparing its position with λ_0, the radial velocity is then calculated for each line and all the values are averaged. The uncertainty is calculated as RMS[3] error. The average value v_r is used to calculate the shift $\delta\lambda$, which then is applied to the spectrum via the formula 2.2.

In Table 2.3 the radial velocities of the targets are listed. The heliocentric values have been corrected for the motion of the Earth around the Sun.

2.6 Median of the spectra

Finally, in order to obtain a better signal/noise ratio, I calculated for each target the median of all spectra. The total number of spectra for each target varies: in case of the fields *bulge 1* and *bulge 2* there are 4 long exposures for each field. Since during the observations, the cosmic ray problem (due, indeed, to long exposures) came out, for the remaining field, *bulge 3*, the exposures were split, obtaining then 9 images.

To obtain a better definition of the H and He I and II lines, all the spectra

---

[3] RMS=root mean square

Table 2.3: Radial velocities for *bulge*1

star	v_r (km sec^{-1})
bulge1	
1001	284 ± 50
1002	-50 ± 40
1003	-138 ± 50
1004	28 ± 50
1005	-204 ± 40
bulge2	
2001	18 ± 20
2002	-28 ± 30
2003	137 ± 30
2004	-20 ± 30
2005	-34 ± 45
2006	74 ± 15
2007	-33 ± 35
2008	12 ± 20
2009	-98 ± 30
2010	34 ± 40
2011	132 ± 30
bulge3	
3001	160 ± 40
3002	174 ± 40
3003	19 ± 30
3004	242 ± 40
3005	103 ± 30
3006	14 ± 60
3007	30 ± 40
3008	170 ± 25
3009	11 ± 40

for one target were scaled to the same flux at $\lambda = 4200$ Å. To do that, the median of the continuum in the region $4150 < \lambda < 4250$ Å was taken and the spectrum was divided by this value.

Before calculating the average spectra, I ought to keep in account that some of the images were taken when the seeing was extremely good. In Fig.2.15 the seeing during the observations night is shown: during the second night it went under 0.4". In this case the point spread function (PSF) of the stars was smaller than the slit width, causing a seeing-limited instead of a slit-limited resolution. Therefore, some spectra have been taken with a different resolution.

The slit width was 0.7" . Keeping into account a pixel scale of 0.126"/pixel (unbinned), this corresponds to a resolution of 4.175 Å. In the moments with the excellent seeing, the resolution went down to 2.75 Å for the first night and 2.2 Å for the second night. In order to produce an homogeneous data set, the spectra taken when the seeing was excellent were convolved with a Gaussian function whose FWHM was $(4.175^2 - 2.75^2)^{1/2}$ the first night and $(4.175^2 - 2.2^2)^{1/2}$. Effectively, this "smooths" the spectra to the resolution of 4.175 Å as given by the slit width.

Finally, the spectra were averaged and fitted with models. In the next pages (see Fig. 2.16, 2.17, 2.18) all resulting spectra are shown. The different wavelength coverage of the spectra is due to different positions of the slits on the CCDs.

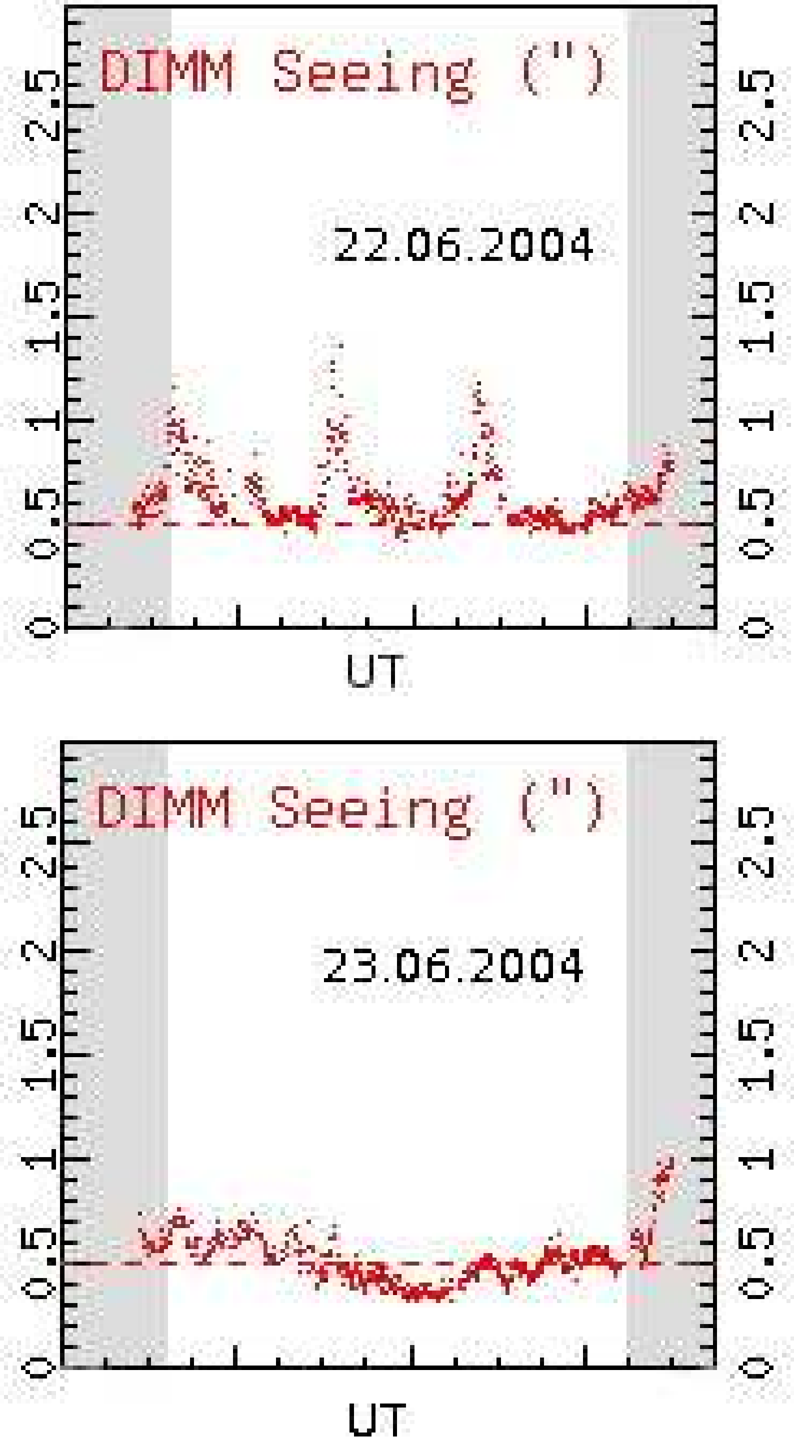

Figure 2.15: Seeing during both nights.

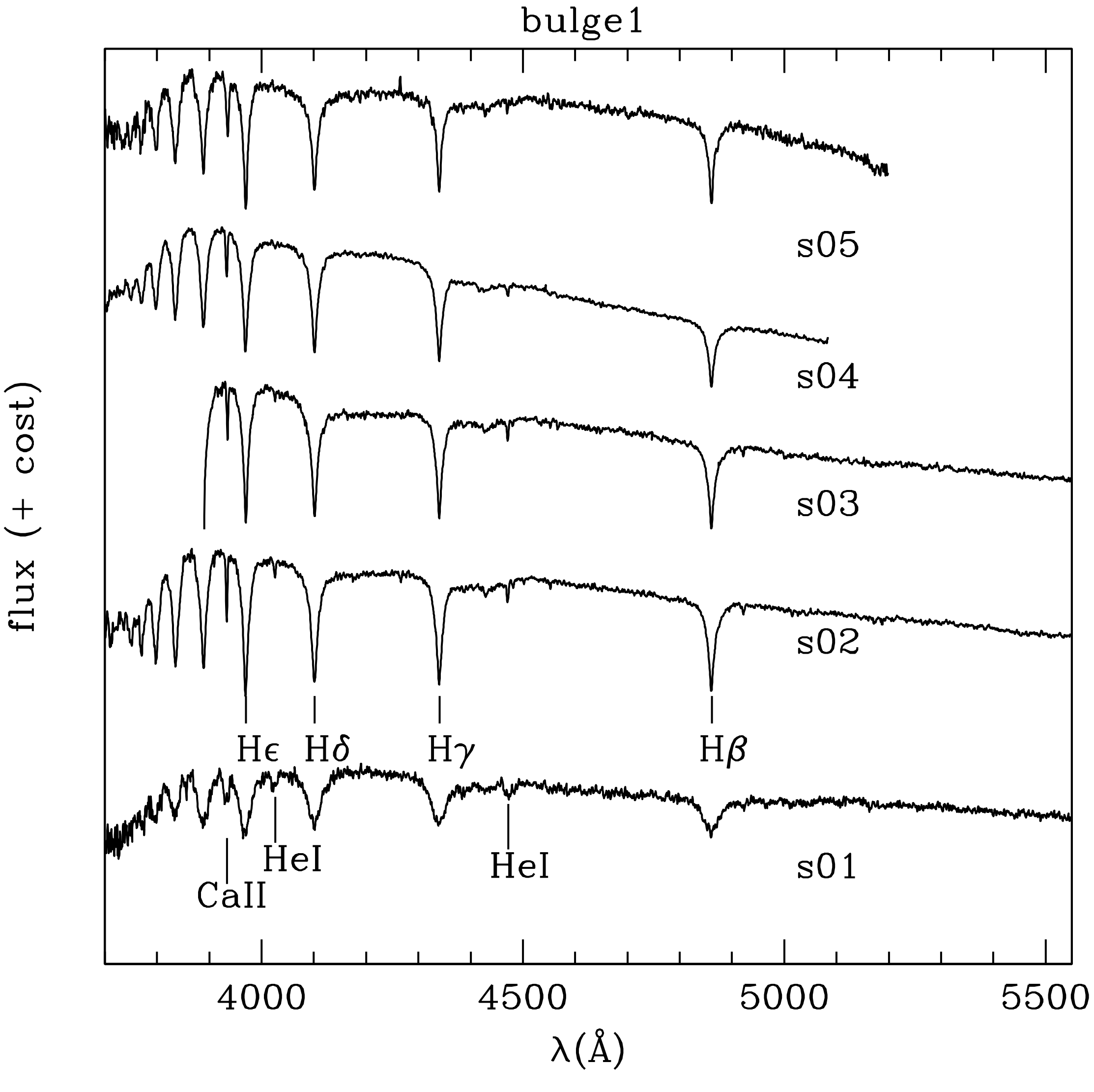

Figure 2.16: Averaged spectra obtained for the field *bulge*1.

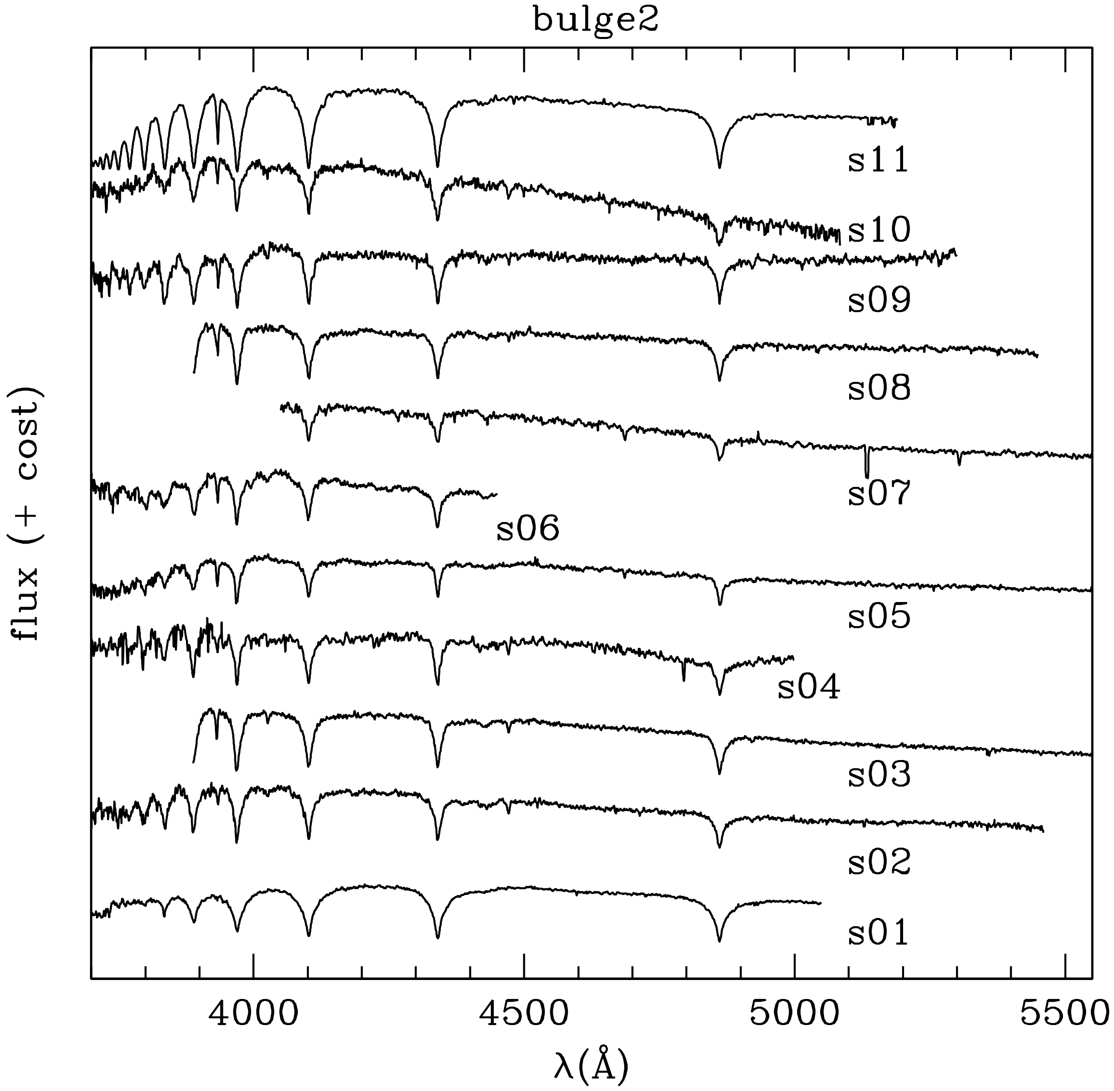

Figure 2.17: Averaged spectra obtained for the field *bulge*2.

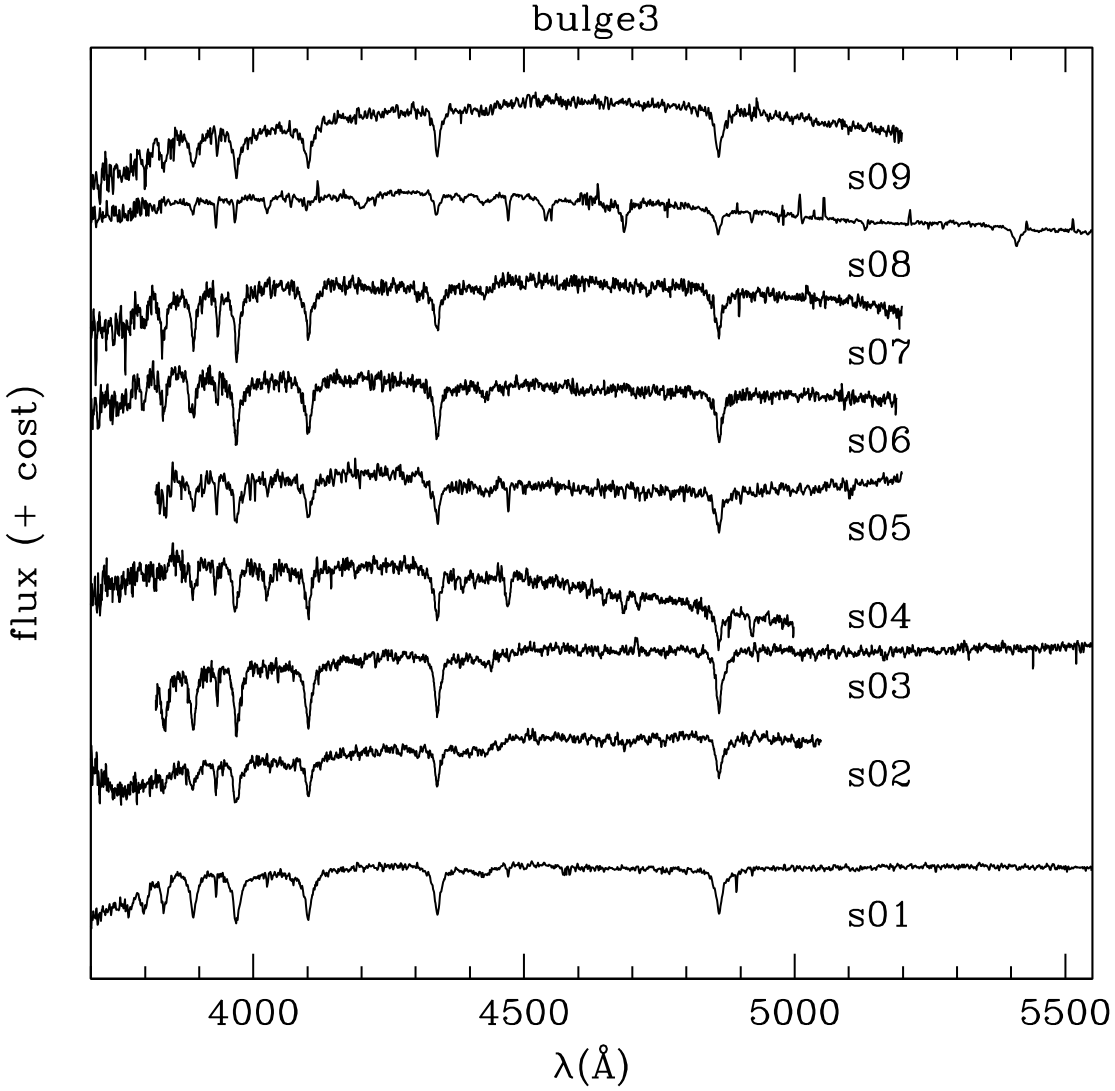

Figure 2.18: Averaged spectra obtained for the fields *bulge*3.

Chapter 3

Analysis of the spectra

To derive effective temperatures, surface gravities and helium abundances and then understand which kind of stars were observed, the Balmer and helium lines were fitted with stellar model atmospheres.

3.1 The models

To fit the spectra, the ATLAS9 model atmospheres (Kurucz [1993]) were used. These models are LTE models, meaning that they assume Local Thermal Equilibrium inside the stellar atmosphere. They are available for scaled solar abundances:

$$[Fe/H] = log\frac{Fe/Fe_{\odot}}{H/H_{\odot}} = -5.0 \div +1.0 \tag{3.1}$$

Stars in the Galactic bulge show different metallicities while the average value is sub-solar (see Sec.1.3.3). I chose the solar metallicity to keep in account effects of radiative levitation, which can enhance the metal contents in the stellar atmosphere. The models have a good coverage with regard to the temperature range (T$_{eff}$=3500$\div$50000 K) and the surface gravity (log$g$=0.0$\div$5.0 cm sec^{-2}); the helium abundance is solar. From these atmosphere models, spectra have been calculated with Lemke's version of the LINFOR program (developed originally by Holweger, Steffen, and Steenbock at Kiel University). During the analysis, some stars showed an enhanced Helium abundance. For these objects I used model atmospheres calculated by Werner & Dreizler [1999].

3.2 Fitting the data

To establish the best fit, I used the routines developed by Bergeron et al. [1992] and Saffer et al. [1994], as modified by Napiwotzki et al. [1999], which employ a χ^2 test. The first step is to normalize the spectral flux, in both observed and model spectra, to a continuum at a fixed distance from the line center. The model spectra are convolved to the observational resolution with a Gaussian profile and interpolated to the observed wavelength scale. The analysis is first performed assuming an initial value of the standard deviation σ equal to the noise in the continuum regions of the spectra. With the values of T_{eff}, $\log g$ and He abundance obtained by minimizing χ^2, a new value of σ is calculated from the rms deviation of the observed spectrum from the best-fit model spectrum.

The lines used for the fit are the Balmer lines H_β to H_{10} (excluding H_ϵ since it is blended with the Ca II H line), the He I lines at 4026, 4388, 4471, 4921 Å and the He II lines at 4542 and 4686 Å.

The result of the fit is given in Tab.3.1, where the χ^2, temperature, surface gravity and He abundances, are listed. Since the errors provided by the fit are underestimated (Napiwotzki 2004, priv.com.) by at least a factor 2, the values in the table are the fit errors multiplied by this factor.

In the next pages all the fitted spectra are shown (Figs. from 3.1 to 3.6). For two stars, 1001 in the *bulge1* field and 3008 in the *bulge3* field, the fit was really poor and I left them out from the analysis.

id	χ^2	T_{eff}	logg	logHe
1002	3.068	20600 ± 300	5.10 ± 0.04	−2.67 ± 0.02
1003	3.838	27100 ± 200	5.46 ± 0.03	−2.51 ± 0.03
1004	4.829	27800 ± 100	5.41 ± 0.02	−2.97 ± 0.02
1005	2.604	28700 ± 300	5.54 ± 0.04	−2.97 ± 0.06
2001	7.212	23900 ± 100	6.74 ± 0.04	−3.34 ± 0.02
2002	2.762	28500 ± 500	5.68 ± 0.05	−2.03 ± 0.03
2003	3.073	21300 ± 400	5.23 ± 0.07	−2.53 ± 0.03
2004	4.323	31900 ± 700	5.72 ± 0.08	−2.52 ± 0.10
2005	6.321	36300 ± 400	5.45 ± 0.06	−2.71 ± 0.07
2006	2.982	33900 ± 400	5.86 ± 0.06	−2.00 ± 0.06
2007	2.580	44600 ± 1700	5.65 ± 0.15	−2.71± 0.13
2008	3.503	29200 ± 400	5.77 ± 0.05	−2.43 ± 0.05
2009	3.677	24000 ± 700	5.24 ± 0.10	−2.80 ± 0.06
2010	2.176	32000 ± 400	5.86 ± 0.06	−2.04 ± 0.03
3001	2.670	26100 ± 700	5.43 ± 0.07	−2.57 ± 0.08
3002	3.137	39100 ± 600	6.00 ± 0.13	−3.46 ± 0.18
3003	1.473	20300 ± 1100	4.70 ± 0.12	−2.77 ± 0.12
3004	1.965	35700 ± 800	5.79 ± 0.13	−0.54 ± 0.04
3005	1.192	35100 ± 1800	6.10 ± 0.30	−1.51 ± 0.11
3006	1.482	28600 ± 900	5.46 ± 0.12	−3.08 ± 0.14
3007	1.927	31400± 1400	5.36 ± 0.18	−3.82 ± 0.82
3009	2.436	30400 ± 1600	5.67 ± 0.85	−3.15 ± 0.15

Table 3.1: Atmospheric parameters of the sdB stars. The stars are separated by setup (i.e. bulge field); in the first column there is the star id, i.e. 2003 means the third star of the second setup; in the next columns there are χ^2, effective temperature, surface gravity and helium abundance. The errors are the ones provided by the fit program multiplied by 2 (see text).

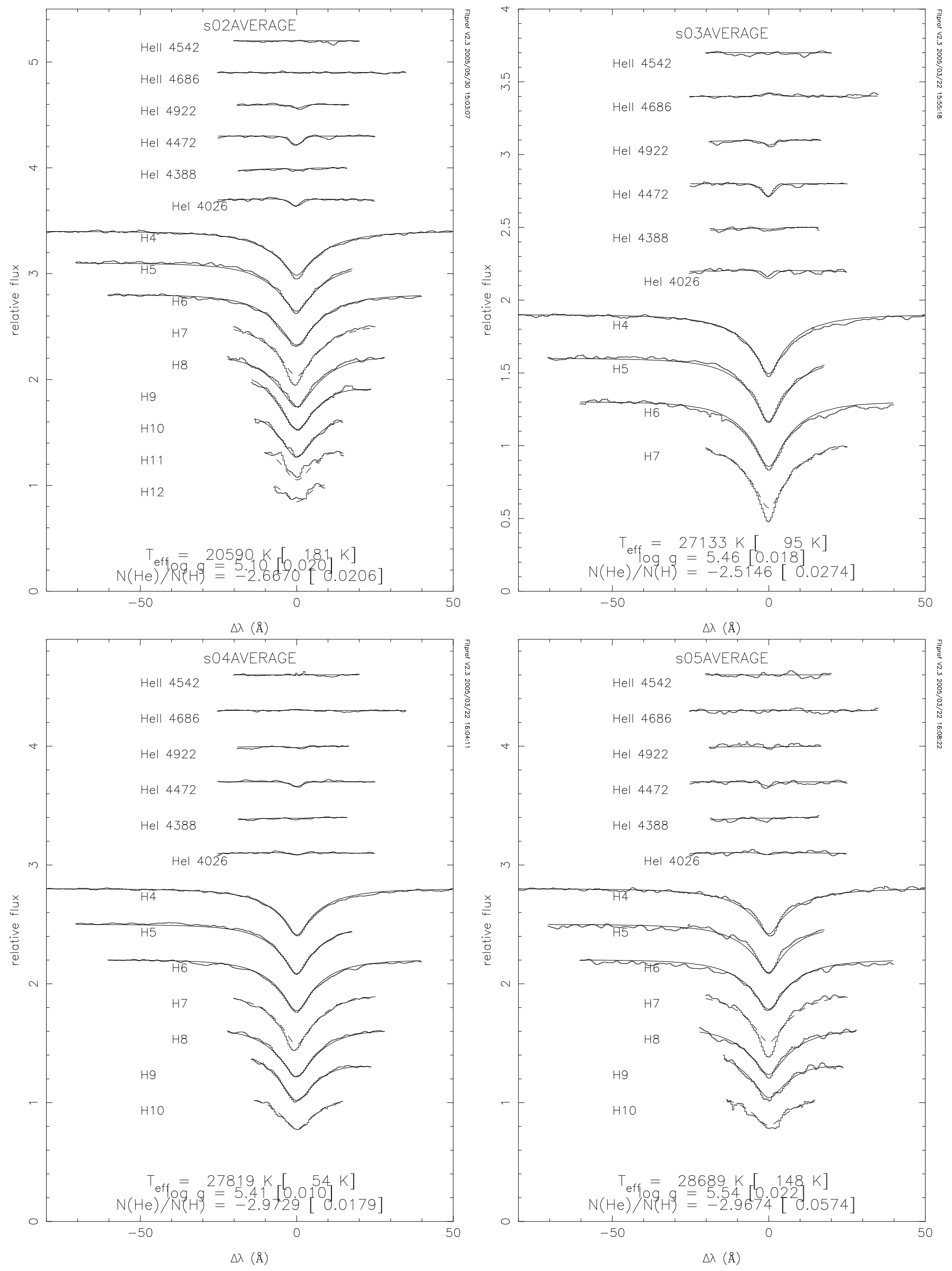

Figure 3.1: Best fit of the sdB star candidates spectra with theoretical models. These stars belong to the first setup, *bulge*1. Each panel is for one star. Observed and fitted line profile are shown. The dashed lines mean that the spectral line has not been used for the fit.

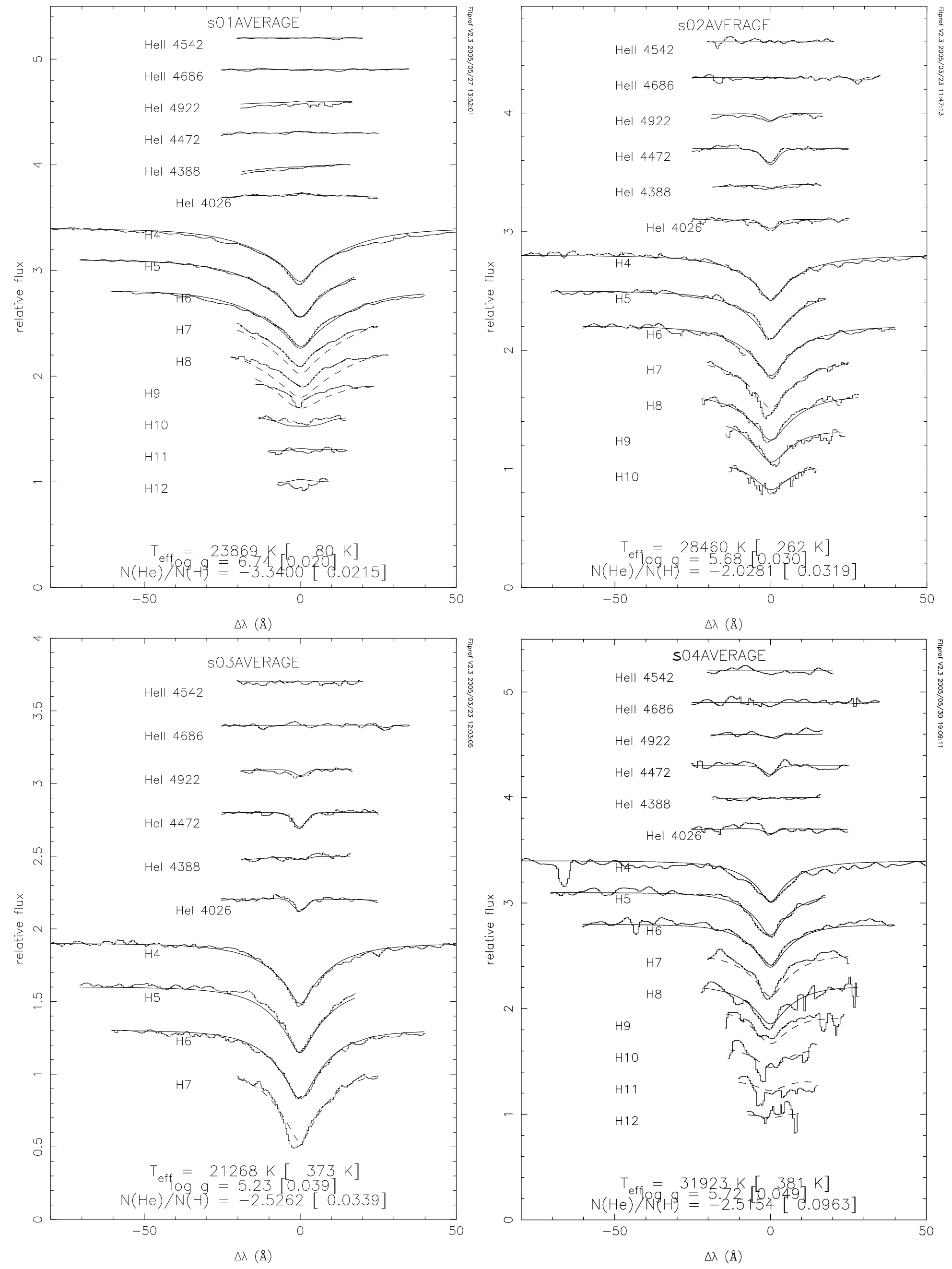

Figure 3.2: As in Fig.3.1, but for the field *bulge*2. The top left star probably has a cool companion, whose flux "raises" the depth of the Balmer lines.

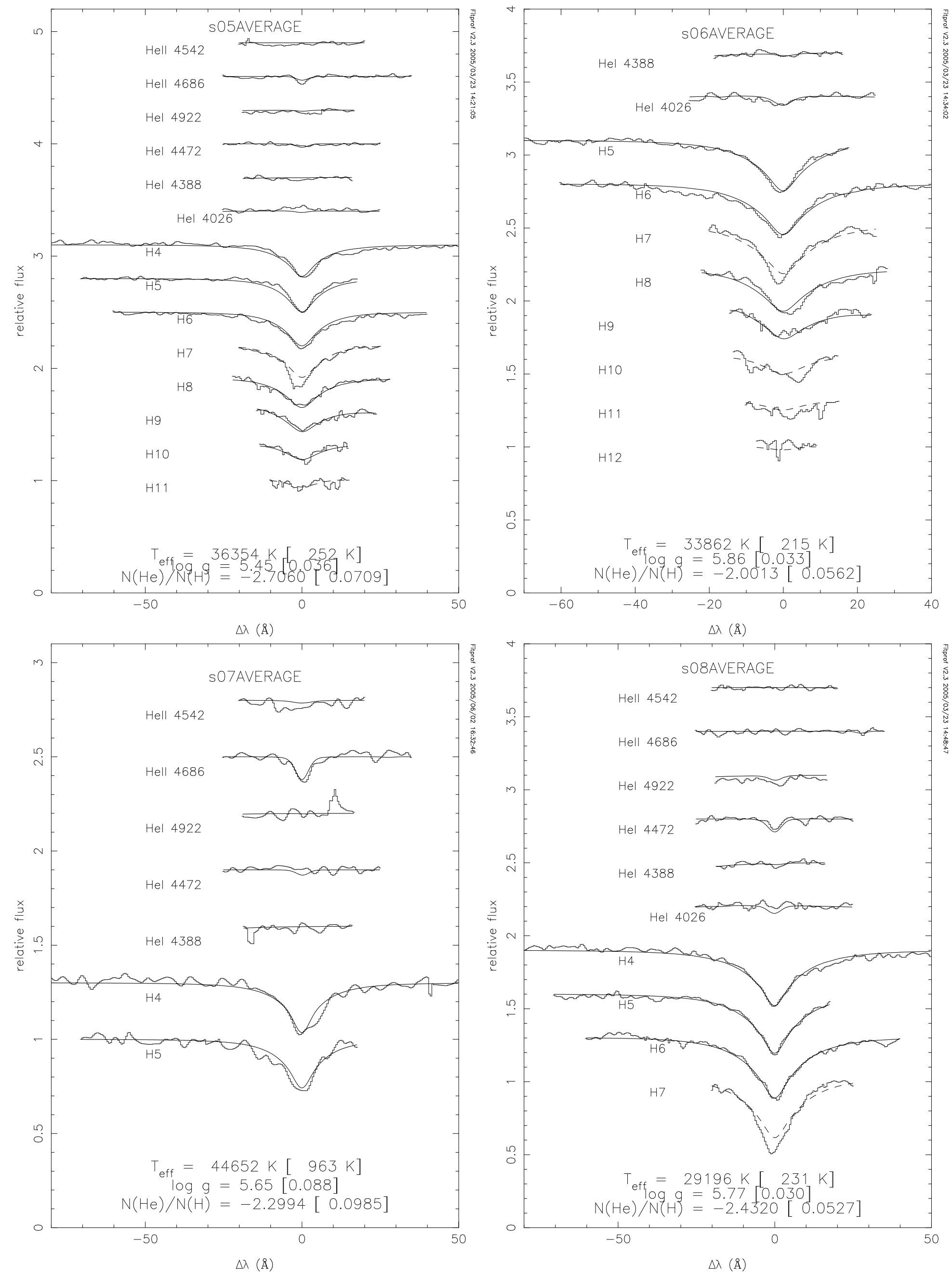

Figure 3.3: As in Fig.3.1, but for the field *bulge*2.

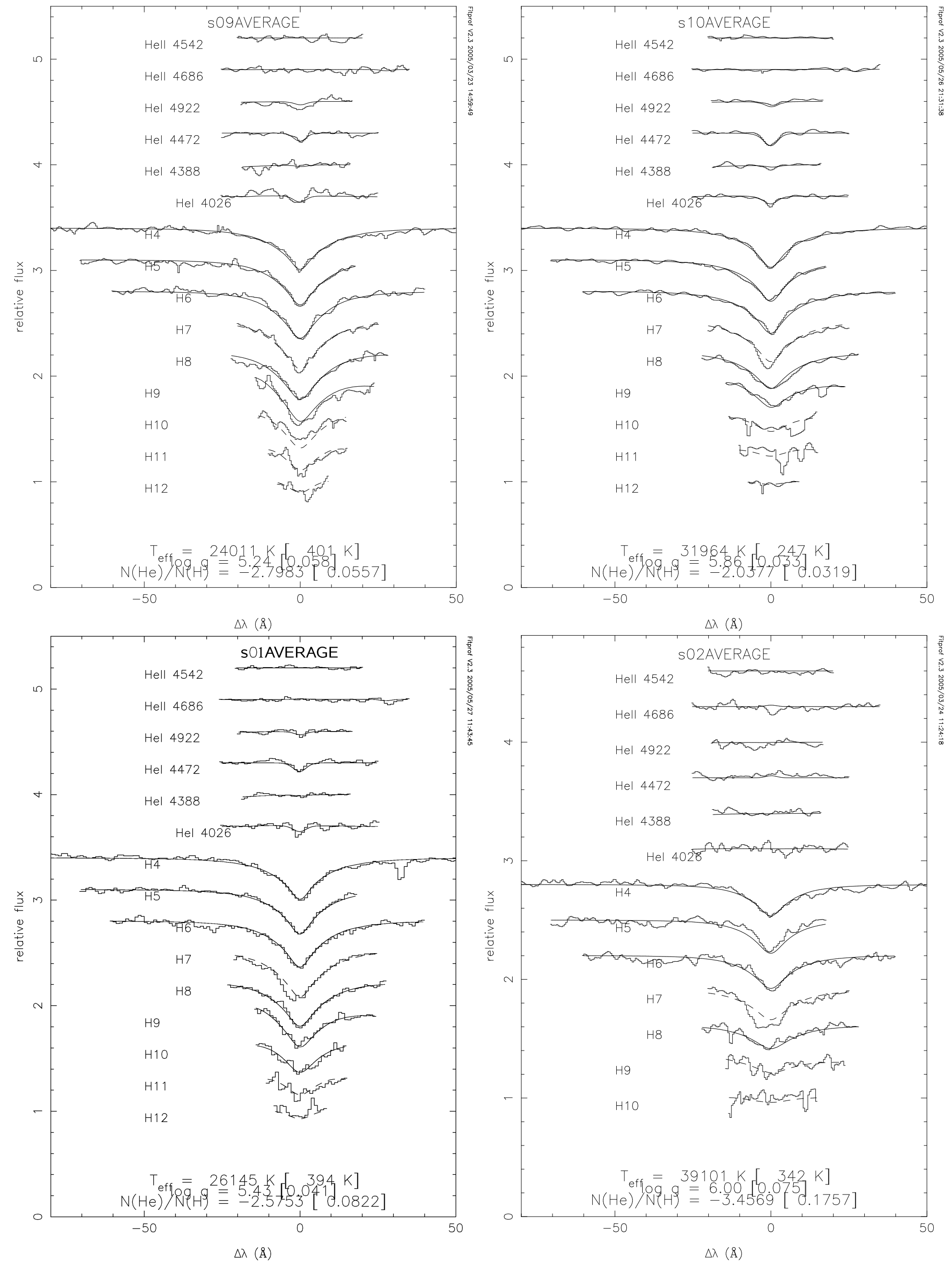

Figure 3.4: As in Fig.3.1, but the first two stars at the top belong to the field *bulge*2, while the two at the bottom belong to *bulge*3

The helium abundances found by the fit show that all stars are He-poor, in agreement with the diffusion, except in one case, where the star shows an

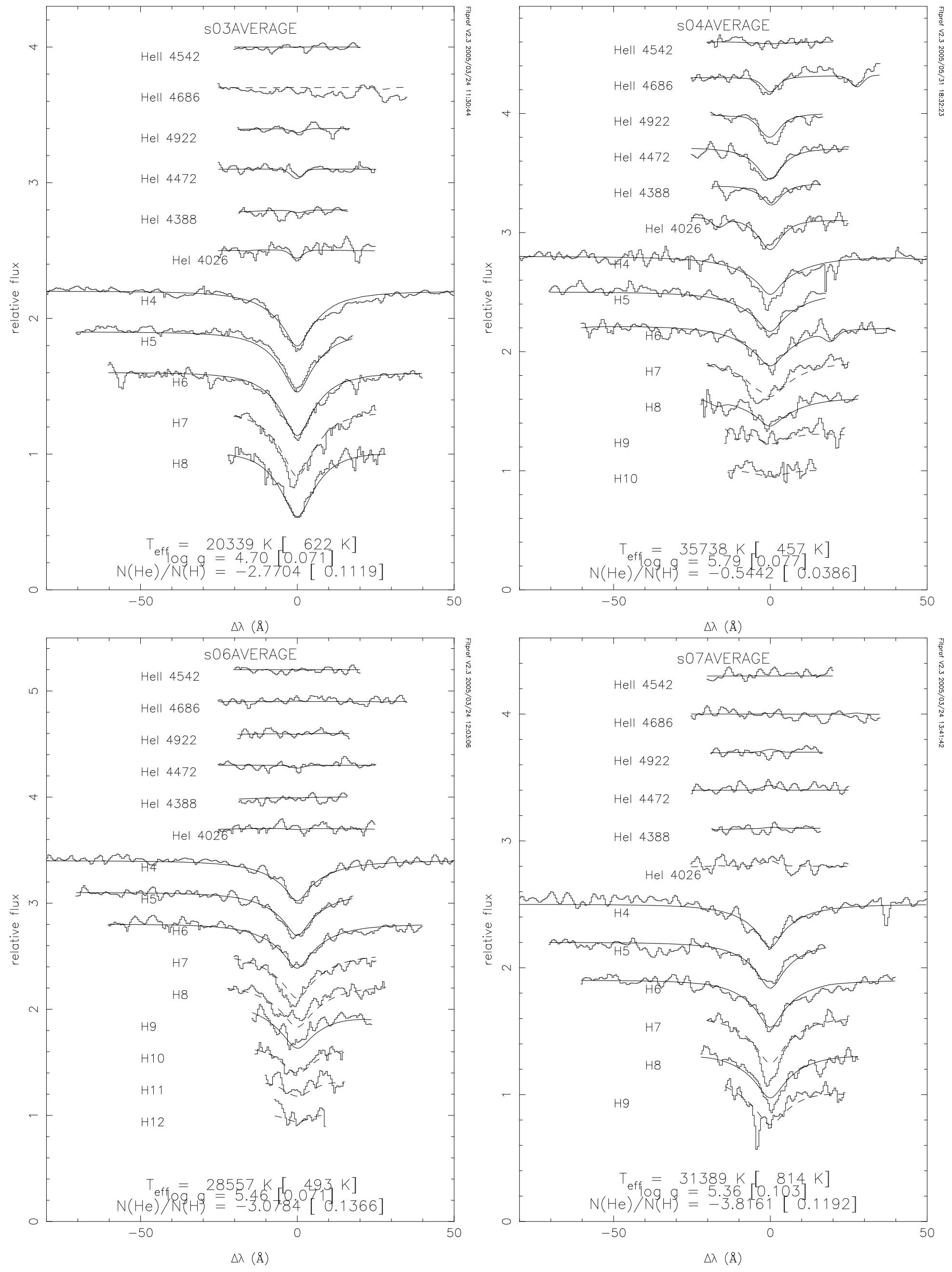

Figure 3.5: As in Fig.3.1, but for the field *bulge*3

unusually high helium abundance. It is the case of the 3004 star (Fig.3.5, top right panel): unfortunately the fit is not perfect because the spectrum is quite noisy. The high noise level is due to two reasons: firstly, the star

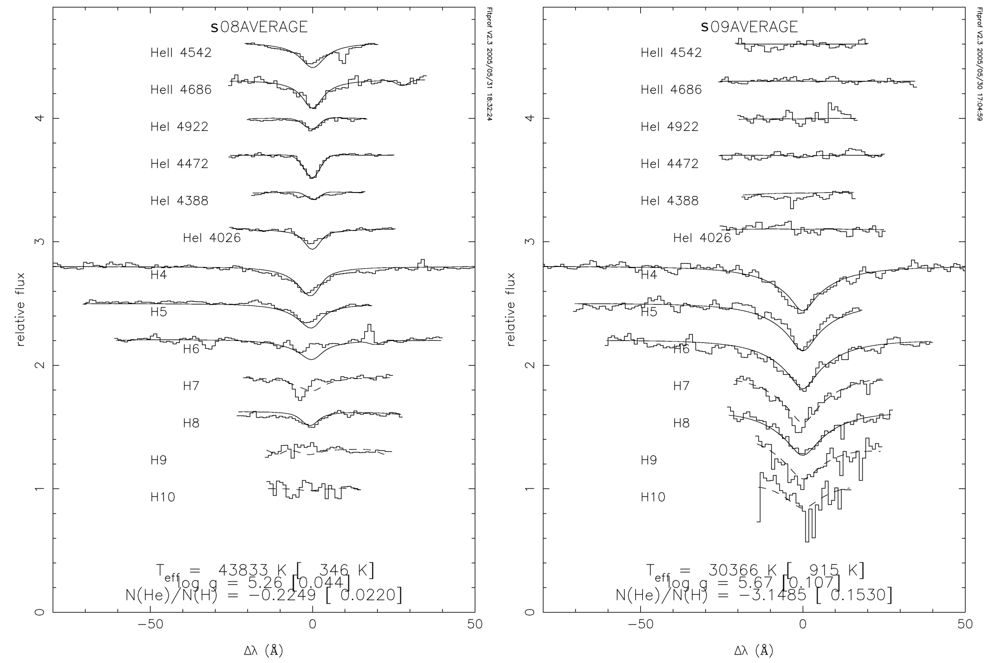

Figure 3.6: As in Fig.3.1, but for the field *bulge*3

is faint, secondly, it has a close companion, so that hte sky subtraction was difficult.

3.3 The log$g$ – T$_{eff}$ diagram

Finally I compared the results with Horizontal Branch theoretical tracks. Fig.3.7 shows the T_{eff},log$g$ diagram. The stars I identified as probable bulge members (see Sec.3.5 and 3.6) are marked with full symbols, while the open symbols represent stars whose membership is unknown or of the disk. The error bars are the formal errors from the fit procedure, but as already mentioned, these errors are underestimated and, in addition, do not include any systematic uncertainties, due to sky subtraction, flux calibration, etc.

Additionally, Fig.3.7 shows the evolutionary tracks which are taken from Yi et al. [1997] with metallicity Z = 0.004, values typical for the bulge population, and helium abundance Y = 0.2416. The zero-age horizontal branch (ZAHB), where a star starts to burn helium in its core quietly, and the terminal-age horizontal branch (TAHB), at which a star has burned 99% of its central helium, are shown together with evolutionary tracks for stars with total masses of 0.49, 0.50, and 0.51 $M_\odot$ (M_{env} of 0.0075, 0.0127, and 0.0226 $M_\odot$, respectively). The tracks end at 0.495 $M_\odot$, corresponding to M_{env} =

0.0075 $M_\odot$. Since EHB stars may have $M_{env} < 0.005$ $M_\odot$, I extrapolated the ZAHB and TAHB to higher temperatures (Fig. 3.7, dashed curves) just to guide the eye.

Different symbols were used to show the different status of the stars: squares indicate the isolated stars, triangles indicates the crowded stars and the pentagon indicates the helium rich star. In general, crowded stars have error bars bigger than isolated stars. As described in Sec.2.4, the preparation of the spectra of these stars requires the subtraction of the companion's spectrum. This procedure increases the noise and thus decreases the S/N ratio.

Most of the observed stars lie between the ZAHB and the TAHB tracks, where the EHB stars spend most of their life and therefore these objects are indeed EHB stars. Some objects are above the TAHB, meaning that they are in the post horizontal-branch phase and thus evolving as AGB-manqué stars (see Sec.1.2).

3.4 Tests with other models

Since these stars reach very high temperatures, it could be possible that the hypothesis of Local Thermal Equilibrium (LTE) is not valid anymore. I tested this possibility trying to fit the hotter spectra, ($T_{eff} > 30000$ K) with Non Local Thermal Equilibrium (NLTE) models (Napiwotzki [1997]). Fig. 3.8 shows a comparison between the results from LTE and NLTE models: the black filled squares represent the fit made using LTE models while the red open squares represent the fit made using NLTE models.

For most of the stars, there is no significant difference between the two fits. Even in the cases with the largest differences, the results of both fits lie inside or close to the mutual error bars. Given that the error bars are underestimated (see Sec.3.2) the LTE and NLTE fits can be regarded as being in agreement.

Since these stars experience diffusion and radiative levitation, it could be possible that their metallicity is increased. It is not possible to see it from these spectra because they are in the optical wavelength range, and to identify metal lines for such hot stars ultraviolet spectra or high-resolution optical spectra with high S/N would be needed. To account for this possibility, I tried then to fit the spectra again with LTE models but at higher metallicity. Since the metal rich models do not extend to higher temperature, we performed the fit only for stars cooler than 30000 K. Fig.3.9 shows a comparison between these two different set of models: the black filled squares represent the fit made using models with solar metallicity while the blue open

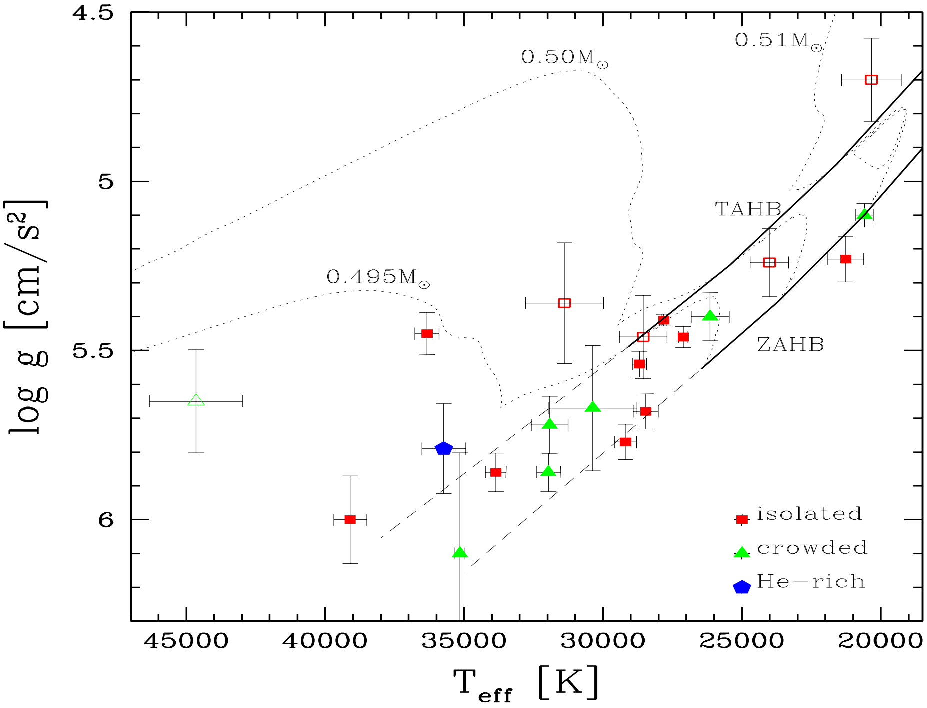

Figure 3.7: The (T$_{eff}$, log$g$) diagram: squares, isolated stars; triangles, crowded stars; pentagon, the He-rich star. The ZAHB and TAHB (Yi et al. [1997]) for Z = 0.004 and Y = 0.2416 are plotted together with evolutionary tracks for 0.495, 0.50, and 0.51 M$_\odot$. The dashed lines are extrapolations of the ZAHB and TAHB tracks.The full symbols represent bulge members, while the open symbols represent stars with membership unknown or of the disk. One star with unknown membership is out of the plot, at 23900 K, log$g$=6.74.

squares represent the fit made using higher metallicity. As before, keeping in mind that the error bars are underestimated, for most of the stars there is no significant difference between the two fits.

3.5 Distances

Comparing theoretical and observed magnitudes, the distances of these stars were estimated. I calculated the theoretical magnitudes V$_{th}$ and I$_{th}$ interpolating the Kurucz colour and magnitude table and picking up the values corresponding to T$_{eff}$ and log$g$ found by the fit. The observed magnitudes

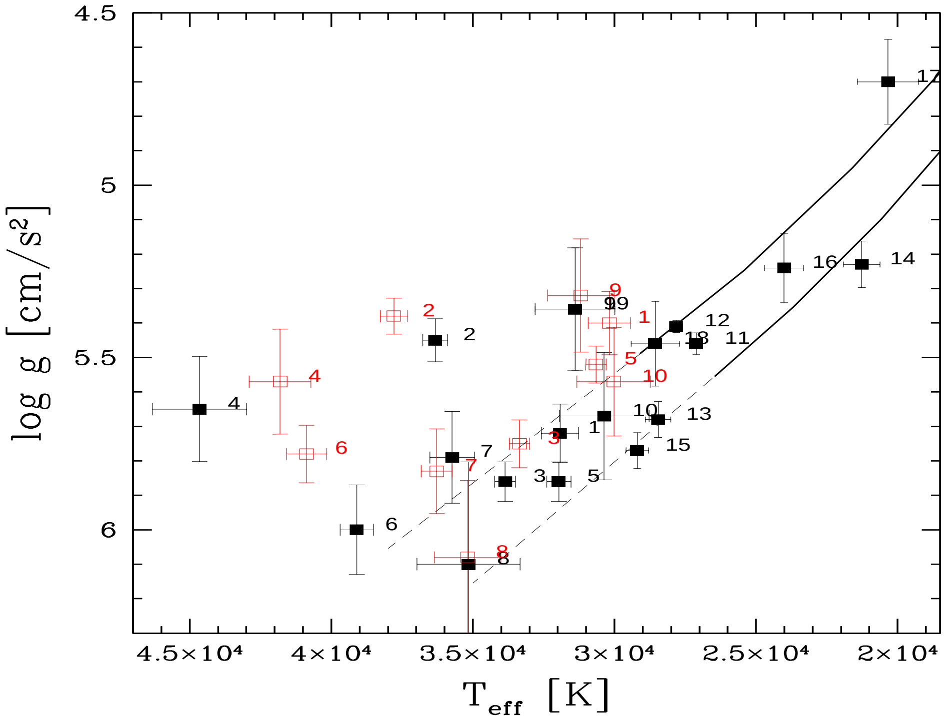

Figure 3.8: Comparison between the fit made using LTE (filled squares) and NLTE (open squares) models:

v and i are obtained from the photometry of Zoccali et al. [2003].

From

$$V - I = v - i - A_V + A_I = v - i - E_{(V-I)} \Rightarrow A_V - A_I = E(V - I)$$

the color excess $E_{(V-I)}$ was calculated.
Keeping in account the relation between the two color excesses:

$$E_{(B-V)} = 0.62E_{(V-I)}$$

and the relation between the absorption in the V band and the reddening $E_{(B-V)}$:

$$\frac{A_V}{E_{(B-V)}} = 3.1$$

it is possible to derive the absorption in the I band:

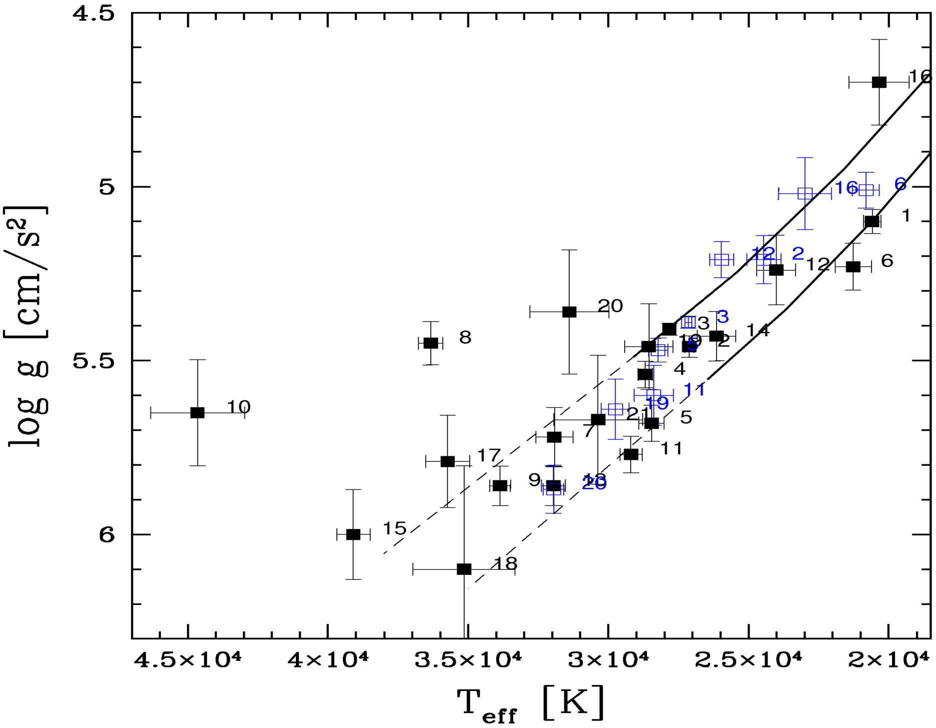

Figure 3.9: Comparison between the fit made using models with solar metallicity (filled squares) and higher metallicity (open squares)

$$A_I = A_V - \frac{E_{B-V}}{0.63}$$

The relation between theoretical and observed magnitude depends on the distance $d_\star$ and radius $R_\star$ of the star. In fact, from

$$I_{obs} - I_{th} = -2.5 \log \frac{R_\star^2}{d_{star}^2} + A_I$$

I can calculate:

$$d^2 = \frac{\pi}{1.196*10^{-9}} \times 10^{\frac{I_{obs}-I_{th}-A_I}{25}} \times R^2$$

where the factor $\pi/1.196 * 10^{-9}$ comes from the conversion of the I magnitudes into flux (Heber et al. [2002]).

Considering the relation between surface gravity g, radius R and mass M of a star:

$$g = GM/R^2$$

where G is the gravitational constant, the relation between the star and the Sun parameters is finally :

$$R_\star = R_\odot \sqrt{\frac{g_\odot}{g_\star}} \sqrt{\frac{M_\star}{M_\odot}}$$

from which it is possible to calculate the star's radius, assuming a mass of 0.5 $M_\odot$ (approximately the mass of a sdB star, Heber [1986]), and finally the distance:

$$d = 0.134902 \times 10^{0.2(I_{obs} - I_{th} - 1.488 E_{B-V}) - \log g/2} \text{ [pc]}$$

In Tab.3.2 the calculated distances are listed.

3.6 Radial velocities

To correct the spectra for the Doppler shift, the radial velocities were found (see Sec.2.5.2). The observed field is at galactic coordinates l=0°, b=−6°, which means that the expected radial velocities for disk stars is around 0 $km\ sec^{-1}$. The heliocentric velocities I calculated are distributed in a range between −200 and +300 $km\ sec^{-1}$ (see Tab.3.2), in agreement with the values found for K giants in Baade's window by Terndrup et al. [1995] between −240 and +194 $km\ sec^{-1}$).

The velocity dispersion was calculated:

$$\sigma_v = \sqrt{\sum_{i=1}^{n} (v - \bar{v})^2/(n-1)}$$

finding a value of 110 ± 17 $km\ sec^{-1}$ from our bulge EHB stars: the expected value for the disk is 50-70 $km\ sec^{-1}$ (Lewis & Freeman [1989]), while Terndrup et al. [1995] found for the Baade's window, at a distance of 8 kpc, 80-110 $km\ sec^{-1}$.

3.7 Bulge membership

Since the formal fit errors are underestimated by a factor of 2-4 (R.Napiwotzki, private communication), a formal error of 0.1 in *log* g implies an error of 25-50 % in the distance. I discussed the bulge membership only for those stars with a formal error in log g of less than 0.1, because for the others (five of 22) the uncertainty on the distance is too large.

Considering a distance from the Galactic Center of ≈ 8.5 kpc and a bulge radius of ≈ 1.5 Kpc, I found that most of these objects are effectively bulge

Table 3.2: Distances and radial velocities of the sdB stars

id	d(Kpc)	v_{rad} $(km\ sec^{-1})$
1002	8.4 ±1.9	-50 ±40
1003	5.6 ±1.3	-138 ±50
1004	5.2 ±1.2	28 ±50
1005	6.4 ±1.5	-204 ±40
2001	0.9 ±0.2	18 ±20
2002	6.5 ±1.5	-28 ±30
2003	8.2 ±1.9	137 ±30
2004	7.5 ±1.7	-20 ±30
2005	6.4 ±1.5	-34 ±45
2006	5.9 ±1.4	74 ±15
2007	9.1 ±2.1	-33 ±35
2008	4.6 ±1.1	12 ±20
2009	9.8 ±2.3	-98 ±30
2010	6.0 ±1.4	34 ±40
3001	6.5 ±1.5	160 ± 40
3002	5.4 ±1.3	174 ±40
3003	15.5 ±3.6	19 ±30
3004	8.1 ±1.9	242 ±40
3005	4.4 ±1.0	103 ±30
3006	10.9 ±2.5	14 ±60
3007	12.0 ±2.8	30 ±40
3009	5.8 ±1.3	11 ±40

stars: of 17 hot stars with reasonable errors in the distance 13 objects are in the bulge within 1σ and three more are in the bulge within 3σ. The remaining star is probably a disk EHB star, meaning that there is a disk contamination of at least 3% in this bulge field (it could be bigger, since 5 stars have unknown membership).

Disk Stars or Bulge Stars?

As the line-of-sight towards the Galactic bulge passes through the disk it is important to estimate the expected number of disk sdB stars in the observations.

To do so, the values of Villeneuve et al. [1995] for the space density of local field sdB stars (2–4 $\times$ 10^{-7} pc^{-3}) were used to derive the expected number of sdB stars along our line of sight from 4.5 kpc (corresponding to $I \approx 18.5$) to 11 kpc ($I \approx 20.5$) within the field of view of the Wide Field Imager (WFI, 30'× 30').

The sdB stars in the field of the Milky Way consist of a mixture of thin and thick disk stars (e.g. Altmann et al. [2004]), so a ratio of 50:50 was assumed. For the thin disk I used a scale height of 325 pc and a scale length of 3.5 kpc and for the thick disk I used values of 900 pc and 4.7 kpc, respectively (Larsen & Humphreys [2003]), adopting the following density law:

$$\rho = \rho_{\odot} \cdot e^{\frac{r}{r_0} - \frac{z}{z_0}}$$

where r is the star distance projected on the Galactic plane, r_0 is the scale length, z is the star height above the Galactic plane and z_0 is the scale height. The expected number of sdBs is then obtained multiplying the density by the volume V I am considering (in this case the WFI area by the line of sight):

$$n = \rho \times V$$

I used a distance to the Galactic center of 8.5 kpc and assumed that the disk ends at a radial distance of 1 kpc from the Galactic Center (Robin et al. [2003]). This way a total number of 4 to 9 sdB foreground stars within the full field of WFI are predicted. Using the values of Ojha [2001] for the scale lengths (2.8 kpc and 3.5 kpc) instead, 7 to 14 foreground sdB stars are expected, i.e. 5–10% of all candidates.

Fig.3.10 shows the color magnitude diagram where I selected the spectroscopic targets. Most the candidates (24 on 29) have been found to be sdB stars, while the others targets resulted to be (foreground and/or differently reddened) cool stars (cyan circles). For two stars it was not possible to obtain a good fit with the models. Of the remaining 22 objects, 16 turned out

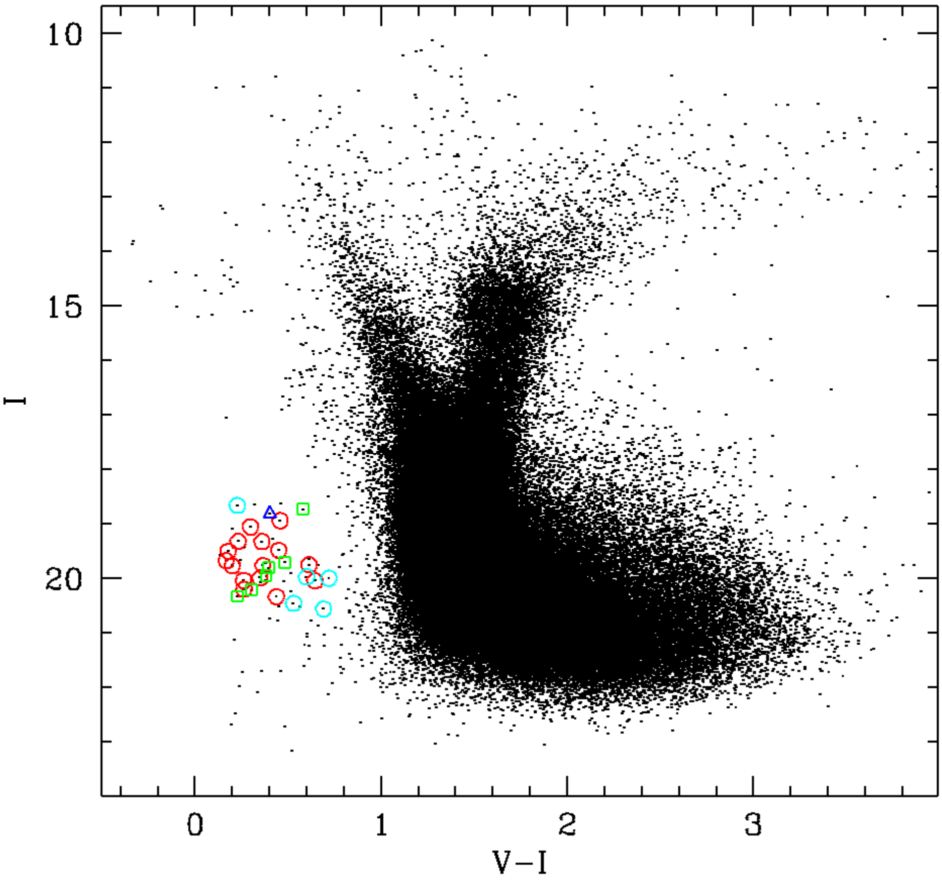

Figure 3.10: Color magnitude diagram of the observed bulge region (Zoccali et al. 2003); the spectroscopic targets are marked: bulge stars are marked with red circle, disk stars with blue triangles and stars whose membership is unknown, with green squares. Cool stars are marked with cyan circles.

to be bulge members, 1 is surely a disk stars, while for 5 the errors in the distance were too big to assign a membership. If some of these stars were disk members, it would agree with both the predictions made above (1.5 to 3 disk stars among 29 candidates).

In Tab. 3.3 the results are summarized. As it possible to see in the color-magnitude diagram, there is no relation between position in the diagram and evolutionary status and/or membership, so that I could not select the others sdB candidates only on the basis of the photometry. I used therefore these stars as sample when I constructed the integrated spectrum (see Ch.6).

	n	percentage on n_{tot}
total targets	29	100%
hot stars	24	83%
cool stars	5	17%

sdBs membership	n	percentage on n_{tot}
bulge	16	55%
disk	1	3%
unknown	5	17%

Table 3.3: Summary of the spectroscopic observations

Chapter 4

The photometric data reduction

4.1 The instrument: WFI@2.2m Telescope

The 2.2m Telescope is on loan to ESO from the Max Planck Gesellschaft and has been in operation at LaSilla (Chile) since 1984. The telescope is a Ritchey-Chretien design mounted on an equatorial fork mount.

The Wide Field Imager (WFI) is a mosaic camera which is mounted at the Cassegrain focus of the 2.2m Telescope. The main features are summarized in Fig.4.1.

The detector is composed of 8 CCDs (see Fig.4.2), each covering a field of 487" × 975", meaning a total field of 0.56×0.54 deg^2. Between the CCDs gaps are present. To exploit the whole field, that is to cover also the gaps, a procedure called *dithering* is often performed: the exposure time is split in shorter exposures and the pointing is slightly shifted to cover the sky region where there are the gaps.

4.2 Observations

The target stars, whose spectra were observed with FORS2 (see chapter 2), belong to a photometric catalogue obtained from WFI photometric data, in the V and I filters, of the Galactic bulge (Zoccali et al. [2003]). These data are part of the ESO Imaging Survey (EIS), a survey ESO carried out in the past years in the B,V,I bands.

The EIS archive was searched therefore with several purposes:

- finding other bulge fields in which to look for sdB star candidates;

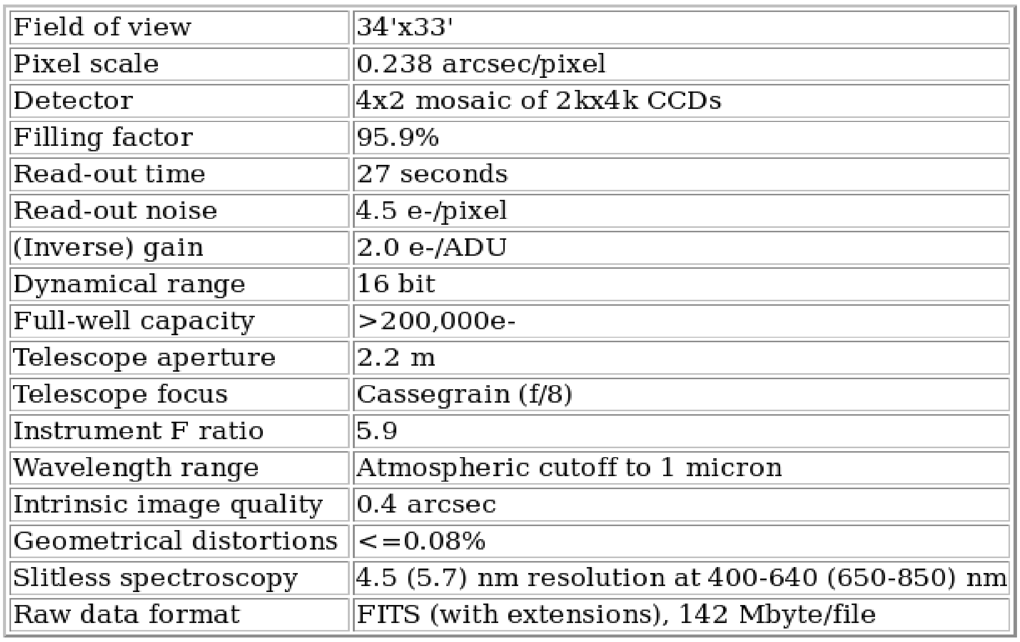

Field of view	34'x33'
Pixel scale	0.238 arcsec/pixel
Detector	4x2 mosaic of 2kx4k CCDs
Filling factor	95.9%
Read-out time	27 seconds
Read-out noise	4.5 e-/pixel
(Inverse) gain	2.0 e-/ADU
Dynamical range	16 bit
Full-well capacity	>200,000e-
Telescope aperture	2.2 m
Telescope focus	Cassegrain (f/8)
Instrument F ratio	5.9
Wavelength range	Atmospheric cutoff to 1 micron
Intrinsic image quality	0.4 arcsec
Geometrical distortions	<=0.08%
Slitless spectroscopy	4.5 (5.7) nm resolution at 400-640 (650-850) nm
Raw data format	FITS (with extensions), 142 Mbyte/file

Figure 4.1: Main characteristics of the Wide Field Imager at the 2.2m Telescope at LaSilla
http://www.ls.eso.org/lasilla/sciops/2p2/E2p2M/WFI/docs/WFInutshell.html

- looking for observations in other filters in order to correct for reddening by means of the two color diagram
- finding suitable disk fields in order to subtract the disk component from the color magnitude diagram of the bulge

In Tab. 4.1 the bulge and disk data retrieved from the EIS archive are listed. The data reduction procedure for all fields is basically the same as in Zoccali et al. [2003] and it is described in the next section.

4.3 Reduction

4.3.1 Pre-reduction

The data retrieved from the EIS archive were already pre-reduced, meaning that the frames were already corrected for bias, flat field, and cosmic rays. The I-band images were corrected also for fringing (the presence of interference patterns in the images). The single CCDs have been relatively homogenized photometrically (Vandame[2002]): a preliminary image was obtained

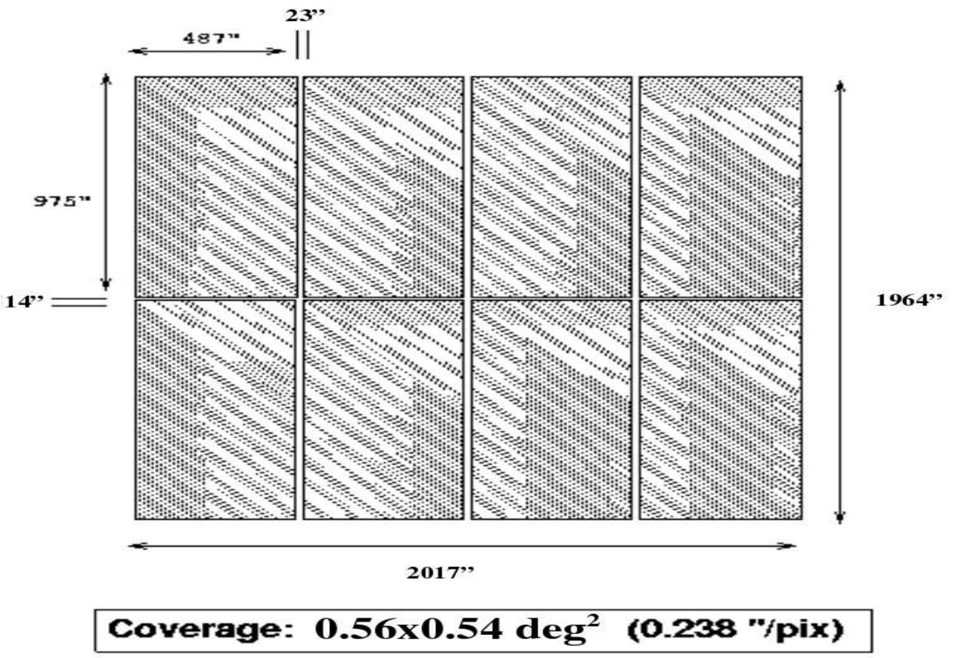

Figure 4.2: The 8 CCDs which compose the whole WFI detector (http://www.ls.eso.org/lasilla/sciops/2p2/E2p2M/WFI/docs/WFInutshell.html)

by stacking a set of sky-subtracted frames, with the background estimated using a median; objects were identified on the stacked image and masks were created; the sky subtraction was repeated neglecting the masked pixels and sigma-clipping the deviant values, producing in this way weight-maps applied on the raw image.

The global sky background value of the image was not subtracted, to allow `DAOPHOT/ALLSTAR` (the program used to do the photometry, Stetson[1987,1994]) to properly measure the flux of the objects on the image. The photometric reduction package was run on the whole image composed by the eight chips. While from the point of view of the reduction this is very handy (because it is not necessary to split the images in the subframes), on the other hand it is time consuming since a whole WFI image is more than 270 MB. To the images I reduced dithering was not applied, so that the gaps are visible in the images.

4.3.2 DAOPHOT II and ALLSTAR

The `DAOPHOT II/ALLSTAR` package was created by Stetson [1987] (see also Stetson [1994]) with the purpose to obtain a good photometry in crowded

Table 4.1: Data retrieved from the EIS archive

field	filter	α_{2000}	δ_{2000}	exposure time (sec)
MW05 (bulge)	B	18:10:17.0	-31:45:15	1×30 + 1×480
MW07 (bulge)	I	18:27:22.5	-33:56:45	1×30 + 1×480
"	V	"	"	1×60+ 1×480
"	B	"	"	1×30+ 1×480
MW08 (bulge)	I	18:35:25.4	-34:37:04	1×30+ 1×480
"	V	"	"	1×60+ 1×480
"	B	"	"	1×30+ 1×480
GC07 (disk)	I	12:59:35.0	-70:52:28	1×30+ 1×480
"	V	"	"	1×30+ 1×480
"	B	"	"	1×30+ 1×480
GC14 (disk)	I	17:25:29.2	-48:25:22	1×30+ 1×480
"	V	"	"	1×30+ 1×480
"	B	"	"	1×30+ 1×480

fields (e.g. globular clusters), in which the photometry is difficult to perform because the stars are close to each other and therefore produce overlapping images.

The program is applied to the pre-reduced frames. The pipeline is as follows:

- finding the stars with the `FIND` command. This routine takes into account the gain and the read out noise of the CCD, it calculates the average sky value along the frame as well as the standard deviation. Then choosing a threshold value, all pixels in which the value is higher then the standard deviation multiplied by the threshold, are picked up as stars. A file is created where the star candidates are listed along with their pixel coordinates.

- making the aperture photometry for the candidates with the command `PHOTOMETRY`. After having chosen a set of values for the aperture radii, the photometry is performed for each value. For each star, the flux inside concentric circles, whose radius is taken from the aperture radii, is calculated. The brighter and more isolated stars are then chosen to calculate the Point Spread Function (PSF) of the image, i.e. the function that best reproduces the stellar profile for each frame.

- calculating the `PSF`: the stellar profile is calculated by means of a least squares fitting method, using the brightest (not saturated) stars to obtain the parameters of the analytical profile, which can be a Gauss, Moffatt, Lorentz and "Penny" (sum of a Gaussian, fitting better the core of the profile, and a Lorentzian, fitting better the wings) function. After some tests, the Penny function was chosen, being the profile for which the χ^2 obtained from the fit was smaller.

- fitting all stars with `ALLSTAR`: this program fits the PSF found with DAOPHOT II to all stars detected by the `FIND` command, giving a better estimate of the center of the stars and rejecting the stars for which the fit is poor (for example, remaining cosmic rays or extended objects, like distant galaxies, whose profile is different from the typical one of the stars). `ALLSTAR` also creates an image where all identified stars are subtracted and where all those stars that were not detected the first time remain, because e.g. they are too close to other stars. The procedure is repeated on the subtracted image and the new stars are added to the first list.

Thus, for each frame a photometric catalogue is obtained. To match the different catalogues, that is to find the correspondence between the different frames of each field, the package DAOMATCH/DAOMASTER (Stetson [1987,1994]) was used.

DAOMATCH takes the brighter stars in the frames, calculates the triangles formed by these stars and finds a preliminary coordinate transformation between the frames in order to match these triangles. For this purpose the long (480s) and short exposures (30 or 60s) were matched separately, since the brightest stars in the short exposures are saturated in the long exposures. The initial coordinate transformation is refined by DAOMASTER, using also the other stars.

4.3.3 Calibration

To calibrate the photometric catalogs, that is to bring the magnitudes to the same reference system, several effects need to be taken in account:

- the exposure time, since there are short and long exposure of the same field

- the atmospheric extinction coefficient, since the observations were taken at different times during the night and therefore the airmass along the line-of-sight is different

For these reasons to all magnitudes the following equation was applied:

$$m_{WFI_i} = m_{instr_i} + 2.5 \times log(t_{exp}/t_{ref}) - ek_i \times am$$

where m_{WFI_i} is the magnitude calibrated in the WFI photometric system (that is the magnitude in the WFI filter system, at 1 second of exposure time and air mass equal to 1), m_{instr_i} is the instrumental magnitude in the filter i (that is the magnitude corresponding to the flux detected by the instrument, $m_{instr_i} = -2.5\log(flux_i)$), t_{exp} is the exposure time, t_{ref} is the reference exposure time (usually 1 second), ek is the atmospheric extinction coefficient (from the ESO webpage[1]) and am is the air mass. The index i indicates the different filters (V,B or I).

To calibrate to the Johnson-Cousin (JC) photometric system it is necessary to apply a zero point in the magnitudes and a color term in the color, since the WFI filters are different from the JC ones (see Fig.4.3.3).

Usually, to do that, standard stars are observed during the same night. Comparing the WFI magnitudes of the standard stars and the JC magnitudes of the same stars, (plotting the difference between the JC and WFI magnitudes versus the JC color, as shown for example in Fig.4.4) the relation between WFI and JC photometric systems is found with equations like the following:

$$\begin{gathered} B - b = zp_B + ct_{B_{B-V}}(B - V) \\ V - v = zp_V + ct_{V_{B-V}}(B - V) \\ I - i = zp_I + ct_{I_{V-I}}(V - I) \end{gathered}$$

where B,V,I are the JC magnitudes, b, v, i are the WFI magnitudes, $zp_{B,V,I}$ are the zero points and $ct_{B,V,I}$ are the color terms. The WFI magnitudes of the stars I want to calibrate are then substituted in these equations (appropriately inverted). The EIS V and I data are already photometrically calibrated, in the sense that this procedure was already performed in the pre-reduction phase (in the header of each image there is in fact the zero point that must be applied). Since the color term does not depend on the photometric conditions but on the filter shape, the value provided by ESO[2] was used:
$ct_{B_{B-V}} = 0.31$; $ct_{V_{B-V}} = -0.10$; $ct_{I_{V-I}} = 0.18$.

When I calibrated the B images for the field MW05, for which the photometry in V and I was already calibrated, a problem arose. For the calibration

---

[1] http://www.ls.eso.org/lasilla/sciops/observing/Extinction.html

[2] http://www.eso.org/science/eis/surveys/readme/EIS2003-03-21T173025666/

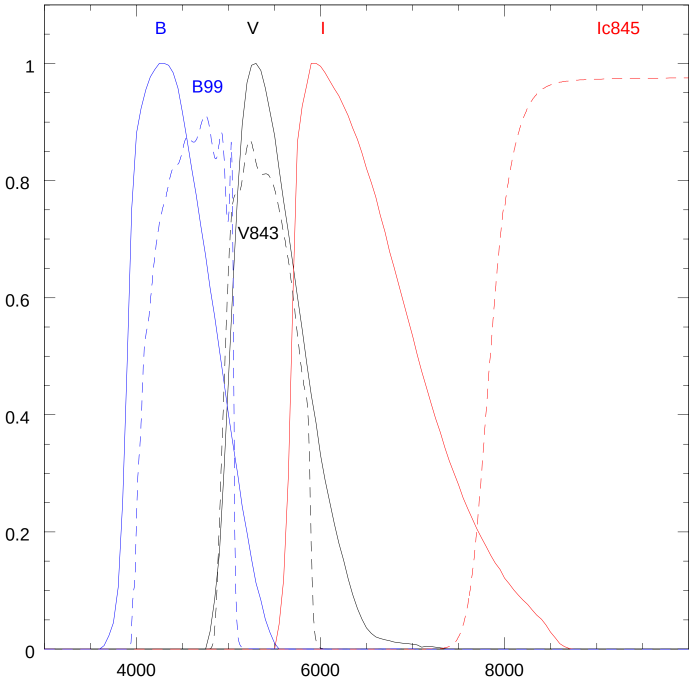

Figure 4.3: Comparison between the Johnson-Cousin (solid line) and WFI (dashed line) filters.

procedure at least two uncalibrated filters are necessary. To solve this problem, the V and I magnitudes were "*decalibrated*" and calibrated again (using zero point and color term used the first time) adding the B magnitudes to the system of equations.

The problem with the B calibration

In order to correct for reddening, the color-color diagram (B-V,V-I) was plotted. The idea was to compare the observed stars with a curve defined by non-reddened standard stars and to find the reddening shifting the observed stars to overlap with the standard curve. It was not possible to apply this procedure because the relative position between the observations and the standard curve was not as it should have been: while the shift in V-I , necessary to overlap observations and standard, was correct (or at least it had sense), the one in B-V was not, since a negative (thus meaningless from the physical point of view) E_{B-V} was requested for the overlapping. Since

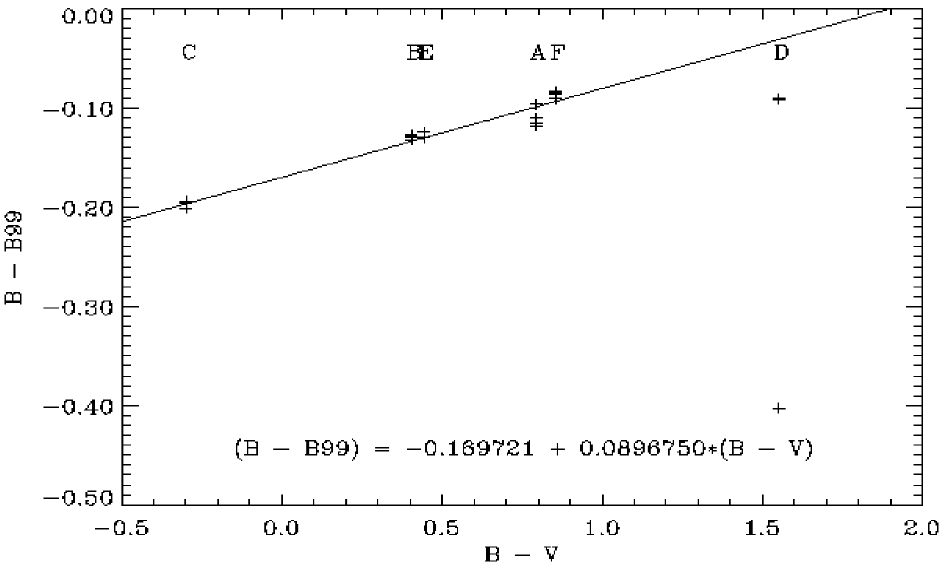

Figure 4.4: Example of relation between the WFI filters and the JC filters: in this case the equation between the JC B and V filters and the WFI B (B/99) is shown (http://www.ls.eso.org/lasilla/sciops/2p2/E2p2M/WFI/zeropoints/ColorEquations/index.html).

the V-I color was correct, it was evident that there was a problem with the B calibration of about 0.5 mag. The reason for that it is not very clear: a difference in 0.2 mag is expected since it is known that the WFI B filter is too red and it has a large color term, but this effect is not large enough to explain the found discrepancy.

The two-colors method was therefore not reliable in this case and reddening maps were used (see next section).

4.4 Reddening correction

To take in account the extinction caused by the interstellar medium, the Schlegel et al. [1998] dust maps were used. These maps were derived combining the data obtained from the two satellites IRAS and COBE/DIRBE.

The reddening values were obtained from the archive set from NASA's infrared and submillimetric astronomy projects[3]. Given the coordinates of the field, the value of the E(B-V) reddening and A_V extinction are retrieved as averages on a region centered on the input coordinates. Since the smallest

---

[3] http://irsa.ipac.caltech.edu

region in which it is possible to do the statistics is a circle with a radius of 5 arcmin (about the half the WFI chip), the reddening was calculated for the 16 regions resulting by splitting the 8 WFI chips in half. An example is given in Fig.4.5.

4.5 Calibration to the Landolt photometric system

Theoretically, after having corrected the calibrated photometry for reddening, the color-magnitude diagrams of the bulge and the disk regions should overlap, or at least the blue main sequence of the disk in the two disk fields and in the two bulge fields. But this (again) did not happen, meaning that the calibration was not good enough.

To try to finally reach a good calibration, the Stetson[4] standard fields (Stetson [2000]) were used. These fields are globular clusters fields and the standard stars belong to the globular cluster. The magnitudes are calibrated to the Landolt system (Landolt [1992]). Both disk fields contain a globular cluster present in the Stetson standard fields, NGC 4833 and NGC 6352 for GC 14 and GC 07, respectively. The Stetson standard stars were identified in the WFI frames and in the photometric catalogues; the relations between the WFI calibrated magnitudes and the Landolt calibrated Stetson standard magnitudes were found (see Figures 4.6 and 4.7) fitting the data points with a linear function whose zero point is the photometric zero point and the slope is the color term. Both zero points are close to zero and, while the color term in the V filter is close to zero as well, the one in the I filter is ~ 0.15. The relation was applied to the whole WFI photometric catalogue. As a check for the goodness for the calibration, the newly calibrated WFI photometry was compared to pre-existing photometry: since in the Padova globular cluster database[5] (Rosenberg et al. [2000]) both NGC 4833 and NGC 6352 are present in the same filters, the region with the cluster was selected in the disk fields and the corresponding photometry was compared with the photometry from Padova database. Fig. 4.8 shows this comparison for both clusters, and the agreement is good.

Regarding the bulge fields, while the MW05 field was calibrated to the Landolt system using standard stars observed in the same night (Zoccali

---

[4] http://cadcwww.daonrc.ca/standards

[5] http://www.astro.unipd.it/globulars

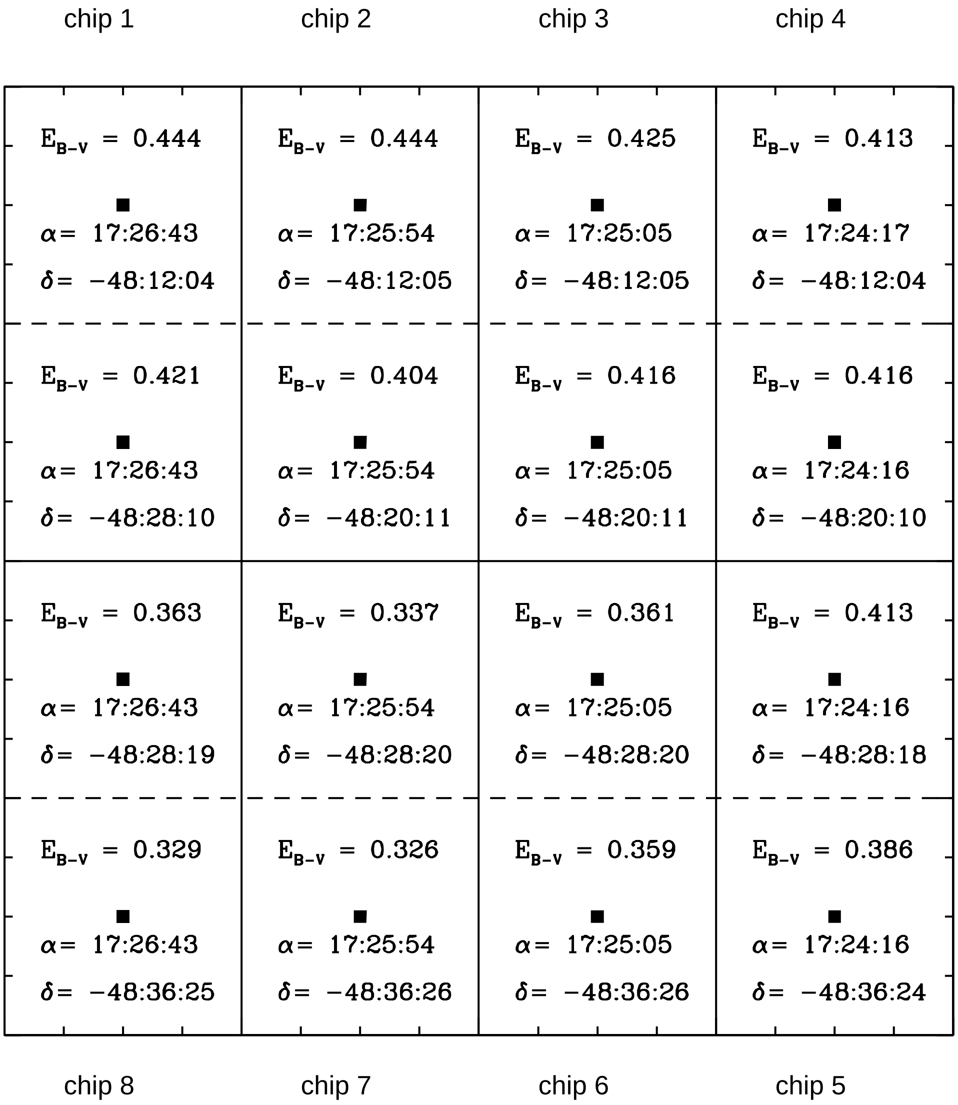

chip 1	chip 2	chip 3	chip 4
E_{B-V} = 0.444 ■ α= 17:26:43 δ= −48:12:04	E_{B-V} = 0.444 ■ α= 17:25:54 δ= −48:12:05	E_{B-V} = 0.425 ■ α= 17:25:05 δ= −48:12:05	E_{B-V} = 0.413 ■ α= 17:24:17 δ= −48:12:04
E_{B-V} = 0.421 ■ α= 17:26:43 δ= −48:28:10	E_{B-V} = 0.404 ■ α= 17:25:54 δ= −48:20:11	E_{B-V} = 0.416 ■ α= 17:25:05 δ= −48:20:11	E_{B-V} = 0.416 ■ α= 17:24:16 δ= −48:20:10
E_{B-V} = 0.363 ■ α= 17:26:43 δ= −48:28:19	E_{B-V} = 0.337 ■ α= 17:25:54 δ= −48:28:20	E_{B-V} = 0.361 ■ α= 17:25:05 δ= −48:28:20	E_{B-V} = 0.413 ■ α= 17:24:16 δ= −48:28:18
E_{B-V} = 0.329 ■ α= 17:26:43 δ= −48:36:25	E_{B-V} = 0.326 ■ α= 17:25:54 δ= −48:36:26	E_{B-V} = 0.359 ■ α= 17:25:05 δ= −48:36:26	E_{B-V} = 0.386 ■ α= 17:24:16 δ= −48:36:24
chip 8	chip 7	chip 6	chip 5

Figure 4.5: Example of reddening correction using the Schlegel et al. [1998] dust maps. The whole WFI field is shown. The dashed line indicates the splitting of the chips. The E_{B-V} for the region whose center corresponds to the center of the half chip (marked with the fill square) and the corresponding coordinates are labeled.

et al. 2003), for the other two fields, namely MW07 and MW08, the same photometric reduction procedure as the disk fields was applied, meaning that also for them a problem in the calibration was present. These two fields do

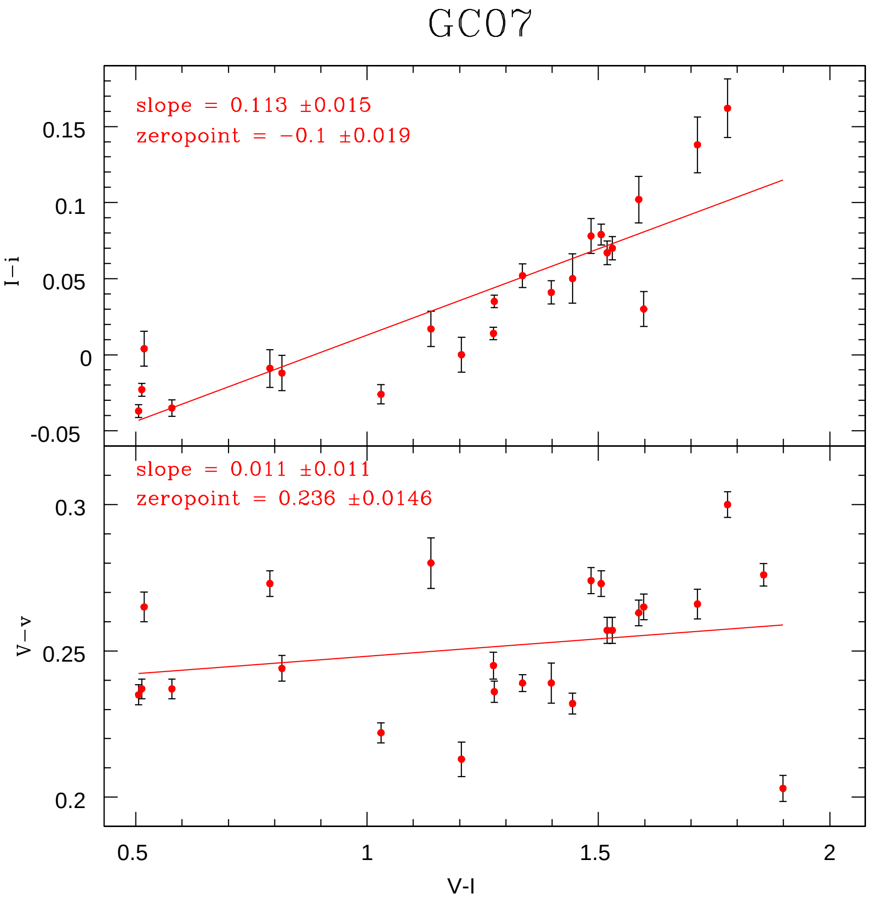

Figure 4.6: Relation between the WFI calibrated photometric system and the Landolt system found with the Stetson standard stars for the disk field GC 07. The error bars are the errors given by DAOPHOT II. The zero points and the slopes (color term) obtained from the fit are labeled.

not contain globular clusters as the two disk fields, it is not possible to adopt the same calibration procedure. To calibrate them to the Landolt system, the average of the zero points and of the color term found for the two disk fields were adopted.

The color magnitude (V-I,V) diagrams of the bulge and disk fields, calibrated to the Landolt photometic system, are shown in Figures 4.9 and 4.10.

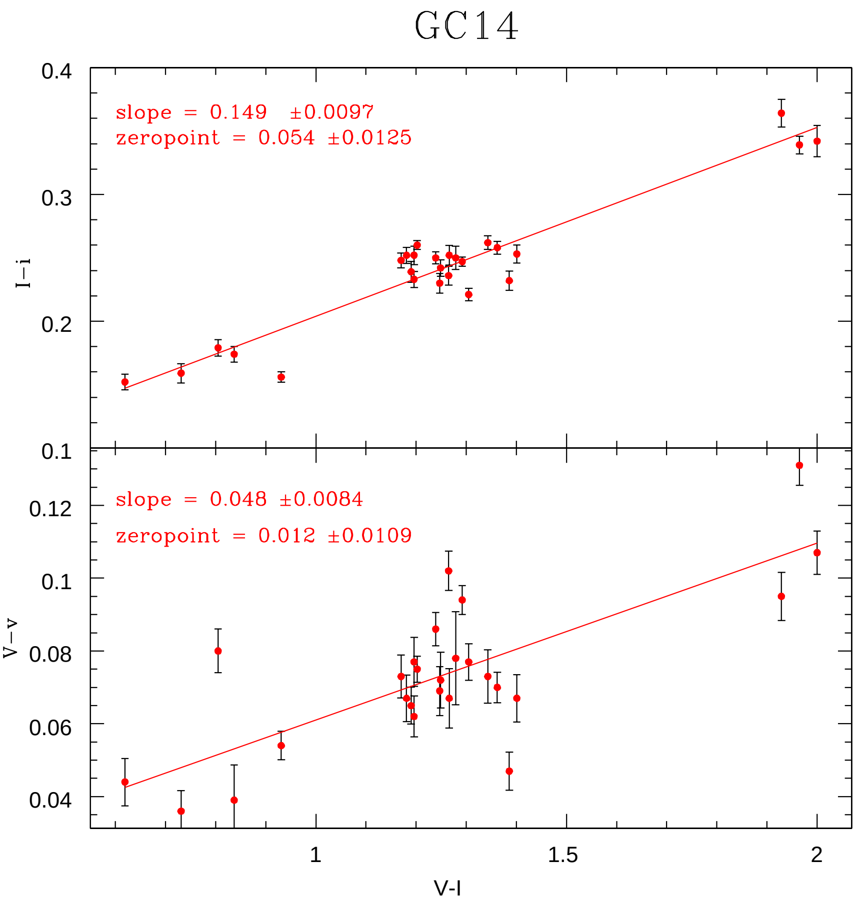

Figure 4.7: As Fig. 4 but for the GC 14 disk field.

4.6 Correction for the contaminating stellar populations

When we observe the galactic bulge, along the line of sight also disk stars are detected. Moreover, some of the stellar fields contain also a globular cluster: NGC 6558, in the MW05 bulge field, and NGC 4833 and NGC 6352 in the GC 07 and GC 14 disk fields respectively. Since the aim of this work is to study the bulge field population, the other stellar components must be subtracted.

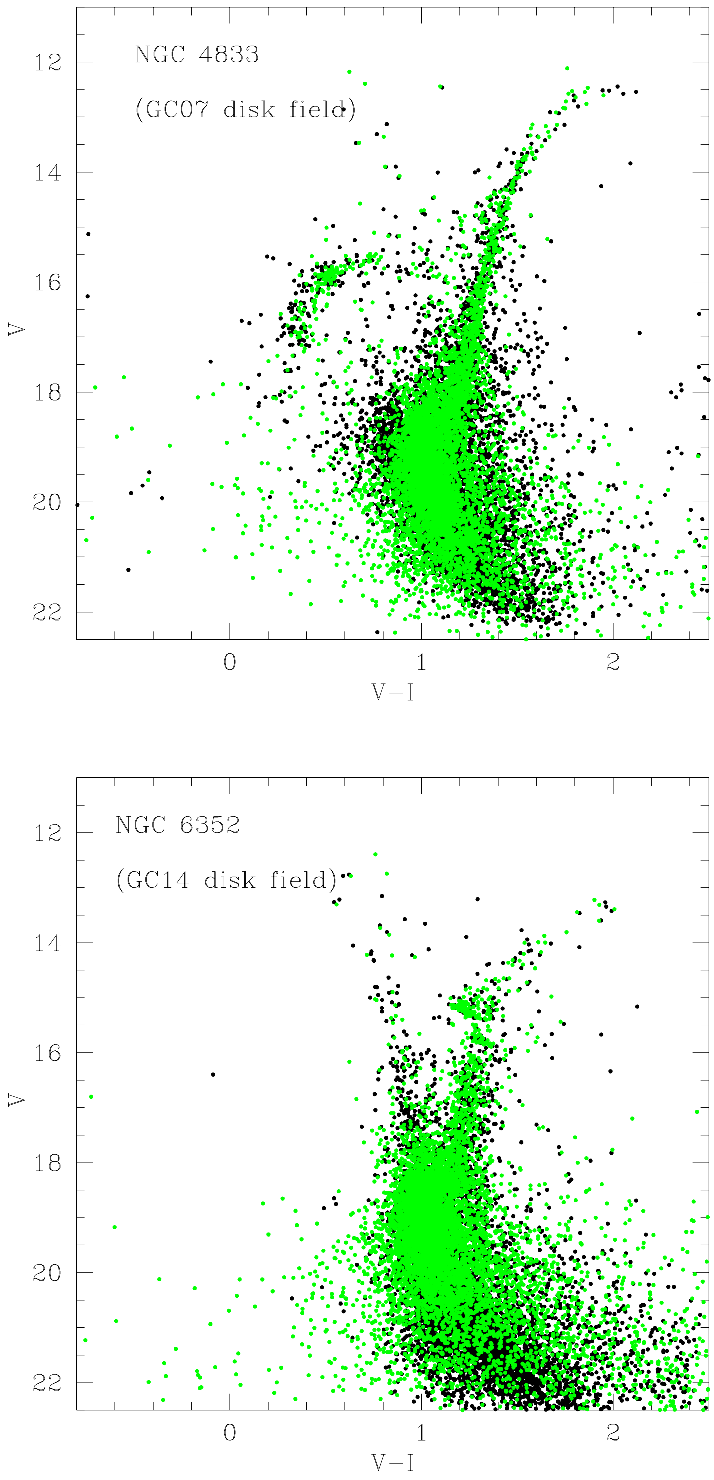

Figure 4.8: Comparison between the WFI photometry calibrated to the Landolt system (in black) and the photometry from the Padova globular cluster catalogue (in green, Rosenberg et al. [2000]).

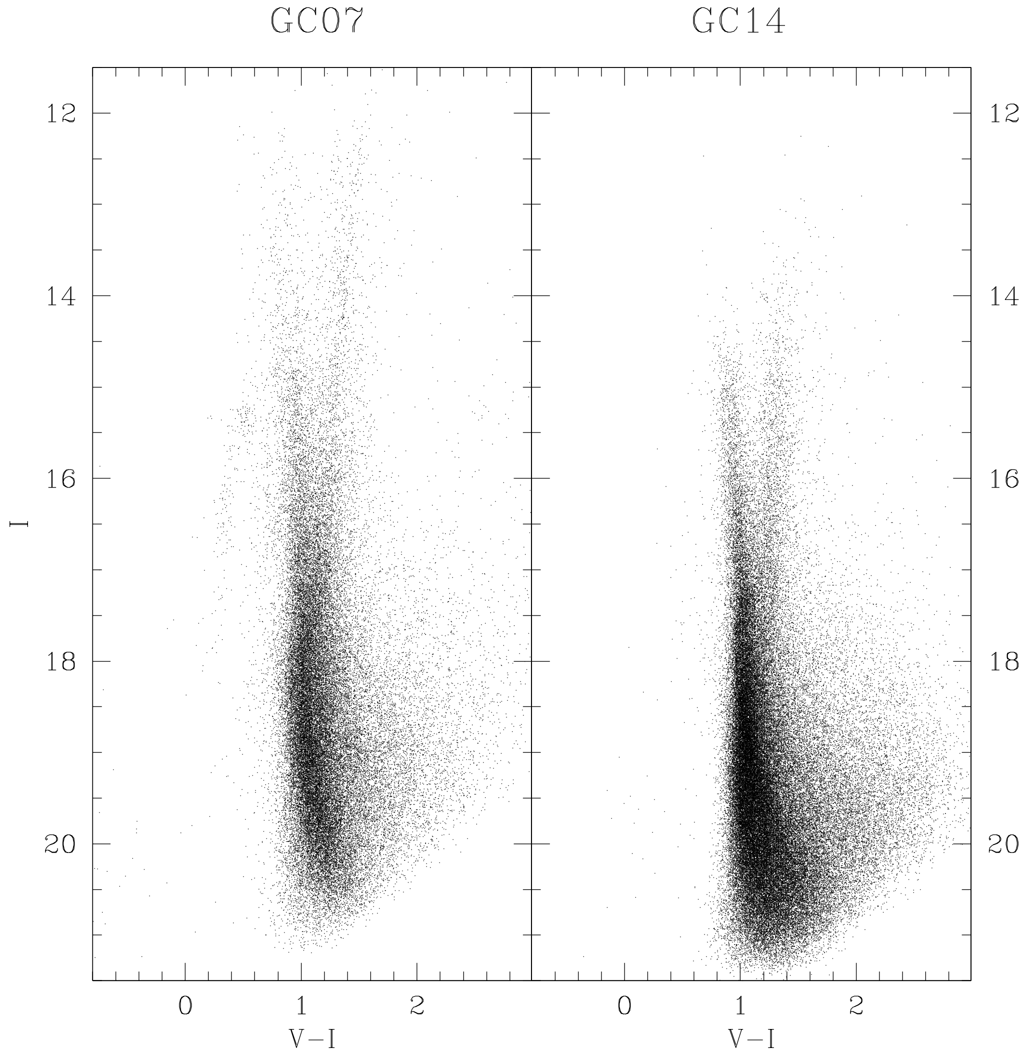

Figure 4.9: Color magnitude diagram (V-I,I) for the disk fields GC07 (left panel) and GC14 (right panel), calibrated to the Landolt photometric system, not corrected for reddening.

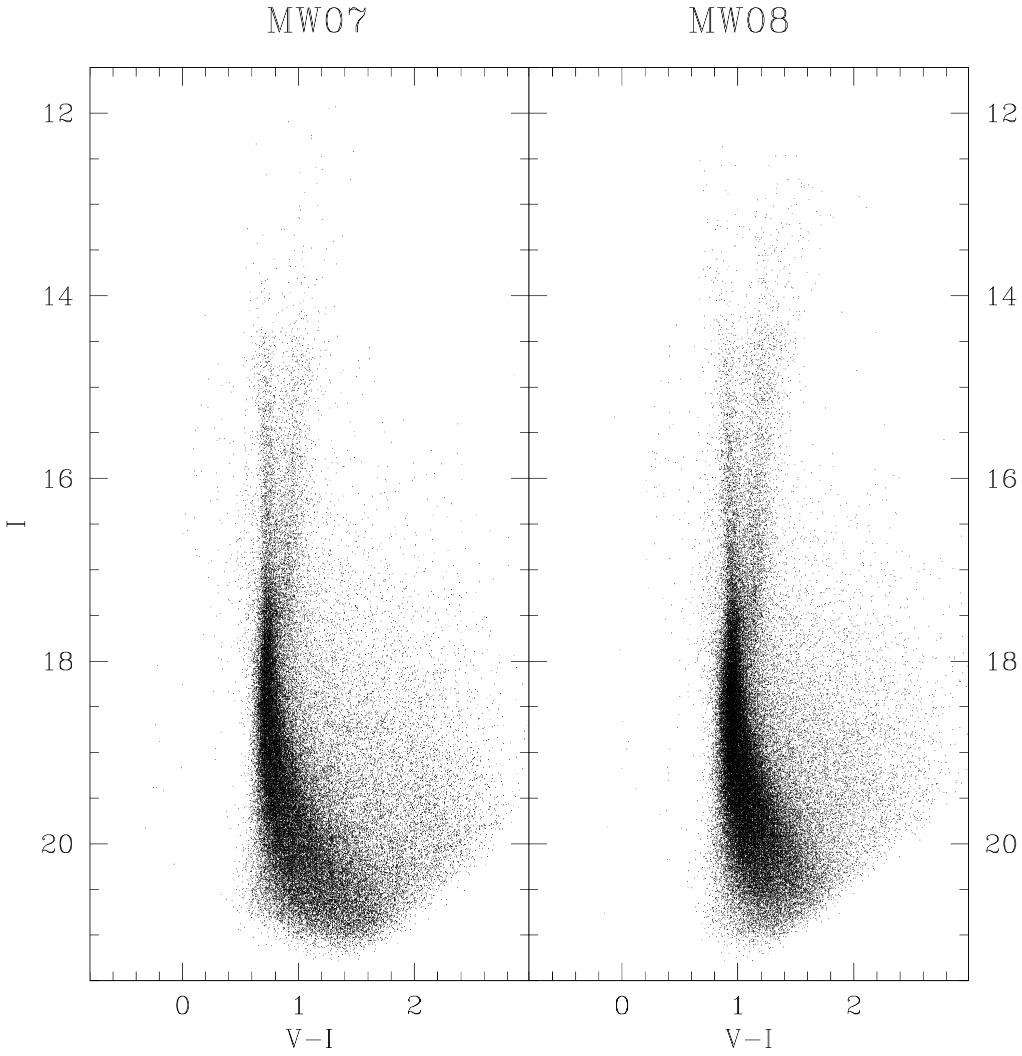

Figure 4.10: Color magnitude diagram (V-I,I) for the bulge fields MW07 (left panel) and MW08 (right panel), calibrated to the Landolt photometric system, not corrected for reddening.

4.6.1 Subtraction of the Globular Cluster population

If two stellar populations have different kinematics, the more precise method to distinguish them is to compare proper motions of the stars, which can be measured only with comparison of the positions of the same stars in two different epochs. In this case though, the observations were taken in one epoch only, not allowing to use this method.

To subtract the globular cluster in each field, a region centered on the center of the globular cluster, with a radius equal to the tidal radius of the cluster, was considered. The tidal radius (r_τ) of a globular cluster is the distance from the center beyond which the stars are not gravitationally bounded to the cluster. To validate this approach, also radial star counts on the image were taken in account: for both clusters, the image was divided in bins along the x and y axis separately; inside each bin the stars were counted and the number of stars per bin was plotted versus the coordinates. In Fig. 4.11 these plots are shown: the peak at the center is obviously the center of the globular cluster, where the star density is highest, while the "holes" at about 2000, 4000, 6000 pixels along the x axis and at 4000 pixels along the y axis are caused by the gaps between the 8 chips covering the whole field. In the external regions, roughly beyond 2000 pixels from the center, the star counts seems to flatten, meaning that there is not more contribution from the globular clusters. Only stars in the external region are then taken.

NGC 6558, NGC 6352 and NGC 4833 have tidal radii of $r_\tau = 10.44, 10.51$ and 8.79 arcmin, respectively. Since in a following step the disk component will be subtracted from the bulge field anyway, and to do that it's necessary to consider the same area in the sky, in all three cases a region with a radius of $r_\tau = 10.44$ (i.e. the tidal radius of the globular cluster in the bulge field) was subtracted (Figures 4.12, 4.13 and 4.14).

I want to note that in MW05, the field and the globular cluster show similar Blue Horizontal Branch morphology. One could argue that the sdBs stars I observed belong to this cluster and not to the bulge. NGC 6558 is metal-poor ([Fe/H]=-1.44, Harris [2003]) and it has a heliocentric radial velocity of ~ -197 km/s (Harris [2003]), with a kinematics more similar to the value expected for the halo (Norris [1986]) than for the bulge. Finally NGC 6558 has an Horizontal Branch reaching V$\sim$ 18 (Rich et al. [1998]), while the Horizontal Branch in the field, well out the tidal radius, reaches fainter magnitudes. Probably, the fact that bulge field and cluster show similar Horizontal Branch is due the fact that in the cluster region there are anyway bulge stars.

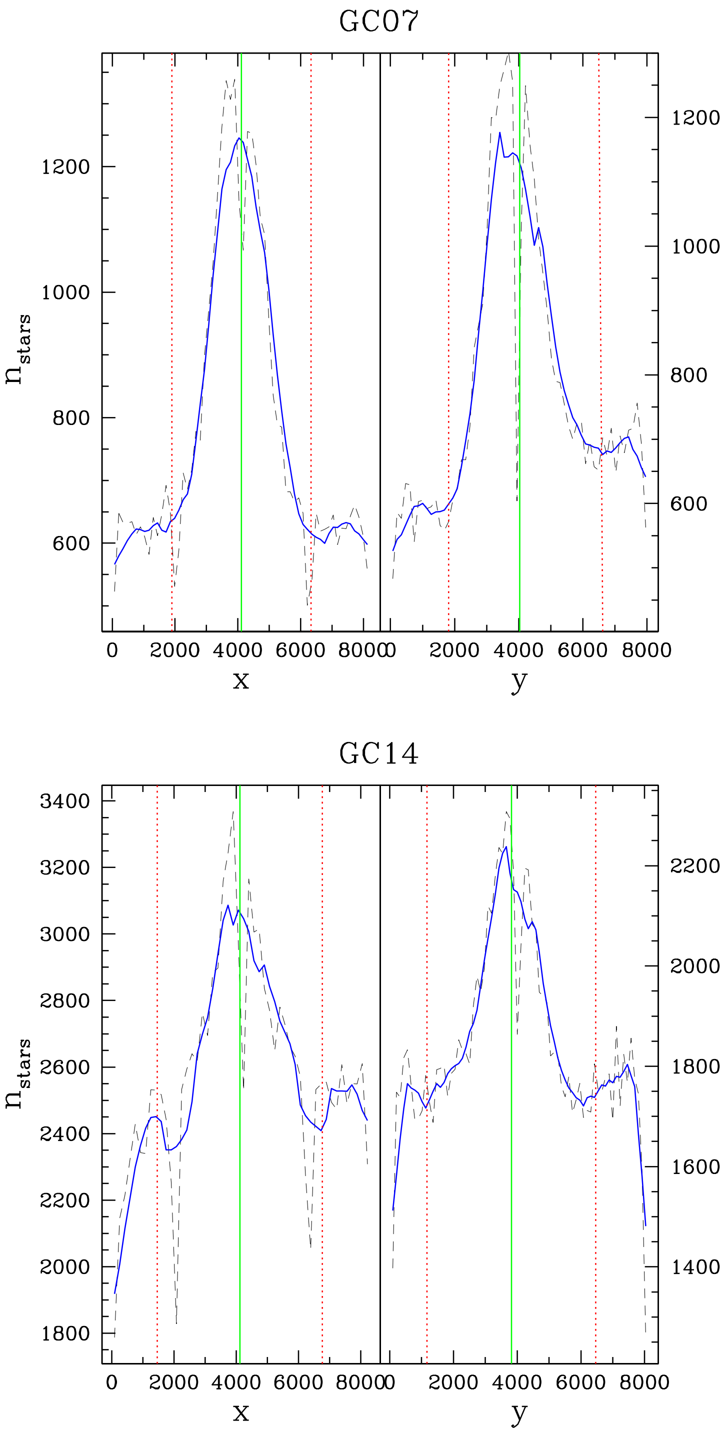

Figure 4.11: Star counts along the x and y axis (left and right panels respectively) for the GC07 (containing the cluster NGC 4833) and the GC14 (containing the cluster NGC 6352) disk fields. The dashed line represents the star counts for each bin, while the solid line is the same but smoothed. The vertical solid line at ∼4000 pixels, both in the x and y direction, represents the center of the globular cluster and the dotted red lines represent the limits given by the tadial radius. The wells at ∼2000, 4000, 6000 pixels along the x axis and at ∼4000 pixels along the y axis are due to the gaps between the 8 chips of the whole WFI fields.

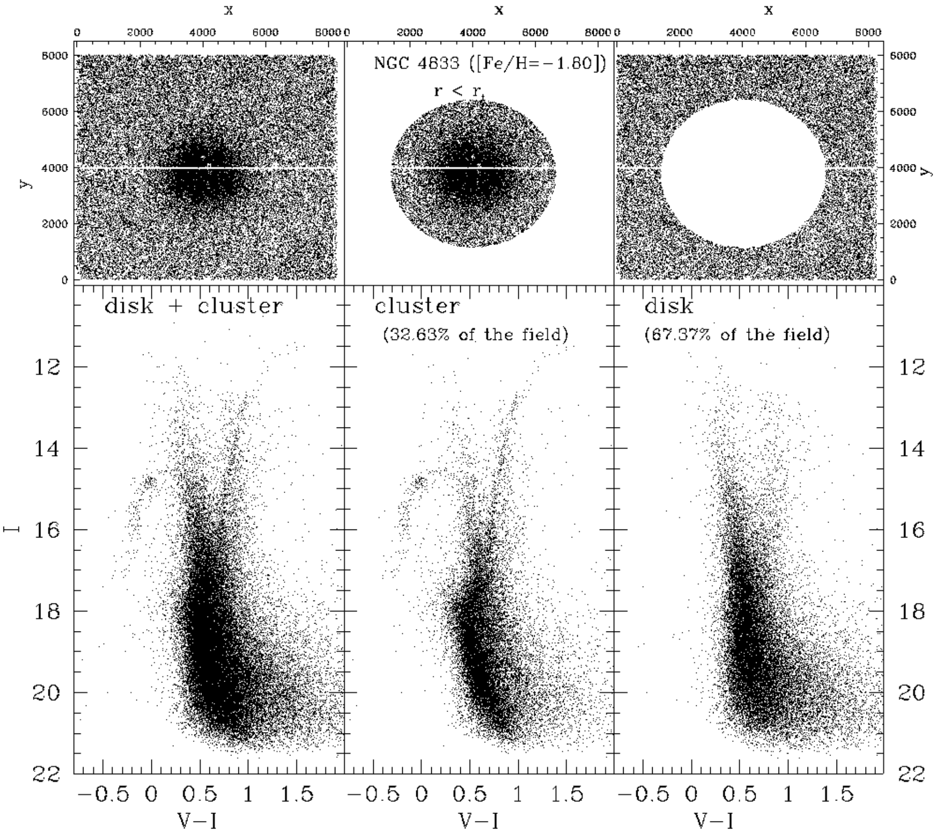

Figure 4.12: Subtraction of the globular cluster NGC 4833 population from the GC07 disk field. The top panels show respectively the whole region, the subtracted one (of the globular cluster) and the remaining one (of the field). The bottom panel show the color-magnitude diagrams of the corresponding regions.

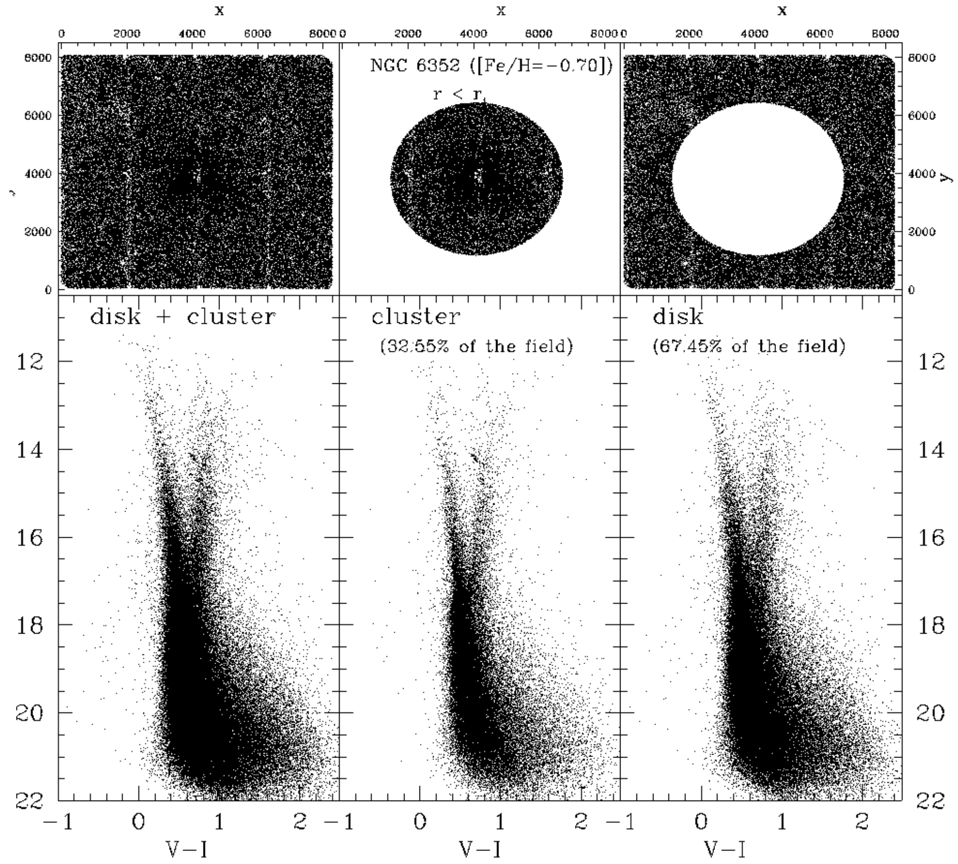

Figure 4.13: Subtraction of the globular cluster NGC 6352 population from the GC14 disk field. The top panels show respectively the whole region, the subtracted one (of the globular cluster) and the remaining one (of the field). The bottom panel show the color-magnitude diagrams of the corresponding regions.

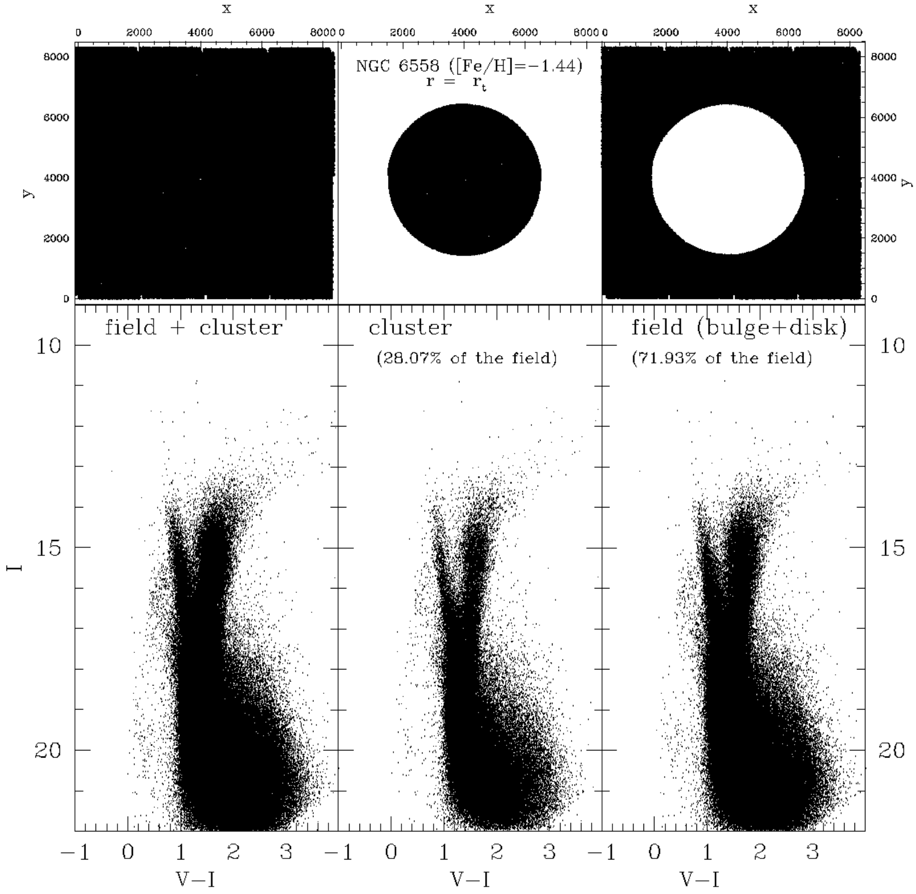

Figure 4.14: Subtraction of the globular cluster NGC 6558 population from the MW05 bulge field. The top panels show respectively the whole region, the subtracted one (of the globular cluster) and the left one (of the field). The bottom panel show the color-magnitude diagrams of the corrisponding region.

4.6.2 Expected and observed star ratios

One of the aims of this work is to look for sdB star candidates in other bulge fields. While such stars are also in the disk of our galaxy, it is expected to find a much smaller number of them, mainly for two reasons: in the disk the density is lower than in the bulge and the stellar population is on average younger, while sdB stars are evolved and thus older stars. In the obtained color magnitude diagrams stars less luminous than the turnoff of the main sequence and with a dereddened color (V-I) bluer than 0, were selected as sdB star candidates. The results are listed in the sixth column of Tab.4.2. The number of sdB candidates varies between bulge and disk fields as expected but it varies also between different bulge fields: while for example in the MW05 field there are more than 140 candidates, in the MW08 field there are only about 20. This can be explained considering the different galactic latitudes of the fields: roughly, at the distance Sun-Galactic center of 8.5 kpc, galactic latitudes of $\sim -6°, -10°, -12°$ and mean distances from the galactic plane of $\sim$ 0.89, 1.48, 1.77 kpc,respectively. Since the bulge radius is about 1.5 kpc, it is clear that, while the MW05 field is well inside the bulge, the MW08 field is on the edge. But to obtain a better estimate it is necessary to consider how many bulge stars are observed along the line of sight at different latitudes: to do that, a bulge density law was integrated over the volume of the bulge we are observing.

The assumed density profile is the luminosity density law provided by Dwek et al. [1995]. It describes a boxy Gaussian distribution, that takes into account the fact that the bulge is a simple spheroid, with possible evidence of a bar:

$$\rho = \rho_0 r^{-0.5 r_s^2}$$

with $r_s^2 = \{[(\frac{x}{x_0})^2 + (\frac{y}{y_0})^2]^2 + (\frac{z}{z_0})^4\}^{1/2}$ is the distance from the Galactic center, which is correlated with the galactic coordinates (l, b) and the distance s along the line of sight by the following relations (see Fig.4.15):

- $x = -s \cos b \sin l$ is the axis pointing toward the decreasing galactic longitude l

- $y = -\mathrm{D} - s\cos b \cos l$ is the axis pointing toward the observer located at (0,-D,0), where D = 8.5 kpc is the adopted distance to the Galactic center.

- $z = s \sin b$ is the axis pointing toward the Galactic north

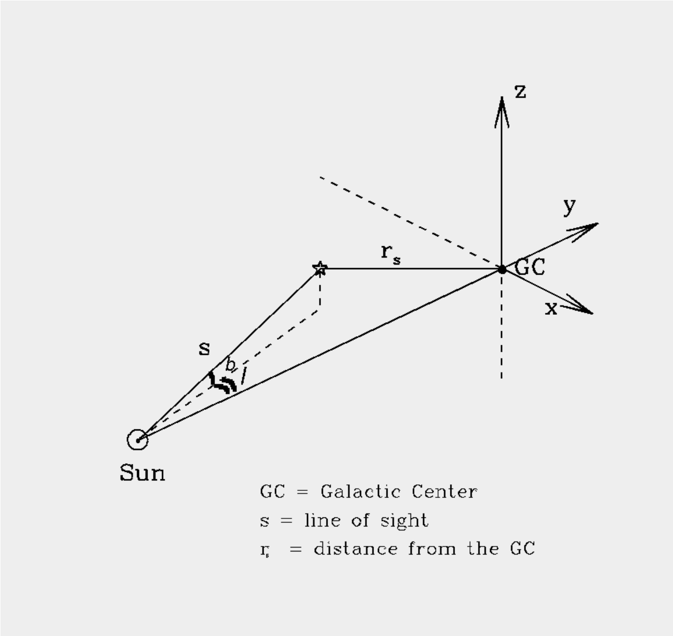

Figure 4.15: Galactic coordinates l and b and xyz system.

- $x_0 = 1.58$ kpc, $y_0 = 0.60$ kpc and $z_0 = 0.45$ kpc are the length scales of the bulge along the x,y,z axis.

The volume is a pyramide whose base A is the field of view of the detector (in this case the WFI field is 34'× 33') and whose height is the line of sight s:

$$V = \frac{1}{3}As^2$$

Integrating the luminosity density ρ along the line of sight between 0 (the observer) and 10 kpc (the farest end of the bulge), the total luminosity L_{tot} is obtained. L_{tot} is proportional to the total number of stars (but different for different ages). Assuming that the stellar population is the same in the whole bulge, at different latitudes the ratio between L_{tot} is proportional to the ratio between the number of stars. The following ratios were then calculated:

$$\frac{L_{MW05(b=-6)}}{L_{MW07(b=-10)}} = \frac{N_{MW05}}{N_{MW07}} \approx 29.3$$

$$\frac{L_{MW05(b=-6)}}{L_{MW08(b=-12)}} = \frac{N_{MW05}}{N_{MW08}} \approx 169$$

$$\frac{L_{MW07(b=-10)}}{L_{MW08(b=-12)}} = \frac{N_{MW07}}{N_{MW08}} \approx 5.8$$

4.7 Disk stars

Since the purpose of the disk fields is to be used as check for the disk population observed in the direction of the bulge, some numbers were calculated also for these regions, that is the number of expected sdB stars and the number of stars along the blue main sequence of the disk. Also in this case a density law is needed. In general the disk profile is a decreasing exponential function, keeping in account a scale height, since at higher latitudes, therefore at higher distances from the galactic plane, the line of sight crosses a smaller portion of the disk, and a scale length, since the disk thickness is not constant but increases toward the galactic center. The simplest models are just like the following:

$$\rho = \rho_0 e^{\frac{r}{r_0} - \frac{z}{z_0}}$$

where ρ_0 is the density in the solar region, r is the distance from the Sun on the Galactic plane toward the Galactic center and r_0 is the scale length, z is the distance from the Galactic plane and z_0 is the scale height.

A more sophisticated model is the one provided by López-Corredoira et al. [2004], which takes into account also the hole that seems to be between the inner region of the disk and the bulge:

$$\rho = [\rho_0 e^{(\frac{R_0}{1970pc} + \frac{3740pc}{R_0})}] e^{-(\frac{R}{1970pc} + \frac{3740pc}{R})} e^{-\frac{|z|}{h_z(R)}} \text{ star pc}^{-3}$$

$$h_z(R) = 285[1 + 0.21kpc^{-1}(R - R_0) + 0.056kpc^{-2}(R - R_0)^2] \text{ pc}$$

where R is the distance from the Galactic center and R_0 the distance of the Sun. The scale height varies with the distance from the Galactic Center but also with the age of the population. The volume sampled along the line of sight is the same as the one for the bulge.

Expected disk sdBs

Since sdBs in the field of the Milky Way consist of a mixture of thin and thick disk (Altmann et al. [2004]), a ratio of 50:50 was assumed. For the old thin disk, values of z_0=325pc and r_0=2.8kpc as in Ojha [2001] were adopted and z_0=325 and r_0=3.5kpc as in Larsen & Humphreys [2003]. For the thick disk, z_0=900pc and r_0=4.7kpc were assumed. In the case of the Lopez-Corredoira et al.[2004] model, the height scale varies with the distance. In Tab.4.2 the number of expected sdB stars for the different disk models and also the number of sdB candidates observed in the different fields are listed. Obviously in the case of the bulge fields, the number of observed sdB candidates is higher as we are observing not only the disk but also the bulge.

field	b	Ojha	L & H	Lopez-C.	observed
MW05 (bulge)	-6	4.2-8.4	2.5-4.9	8.3-17	140
GC14 (disk)	-7	3.9-7.8	2.4-4.9	1.8-3.7	27
GC07 (disk)	-8	1.7-3.3	1.0-1.9	6.4-13	16
MW07 (bulge)	-10	0.7-1.3	0.4-0.8	3-6	40
MW08 (bulge)	-12	0.4-0.7	0.2-0.5	2.4-4.9	19

Table 4.2: Number of predicted (in column 3,4,5, Ojha [2001], Larsen & Humphreys [2003], Lopez-Corredoira et al. [2004] respectively) disk sdBs and observed (column 6) sdB candidates for the different galactic fields.

Number of expected Blue Main sequence stars

In order to correct the bulge fields for the disk population, it is necessary to find a normalization factor, since, as just seen, the number of disk stars is different at different latitudes. To estimate this factor, the number of blue bright stars was estimated, since this kind of stars, belonging to the younger population of the disk, are observed only in the disk and not in the bulge. To do that, I adopted the same disk models described before, but now using the scale height of the young thin disk z_0 =90 pc, according to Larsen & Humphreys [2003]. The model of López-Corredoira et al. [2004] does not distinguish between young and old thin disk: therefore, to have a rough estimate, the adopted scale height was divided by a factor 3 (but still depending on the distance). Assuming a local density of 0.05 star pc^{-3} (Lopez-Corredoira et al. [2004]), the expected numbers of young stars for the galactic fields are listed in Tab.4.3:

field	l	Larsen & Humphreys 2003	Lopez-C. et al.2004
GC07	-7	1.34×10^7	2.60×10^7
GC07	-8	1.34×10^7	2.60×10^7
MW07	-10	0.38×10^7	0.79×10^7
MW08	-12	0.14×10^7	0.29×10^7
GC07/MW07		3.52	3.29
GC07/MW08		9.57	8.97
MW07/MW08		2.71	2.72

Table 4.3: Expected number and ratios of bright blue stars in the different fields

Since the value I need is the normalization factor between the different fields, the ratio between the expected numbers was calculated and it is listed in Tab. 4.3 too. While the expected number of stars is different following the models of Larsen & Humphreys [2004 and Lopez-Corredoira et al. [2004], the ratios instead agree.

4.7.1 Subtraction of the Disk population (observed)

The observed disk fields differ because they have different coordinates (i.e. different part of the galactic disk are sampled) and different sizes (the disk fields are smaller since the region containing the globular cluster was subtracted). To account for these factors, for all fields the number of blue bright Main Sequence stars was calculated, since they are typical only of the young disk population, while in the bulge they are already evolved away from the main sequence.

Obviously it is necessary to compare the number of blue stars in the same region of the bulge CMD and of the disk CMD to be subtracted. Overplotting the disk CMD on the bulge CMD, in order to find the ratio between the blue stars in the different fields, a problem arose, that is the slope of the blue Main Sequence looks different in the fields (an example is shown in Fig.4.16)

OGLE bulge fields

In order to verify if the different slope was caused by an error in the calibration and/or in the reddening correction, bulge fields from the Optical Gravitational Lensing Experiment (OGLE) were analyzed. The aim of the OGLE project is to find gravitational lensing events in crowded environments (as is the galactic bulge, see also Ch.1). On the OGLE website[6], the photometry of several bulge fields in the V,I filters is available (Udalski et al. [2002]) and for each field also the appropriate reddening map is provided (Udalski [2003]). Unfortunately, no disk fields close to the WFI disk fields are available, but to check if different fields show disk blue Main Sequences with different slopes, I analysed fields with different latitudes (i.e. sampling different parts of the disk). The photometry was corrected for the appropriate reddening value, obtained from the reddening maps provided by OGLE, and the color magnitude diagrams were overplotted. Two of these fields are shown in Fig. 4.17.

Also in the case of OGLE fields, that is a different set of observations, taken with different instruments, calibrated in an independent way, the different slope is still evident. This feature could be caused by the fact that we

---

[6] http://bulge.princeton.edu/∼ogle/

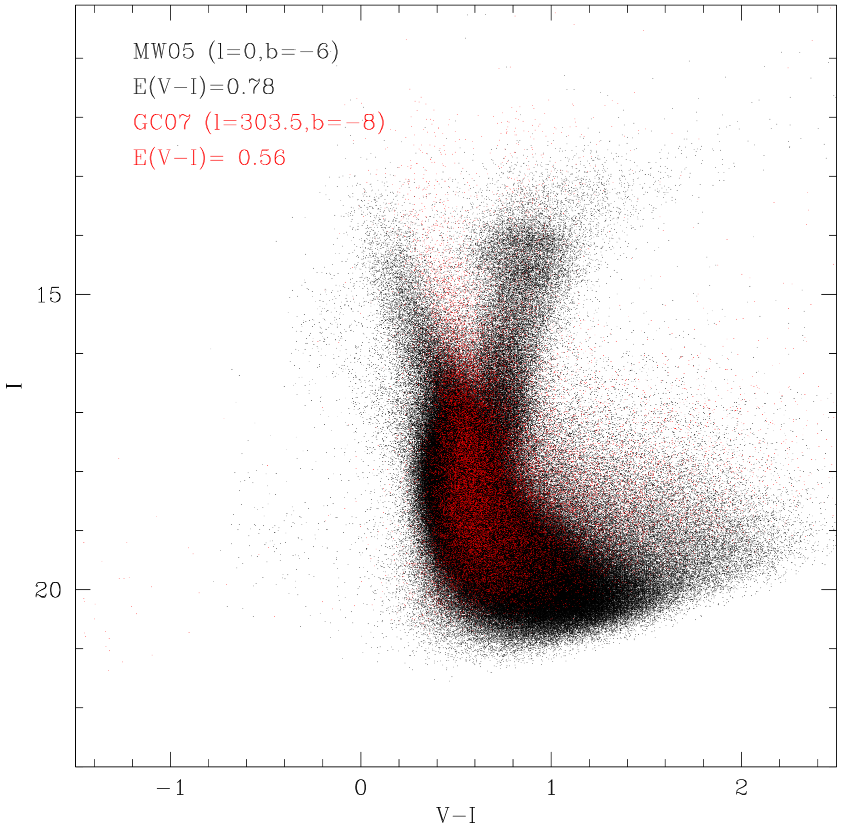

Figure 4.16: Comparison between the color magnitude diagrams of the bulge field MW05 (in black) and the disk field GC07 (in red). The different slope of the blue bright Main Sequence is evident.

are looking in different directions at stars at different distances: the closest stars are apparently brighter and less reddened (hence bluer) with respect to the farest stars that are apparently less luminous and redder, and this tilts the Main Sequence along a reddening line. In a different direction, this tilt can be different because e.g. an interstellar gas cloud is present in one field only, causing a different reddening. Unfortunately, the reddening correction and the color magnitude diagram does not allow to distinguish between a more reddened bright star and a less reddened more distant star.

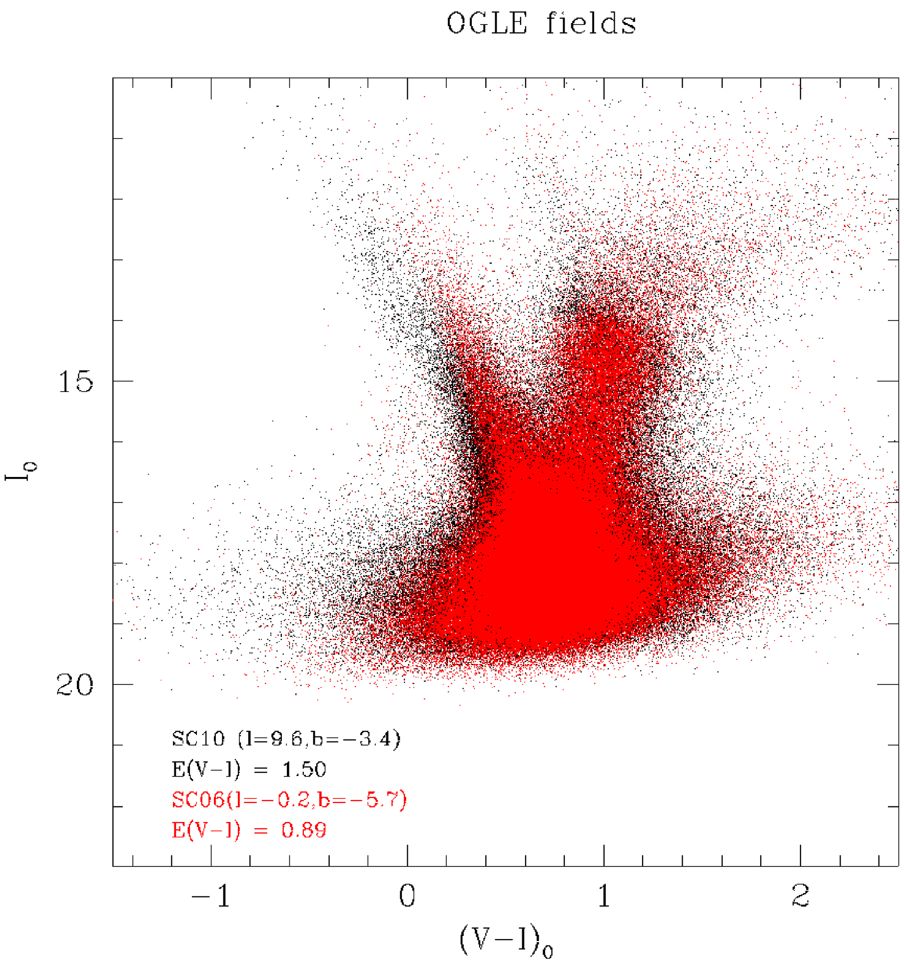

Figure 4.17: Comparison between the color magnitude diagrams of two OGLE bulge fields, corrected for reddening using the OGLE reddening maps. The coordinate of the two fields are labeled. Also in this case the different slope of the blue main sequence is evident.

Correction for different slope

To calculate the number of blue main sequence stars in the same region of the color magnitude diagram for both bulge and disk fields, I applied a transformation to the disk photometry, in order to make the two blue main sequence overlap.

For both fields, the upper blue main sequence, where the slope difference is more evident, was fitted with a straight line (see Fig.4.18) according to:

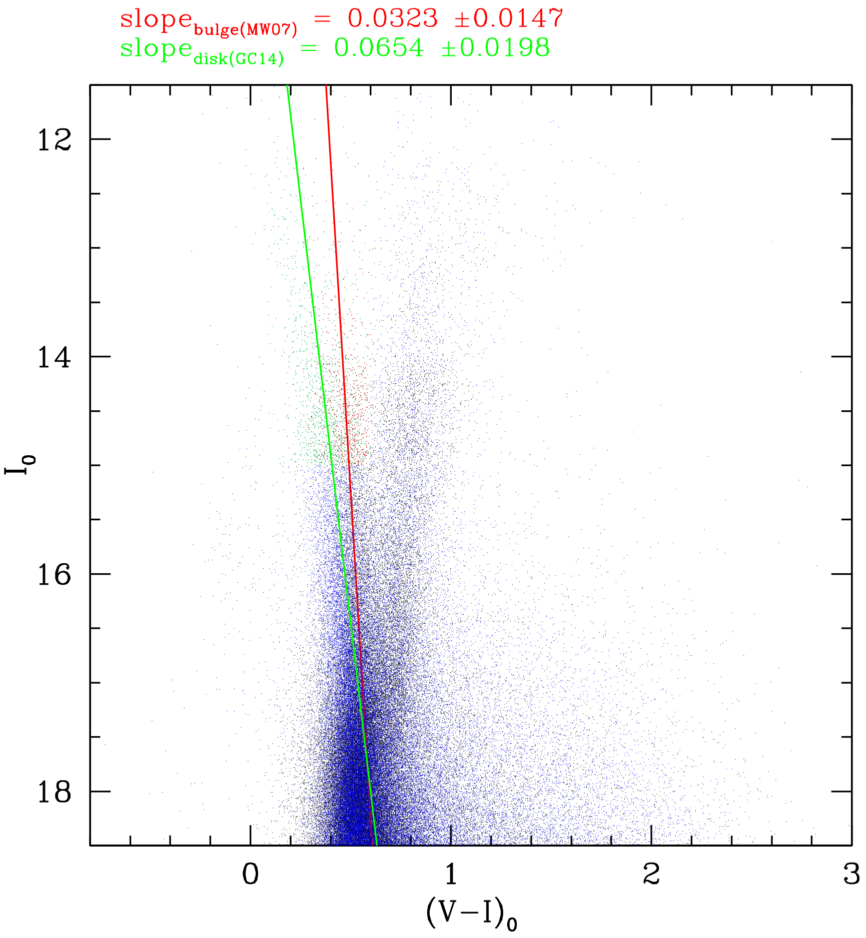

Figure 4.18: Comparison between the bulge field MW07 (black) and the disk field GC14 (blue). The upper blue main sequence was selected in both fields and fitted with a straight line (red for the bulge field and green for the disk field. The slopes of the lines are labeled.)

$$I = a * (V - I) + b,$$

where a is the slope and b is the intercept.

Then the following transformation was applied to the whole disk color magnitude diagram:

$$(V - I)'_{disk} = (V - I)_{disk} + (a_{bulge} - a_{disk}) * I_{disk} + b_{bulge} - b_{disk}$$

where $(V-I)'_{disk}$ is the transformed color, a_{bulge} and a_{disk} are the slopes of the two fitted lines and b_{bulge} and b_{disk} are the intercepts of said lines. In Fig.4.19,

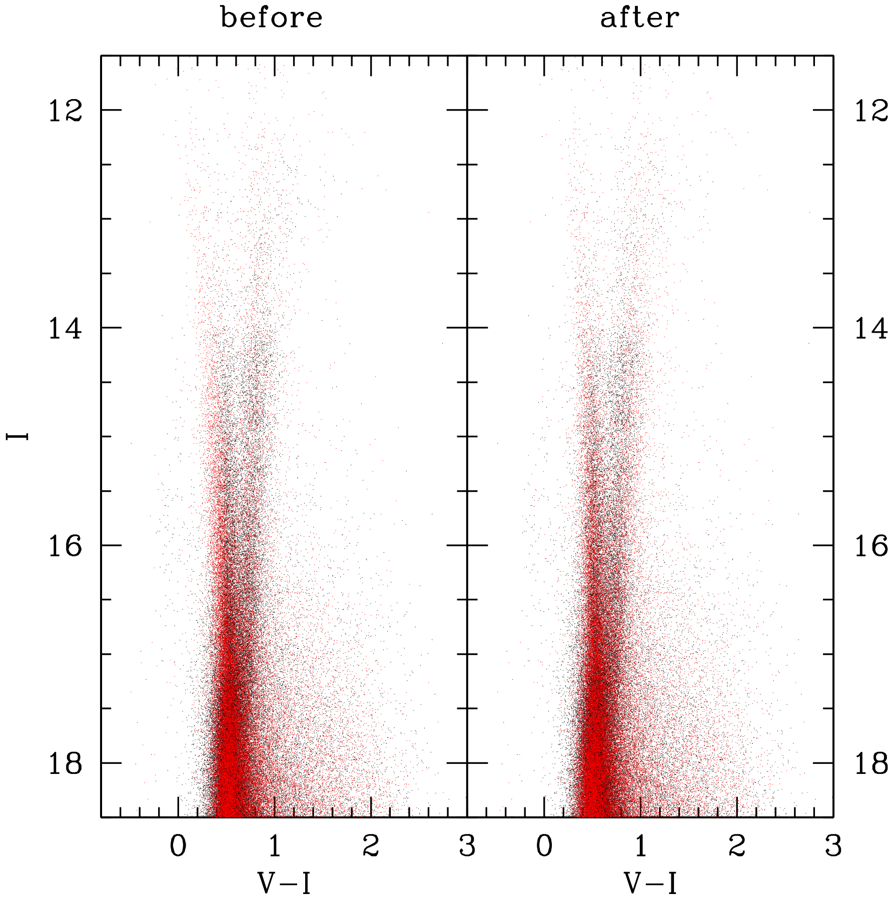

Figure 4.19: Comparison between the bulge field MW07 (black) and the disk field GC14 (red) before (left panel) and after (right panel) the correction applied to make the blue main sequence of both fields overlap.

the comparison between the two fields before and after the transformation is shown. Since the cause of the different slope is a combined effect of reddening and distance that affects all stars, I applied the trasformation to all stars.

Ratio between the blue main sequence stars of bulge and disk fields

Once the blue main sequences overlap, a box was chosen in the color magnitude diagram to calculate the ratio of these stars in the different fields. The position and the size of the box influence this ratio:

- if the box is shifted too far towards the red part of the diagram, it could contain also red giant branch bulge stars;

- for the same reason it cannot be too extended toward fainter magnitudes, since it could contain main sequence bulge stars;
- it cannot be too small, because the sample would not be significant from the statistical point of view.

Another point to keep in mind is that we are looking at disk fields at different galactic latitudes and longitudes, i.e. we are sampling not only different part of the disk but also different depths. For example, for $b = 6°$ the line of sight leaves the disk at a larger distance compared to a field with $b = -10°$, whose line of sight leaves the disk earlier (see Fig.4.20).

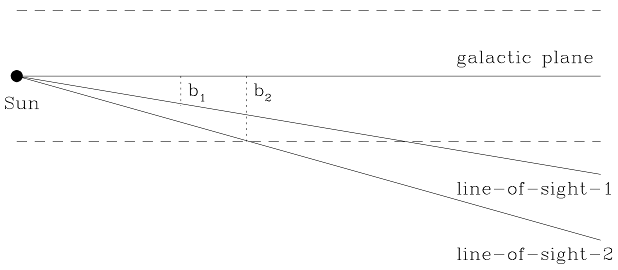

Figure 4.20: Schematic representation of the Galactic disk (between the two dashed lines): at different galactic latitudes b, the line of sight crossed different portions of the disk.

Fig. 4.21 shows an example of the choosing of the box for the bulge field MW07 (in black the total CMD and in blue inside the box) and the disk field GC14 (in red the total CMD and in green inside the box). Also the ratio between the MW07 and GC14 stars inside the box is labeled: in this case the value ∼0.77 is explained by the fact that the absolute latitude of the GC14 field (b$\sim -7°$) is smaller than the MW07 field (b$\sim -10°$), meaning that in the GC 14 field direction, a bigger portion of the disk is sampled (see Fig.4.20).

The statistical subtraction

Once the normalization factor is found, the disk field was used to statistically decontaminate the bulge CMD from the foreground disk stars. For each disk

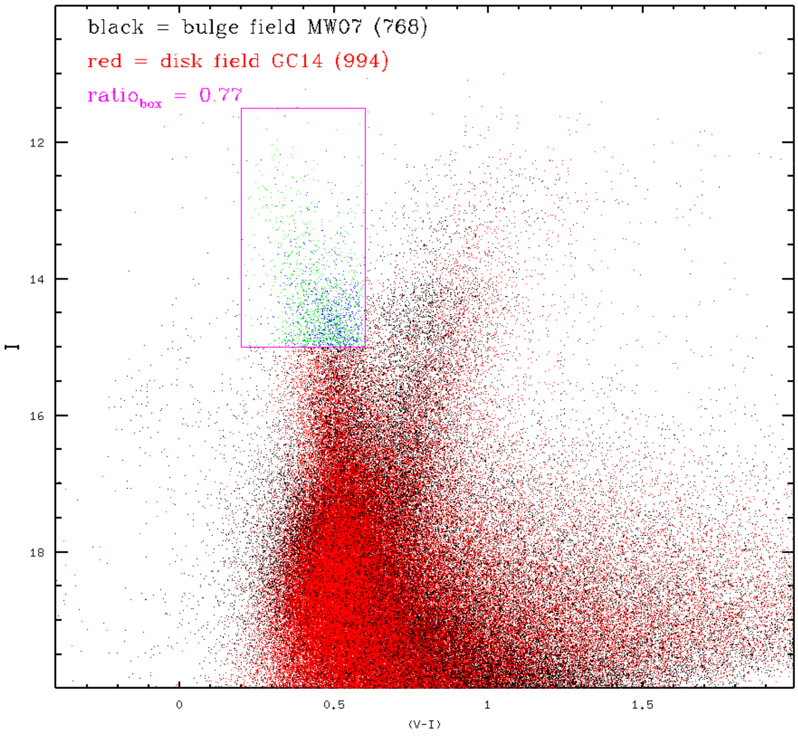

Figure 4.21: Example of choosing of the box to calculate the normalization ratio between the blue Main Sequence in the MW07 bulge field and the GC14 disk field. In this case, the ratio value is ≈ 0.77, meaning that for each disk star in GC14, 0.77 stars in the bulge CMD were subtracted.

star in the disk CMD (Fig.4.22, top right panel) I picked up the closest star in the bulge CMD and subtracted it according to the normalization factor explained above. The "photometric" distance on the CMD from a disk star to each bulge star was defined as:

$$d = \sqrt{[7 \times \Delta(V-I)]^2 + \Delta I^2}.$$

and the bulge star whose distance from the disk star was minimal was subtracted. The color difference has been enhanced by a factor of 7 because the color is much less sensitive than the magnitude to physical differences (in the distance, reddening or mass) between a given disk star in the control field, and another disk star along the bulge line of sight. The resulting, cleaned CMD of the bulge is shown in the left bottom panel of Fig.4.22, while the CMD of the stars statistically removed from the bulge CMD is shown in the right bottom panel. In each panel, the number of stars (in red) used to calculate the normalization factor is labeled. During the subtraction, some disk stars were not subtracted because the corresponding stars in the bulge CMD were not found (in green in Fig.4.22), that is when the minimum distance between two stars is too big.

As the bottom panel of Fig.4.22 shows, the subtraction was not very successful, mainly for two reasons: the red giant branch of the bulge is missing and there are still some stars (in red) in the box region used for the normalization, while no one is expected. While this is only an example of the statistical subtraction (and actually it is one of the best examples), several tests were made, using the other disk field (GC07), not only on MW07 but also on the other bulge fields (MW05 and MW08), and no one was good enough to be employed in the construction of the UV spectrum. The reason of this failure could be that we are looking at different regions of the galactic disk, where the stellar population could be different and affected by different reddening, and the attempts to correct for these effects were not sufficiently successful.

4.7.2 Subtraction of the Disk population (simulated)

Since the correction of a bulge field with an observed disk field was not successful, another attempt was made using instead for the disk a synthetic color magnitude diagram, that is a diagram where the magnitudes and colors of the disk stars in the direction of the observed bulge field were simulated.

The simulated color magnitude diagrams were provided by S. Ragaini (private communication, Ph.Thesis) at the University of Padua. For a detailed description of the simulations, I refer to the papers Bertelli et al. [1995],

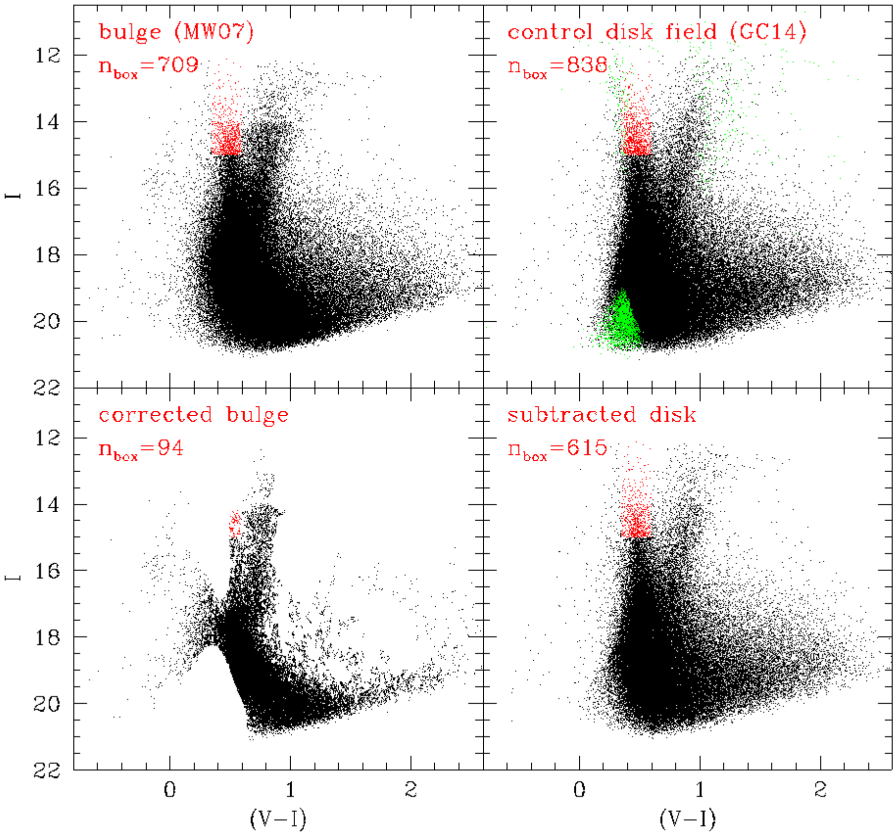

Figure 4.22: Example of the statistical subtraction of the disk field GC 14 from the bulge field MW 07. In each panel the number of stars (in red) used to calculate the normalization factor is labeled. Top left panel: bulge field CMD; top right panel: disk field CMD, where also the number of disk stars no found (in green) in the bulge CMD is labeled; bottom left panel: bulge CMD after the disk subtraction; bottom right panel: subtracted disk CMD.

Bertelli et al. [2003], Vallenari et al. [2000], Vallenari et al. [2006] while here I give a brief outline: first synthetic populations are generated by varying the parameters age, metallicity range, star formation law and initial mass function; then the stars are distributed along the line of sight following a model of the Galaxy, where the thin disk is assumed to have a metallicity of Z=0.008÷0.03 and age of between 1-5$\times 10^8$yrs (for the young thin disk) and 10$\times 10^9$yrs (for the old thin disk), while the thick disk is assumed to have metallicity Z=0.0006÷0.008 and age 8-12$\times 10^{10}$yrs. The photometric completeness and errors of the data are taken into account.

Since the slope of the blue main sequence is governed by extinction (see also Sec.4.7.1), from this slope the "local" extinction was determined, starting with an initial guess for the reddening values. It was possible to make these simulations for the bulge field MW05 only, but simulations also for the other fields are planned.

Since MW05 is the more populated bulge field (with $\sim 5 \times 10^5$ stars), the disk simulations were made chip by chip to avoid problems with the reddening estimate and also to speed up the running of the program. Fig.4.23 shows the comparison between the observations (top left panel) and the simulated disk (top right panel). There is very good agreement between the two CMDs, except for the low luminosity tail for (V-I)$\gtrsim$2 and in general at low luminosity, where there seems to be more disk stars than observed, probably caused by some errors in the completeness. The "red" tail could be explained with the photometric errors that have been taken into account to do the simulations: it is known that the photometric errors provided by `DAOPHOT/ALLSTAR` are underestimated by a factor at least 3 and since the photometric errors increase with the magnitude, at low magnitudes the difference between the observations and simulation appear more evident.

Following the same procedure described in the section 4.7.1, the simulated disk was subtracted. In this case the normalization factor was 1 since the disk simulation was created using the very same observed disk in the bulge field and it was verified counting the stars in the upper blue Main Sequence. Fig.4.23 shows an example of the statistical subtraction for the chip 1 of the MW05 field.

The final MW05 bulge field CMD

The remaining bulge stars were corrected for the reddening chip by chip, as explained in the section 4.4, and then combined to obtain the final CMD for the bulge field MW05 shown in 4.24. In this figure the typical bulge sequences (in black), as the main sequence, the red giant branch, the red horizontal branch clump (at (V-I)$\sim$0.6 and I$\sim$14) are evident.

The grey stars are stars that remain after the disk subtraction, because, as explained in 4.7.2 the simulations do not manage to reproduce well the photometric errors. In the disk subtraction using the observed disk field (Sec.4.7.1) these stars are subtracted because obviously in this case the observed disk field shows the "tail" caused by the errors. The same reason could explain the "horn" at (V-I)$\sim$0.3, which stars are marked in cyan.

The stars marked in red seem to form an extended Horizontal Branch (HB) sequence. HB stars have been previously observed in the bulge by Peterson et al. [2001] and moreover an extended HB is not typical for the

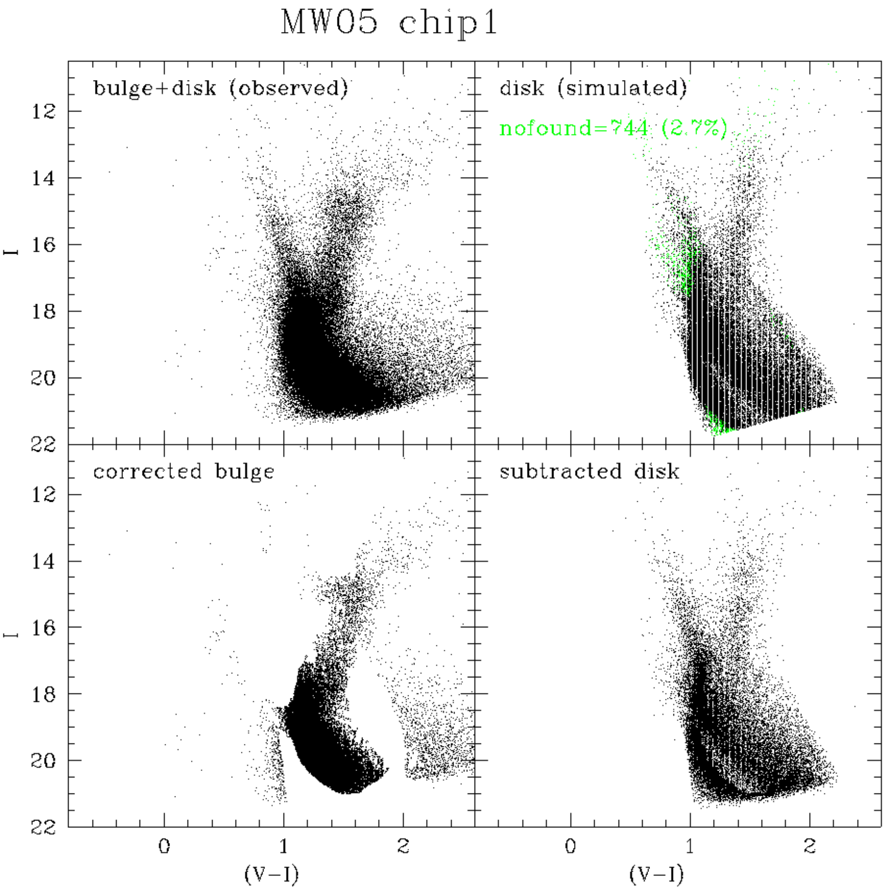

Figure 4.23: Example of the statistical subtraction of the simulated disk field from the observed bulge field MW05. Top left panel: bulge field CMD; top right panel: simulated disk field CMD, where also the number of disk stars no found (in green) in the bulge CMD is labeled; bottom left panel: bulge CMD after the disk subtraction; bottom right panel: subtracted disk CMD.

disk population. The blue stars could possibly be post-HB stars, but there are too many of them: the number of expected post-HB stars is 0.1 stars per HB stars. Probably the blue stars are a combination of real post-HB stars and remaining disk blue Main Sequence stars. Since there is no way to disentangle the two populations in this case and since post-HB stars should have only a marginal role in the UV excess (Brown et al.[1997]), I left them out from the construction of the integrated spectrum. The purple stars represent the sdB star candidates and they are a mixture of real sdB stars and cooler stars with lower reddening. The green stars could be Blue Straggler stars but previous

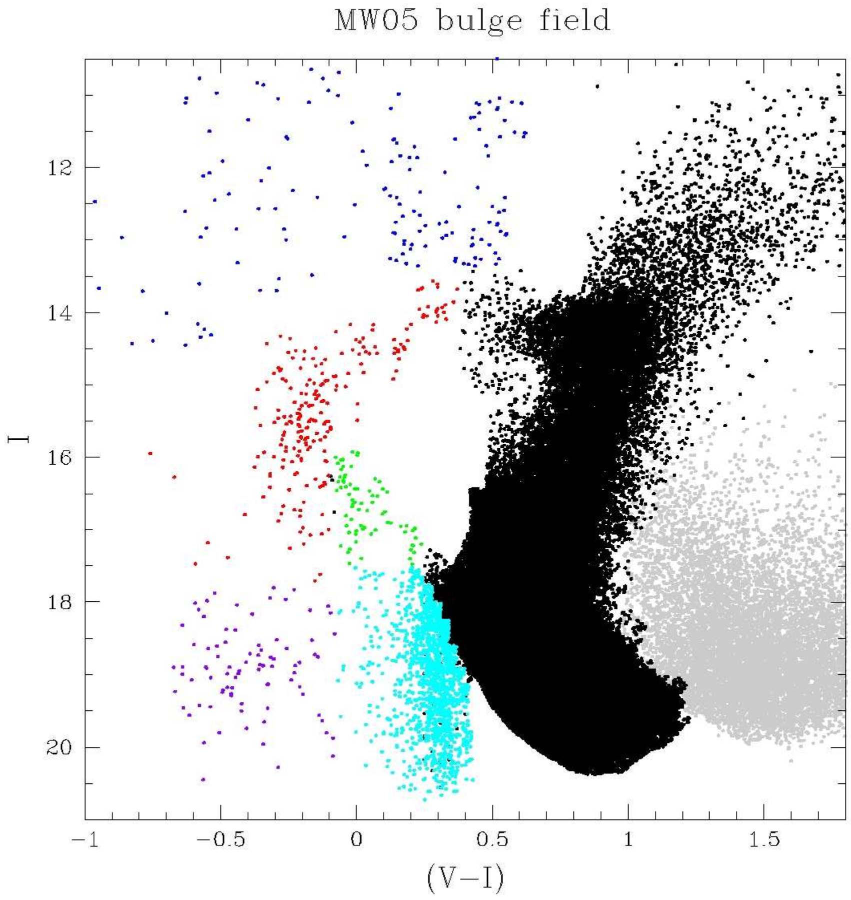

Figure 4.24: Final color magnitude diagram for the bulge field MW05. See text for the stars shown in different colors.

studies as Kuijken & Rich 2001 (based on the study of the proper motion of stars) ruled out the presence of Blue Stragglers in the bulge. Probably this feature is caused again by a non-perfect subtraction of the disk, due to the underestimate of the photometric errors (like the grey and cyan stars).

For the construction of the integrated spectrum I used only the black (Main Sequence, Red Giant Branch, Red Horizontal Branch), the red (Blue Horizontal Branch) and the purple (Extended Horizontal Branch) stars.

Chapter 5

The stellar libraries

In order to construct the integrated spectrum of the Bulge, a spectral library is necessary. There are two kinds of spectral libraries: observed libraries and theoretical ones, both showing advantages and disadvantages. An observed library is a collection of observed stellar spectra, usually of different spectral types; it has the advantage to have examples of real stars (so for instance, effects like diffusion are correctly taken into account) but often it does not cover the whole range of spectral types, luminosity class and metallicities, and usually it does not cover the full wavelength range, especially outside the optical domain. A theoretical library instead is a collection of synthetic spectra, obtained modeling stellar atmospheres; it has the advantage to provide a wide range of gravity, temperature and metallicity, but, as close to reality as those spectra are, they are indeed synthetic and there could be some problems in the calibration, e.g. because of missing lines, non-scaled solar abundances, mass loss, etc. The observed and theoretical spectral libraries which have been considered are listed in Tab. 5.1 and 5.2 respectively. For the empirical libraries the table gives the wavelength coverage, the resolution, the number of star spectra the library provides, the spectral types and luminosity classes of the stars and their metallicities. In the case of the theoretical libraries, the wavelength coverage and the resolution of the library, the temperatures, the surface gravities and metallicities of the spectra are given. To choose the library, the following parameters have been taken into account: the wavelength range, the resolution, spectral type, luminosity class, metallicity coverage. Among the observed libraries, the Pickles [1998] library has been chosen because it is the only one extending from the ultraviolet to the infrared, while the others cover only the UV range, like for example the EUVE library, or only in the optical; and for the same reason the BaSeL library (Lejeune et al. [1997]) has been picked among the theoretical ones. These two libraries are discussed in details in the next section.

Table 5.1: List of observed spectral library

Reference	λ range (Å)	$\lambda/\Delta\lambda$	n stars	Spectral Type	Luminosity class	metallicity
Gunn & Stryker [1983][1]	3130-10800	~ 200	175	O-M	III,IV,V	
Silva & Cornell [1992][2]	3510-8930	~ 500	72	O-M	I-V	solar with some metal-rich ([Fe/H]> 0.15) and weak ([Fe/H]< -0.2)
Craig et al. [1997][3] (EUVE)	70-760	~ 260	95	B-M, WD DA-DO	I-V	
Pickles [1998][4]	1150-10620	500	131	O-M	I-V	$-0.5 <$[Fe/H]< 0.5
	1150-25000	500	~ 65			
Meyer et al. [1998][5]	5600-6600	3000	85	O7-M5	I-V	solar
Wallace et al. [2000]	J-band (1.05-1.34 μm)	300	88	O7-M6	I-V	
Montes et al. [1999][6]	3800-10000	12000	130	F-M	III,IV,V	depends on the star
Le Borgne et al. [2003][7]	3200-9500	2000	249	O-M	I-V	$-2.75 <$[Fe/H]< 0.48 depending on the spectral type

[1] http://cdsweb.u-strasbg.fr/htbin/Cat?III/88

[2] http://zebu.uoregon.edu/spectra.html

[3] http://www.ssl.berkeley.edu/ euve/sci/Resources_pubs_atlas.html

[4] http://www.ifa.hawaii.edu/users/pickles/AJP/hlib.html

[5] ftp://ftp.noao.edu/catalogs/medresIR/

[6] http://www.ucm.es/info/Astrof/fgkmsl/FOEfgkmsl.html

[7] http://www.ast.obs-mip.fr/article181.html

Table 5.2: List of theoretical spectral library

Reference	$\Delta\lambda$	ΔT	[M/H]	$log g$	$\lambda/\Delta\lambda$
Kurucz [1993][8]	1000-10000 Å	3000-50000 K	-5.0…1.0	0.0…5.0	$\sim$ 390 (1000-2900 Å) $\sim$ 320 (2900-10000 Å)
Kurucz for STIS[9] Leitherer et al. [1996]	1000-10000 Å	3050-44500 K	-5.0…1.0	0.0…5.0	$\sim$ 1100 ($\sim$2400 Å) $\sim$ 2500 ($\sim$3200 Å) $\sim$ 4000 ($\sim$5500 Å)
Gray & Corbally [1994][10] based on Kurucz models	3900-4500 Å	4500-25000 K	solar	4.0…4.5	$\sim$ 1500
Gummersbach [1998] based on Kurucz models	3000-10000 Å	B-Main Sequence	solar	4.0	20000
Lejeune et al. [1997, 1998][11] based on Kurucz, Bessel and Flucks libraries	90-160000 Å	3500-50000 K (K.) 2500-3800 K (B. and F.)	-5.0…1.0 -1.0…0.5	0.0…5.0 -1.02…0.83	10-20 Å
Westera et al. [2002][11] metallicity calibration of the previous library	“	2000-50000 K	“	“	“
González Delgado & Leitherer [1999]	3700-5000 Å	4000-50000 K	solar	0.0…5.0	$\sim$ 1000
Straižys et al. [2002] comparison between Kurucz models and real stars	1000-10000 Å	4000-9000 K	metal poor	1.0…4.5	
Murphy & Meiksin [2004] based on Kurucz model spectra	3000-10000 Å	5250-50000	-5.0…1.0	0.0…5.0	250000

[8] http://www.stsci.edu/hst/observatory/cdbs/k93models.html

[9] http://www.stsci.edu/STIS/stis_models.html

[10] http://www1.appstate.edu/dept/physics/spectrum/spectrum.html

[11] ftp://tangerine.astro.mat.uc.pt/pub/BaSeL

5.1 The observed library

The Pickles (1998) library is a compilation of several spectral libraries with different wavelength ranges, resolution and sampling (in Tab. 5.3 the library sources are listed).

The first library listed is the one provided by Sviderskiene [1988], with a very low resolution (R=50) but with a very good wavelength coverage (1200-10500Å). It consists of 98 spectra covering a wide range of spectral types and all luminosity classes at solar abundances. Because of the low resolution, the library was not used in the combination of all the other spectral libraries, but it was an ideal check on all other input spectra for flux calibration and accuracy: the Sviderskiene [1988] spectra were utilized as reference spectral energy distribution (SED).

All other spectra were combined to create a new library with a wavelength coverage 1150–25000 Å, a sampling interval of 5 Å/pixel and a resolution of ≈500, which is a compromise among the input data from all libraries. Higher resolution spectra were binned or filtered to provide the chosen resolution of 500. The input spectra were normalized to unity at 5556 Å. If in a source library there were multiple spectra of the same kind (i.e. same spectral type and luminosity class), these spectra were averaged in order to obtain an average spectrum for each spectral type for that library. Then the averaged spectra of different libraries were averaged. This combination was such that, in a wavelength range where only one library existed, the pre-averaged spectrum became the output spectrum. An example of the combination is given in Fig. 5.1, where the Sviderskiene [1988] reference SED, the contributions from the other libraries and the final combination are shown.

Table 5.3: Stellar libraries input source summary (Pickles 1998)

Library reference	Spectral Types	Luminosity Class	λ_{start} (Å)	λ_{end} (Å)	R $\lambda/\Delta\lambda$	sampling (Å/pixel)
Sviderskiene (1988)	O–M	I–V	1200	10500	50	50
Heck et al. (1984) (*IUE*)	O–G	I–V	1153	3201	500	2
Gunn& Striker (1983)	O–M	I–V	3160	10620	250	10/20
Kiehling (1987)	F–M	I–V	3200	8800	500	10
Jacoby et al. (1984)	O–M	I–V	3510	7427	1200	1.4
Silva & Cornell (1992)	O–M	I–V	3510	8930	500	5
Pickles (1985)	O–M	I–V	3600	10000	500	3
Pickles & van der Kruit (1990)	K	III	3800	6800	400	6
Serote Roos et al. (1996)	GKM	I/III	4800	8920	6000	0.43
Danks & Dennefeld (1994)	O–M	I–V	5804	10200	800	4
Lancon & Rocca-Volmerange (1992)	O–M	I–V	14300	25000	500	7
Dallier et al. (1996)	O–M	I,III,V	15700	165000	2000	3/6
Kleinmann & Hall (1986)	F–M	I–V	20100	24100	3000	72
Cohen et al. (1995, 1996)	AGKM	III,V	10000	350000	100	100
Fluks et al. (1994)	M	III	995	125000	5000	1

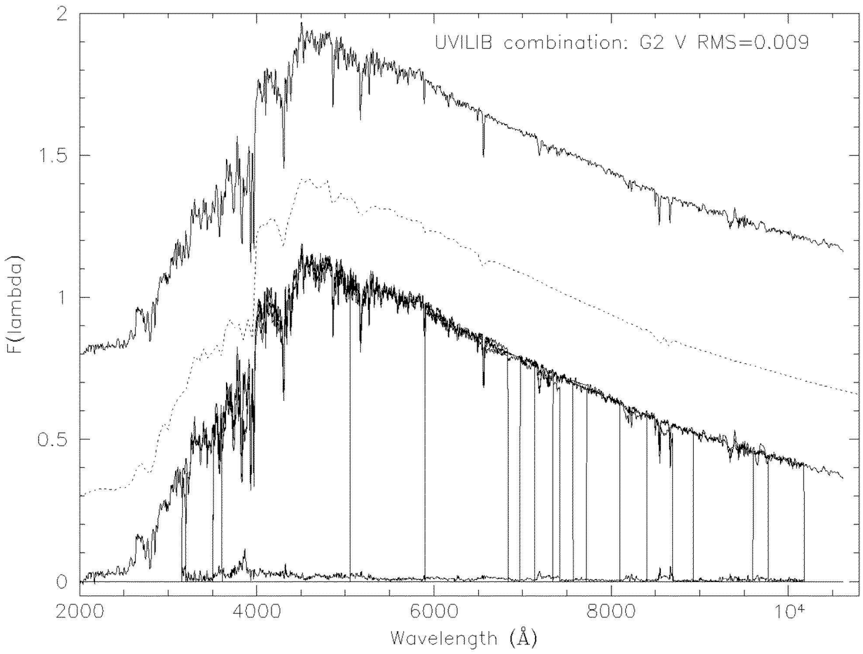

Figure 5.1: Example of the spectral combination for the Pickles 1988 library: the dotted line shown offset by 0.3 here is the reference SED spectrum from Sviderskiene 1998; the bottom spectrum is the overlapping of the other libraries components and vertical lines indicate the start and end wavelength regions of the various components; the final combination is shown offset by 0.8 above (Pickles 1995).

The library coverage in the color-magnitude diagram

For each spectrum synthetic magnitudes and colors were obtained convolving the spectrum with the appropriate filter transmission profiles. Since the spectra have been arbitrarily normalized to unity around 5556 Å, the magnitudes are relative. If T_a and Z_a are the transmission profile and magnitude zero point for the generic filter "a", then the magnitude is

$$MAG_a = -2.5log_{10}(< F_\lambda >) - Z_a$$

where

$$< F_\lambda >= \Sigma(T_a F_\lambda \Delta\lambda)/\Sigma(T_a \Delta\lambda).$$

Color measurements were made by differencing these filter magnitudes and the synthetic colors were compared to observed colors for each stellar

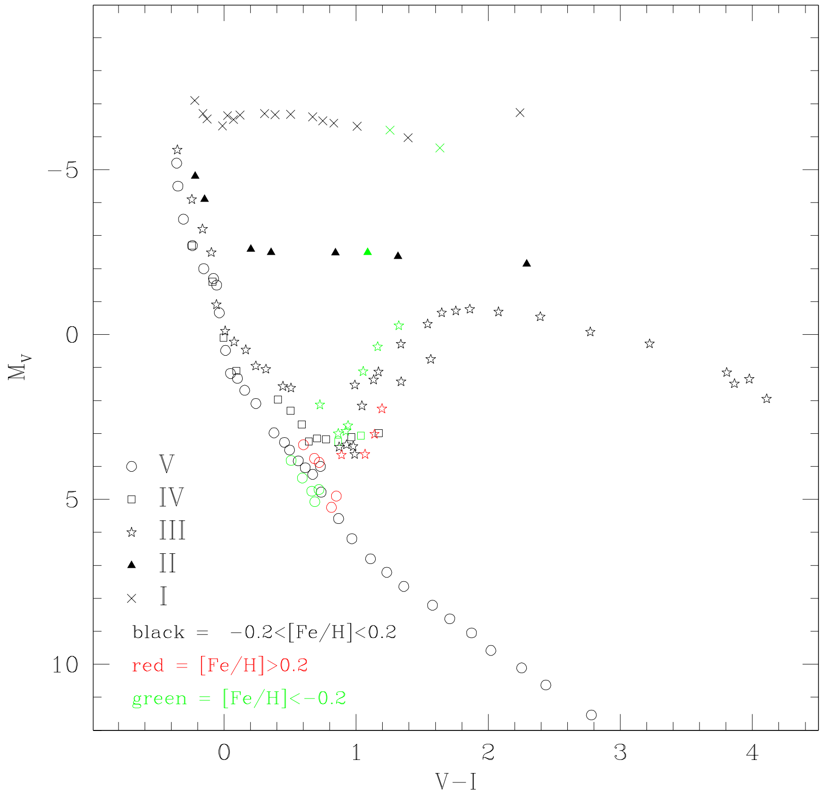

Figure 5.2: Color magnitude diagram obtained from the synthetic photometry of the spectral library. Different symbols and colors indicate different luminosity classes and metallicities respectively (see legend)

type. The filter profiles for the Johnson system colors *UBV* were taken from Buser [1978] for the *U* filter and from Ažusienis & Straižys [1969] for the *B* and *V* filters. The same *V* filter profile was also used for the Cousin system colors, where the R_C and I_C filter profiles were taken from Bessell [1979]. The magnitude zero points were calculated from the digital photometry of the standard spectra from Sviderskiene [1988]. A color-magnitude diagram obtained with the synthetic photometry of the spectral library is plotted in Fig.5.2, where different symbols indicate different luminosity classes and different colors indicate different metallicities.

5.2 The synthetic library

The BaSeL library (Lejeune et al. [1997]) was constructed according to the following precepts: (i) to cover the largest possible ranges in stellar parameters (T_{eff}, log$g$ and [M/H]); (ii) to provide flux spectra with useful resolution on the uniform grid of wavelengths adopted by Kurucz (1995); and (iii) to provide synthetic broad-band colors which are highly realistic for the largest possible parameter and wavelength ranges. It was obtained from different grids of atmosphere models (Bessell [1979], Fluks et al. [1994], Kurucz [1995, priv.comm.], Allard & Hauschildt [1995]), whose parameters and wavelengths are summarized in Tab.5.4.

	Kurucz [1995]	Bessell et al. [1989, 1991]	Fluks et al. [1994]
T_{eff}	3500. . .50000 K	2500. . .3800 K	2500. . .3800 K
log$g$	0.0. . .5.0	-1.0. . .+1.0	red giant sequence
$[M/H]$	-5.0. . .+1.0	-1.0. . .+1.0	0.0
$\lambda(nm)$	9.1. . .160000	491. . .4090	99. . .12500

Table 5.4: Parameter and wavelength coverage of the different model atmosphere libraries.

To obtain a realistic library, for each value of the effective temperature and for each wavelength, the correction function that must be applied to a (theoretical) model flux spectrum in order to obtain synthetic UBVRIJHKL colors matching the (empirical) color-temperature calibrations derived from observations was calculated as explained below. This correction function was obtained from empirical color-temperature relations:

- For the red giants and supergiants the Ridgway et al. [1980] empirical relation between the temperature and color $(V-K)$ was adopted; using observations of a large sample of bright M-giant stars, color-color relations were derived ($(V-I)$-$(V-K)$,$(U-B)$-$(V-I)$,etc..), allowing to translate the Ridgway et al. [1980] relation to all the other colors. Fig. 5.3 shows an example of this color-color calibration.

- For the main sequence stars the Schmidt-Kaler [1982] calibration was chosen to relate T_{eff} to $U-B$, $B-V$ or $R-I$ colors and the two-color relations established by Fitzgerald [1970], Bessell [1979] and Bessell & Brett [1988] were then adopted to derive the temperature scales for the remaining colors.

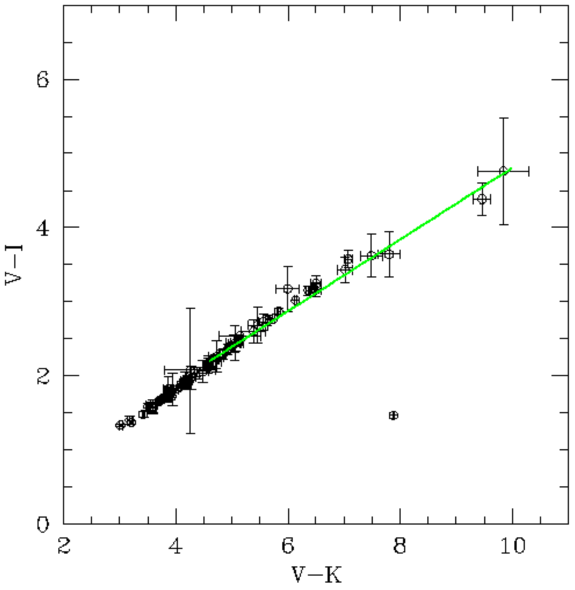

Figure 5.3: Example of two color calibration for the BaSeL library. In this case, the relation between $(V - I)$ and $(V - K)$ is shown: the symbols represent observations while the solid line is a linear least-squares fit to the data. (Lejeune et al. [1997])

The calibration algorithm

Since the empirical color-temperature relations do not provide direct information about the stellar continua, for each temperature pseudo-continua were calculated from both the empirical and the theoretical colors.

The pseudo continuum $pc_\lambda(T_{eff})$ is defined as that of a black body of color temperature $T_c(\lambda)$ varying with the wavelength:

$$pc_\lambda(T_{eff}) = \alpha(T_{eff}) \cdot B_\lambda(T_c(\lambda))$$

where $\alpha(T_{eff})$ is a scale factor and $B_\lambda(T_c)$ is the black body function. In the case of the empirical colors, the pseudo continuum was determined fitting the observed magnitudes (see Fig. 5.4, left and right top panels). In the case of the library spectra, the spectrum was convolved with the filter profiles to obtain the synthetic magnitudes and colors, from which the pseudo-continuum was calculated (see Fig. 5.4. left and right middle panels). The ratio $\Phi_\lambda(T)$ between the empirical and theoretical pseudo continua is the correction function (see also Fig. 5.4, right bottom panel):

$$\Phi_{lambda}(T) = \frac{pc_\lambda^{emp}(T_{eff})}{pc_\lambda^{syn}(T_{eff})}$$

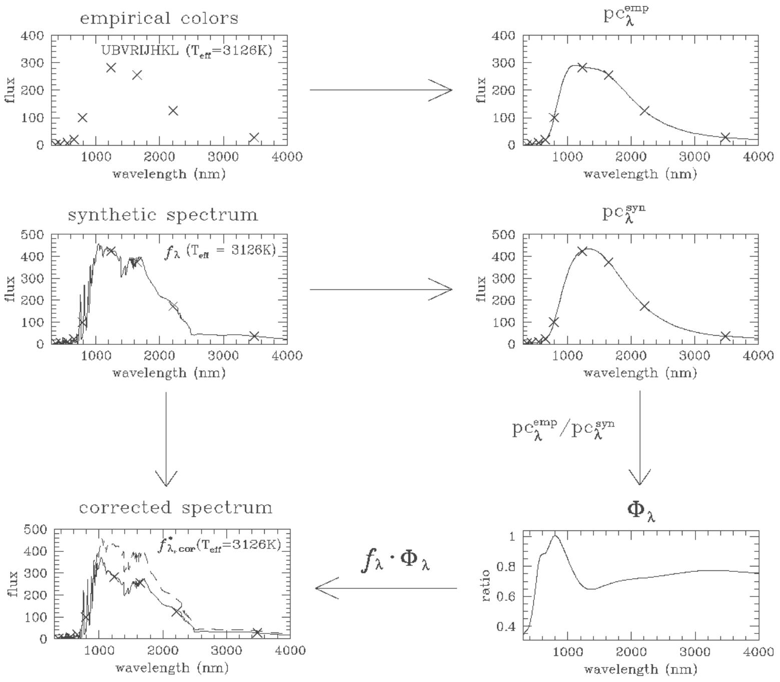

Figure 5.4: Correction procedure for the BaSeL library spectra: at the top the definition of the pseudo continuum from the empirical colors; in the middle the definition of the pseudo continuum form the synthetic spectrum; at the bottom, in the right panel the correction function that is applied to the synthetic spectrum and in the left panel the corrected spectrum (Lejeune et al. [1997], Fig.10)

that was applied finally to the synthetic spectra (Fig. 5.4, left bottom panel):

$$f^{\star}_{\lambda,corr}(T,\log g,[M/H]) = f_\lambda(T,\log g,[M/H]) \cdot \Phi_\lambda(T)$$

5.3 The sdBs archive

During the planning of the DIVA[12] satellite mission, which was supposed to be measuring proper motions, parallaxes and spectrophotometric data of approximately 35 millions of stars, a library of spectrophotometric standard stars distributed all over the sky was required. Unfortunately the mission

---

[12] http://www.ari.uni-heidelberg.de/diva/diva.html

was canceled but the collection of data has been continued since it could be useful for other projects. The database is now a collection of photometric, spectral and astrometric data of mainly blue hot stars: among them, I chose sdB stars for this thesis.

The data are basically a collection of *IUE*[13] data, which provide the UV spectra of the stars, and optical data taken during various runs using the 2.2m Telescope with CAFOS at Calar Alto as well as the 1.54m Danish Telescope with DFOSC at LaSilla. Some objects have only the UV part, while others have only the optical part. I selected only stars with both spectral components.

The *IUE* spectra

The *IUE* satellite performed spectrophotometry at high (0.1-0.3 Å) and low (6-7 Å) dispersion, however all selected sdBs spectra have low resolution. For each star, two spectra where taken: at 1150-1980 Å for short wavelength and 1850-3350 Å for long wavelength.

The DIVA archive spectra were already flux-calibrated, therefore, to create a single spectrum for each star extending from 1150 to 3350 Å, the two spectra were simply "sticked together". In the region where they overlap the average of the two was taken, as shown in Fig. 5.5 (top).

Merge with the optical part

Since the resolution of the UV and optical spectra are different, first of all the two components were rebinned to the same step width of 0.5Å. After that, in the same way as the two UV components were attached, the *IUE* spectrum was merged with the flux-calibrated optical spectrum. An example is shown in Fig. 5.5 (bottom). All spectra were then corrected for reddening, using the `MIDAS` task `EXTINC/SPEC`, which adopts Savage & Mathis [1979] reddening law (see Fig. 5.6 for a comparison between the reddened and corrected spectrum in the case of the star PHL 932).

---

[13] *International Ultraviolet Explorer* satellite, http://archive.stsci.edu/iue/

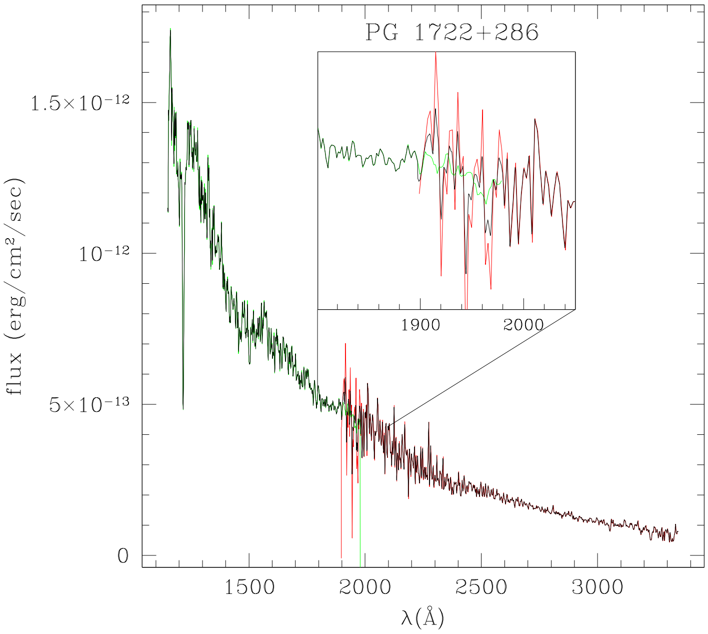

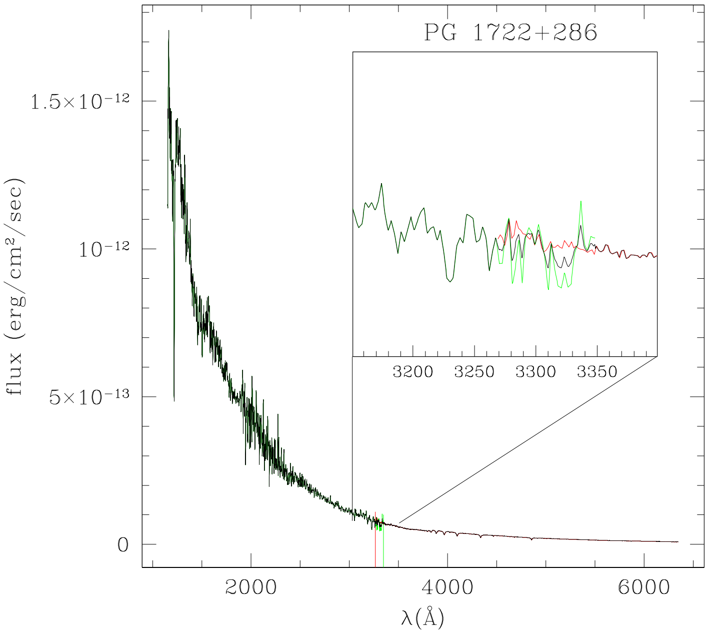

Figure 5.5: Top: example of *IUE* spectrum: merge of the short wavelength spectrum (1150-1850 Å, in green) with the long wavelength spectrum (1850-3350Å, in red) for the star BD 48 2721. In the overlapping, the average of the two spectra was taken. Bottom: example of DIVA library spectrum: merging *IUE* spectrum (1150-3350Å, in green) with the optical spectrum (3200-6400Å, in red) for the star PG 1722+286. In the overlapping (plot in the box) the average of the two spectra was taken.

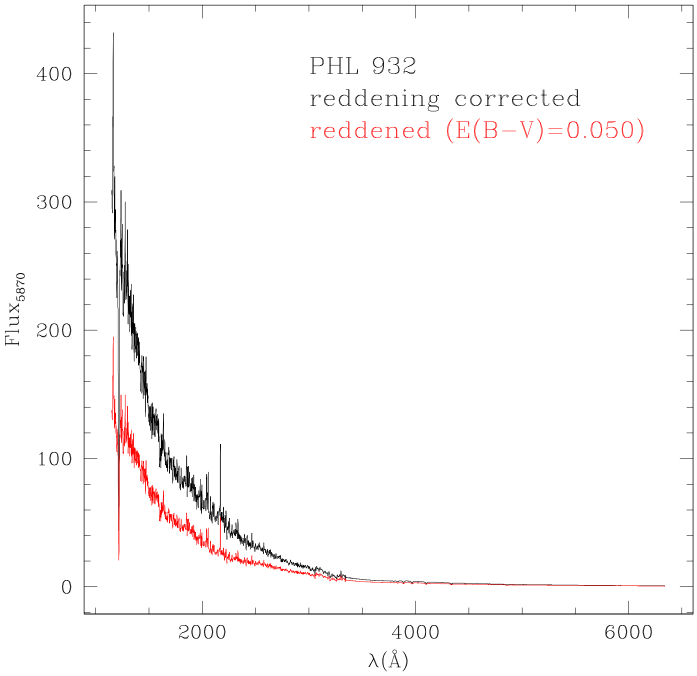

Figure 5.6: Comparison between the sdB star PHL 932 spectrum corrected for reddening (in black) and not corrected (in red).

Chapter 6

The synthetic spectrum

6.1 The sdB stars integrated spectrum

6.1.1 The selection of the stars

To construct the sdB spectrum, first of all it was necessary to decide which of the sdB star candidates in the color magnitude diagram will be taken into account. I selected only stars with a good photometry (error in magnitude smaller than 0.1), as shown in Fig. 6.1, obtaining 112 sdB star candidates.

The disk simulation, while taking into account the presence of Horizontal Branch stars, does not include sdB stars which remain in the disk corrected CMD. However from the analysis of the spectra (see Ch.3), I have found that only ∼80% of the candidates are really sdB stars and not all these stars have turned out to belong to the Galactic bulge. The percentages listed in Sec. 3.7 were applied to the total number of sdB stars candidates, since there is no reason to assume that peculiar stars were picked up during the selection of the targets whose spectrum should have been observed: of 112 candidates therefore, only 55 % have been considered stars of the bulge, the remaining ones being cool stars or hot stars belonging to the disk or whose membership it was not possible to determine, and narrowing the sdBs sample to 62 candidates.

The observed sdBs spectra have different wavelength ranges (see Figs. 2.16, 2.17, 2.18) and cover only the optical region, but they do not reach $\lambda = 5870$ Å that will be used as reference wavelength in the construction of the UV spectrum (see below). To obtain a homogeneous set of spectra, the spectra of the DIVA archive (see Sec. 5.3) most similar to the observed sdBs were used to construct the integrated spectrum. I associated each observed sdB star to one of the sdB spectra of the DIVA archive, choosing from the archive the star with temperature and gravity closest to the observed sdB

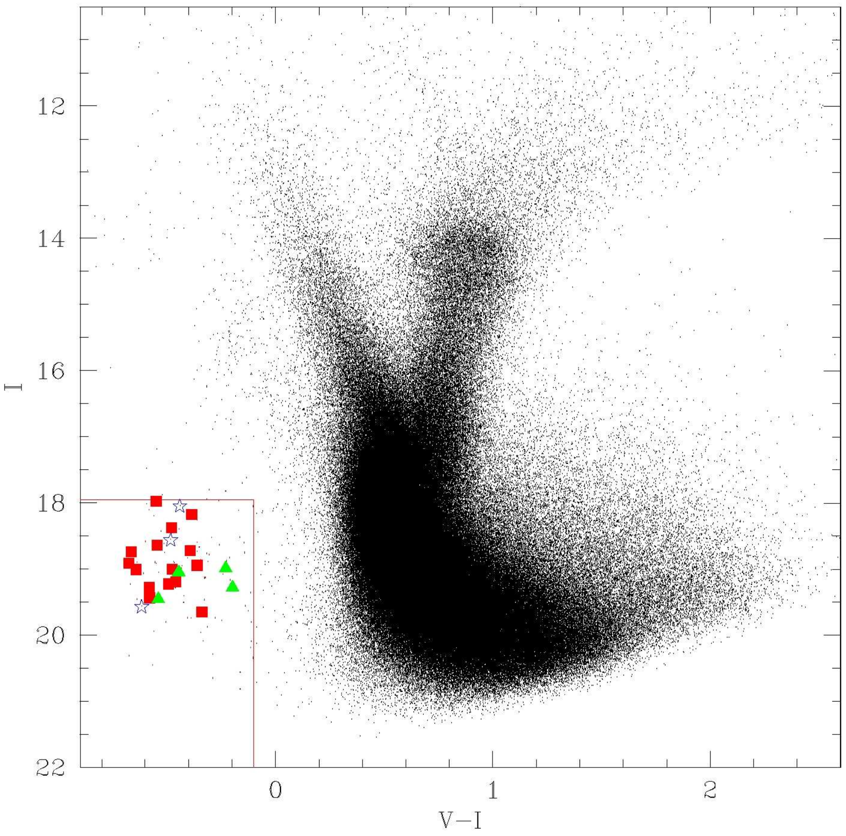

Figure 6.1: Color magnitude diagram of the bulge field MW05, where the bulge sdB stars analyzed in Ch.3 are marked with red squares, the disk sdB stars are marked with green triangles and the stars with unknown membership are marked with blue stars. The stars in the box are used to construct the integrated spectrum.

star. In some cases, it was not possible to make the association between the observed sdB star and one of the archive spectra because the difference of temperature between observed star and archive one was too big: for example, there are some observed stars with T$_{eff}$ ~28000 K (see Tab 6.1), but in the archive the available closest in temperature stars have T$_{eff}$ 25400 K and 31700 K. In this case I made an interpolation between the two archive stars to obtain the spectrum at the desired temperature. In Tab. 6.1, the observed sdB are listed with the associated archive stars.

observed sdB	T_{eff}	logg	archive sdB	T_{eff}	logg
1002	20600	5.10	BD+48 2721	21000	4.85
1003	27100	5.46	int28300*	28300	5.50
1004	27800	5.41	int28300*	28300	5.50
1005	28700	5.54	int28300*	28300	5.50
2001	23900	6.74	int24000*	24000	6.00
2002	28500	5.68	int28300*	28300	5.50
2003	21300	5.23	BD+48 2721	21000	4.85
2004	31900	5.72	PG 1722+286	31700	5.40
2005	36300	5.45	PHL 932	35000	5.93
2006	33900	5.86	PHL 932	35000	5.93
2007	44600	5.65	PHL 932	35000	5.93
2008	29200	5.77	int28300*	28300	5.50
2009	24000	5.24	int24000*	24000	5.00
2010	32000	5.86	PG 1722+286	31700	5.40
3001	26100	5.43	PG 2110+127	25400	4.20
3002	39100	6.00	PHL 932	35000	5.93
3003	20300	4.70	BD+48 2721	21000	4.85
3004	35700	5.79	PHL 932	35000	5.93
3005	35100	6.10	PHL 932	35000	5.93
3006	28600	5.46	int28300*	28300	5.50
3007	31400	5.36	PG 1722+286	31700	5.40
3009	30400	5.67	PG 1722+286	31700	5.40

Table 6.1: Association between observed and archive sdB spectra: the stars are separated by setup (i.e. bulge field); the first column lists the star id whose effective temperature and surface gravity are in the 2^{th} and 3^{th} column respectively. The associated archive star is in the 4^{th} column and its parameters in the 5^{th} and 6^{th} column. The spectra obtained with the interpolation (see text) are indicated with an asterisk.

Fig. 6.2 shows the relation (or better lack of) between the apparent magnitudes V, I and the color V-I and the temperature of the targets. Regarding the magnitudes, this is explained by the fact that we are looking at stars at different distances along the line of sight, and, for example, stars with same temperature (thus same absolute magnitude) but different distance are located at different apparent magnitude. The lack of relation between the color and the temperature is due to the saturation of the color with the temperature at higher T_{eff} and to remaining differential reddening.

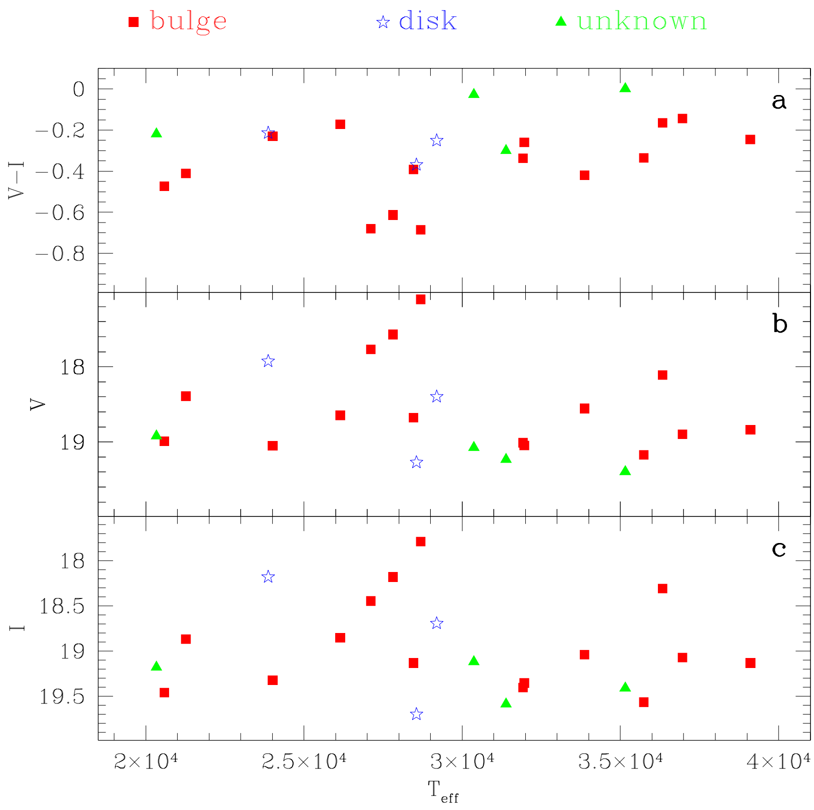

Figure 6.2: Relation between the V (panel b), I (panel c) apparent magnitudes, color (panel a) and the temperature of the observed sdB stars. Stars with different membership are shown with different symbols: filled squares, stars and filled triangles represent respectively bulge, disk and unknown stars.

Thus it is not possible to use the magnitude to assign one of the archive spectra to the sdBs candidates for which there is no spectrum available. To make the association, the observed sdBs sample was again used as template: since for stars with similar temperature, the same archive spectrum was associated, the percentage of star with the same adopted archive spectra was applied: for example if there are 3 stars with the same adopted extended spectrum, meaning a percentage of the 18.75% on the sample of 16 bulge sdBs, then 18.75% of 62 sdB star candidates were adopted to have the same spectrum.

The distance of the bulge stars

To construct the integrated spectrum, the absolute magnitude is necessary (see following section). Since it is not possible to obtain the distance for all the stars in the bulge CMD, I estimated the most probable distance of the bulge stars. To do that I considered a bulge luminosity density model (Dwek et al. [1995]):

$$\rho_L = \rho_0 e^{-0.5 r_s^2}$$

$$r_s^2 = \{[(\tfrac{x}{x_0})^2 + (\tfrac{y}{y_0})^2]^2 + (\tfrac{z}{z_0})^4\}^{1/2}$$

where r_s^2 is the distance from the Galactic center along the line of sight and x, y, z are function of the galactic coordinates l and b. I calculated how the integrated luminosity varies with the distance, per unit of distance, that is I integrated the luminosity density in following steps on the volume I am sampling along the line of sight (see also 4.6.2). The integrated luminosity has a maximum at s =8.15 kpc (see Fig. 6.3). Since the total luminosity depends on the total number of star in the volume I am sampling, I assumed 8.15 kpc as most probable distance for the stars in my field.

6.1.2 Construction of the sdBs integrated spectrum

To synthetize the integrated spectrum, I adopted the method of Santos et al. [1990] and Santos et al. [1995b]. First of all, all spectra were normalized to the same reference wavelength, that is λ = 5870Å. Each sdB spectrum contributes to the synthetic spectrum with a weight that is proportional to the total V flux of the stars with that spectrum. For example, if n_j sdB candidates are associated with a certain archive sdB spectrum f_j, it contributes to the total spectrum with a weight:

$$C_j = n_j 10^{-0.4(<M_v>_j - m_{vj})}$$

where

- m_{vj} is the result of the convolution of the spectrum j normalized at 5870 Å with the V filter

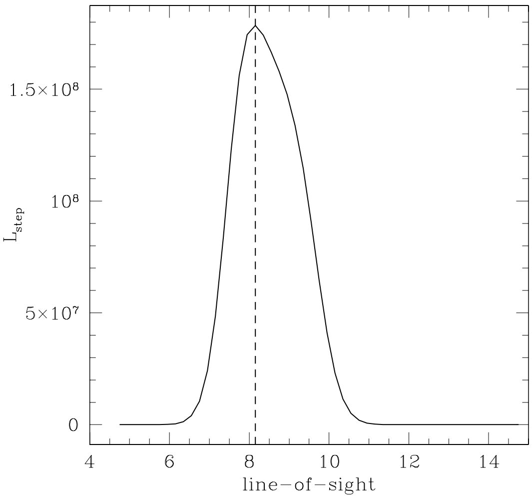

Figure 6.3: Integrated luminosity along the line-of-sight s.

- following Santos et al. [1995b], $< M_v >$ is the mean absolute V magnitude of the n_j stars represented by the spectrum f_j. As shown in Fig. 6.2, there is no correlation between V magnitude and temperature for these sdBs, as the stars are distributed quite homogeneously in this region of the color magnitude diagram, and it is not possible to say which sdB candidate should have which spectrum. Therefore the same $< M_v >$ was assumed for all the archive spectra, that is the mean magnitude of all the 62 candidates. The weight is different for each spectrum because the number of associated stars is different.

$$< M_v >= -2.5log[\Sigma_{i=1}^{n} 10^{-0.4M_v}/n_j]$$

In Tab. 6.2, the archive sdB stars are listed, with their respective values for n_j, $< M_v >$ and C_j, while in Fig. 6.4 their spectra, normalized at the reference wavelength λ=5870Å are shown.

The total spectrum $\mathcal{F}$, shown in Fig. 6.5, is finally obtained by:

$$\mathcal{F}_{sdB} = \Sigma_{n=1}^{6} C_j f_j$$

star	%	n_j	$< M_v >$	m_{v_j}	$C_j(\times 10^{-6})$
BD 48 2721	13.63	8.45	3.812	-12.223	3.257
PG1722+286	18.18	11.27	3.812	-12.193	4.462
PG2110+127	4.54	2.81	3.812	-11.995	1.336
PHL 932	27.28	16.91	3.812	-12.127	7.118
int24000	9.09	5.64	3.812	-12.071	2.500
int28000	27.28	16.91	3.812	-12.089	7.371

Table 6.2: Archive sdB stars used to construct the integrated spectrum: n_j is the number of sdB candidates stars associated with the archive spectrum, where n_j corresponds to the percentage listed in the $2nd$ column on the total number of sdBs; $< M_v >$ is the mean absolute V magnitude (the same for all spectra, see text); C_j is the weight with which each spectrum contributes to the integrated spectrum.

6.2 The bulge integrated spectrum

To obtain the total integrated spectrum, that is the one taking in account not only the sdB stars but also the other stars on the CMD, I plotted the Pickles [1998] spectral library (see Sec. 5.1) on the cleaned and reddening corrected CMD of the bulge region, as shown in Fig. 6.6. In this figure, the library points are marked in different colors, depending on the luminosity of class (yellow: dwarfs(V); red: subgiant(IV)); green: giants (III)). Each different point corresponds to a library spectrum with different temperature. I have chosen the boxes on the CMD such that every box contains a library point. In some cases, there are more than one library point inside a box. These library stars have same temperature but slightly different metallicity (for example [Fe/H]=0 and -0.1), and their spectra are only slightly different. Since there is no way to know which is the correct value (since the bulge shows a spread in metallicity, as explained in Sec. 1.3.3), I took the average between the spectra inside the same box.

However, the Pickles spectra library does not contain Horizontal Branch (HB) stars. To associate the HB stars with a temperature (and therefore a library spectrum), I used a theoretical Zero Age Horizontal Branch (ZAHB), of solar metallicity: since the position of a star along the HB is determined basically by its temperature, every magenta point corresponds to a different temperature. To each box on the HB I associated the Pickles library spectrum of luminosity class V (dwarfs) with appropriate temperature. As in the case of the sdB spectrum, where the appropriate temperature was not available, I interpolated the closest library spectra to obtain the one needed. The sdB stars in the blue box have been considered in the previous section.

Once the CMD was divided in boxes, each associated to a library spectrum, I followed the same procedure adopted to calculate the sdB stars integrated spectrum (see Sec. 6.1.2): for each box, I calculated the mean absolute magnitude $< M_V >_j$ of the stars in the j-th box (assuming a distance of 8.15 kpc), the corresponding spectrum "magnitude" m_{v_j} obtained from the convolution with the V filter, and the weight C_j. In Tab. 6.3 all these parameters are listed.

Finally, I calculated the total integrated spectrum of this bulge region as sum of all spectra associated to the CMD boxes, taking in account their weights, adding as well the sdB stars integrated spectrum calculated in sec. 6.1.2:

$$\mathcal{F}_{TOT} = \Sigma_{n=1}^{N} C_j f_j + \mathcal{F}_{sdB}$$

The result is shown in Fig.6.7. The first impression is that there is no UV excess: at λ <2300 Å, the spectrum shows only a very small upturn, and then it keeps on decreasing, but showing again, at λ <1700 Å, a small increase caused indeed, as it possible to see in the small panel, by the sdBs stars.

6.2.1 Comparison with other spectral libraries

The BaSeL spectrum

I repeated the whole procedure using instead the BaSeL (Lejeune et al. [1997]) syntethic spectral library (see Ch.5). I selected in the BaSeL library the spectra at solar metallicity, with temperature and luminosity class corresponding to those of the Pickles [1998] stars: I associated the luminosity class to the surface gravity of the spectra models and I interpolated in temperature to obtain the proper value. I convolved the resulting spectra with the V filter in order to obtain the "magnitude" m_{V_j} of the spectrum, while the weights C_j are the same since they depend on the color magnitude diagram and not on the spectrum. Tab.6.4 shows the m_{V_j} values obtained with both Pickles and BaSeL libraries and their differences as well: the two libraries are in quite good agreement for all stars in the color magnitude diagram but the brighter and cooler red giants, where the difference can be 0.5 mag. This is explained by the fact that these stars have a convective envelope and so far the convection in stellar atmospheres is not very well known, causing the discrepancy between observations and models. I followed the procedure as before and I added also in this case the sdBs integrated spectrum.

The Bruzual & Charlot spectrum

To check the bulge integrated spectrum, I compared it with a theoretical stellar population spectrum. The library of Bruzual & Charlot [2003] provide integrated spectra for stellar populations for different ages and star formation histories. I chose two single stellar populations with an age of 11 Gyr and metallicity z=0.008 and z=0.02 (corresponding to [Fe/H] values of about -0.5 and -0.09 respectively). A single stellar population (SSP) is defined as a population that is undergone an instantaneous burst of star formation. The flux of spectra provided by the library is in units of solar luminosity per Angström and to compare them with the integrated spectra, I normalized them to the same reference wavelength λ=5870 Å .

6.2.2 Discussion

The comparison between integrated bulge spectra, constructed with both observed (in black) and syntethic (in blue) spectra library, and two SSP spectral energy distribution (at metallicity z=0.008 and z=0.02 in red and green respectively) is shown in Fig. 6.8. A first glance tells that there is an overall good agreement between all the spectra.

The two integrated spectra are very similar, both in the optical and UV range (see bottom panel), as expected from Tab. 6.4: the differences in the magnitudes obtained from the spectra convolution with the filter are very small, except for the red giants. These stars emit most of their flux in the infrared, therefore they do not have much weight in the optical and UV range. Neither the SSP at z=0.008 ([Fe/H]~ -0.5) nor the one at z=0.02 ([Fe/H]$\sim$-0.09) agree perfectly with the integrated spectra, particularly in the region between 3300 and 4000 Å, where the two synthetic spectra bracket the integrated one. Probably a population with an intermediate metallicity would fit better. It is necessary to keep in mind though that the bulge is not a single stellar population with only one value for the metallicity, but it has a metallicity distribution (see Sec. 1.3.3), from metal-poor (up to [Fe/H]~ -2) to metal-rich (up to [Fe/H]$\sim$0.5), with a peak at [Fe/H]~ -0.2 (Zoccali et al. [2003], Rich & Origlia [2005]), intermediate between the metallicity of the two single stellar populations I adopted.

The expected age for the bulge is 10-13 Gyr (see sec. 1.3.4) while the adopted single stellar populations are 11 Gyr old. Also the fact that the spectrum belongs to a single stellar population, hence formed in an instantaneous burst, is in agreement with previous works: Zoccali et al. [2006], by means of α elements analysis, found that probably the bulge formed very quickly.

Integrated and synthetic spectra do not match in the UV instead, with the synthetic spectra showing a larger UV flux. This could be explained with two reasons. Firstly, in their stellar population synthesis, Bruzual & Charlot [2003] take into account also post-HB and post-AGB (see sec.1.2), which have a strong flux in the UV range. I did not account for these stars instead since it was not possible to disentangle them from the disk population. Secondly, probably my selection of sdBs stars was too strict. On the base of the spectroscopic analysis, I selected, as bulge sdBs, on the color magnitude diagram only 55% of the candidates to construct the integrated spectrum. Taking into account also the stars with unknown membership the percentage would raise to 72%, increasing the UV flux of $\sim 30\%$.

Thus the Galactic bulge probably shows only a very weak UV excess, contrarily to observed in the bulge of M31, a closest spiral galaxy very similar to the Milky Way. It could appear like a discrepancy but UV observations of the closest systems show that this feature can largely vary from object to object and extragalactic observations (Rich et al. [2006]) indicate the UV excess has not correlations with physical parameters as metallicity and velocity dispersion. A correlation with age appears more probable but it would be visible only at high redshift (Brown et al.[2003]), while both Milky Way and M31 belong to the Local Group and are therefore coeval.

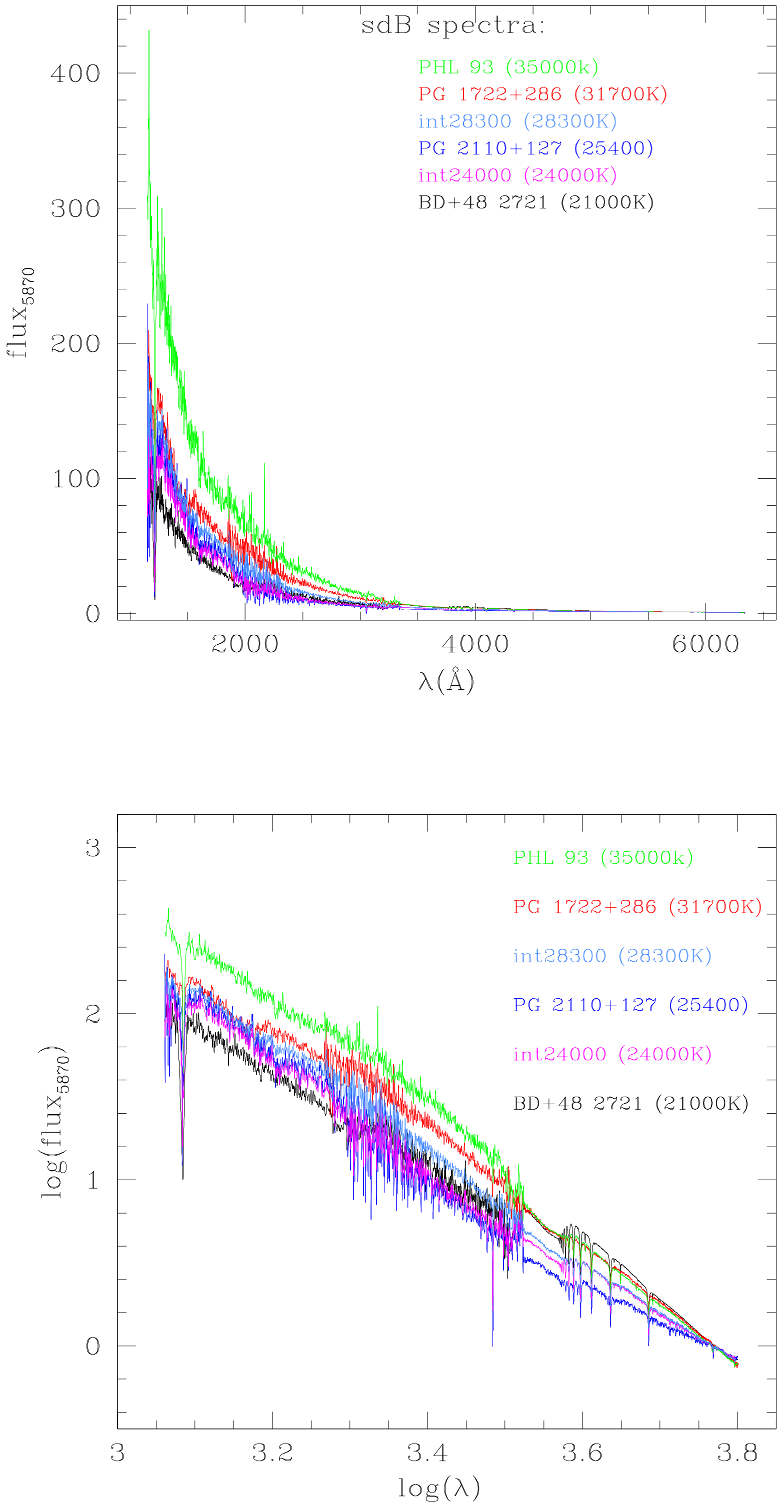

Figure 6.4: In the top panel, the spectra, normalized at $\lambda = 5870$ Å, of the archive sdB stars used to construct the integrated spectrum, shown in different colors. In the bottom panel, the same plot but on logarithmic scale.

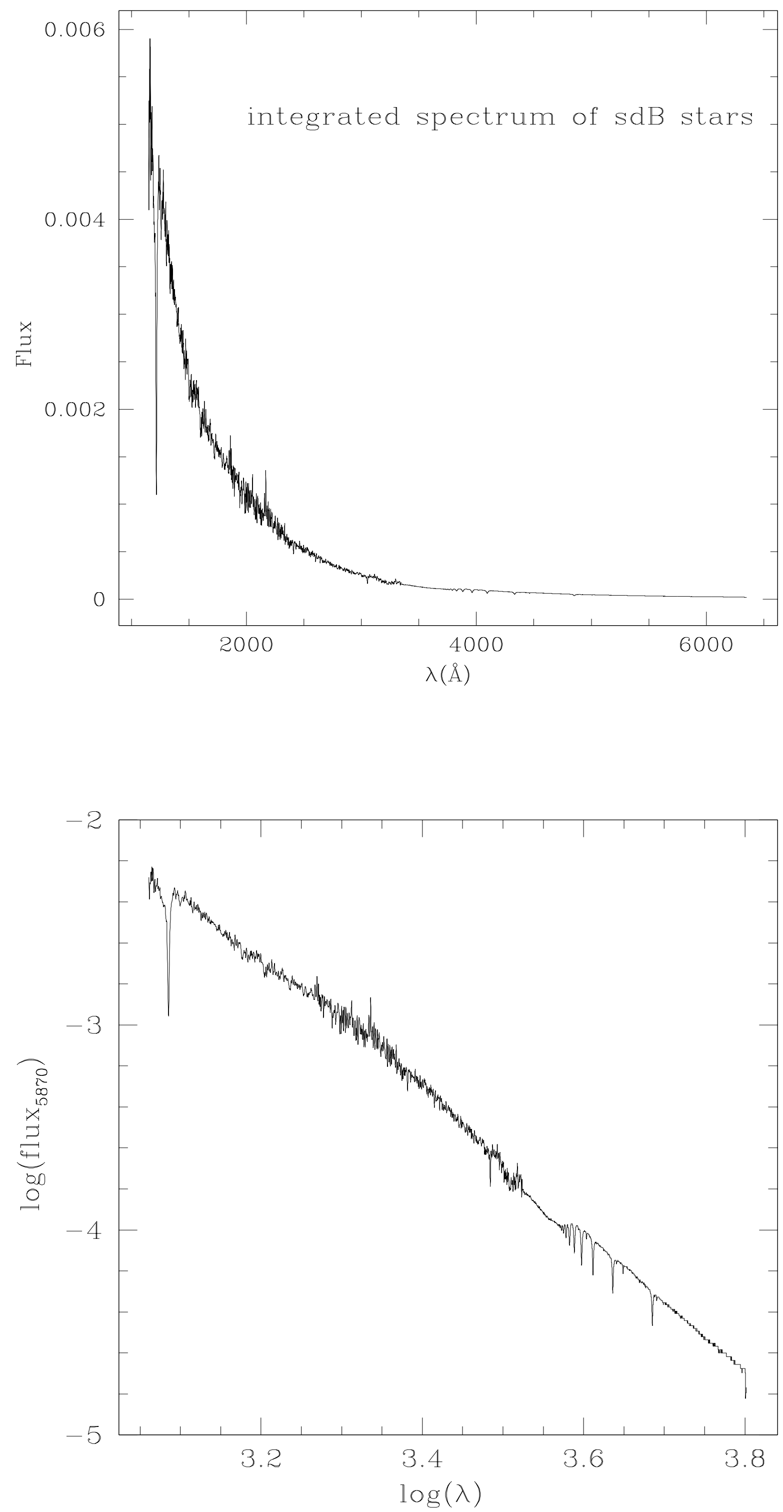

Figure 6.5: In the top panel, integrated spectrum of the bulge sdB candidates, from the UV to the optical. In the bottom panel, the same plot but on logarithmic scale.

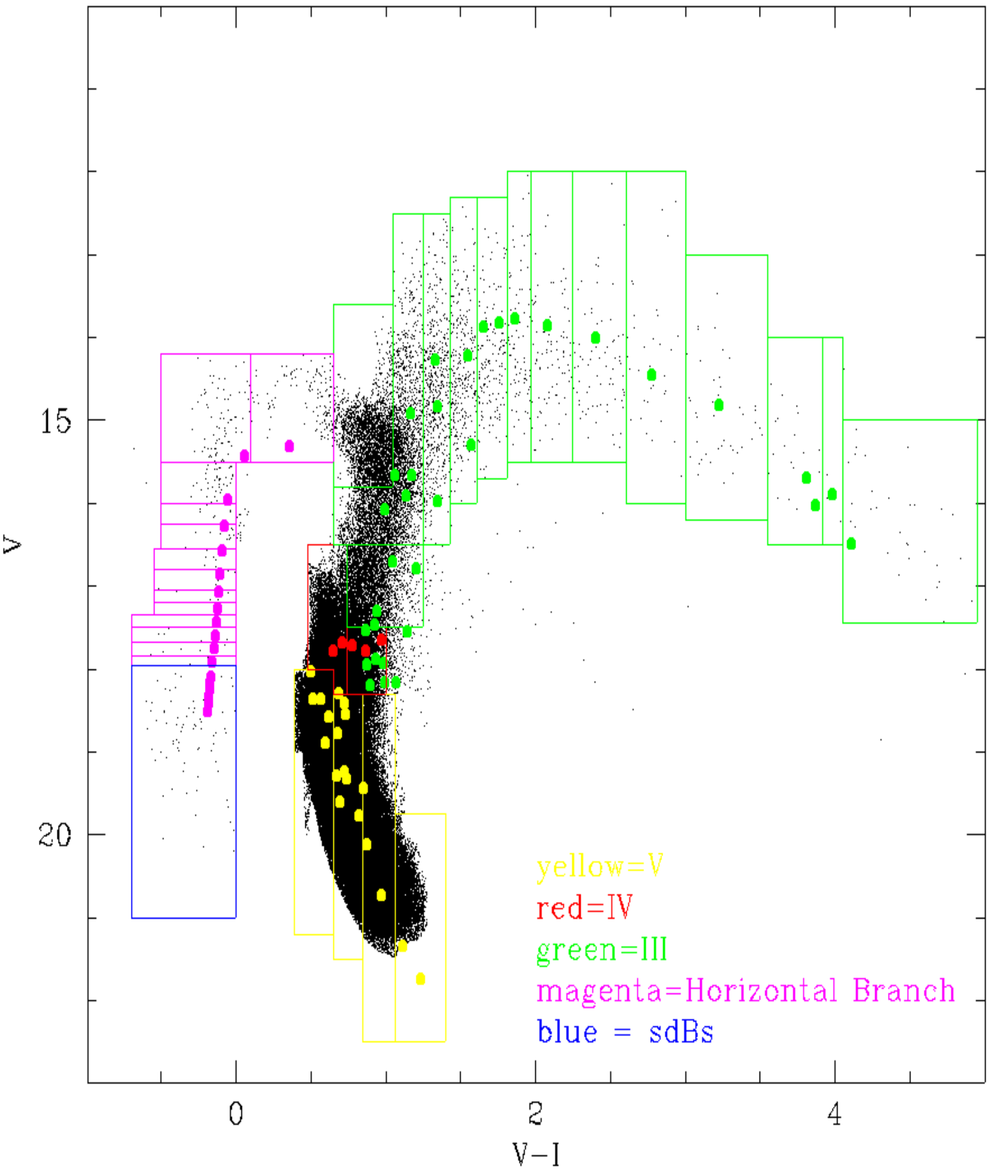

Figure 6.6: Association between library spectra and CMD: the spectra library points are marked in different colors (yellow: dwarfs(V); red: subgiant(IV)); green: giants (III); magenta: horizontal branch stars; blue (sdB stars). For each kind of stars, each point has different temperature. Every CMD star has been associated to the library spectrum corresponding to the box where the star belongs.

box	n_j	$< M_v >$	m_{v_j}	$C_j(\times 10^{-6})$
Main Sequence				
kVa	7966	6.008	-11.642	693.986
kVb	49053	5.443	-11.774	636.798
gVa	119840	4.721	-11.843	28401.729
fV	56425	3.954	-11.907	25545.383
Sub Giants				
kgIVa	22115	3.069	-11.851	23794.012
kgIVb	7578	3.266	-11.784	7233.121
Red Giants				
kIIIa	5313	2.348	-11.779	11866.421
kIIIb	5210	0.944	-11.697	45764.875
bump	3755	0.578	-11.793	42287.808
kIIIc	598	-0.202	-11.619	16210.757
kIIId	312	-0.469	-11.613	10884.264
mIIIa	7163	-0.610	-11.642	6303.584
m2III	88	-0.898	-11.664	4343.994
m3III	91	-0.660	-11.803	3176.254
m4III	75	-0.551	-11.947	2073.557
m5III	33	-0.727	-12.019	1003.287
m6III	44	0.119	-12.042	601.313
mIIIb	18	0.599	-12.201	136.534
m10III	3	1.261	-13.348	4.299
m8III	31	1.446	-12.482	83.213
Horizontal Branch				
f5v	136	0.054	-11.914	2219.940
a5v	82	0.286	-12.029	971.757
hb1	44	1.078	-12.078	240.356
b8v	7	1.451	-12.102	26.523
hb2	13	1.723	-12.120	37.744
hb3	8	2.029	-12.108	17.703
hb4	5	2.268	-12.159	8.469
hb5	6	2.449	-12.154	8.647
hb8	6	2.957	-12.139	5.490
hb9	6	3.121	-12.139	4.721
hb10	2	3.250	-12.169	1.400

Table 6.3: Parameters of the boxes used to construct the integrated spectrum: n_j is the number of stars in the box, associated with the archive spectrum; $< M_v >$ is the mean absolute V magnitude of the stars in the box; C_j is the weight with which each spectrum contributes to the integrated spectrum.

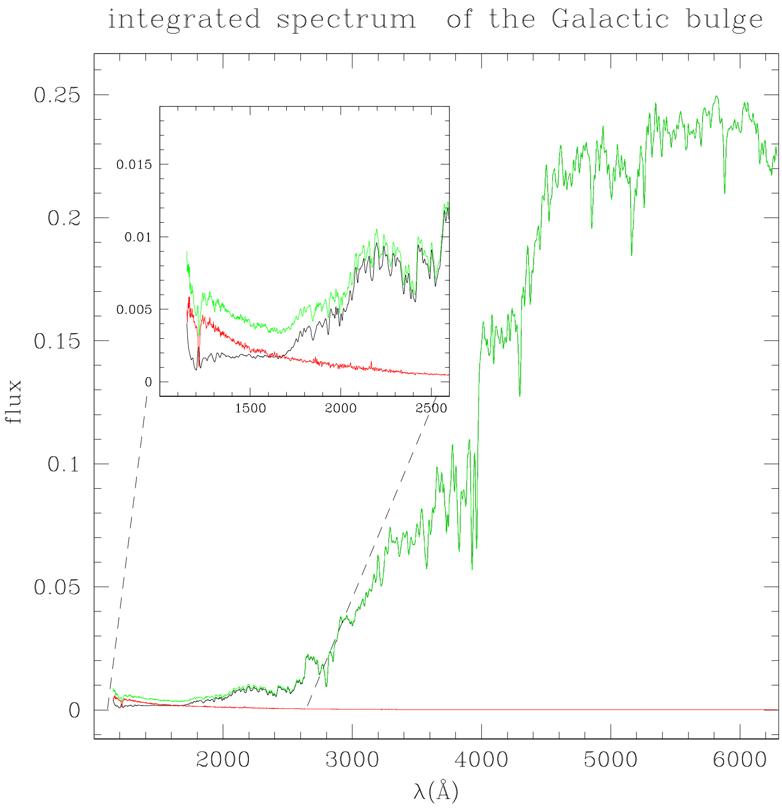

Figure 6.7: Bulge integrated spectrum from UV to optical wavelength: n black the integrated spectrum obtained without sdBs, in red the sdB stars integrated spectrum and in green the total sum. The UV region in particular is shown in the small panel.

box	m$_{v_j}$ Pickles	m$_{v_j}$ BaSeL	Δ
Main Sequence			
kVa	-11.642	-11.624	-0.018
kVb	-11.774	-11.702	-0.072
gVa	-11.843	-11.758	-0.085
fV	-11.907	-11.858	-0.049
Sub Giants			
kgIVa	-11.851	-11.804	-0.047
kgIVb	-11.784	-11.719	-0.065
Red Giants			
kIIIa	-11.779	-11.684	-0.095
kIIIb	-11.697	-11.630	-0.067
bump	-11.793	-11.705	-0.088
kIIIc	-11.619	-11.546	-0.073
kIIId	-11.613	-11.482	-0.131
mIIIa	-11.642	-11.440	-0.202
m2III	-11.664	-11.419	-0.245
m3III	-11.803	-11.420	-0.383
m4III	-11.947	-11.440	-0.507
m5III	-12.019	-11.537	-0.482
m6III	-12.042	-12.517	0.475
mIIIb	-12.201	-12.619	0.418
m10III	-13.348	-13.071	-0.277
m8III	-12.482	-12.483	0.001
Horizontal Branch			
f5v	-11.914	-11.888	-0.026
a5v	-12.029	-12.023	-0.006
hb1	-12.078	-12.042	-0.036
b8v	-12.102	-12.044	-0.058
hb2	-12.120	-12.065	-0.055
hb3	-12.108	-12.074	-0.034
hb4	-12.159	-12.082	-0.077
hb5	-12.154	-12.088	-0.066
hb8	-12.139	-12.107	-0.032
hb9	-12.139	-12.116	-0.023
hb10	-12.169	12.116	-0.053

Table 6.4: m_{V_j} magnitudes obtained from the convolution of the spectra (1^{th} column) with the V filter in the case of the Pickles [1998] (2^{th} column) and BaSeL (3^{th} column). The difference between them is listed in the 4^{th} column.

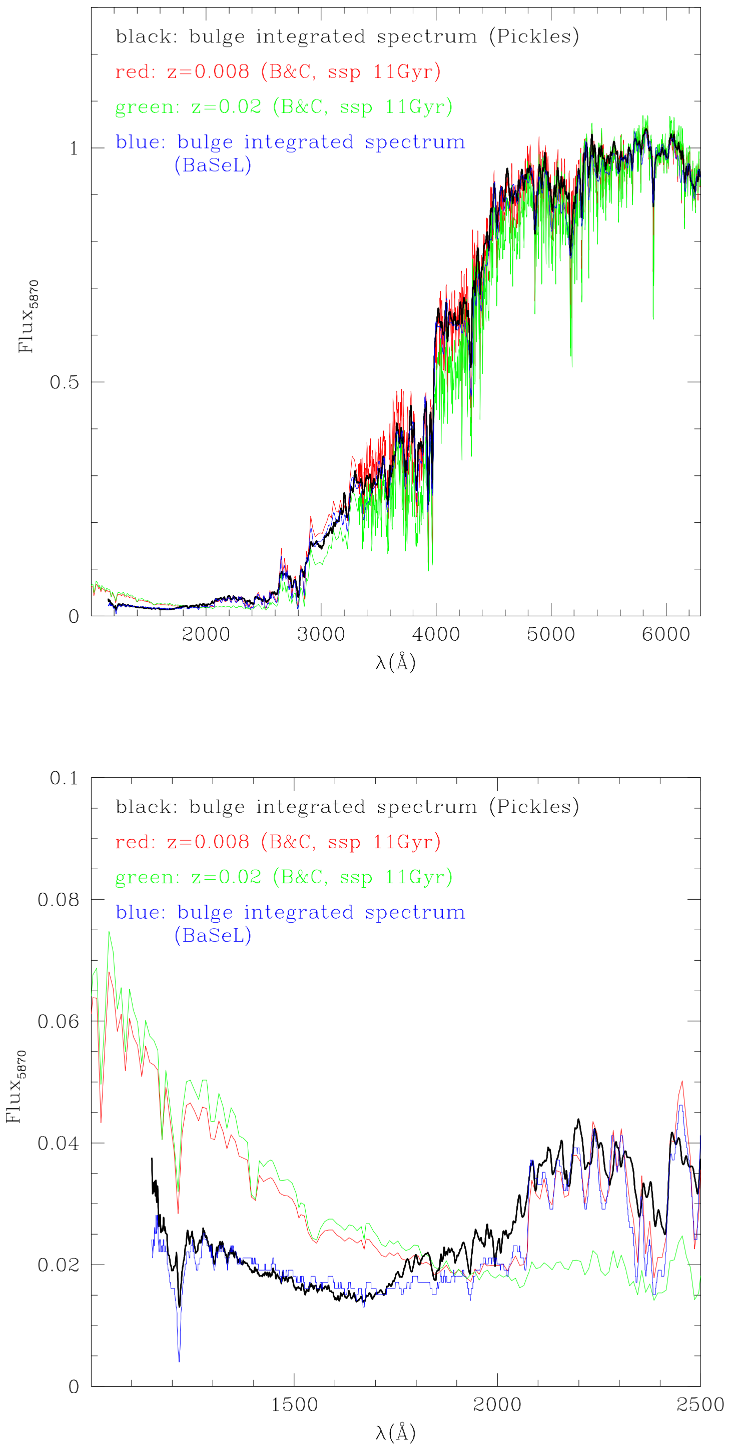

Figure 6.8: Comparison between integrated spectra and single stellar population SED. Top panel: The integrated bulge spectrum obtained with the Pickles [1998] and Basel (Lejeune et al. [1997]) library are shown in black and in blue respectively. The Bruzual & Charlot [2003] spectra for a single stellar population 11 Gyr old and with metallicity z=0.008 and 0.02 are shown in red and green respectively. To allow the comparison the spectra were scaled at λ =5870 Å. Bottom panel: as top panel, but in the UV range.

Chapter 7

Two bulge Globular clusters

The sdB stars I analyzed are not the only sdBs detected in the Galactic bulge, since they are evident also in the color magnitude diagram of two Galactic globular clusters, NGC 6388 and NGC 6441. These two objects are indeed located in the bulge and they are metal-rich ([Fe/H]= −0.60 for NGC 6388 and [Fe/H]= −0.53 for NGC 6441, from the 2003 revised catalogue of Harris [1996]).

Hubble Space Telescope (HST) observations of these two metal-rich clusters NGC 6388 performed by Rich et al. [1997], showed that both objects present an Extended Horizontal Branch (see Fig. 7.1). Furthermore, IUE spectra (Rich et al. [1993]) showed that both clusters have a mild raising flux in the UV, similar to the one observed in the elliptical galaxies. These two evidences are another strong indication of the role that EHB stars have in the UV excess typical of the elliptical galaxies.

The photometric data of Rich et al. [1997] disclosed a number of quite important and unexpected empirical facts:

- both clusters show not only the red HB characteristic of clusters with metallicity like 47 Tuc ([Fe/H]= −0.76, Harris [2003]), but also quite extended blue HBs. The effective temperature reached by the HB stars in both clusters are such that their V magnitudes are dominated by the huge bolometric corrections, and the (B-V) color index is no more a good $T_{\rm eff}$ indicator. As a consequence, the blue HB appears as a vertical branch, this occurrence hampering a more detailed investigation of the hottest HB stellar populations in these clusters using optical photometry. The fact that NGC 6388 and NGC 6441 show not only the 'canonical' red stubby HB, but also an extended blue tail was the first sound evidence that the second parameter[1] is also at work in old,

---

[1] The first parameter that governs the HB morphology is the metallicity, but clusters

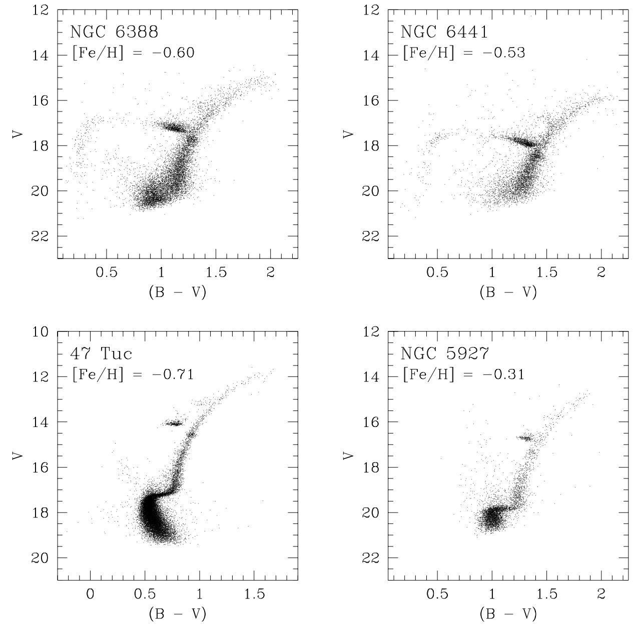

Figure 7.1: CMDs obtained from Rich et al. 1997

metal-rich globular clusters;

- even more surprisingly, the color-magnitude diagram of Rich et al. [1997] clearly showed that the mean HB brightness at the top of the blue HB tail is roughly 0.5 magnitudes brighter in the V band than the red HB portion, which appears significantly sloped as well.

In an attempt to interpret the occurrence of the blue tail along the HB as well as of the tilted morphology, many non-canonical scenarios and/or observational effects have been suggested (Sweigart & Catelan [1998], Raimondo et al. [2002], Moehler & Sweigart [2006a] for NGC 6388 and NGC 6441; for a more complete review see Catelan [2004]).

With the aim of better understanding the observational properties of the Horizontal Branch stars belonging to these clusters, I present here the results of an HST project (GO8718, PI: G. Piotto) devoted to collect HST WFPC2 multiband photometry in the filters: F255W, F336W, F439W and F555W, where the first is a UV filter and the other three correspond to the Johnson

---

with same metallicity show different HBs, hinting to the presence of one or more other parameters. In general this is called "the second parameter problem".

	NGC 6388	NGC 6441
l	345.56	-353.53
b	-6.74	-5.01
$R_\odot$	10.0	11.7
[Fe/H]	-0.60	-0.53
E(B-V)	0.37	0.47

Table 7.1: Fundamental parameters of NGC 6388 and NGC 6441. l and b are respectively galactic longitude and latitude, $R_\odot$ is the distance from the Sun (in Kpc), [Fe/H] is the metallicity, and $E(B-V)$ is the reddening (from the 2003 update of Harris [1996] catalog)

system U, B, V filters respectively (see Fig. 7.2). The main parameters of NGC 6388 and NGC 6441, as given by Harris 2003 are summarized in 7.1.

7.1 The instrument: WFPC2@HST

The Wide Field and Planetary Camera 2 (WFPC2) is a two-dimensional imaging photometer which is located on the Hubble Space Telescope (HST) and covers the spectral range between approximately 1150 Å and 10500 Å. The WFPC2 field of view is divided into four cameras by a four-faceted pyramid mirror near the HST focal plane. Each of the four cameras contains an 800×800 pixels CCD detector. Three cameras operate at an image scale of 0.1" per pixel and comprise the Wide Field Camera with an "L" shaped field of view (see Fig. 7.3). The fourth camera operates at 0.046" per pixel and is referred to as the Planetary Camera.

7.2 Observations and data reduction

Tab. 7.2 summarizes the most relevant information on the observational data set used in this work. The data come from observations taken with the HST WFPC2, in all cases the PC camera was centered on the cluster center. The images were processed following the recipe in Silbermann et al. [1996]: the vignetted pixels and bad pixels and columns were masked out using a vignetting frame created by P.B. Stetson, together with the appropriate data-quality file for each frame. The single chip frames were extracted from the 4-chip-stack files and analyzed separately.

The photometric reduction was carried out using the DAOPHOTII/ALLFRAME

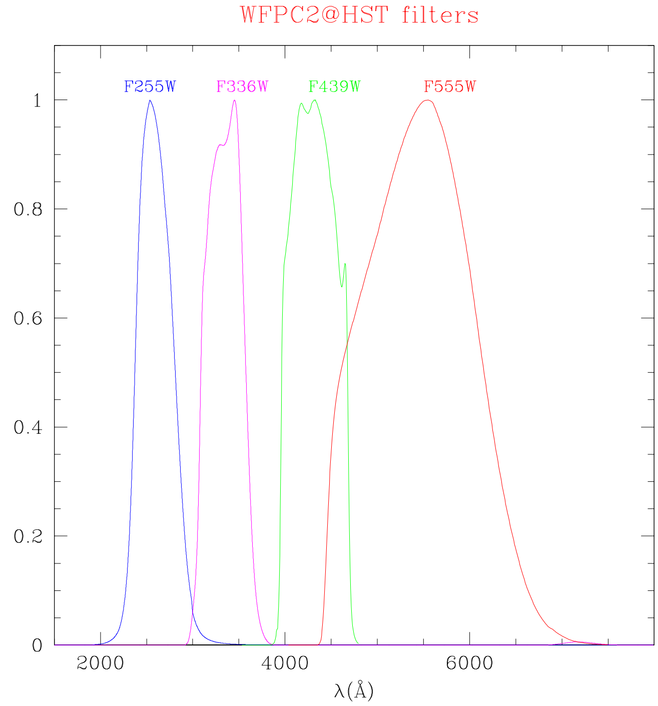

Figure 7.2: WFPC2@HST filters. F255W is a UV filter; F336W, F439W and F555W correspond to the Johnson system U, B, V filters respectively.

package (Stetson [1987, 1994]). The F439W and F555W data were reduced by Piotto et al. [2002]), while I reduced the F255W and F336W data, during my Laurea thesis. For each image I calculated the appropriate Point Spread Function (PSF). The stars used to calculate the PSF were selected carefully, as many cosmic rays were present in the UV images, especially in the F255W band.

With ALLSTAR, I fitted on each image the best PSF, obtaining an approximate list of stars for each single frame. This list was used to match the different frames accurately and to find the correct coordinate transformations among the frames.

ALLFRAME is a program that fit simultaneously the PSF in all frames, allowing a better determination of the star centroids and therefore a better photometry. It needs also an input star list. I ran this program with two star lists: the first one was obtained from the median image coming from all the F255W images, and the second one was obtained on the median image of the F336W frames.

For each of the WFPC2 chips, a catalog of mean magnitudes was cre-

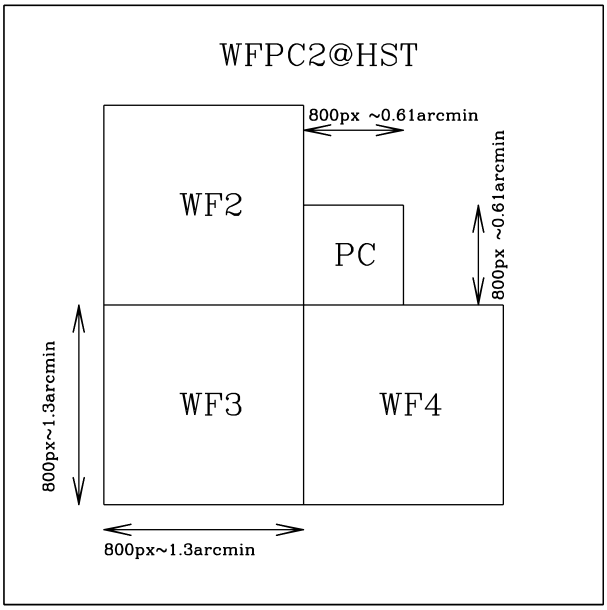

Figure 7.3: The four cameras of the WFPC2@HST instrument.

ated for both F255W and F336W bands; for the photometry in F439W and F555W bands, I used the Piotto et al. [2002] data. The four photometries were finally combined in order to obtain the various color magnitude diagrams.

7.2.1 The photometric calibration

In order to calibrate the photometry, I followed the procedure outlined by Dolphin [2000], which allows also to correct the observed magnitudes for charge-transfer efficiency effect (CTE). After having measured the zero point differences between the ALLFRAME magnitudes and the reference aperture of 0".5 for the brightest stars, I applied the following calibration equation to transform the magnitudes into the Flight Photometric System, that is the photometric system of the WFPC2:

$$WFPC2 = -2.5log(DN\ \mathrm{s}^{-1}) + Z_{FG} + \Delta Z_{FG} - CTE$$

where DN is the flux in digital counts, CTE is the CTE correction, Z_{FG} is the zero point, different for each filter, and ΔZ_{FG} is the zero-point modification

Cluster	Filter	n. images	t_{exp} [s]	Program ID
NGC 6388	F255W	7	$1 \times 1100, 3 \times 1300, 3 \times 1400$	GO8718
	F336W	3	$1 \times 260, 2 \times 400$	GO8718
	F439W	3	$1 \times 50, 2 \times 160$	GO6095
	F555W	2	$1 \times 12, 1 \times 50$	GO6095
NGC 6441	F255W	7	$1 \times 1100, 3 \times 1300, 3 \times 1400$	GO8718
	F336W	3	$1 \times 260, 2 \times 400$	GO8718
	F439W	3	$1 \times 50, 2 \times 160$	GO6095
	F555W	2	$1 \times 14, 1 \times 50$	GO6095

Table 7.2: Log of the observations

for chip and gain settings.

7.3 The optical and UV CMDs and star counts

7.3.1 The color-magnitude diagrams

Fig. 7.4 shows the optical and UV band color magnitude diagrams for both clusters. Already a quick look at the two optical CMDs clearly shows the most relevant common properties of these two clusters, i.e., the occurrence of an extended HB, and the tilt of the HB, with the HB on the blue side of the instability strip being brighter than the branch on the red side. However, the HB morphology in the optical CMDs differs in the two clusters in a number of significant aspects:

- The HB on the blue side of the instability strip appears more populated in NGC 6388 than in NGC 6441. This is not due to a sampling effect, since the number of the sampled bright stars is very similar for the two clusters, as discussed below.

- The blue tail of NGC 6388 seems to be more extended than in NGC 6441. In NGC 6388 the blue tail extends to more than 1 magnitude fainter than the cluster turn-off (down to $F555W \approx 21.5$); whereas in the case of NGC 6441 it barely reaches the turn-off brightness, at $F555W \approx 20.5$, since I did not consider the two stars at $F555W \approx 22$ because they are quite separated from the HB blue tail and they may not belong to the cluster but instead to the bulge population (hot HB stars have been found also in other bulge fields (see Ch. 3 and Ch. 4);

- In the CMD of NGC 6441 there is a gap at $F555W \approx 18.5$, about one magnitude below the HB turning down; no such gap is visible in the

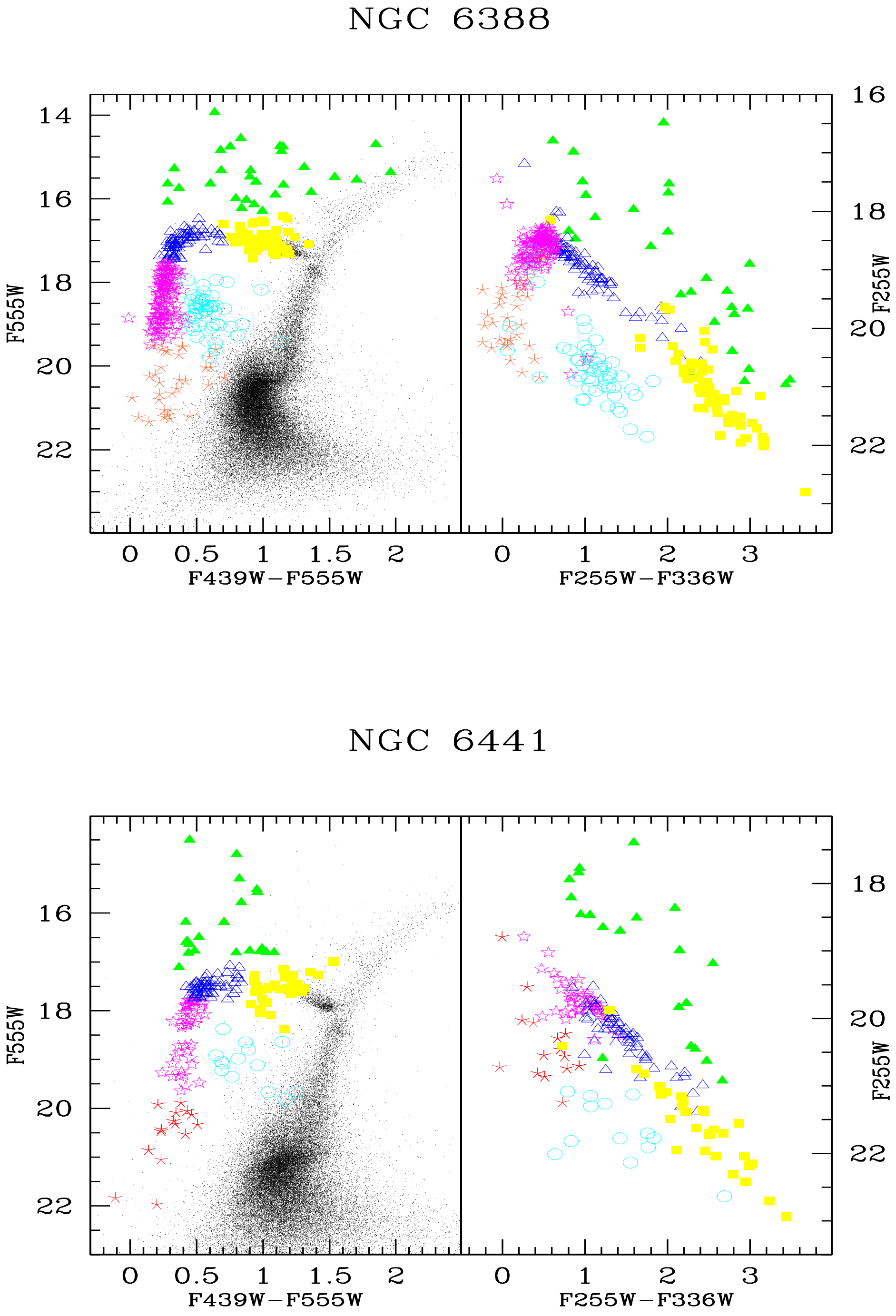

Figure 7.4: Optical and UV CMDs for NGC 6388 (upper panels) and NGC 6441 (lower panels). The different symbols and colors refer to the same group of stars appearing both in the optical and UV CMD: yellow filled squares indicate the red HB, blue open triangles the blue HB, magenta open stars the extended blue HB tail, the filled green triangles the post HB, the cyan open circle the Blue Stragglers candidates and the orange asterisks are the blue hook candidates.

HB of NGC 6388, which, instead seems to show a gap (or at least a reduction of the stars density) at $F555W \approx 19.8$. The latter is not present in NGC 6441, but this could be due to the smaller number of stars present in that region of its HB combined with photometric errors and to the lower sensibility to the temperature of the F255W-F336W color at that temperature;

The right panels of Fig. 7.4 show the UV CMDs for both clusters. I used different symbols and colors for different stellar groups in order to make easier the cross-identification of the same sequences in the optical and UV color magnitude diagrams. In the UV photometry, only the hottest stars are sufficiently bright to be properly measured, namely the blue stragglers (BS), the bluer HB stars, the EHB stars and the post-HB stars. The coolest stars of the red HB clump are totally missed. It is also worth noting how well the BS sequence is separated from the HB blue tail in the UV CMD. This fact is more evident for NGC 6388 than for NGC 6441, possibly as a consequence of the larger differential reddening which characterizes NGC 6441 (see discussion in Sec. 7.6.1).

Also the UV CMDs for both clusters show some noteworthy features:

- Contrary to intuitive expectation, in both CMDs the brightest stars in the F255W band are not the stars populating the hottest portion of the blue tail in the optical CMD;
- The gaps visible in the optical bands are not clearly visible in the UV CMDs, making it impossible to establish whether these gaps are real features (as clearly seen in another Globular cluster, NGC 2808, Sosin et al. [1997], Bedin et al. [2000]) or simply a statistical fluctuation in the distribution in temperature along the HB. The only possible exception is the abrupt drop in the NGC 6388 HB star counts at F255W$\approx$ 19.4 and (F255W-F336)$\approx$ 0.2, which corresponds to the gap at F555W$\approx$ 19.8 in the optical CMD. This feature is relevant for the discussion in Sec. 7.5.
- There is a large color spread at the hot end of the observed HB sequence, of the order of ~ 0.5 magnitudes in $F255W - F336W$, larger than the photometric errors (less than 0.1 magnitudes).

7.3.2 Star counts

Tab. 7.3 lists the star counts in a number of relevant parts of the CMD for the two clusters. N_{RGB} is the number of RGB stars from the magnitude level

	NGC 6441	NGC 6388	ratio(NGC 6388/NGC 6441)
N_{RGB}	705	664	1.06±0.06
N_{HB}	1289	1293	1.00±0.04
N_{rHB}	1122	1056	1.06±0.05
N_{vHB}	21	19	1.11±0.35
N_{bHB}	146	218	0.70±0.07
N_{gHB}	61	154	0.40±0.06

Table 7.3: Star counts for selected regions of the CMDs of the two clusters.

corresponding to the average magnitude of the red HB to the RGB tip, $N_{\rm HB}$ is the total number of HB stars, $N_{\rm rHB}$ is the number of stars redder than the instability strip, $N_{\rm vHB}$ the number of stars within the instability strip, $N_{\rm bHB}$ the number of stars bluer than the instability strip, $N_{\rm gHB}$ the number of stars bluer than the Grundahl et al. [1999] jump, at $T_{\rm eff} \sim$ 11,500 K (see also the discussion in Sec. 7.6.2). The HB and RGB stars have been extracted from the (F336W-F555W, F555W) CMD, as in this diagram it is easier to separate the different CMD parts (see Fig. 7.5, left panels), while the stars counts $N_{\rm rHB}$,$N_{\rm vHB}$ and $N_{\rm bHB}$ has been extracted from the (F439W-F555W,F555W) diagram (see Fig. 7.5, right panels). The stars hotter than the Grundahl et al. [1999] jump[2] have been counted in the (F336W-F555W,F336W) diagram (see Fig. 7.13) and a consistency check has been carried out using the (F439W-F555W, F555W) CMD, obtaining very similar counts. Now, the ratio of the number of RGB stars (NGC 6441/NGC 6388=1.06 ± 0.06) tells us that approximately the same total number of bright stars are sampled in the two clusters. Consistently, also the ratio of the total number of HB stars (NGC 6441/NGC 6388=1.00 ± 0.04) is comparable. Interestingly enough, the relative number of red HB stars is the same for the two clusters (ratio NGC 6441/NGC 6388=1.06 ± 0.06), and consistent with the total number of sampled stars (it is the same ratio of the RGB stars). The relative number of stars within the instability strip is not very informative (too few stars), and it must be noted that this is also the region with the highest contamination by field stars. In any case, it is important to note that NGC 6388 has 9 known RR Lyrae, while NGC 6441 has 43 RR Lyrae (Catelan [2004]), confirming an

---

[2] The Grundahl et al. (1999) jump is a feature in the blue HB, in which stars in the range 11500 K $\lesssim T_{eff} \lesssim$ 20000 K deviate systematically from canonical zero-age HB model (in the sense of appearing brighter and/or hotter than the theoretical sequence). It was observed for the first time in globular clusters with low and intermediate metallicity, which show a blue HB. In the metal rich clusters (most of whose have not a blue HB reaching high temperature) it is not always possible to observe.

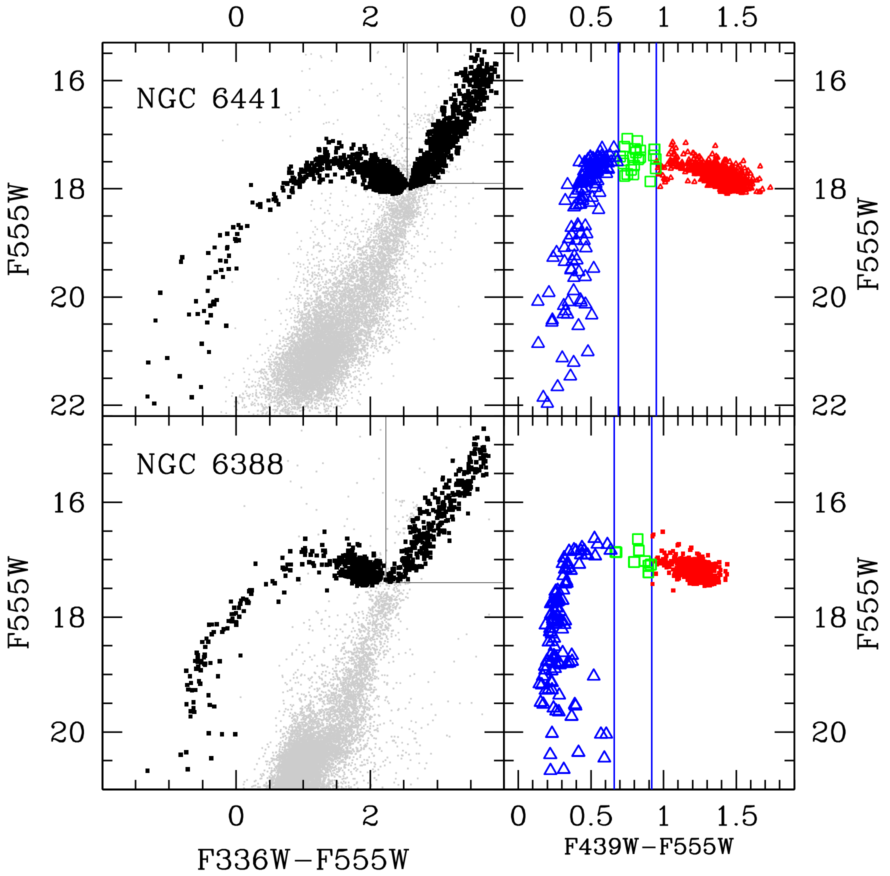

Figure 7.5: In the left panels, the (F336W-F555W,F555W) diagrams for both clusters, where the RGB (in the top box) and HB selection are shown marked in black.In the right panels, for both clusters the selection in the (F439W-F555W,F555W) for red (points), variable (open squares) and blue (open triangles) HB stars. The two vertical lines represent the instability strip borders (0.21 <F439W-F555W< 0.47), reddened considering E(B-V)=0.45 for NGC 6388 and E(B-V)=0.48 for NGC 6441.

overabundance of RR Lyrae in the latter. Most interestingly, as suspected from the first visual impression, the blue HB in NGC 6441 is much less populated than in NGC 6388, and the lack of hot stars in NGC 6441 with respect to NGC 6388 is even more pronounced for $T_{\rm eff} \geq 11,500$K, i.e. beyond the Grundahl et al. (1999) jump. Only $11 \pm 1\%$ of the HB stars of NGC 6441 populate the HB on the blue side of the instability strip, to be compared with the $17 \pm 1\%$ of blue HB stars in NGC 6388. NGC 6441 has only $4.7 \pm 0.6\%$ of its stars hotter than the Grundahl et al. [1999] jump, while $11.9 \pm 1.0\%$ of NGC 6388 HB stars are beyond the jump.

7.4 The anomalous HBs of NGC 6388 and NGC 6441

So far, both the evidence of the tilted Horizontal Branch and the presence of an Extreme Horizontal Branch have not found a firm interpretation. In this work, I tried to take advantage of the availability of multi-band photometric data in order to provide additional pieces of information useful for constraining the evolutionary scenario.

In order to perform a detailed comparison between theory and observations, I have adopted the ZAHB models provided by Pietrinferni et al. [2006], supplemented by additional computations performed for this specific project. I have adopted a metallicity Z=0.008 (corresponding to $[M/H] \sim -0.35$), and a He content Y=0.256. All of the He-burning models used for the present work correspond to an RGB progenitor whose age at the RGB tip is equal to about 13 Gyr.

7.4.1 Effects of the reddening in UV bands

Bolometric magnitudes and effective temperatures have been transformed into HST magnitudes and colors according to transformations provided by Origlia & Leitherer [2000] based on the atmosphere models computed by Bessell et al. [1998].

The transformation from the theoretical to the observational plane of the stellar models imply also a correction for the effect of reddening and extinction. Both NGC 6388 and NGC 6441 are affected by substantial interstellar extinction (see data in Tab. 7.1). As a consequence, an appropriate correction for reddening has to be applied before comparing models with observations. It is a common procedure to adopt an average extinction law for all stars, regardless of their spectral types. However, the reddening correction depends on the stellar effective temperature. While the commonly adopted approach is surely suitable for stellar systems with a low extinction ($E(B-V) \leq 0.10-0.15$), it is inappropriate for heavily reddened objects, and the problems increase for blue/UV photometric bands.

It is evident that the presence of a huge amount of interstellar extinction has no relation at all with the presence of an extended blue tail along the HB of both clusters. However, it could - at least partially - help in explaining the other striking feature observed in the HBs, i.e. their tilted morphology.

In order to adopt an accurate reddening correction, its dependence on $T_{\rm eff}$ was determined by applying the extinction law of Savage & Mathis [1979] to the convolution of the appropriate model atmosphere of Bessell et al. [1998] with the filter bandpass. Fig. 7.6 shows the size of this effect. For the filters F555W and F439W, the extinction correction marginally depends on the stellar $T_{\rm eff}$, and the average value provided by the table in Holtzman et al. [1995] can be safely used to correct for extinction in these bands. This finding clearly shows that the fact that both clusters are affected by a sizeable interstellar reddening can not explain the tilted HB morphology through the effect of temperature dependence of reddening corrections for the optical bands. However, it is also worth remembering that both clusters are also affected by a significant differential reddening, i.e. variations of reddening across the field the clusters. As extensively discussed by Raimondo et al. [2002], the occurrence of differential reddening can contribute in explaining the tilted HB morphology but mainly for the red portion of the HB. I discuss this issue more in detail in the following paragraph.

From data shown in Fig. 7.6, it appears that, for the bluer filters the difference is large, and it becomes rather significant for the F255W band, being of the order of 0.5 magnitudes for $T_{\rm eff} < 10,000$K.

The effect of using an appropriate reddening correction for transferring the models in the UV observational plane is shown in Fig. 7.7. As one can expect on the basis of the results shown in Fig. 7.6, only models cooler than about 10,000K are significantly affected by the different approach in applying the reddening correction. This figure shows that even if the temperature dependence of reddening correction in the UV bands can be large, the quality of the fit procedure between theory and observations is affected only marginally. This occurrence is due to the fact that the hot HB models are marginally affected by this dependence; whereas for the cooler HB models the dependence of reddening corrections on the T_{eff} causes a shift of the models along the ZAHB locus obtained for a constant reddening correction.

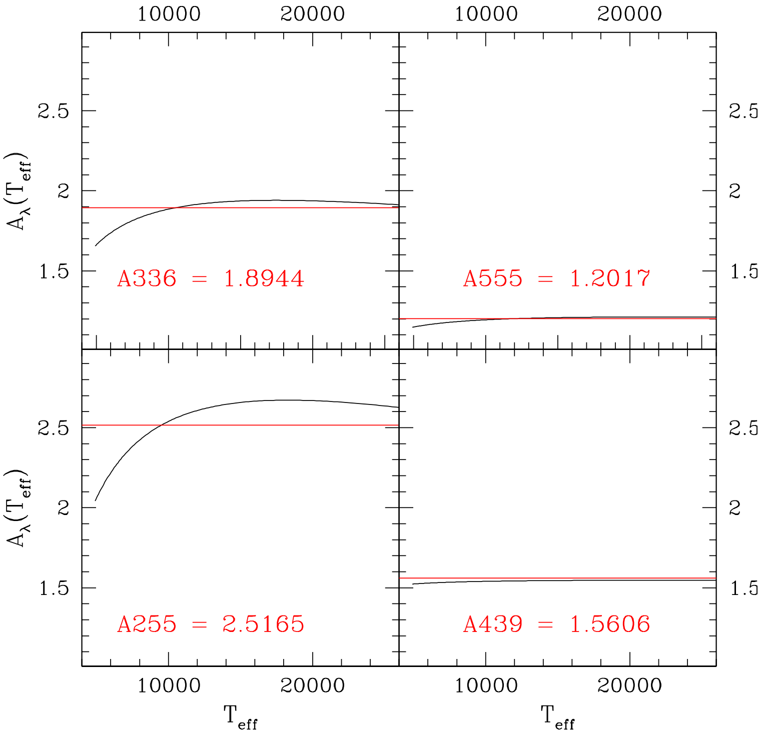

Figure 7.6: The extinction coefficients are plotted as a function of the effective temperature for the various photometric bands used in the present work. The horizontal line shows the average extinction coefficients for the same bands as provided by Holtzman et al. [1995].

7.4.2 The HB morphology in various photometric bands

Figs 7.9 and 7.10 show a comparison in the various photometric planes between the ZAHB models and the HB sequence of NGC 6388 and NGC 6441, respectively. For reasons that will be clear in the following discussion, I have arbitrarily adopted the reddening and distance modulus which best fit the red HB clump in the CMD (F336W-F439W, F439W) shown in Fig. 7.8, and indicated in the figure inset.

The comparison between theoretical models and empirical data clearly shows that it is not possible to have an overall fit of the entire HB. If I impose to the models to fit the red HB, there is no way to fit the blue part, and vice versa. The striking evidence is that this is true for all combinations of colors and magnitudes, which raises the suspicion that there must be a real mismatch between the canonical ZAHB models and the observed HBs,

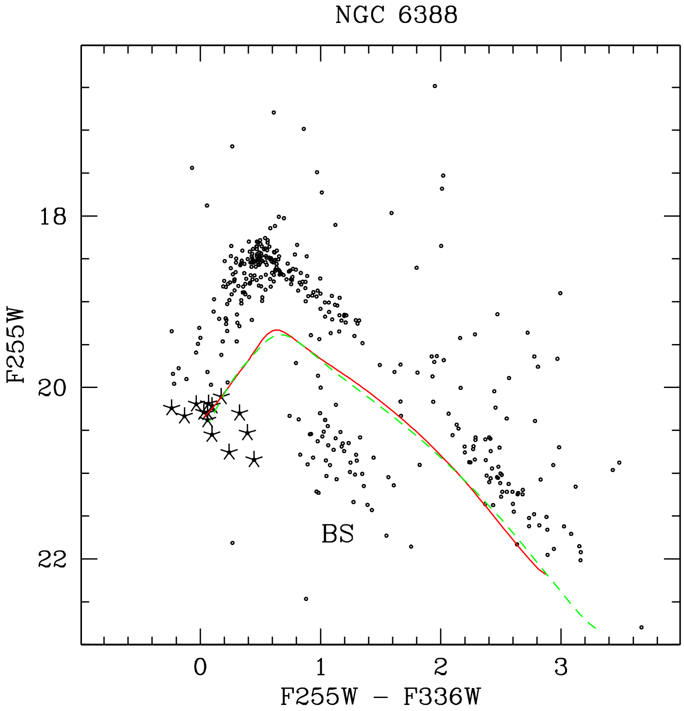

Figure 7.7: UV color magnitude diagram of NGC 6388. The ZAHB models transformed into the observational plane by applying a reddening correction as a function of the effective temperature $T_{\rm eff}$ are plotted as a red solid line, while the models with applied only a constant reddening correction are shown as a green dashed line. I overplotted the hot HB by using for both theoretical sequences a reddening $E(F439W-F555W)=0.4$ and a distance modulus $(m-M)_{F555W}=16.15$ (from Harris [1996,2003]). The clump of stars fainter than the HB corresponds to a sub-sample of the cluster blue stragglers population. The objects marked as asterisks are blue hook star candidates, very hot EHB stars (see Sec. 7.5).

for both clusters. Apparently, it is not possible to find a unique combination of the distance modulus and reddening that allows to properly fit the HB in the various observational planes, even if we consider only the red part of the HB. This occurrence is quite evident in the (F255W, F439W-F555W) CMD, and it is likely due to the combination of the differential reddening and of the fact that for the red portion of the HB we start to lose stars (because they are too faint) when using the F255W magnitudes.

Concerning the role played by differential reddening, it is important to

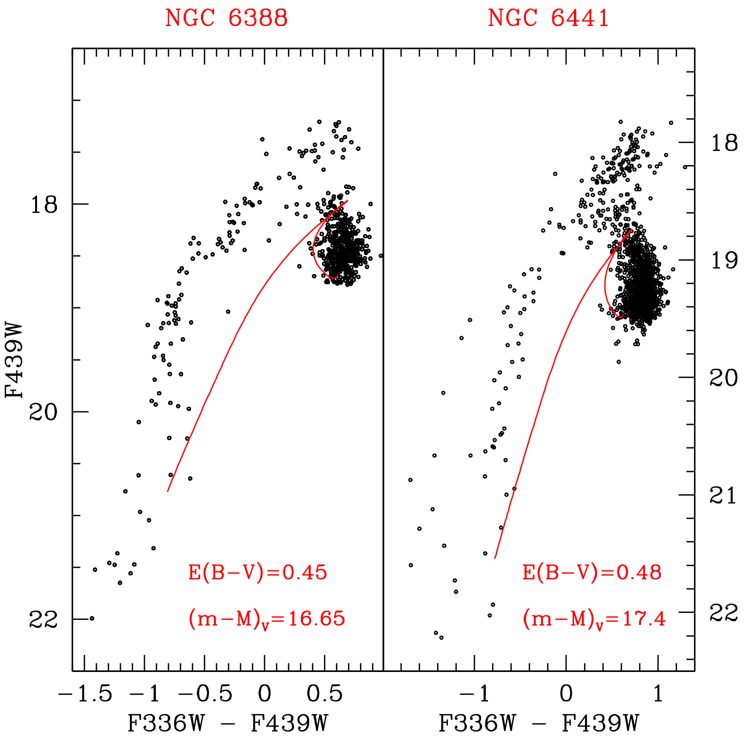

Figure 7.8: (F336W-F439W,F439W) diagram of NGC 6388 and NGC 6441. The reddening and distance modulus values, determined by best fitting in this diagram the red clump with the ZAHB models, are used in all the other photometric planes.

note that the slope of the red portion of the HB is not the same as the slope of the reddening vector shown in Figs. 7.9, 7.10. More specifically, when analyzing the optical plane (F555W, F439W-F555W), a tilt is evident when moving from the red HB clump toward bluer color (see also Rich et al. [1997] and Raimondo et al. [2002]), with stars close to the HB turnover being ≈ 0.5 magnitudes brighter than the average magnitude of the red HB. It is worth noting once again that this tilt is present in all photometric planes, and it appears even more evident in the UV CMDs, where the blue part of the HB is up to ≈ 1 magnitudes brighter than the red part.

It appears - at least in some CMDs, such as the (F336W-F439W, F336W) - that the red portion of the theoretical ZAHB is not able to approach the reddest colors of the observed red HB. Again, this occurrence could be due either to some problems in the adopted color-$T_{\rm eff}$ relation, or to an effect of the differential reddening affecting these clusters or a combination of both

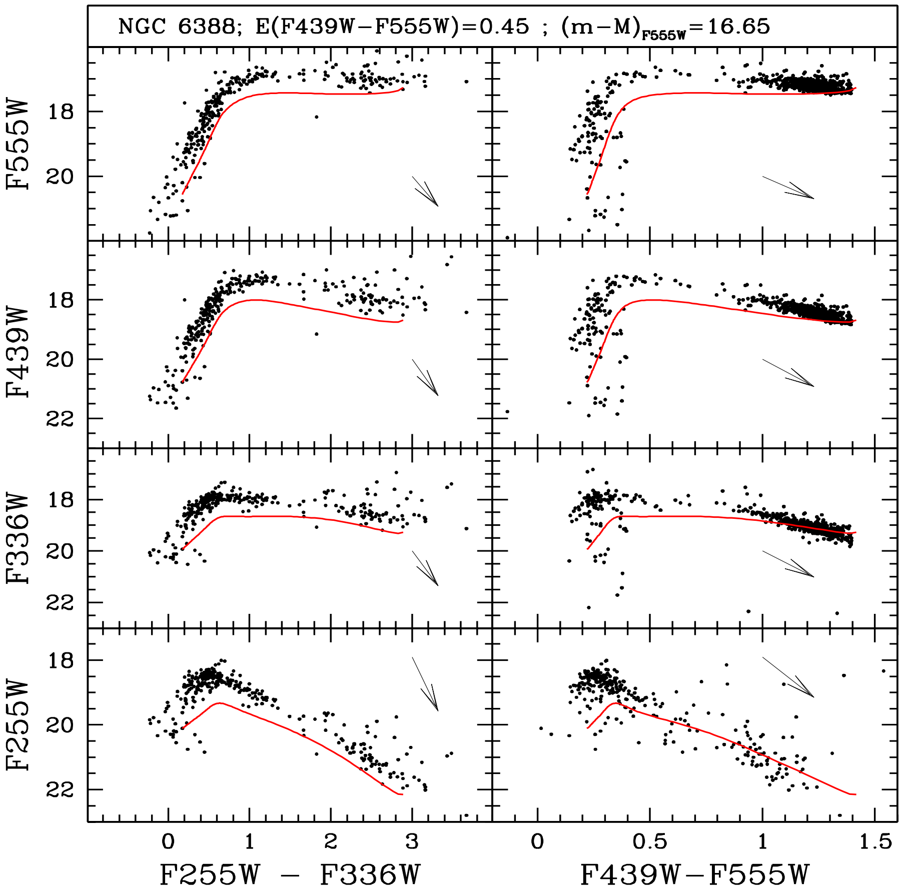

Figure 7.9: The HB of NGC 6388 in different photometric planes. The solid line shows the location of a theoretical ZAHB locus for a metallicity Z=0.008. The ZAHB models account, in all cases, for a reddening correction depending on $T_{\rm eff}$ (see text for details). The adopted distance modulus and mean reddening are labeled in the figure, and they have been fixed according to our (arbitrary) choice of imposing a best fit between models and the lower envelope of the red HB portion in the (F439W, F336W-F439W) CMD (see Fig. 7.8). The arrows represent the reddening vector in the different photometric planes. Note that the scale adopted in the plots on the right panels is different from that used in the left panels.

effects.

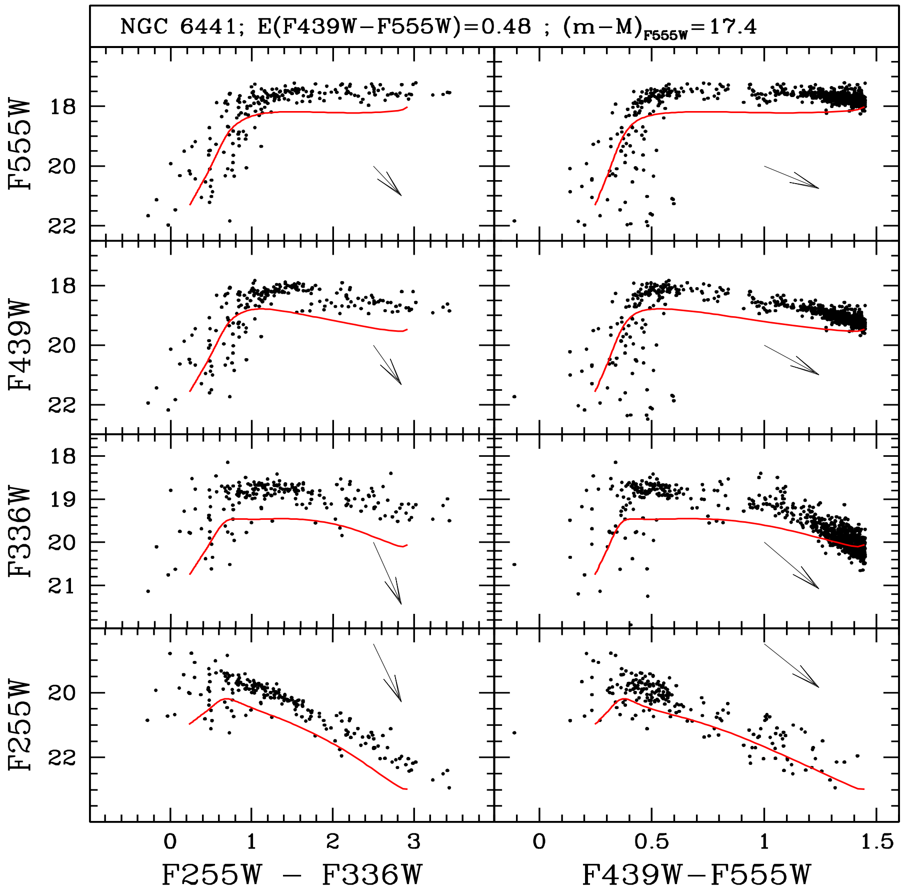

Figure 7.10: As Fig. 7.9 but for NGC 6441.

7.5 The blue–hook star candidates

The data shown in Figs. 7.9 and 7.10 reveal that canonical models are not able to reproduce the peculiar morphology of the HB in both target clusters. Although this is the most evident shortcoming of models, a careful look to the same figures shows also that the models are not able to reproduce the color of the hottest HB stars in the color magnitude diagram. This empirical finding could be interpreted as an evidence that the effective temperature of these stars is significantly larger than that of the hottest HB structures (those whose total mass is virtually coincident with the He core mass) that can be envisaged on the basis of canonical stellar evolution theory. This occurrence is evident for NGC 6388 (Fig. 7.9), but much less clear in NGC 6441 (Fig. 7.10), which is not surprising, as we already noted that the latter has a much less populated and less extended blue HB. The extension of the observed HB beyond the theoretical one is visible in almost all the CMDs of Fig. 7.9, in particular in all the UV CMDs, more appropriate for the study of the hottest stars. Again, this mismatch could be an artificial effect of the transformation from the theoretical to the observational plane and/or to the differential reddening. However, the presence of a possible gap (see discussion in Sec. 7.3), just beyond the location of the hottest stars in the canonical models, suggests that the stars observed beyond the gap could have a different nature: it is tempting to associate them to the Blue Hook stars observed for the first time by D'Cruz et al. [2000] in ω Centauri (NGC 5139), and by Brown et al. [2001] in NGC 2808. Blue Hook stars are very hot (T_{eff} >30000 K) EHB stars that in the UV color magnitude diagram form a hook-like feature that extends up to 0.7 mag below the hot end of the zero-age HB (ZAHB).

Although Brown et al. [2001] and Cassisi et al. [2003] have shown that the observational properties of these objects cannot be understood in the framework of canonical stellar models, I have adopted the same canonical theoretical ZAHB models in order to obtain a rough estimate of their effective temperature and make a comparison : they appear to have a $T_{\rm eff}$ larger than about 25000K.

It is worth noticing that such effective temperature limit appears significantly lower than the estimated minimum effective temperature (Brown et al. [2001] and D'Cruz et al. [2000]) for Blue Hook stars. Present analysis does not allow us to verify if this difference is due to the rather crude approach used for estimating the temperature of these stars, or whether it reflects a real intrinsic difference between Blue Hook stars in metal-intermediate clusters such as NGC2808 or ω Cen and metal-rich ones as NGC 6388 and NGC 6441. Figs. 7.4 and 7.7 put into evidence the first detection of this feature in metal-rich stellar systems.

The Blue-Hook extension is different in the two clusters: in NGC 6388 the sample of Blue Hook star candidates (asterisks in Fig. 7.4 and 7.7) is much larger, and its location in the CMD is quite more defined than in the case of NGC 6441. In NGC 6388, the stars belonging to the blue hook show on average increasing color when moving towards fainter magnitudes, while in NGC 6441, the hottest part of the CMD is more dispersed and, on average, the hottest stars have a similar color as the brighter and cooler stars along the HB sequence. This difference in color could be, at least in part, the consequence of the larger absolute and differential reddening affecting this cluster. Another possibility to explain the significant color spread in the candidate blue hook stars could be related to the properties of the physical mechanism which has been suggested to be at the origin of these peculiar objects, i.e. the so-called delayed He Flash scenario discussed in the following.

As noticed by many authors since Rich et al. [1997], the existence of EHB stars in NGC 6388 and NGC 6441 is quite difficult to be accounted for in the framework of canonical stellar evolution theory, which predicts that the He flash takes place at the tip of the Red Giant Branch. None of these stars would have a hot enough location on the HB able to explain the presence of extended blue tails in any galactic globular clusters, though, as recently shown by Castellani et al. [2006], this problem could be less severe than previously claimed. Castellani & Castellani [1993] have suggested the so-called delayed He flash scenario in order to explain the existence of blue tails. This scenario envisages that, as a consequence of a high mass-loss efficiency during the Red Giant Branch evolution – as due to enhanced stellar wind and/or dynamical interactions within dense cluster cores – a stellar structure can lose such a large amount of envelope mass that it fails to ignite the He flash at the Red Giant Branch tip, being forced to evolve toward the White Dwarfs cooling sequence. Depending on the amount of residual envelope mass, it will be still able to ignite He-burning either at the bright end of the White Dwarfs cooling sequence (the so-called 'early' hot flasher) or along the White Dwarfs sequence (the so-called 'late' hot flasher). After the He flash, the star will settle on its Zero Age Horizontal Branch (ZAHB) location, but due to the low mass of the remaining H-rich envelope, its ZAHB location will be significantly hotter than that of canonical stellar models. The first attempt to find a connection between the scenario outlined by Castellani & Castellani [1993] for early hot flashers stars and the presence of the Blue-Hook was made by D'Cruz et al. [2000], though they found that the ZAHB location of early hot flashers is not hot enough for explaining the empirical evidence.

This scenario has been analyzed also by Sweigart [1997b] and more recently by Brown et al. [2001], who devoted a particular attention to the evolution of late hot flashers: this analysis showed that the convection zone arising by the late He flash - which occurs under conditions of extreme electron degeneracy - is able to penetrate into the H-rich envelope, causing the mixing of H into the hot He-burning regions (He flash induced mixing) where it is burnt quickly. A successive dredge-up process of matter that has been processed via both H- and He-burning would enrich the stellar envelope by helium, carbon and nitrogen. According to the quoted authors, these chemical abundance changes in the stellar surface would cause a discontinuous increase of the effective temperature along the HB at the transition between unmixed (early hot flasher) and mixed (late hot flasher) models, thereby producing a gap at the hot end of the HB as indeed observed by Bedin et al. [2000] in NGC 2808, and which could be tentatively related to the possible gap at $F555W \approx 19.8$ in the HB of NGC 6388. From an observational point of view, further support to this scenario was provided by the spectroscopical measurements made by Moehler et al. [2002] and Moehler et al. [2004] for the Blue-Hook stars belonging to NGC 2808 and ω Cen: the most important finding was the evidence that Blue-Hook stars are both hotter, and more helium-rich than predicted by canonical models of EHB stars. In recent times, the results of Brown et al. [2001] have been fully confirmed on the basis of full self-consistent evolutionary computations performed by Cassisi et al. [2003].

The changes in the surface chemical composition in the late hot flasher structures is really crucial for explaining the fact the Blue-Hook stars appear to be fainter than the 'normal' hot HB stars. Indeed, late hot flasher stars, as the early hot flashers, do have smaller He cores at the He flash with respect to canonical models, but the expected smaller core mass implies a reduction in the bolometric luminosity of only ≈ 0.1 magnitudes. However, it has been nicely shown by Brown et al. [2001] that late hot flashers have significantly different spectra with respect the other stars belonging to the same clusters, but which have not experienced the He flash mixing process. In a normal stellar atmosphere composed mostly by hydrogen, the opacity associated with hydrogen for wavelengths shortward of about 910 $\AA$ redistributes the flux in the extreme ultraviolet to longer wavelengths; if He is enhanced in the stellar atmosphere as in late hot flasher stars, the quoted opacity source is strongly reduced and so much more flux is emitted in the extreme-UV, decreasing the outgoing flux at longer wavelengths. As a consequence, late hot flasher stars should appear fainter in the far and intermediate UV bands (as F255W band is) with respect to early hot flasher and normal HB stars. It is worth noting that, depending on the properties of the He flash induced mixing and on the efficiency of the following dredge up, one can expect no-negligible differences in the surface abundances in the sense that some late hot flasher stars might appear more enriched in Helium and Carbon than others. This occurrence could result in a sizeable spread both in brightness and colors between the late hot flasher stars (as it appears in the case of the Blue Hook candidates in the target clusters).

The empirical data presented for NGC 6388 and NGC 6441, nicely confirm these predictions, and reproduce similar findings in NGC 2808 (Bedin et al. [2000], Brown et al. [2001], Castellani et al. [2006]) and ω Cen (D'Cruz et al. [2000]). What is interesting to note in the case of NGC 6388 (for NGC 6441, the number of stars does not allow a firm conclusion) is that the brightness width of the Blue Hook seems to be larger than in the other quoted clusters. It is not possible to clarify, with the present data, whether this occurrence is a signature of a real intrinsic difference between the blue hook stars belonging to the different clusters, or if it is due to the different photometric bands adopted in the different works (see the discussion on this topic in Brown et al. [2001]), or to photometric errors/contamination by foreground stars, or more simply due to larger differential reddening in NGC 6388. In any case, it is evident that an accurate spectroscopic investigation of the blue-hook stars in – at least – NGC 6388 as already done for NGC 2808 and ω Cen (Moehler et al. [2002]) is mandatory. Moehler and Sweigart [2006] have tried to spectroscopically measure at least the temperature and gravity of the hottest stars in NGC 6388, but they had to conclude that crowding might be a severe obstacle for ground-based spectroscopy in NGC 6388. HB stars are rare in the cluster outskirts, and mixed with bulge objects. A selection of cluster stars (possibly based on proper motions on wide-field images) would be of great help in this kind of investigation.

7.6 The tilted HBs

Another intriguing property of the HB of NGC 6441 and NGC 6388 is the occurrence of the tilt for which a convincing explanation has not yet been found. In the following, I wish to briefly summarize the state-of-art of the investigations on this interesting feature, and provide further evidence which could help in interpreting it.

On a purely empirical ground, Raimondo et al. [2002] have shown that the tilted red HB is a common occurrence among all metal-rich GCs. This feature appears quite more evident in NGC 6388 and NGC 6441 since these clusters are the only ones showing a blue extension of their HB. The most simple explanation for the occurrence of such a feature is to assume that two stellar populations, characterized by distinct metal abundance exist in these clusters. According to this scenario the blue HB stellar sample would be associated with the metal-poor population, while the red clump would be produced by the metal-rich component. However, this possibility has been completely ruled out by both the analysis performed by Raimondo et al. [2002], who showed that in the two clusters there is not a corresponding sizeable number of RGB stars blueward of their RGB, and by the spectroscopic measurements of individual metal abundances of red giant branch stars performed by Carretta (private comunication) and Gratton et al. [2006]. In NGC 6388, Carretta has found an average metallicity of [Fe/H]$=-0.44$, with no evidence of metallicity spread among the 7 red giant branch stars for which high resolution UVES@VLT spectra have been obtained. Again, from high resolution UVES@VLT spectra of 5 NGC 6441 red giants, Gratton et al. [2006] found an average metallicity [Fe/H]$=-0.39$, with no indication of a metallicity spread larger than their measurement errors. On the other hand, it must be mentioned that Clementini et al. [2005] have found that out of 11 RR Lyrae in NGC 6441, 9 objects have a remarkably similar metal content [Fe/H]$= -0.57$, whereas 2 objects have a metallicity [Fe/H]≈ -1.3, though, in this case, the membership of the RR Lyrae is not certain. In view of the results by Gratton and collaborators, a more accurate analysis of the RR Lyrae membership is necessary in order to obtain a firmer result. In any case, also a metallicity as low as [Fe/H]$= -1.3$ could not explain the presence of an EHB in NGC 6441. Moreover Moehler & Sweigart [2006b] by mean of high resolution spectroscopy, rule out the scenario at low metallicity for NGC 6388.

Piotto et al. [1997] suggested also the possibility that in NGC 6441 and NGC 6388 there are two populations with different ages: the oldest population should be responsible for the blue HB, while the younger one creates the red HB. This possibility would indeed explain the bimodal HB, but it would not be able to account for the tilted HB.

An attempt of simultaneously interpreting the occurrence of the blue tail and of the tilt was made by Sweigart & Catelan [1998] by suggesting three different non-canonical scenarios: i) a very high initial He content, ii) a spread in the He core mass as due to stellar rotation, iii) deep mixing along the RGB. Each one of these mechanisms can - in principle - explain the presence of both the blue tail and the tilt. However, as clearly shown by Raimondo et al. [2002] and Moehler and Sweigart [2006] all of them are ruled out by some indisputable empirical evidence. The primordial high He content is excluded by (i) the luminosity of the bump along the Red Giant Branch, which is consistent with theoretical predictions based on a canonical assumption about the initial He content, and (ii) the ratio between the number of Horizontal Branch and Red Giant Branch stars - the so-called R parameter - which are consistent with a canonical He content (Cassisi et al. 2003]).

Fast rotation is a quite unlike possibility because, as shown by Recio-Blanco et al. [2002], in all globular clusters with blue HBs, no stars hotter than $T_{\rm eff} \sim 11,500$K have a rotation velocity $v\ sin\ i > 10$ km/s (while some cooler star can have rotation velocities exceeding 50 km/s). Since these two clusters are quite peculiar though, it is not possible to dismiss definitively the existence of fast rotating stars for NGC 6388 and NGC 6441.

Finally, the deep mixing along the Red Giant Branch, often invoked to explain the metallicity anomalies in RGB stars, has been recently seriously questioned by the identification of the same anomalies among main sequence stars (see Gratton et al. [2004] for a discussion), which points towards a primordial origin of the abundance anomalies.

In the following sections, I will discuss in some detail some additional effects which are surely at work in both clusters, and that contribute to explain, though only in part, the presence of a tilted HB: any attempt to explain the anomalies of the HBs of NGC 6388 and NGC 6441 must take into account also these effects.

7.6.1 Differential Reddening

In the previous sections, I have shown that the use of a reddening correction depending on the stellar effective temperature does not improve the fit of the observations with the models, and it is not able to explain the occurrence of the tilt. This result could be somehow expected, since I have also shown that the two different approaches adopted for determining the interstellar extinction (constant correction, or correction depending on the stellar $T_{\rm eff}$) yield practically indistinguishable results in the optical bands, while the tilt is clearly visible also in the optical color magnitude diagrams. However, this approach assumes an average reddening, while it is well known that both clusters are affected by a sizeable amount of differential reddening (Piotto et al. [1997], Layden et al. [1999], Raimondo et al. [2002]). I have applied the same procedure used by Raimondo et al. [2002] to both clusters in order to estimate the size of this effect. I divided the Planetary Camera field into 16 regions of $9\times$ 9 arcsec^2, and, for each region, the corresponding CMD has been plotted. I selected one of these CMDs as the reference CMD, and extracted its fiducial points by drawing a line by hand. In Figs. 7.11 and 7.12 the CMDs for the various regions in the two clusters are compared with the fiducial line obtained by fitting a spline to the fiducial points of the reference CMD. The average displacement in color of the CMD from the fiducial sequence is also listed.

Fig. 7.12 is similar to the corresponding figure in Raimondo et al. [2002] for NGC 6441, confirming the presence of differential reddening of the order of 0.10-0.12 magnitudes also on scales of the order of 10 arcsec. Fig. 7.11 shows that also NGC 6388 is affected by differential reddening, though the effect is half as large as in NGC 6441. On the other hand, the slope of the tilted HB in the two clusters is quite similar ($dV/d(B-V) \approx 1.5$), suggesting that the differential reddening plays a marginal role in determining the size of the tilt. This evidence is further supported by the fact that the HB of each cell of Figs. 7.11 and 7.12 shows a slope consistent with that observed for the whole sample[3], also in those regions where the narrowness of the

---

[3] In a few cases this is not clearly visible, because of the small number of stars in the selected region

RGB suggests that no strong residual differential reddening is present. In summary, as in Raimondo et al. (2002), the conclusion is that the sloped HB is the consequence of an intrinsic property of the HB stars in NGC 6388 and NGC 6441.

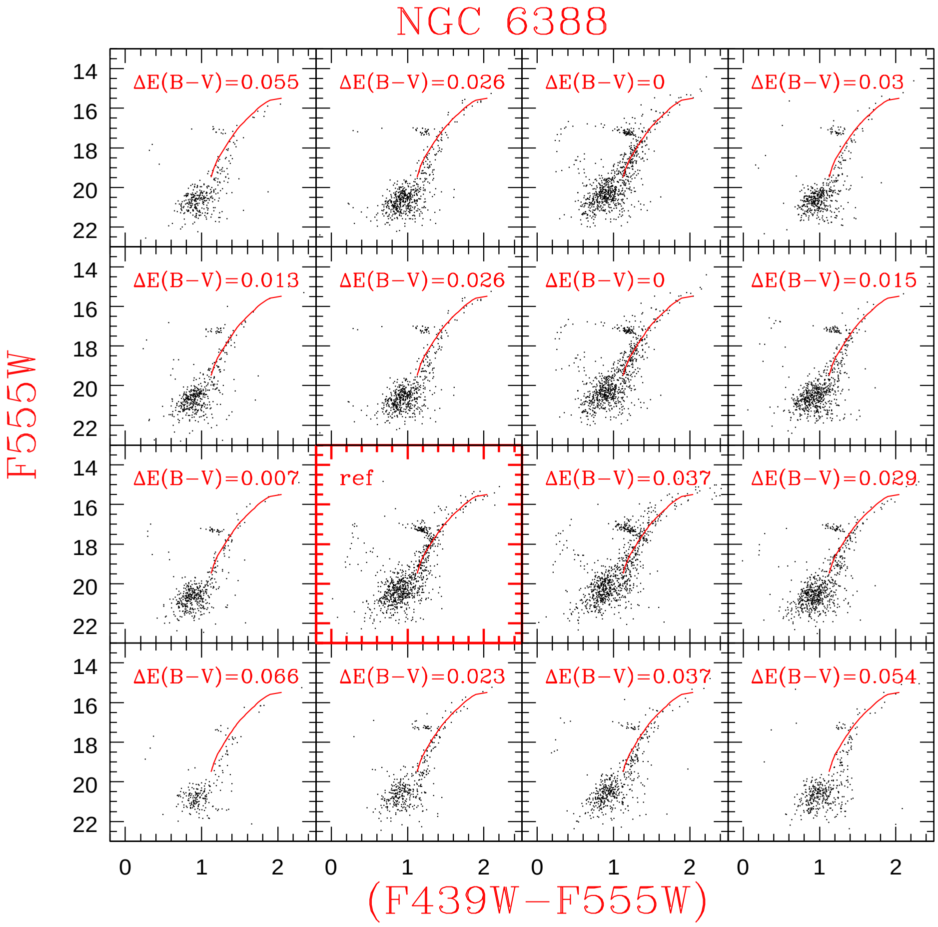

Figure 7.11: The CMDs from the Planetary Camera field divided into 16 cells of 9×9 arcsec^2. These CMDs have been used to estimate the spatial variation of the reddening in the central region of NGC 6388. The CMD of the bold red panel, labeled with *ref*, has been arbitrarily adopted as the reference CMD. The reddening relative to the reference CMD is displayed at the top left of each region.

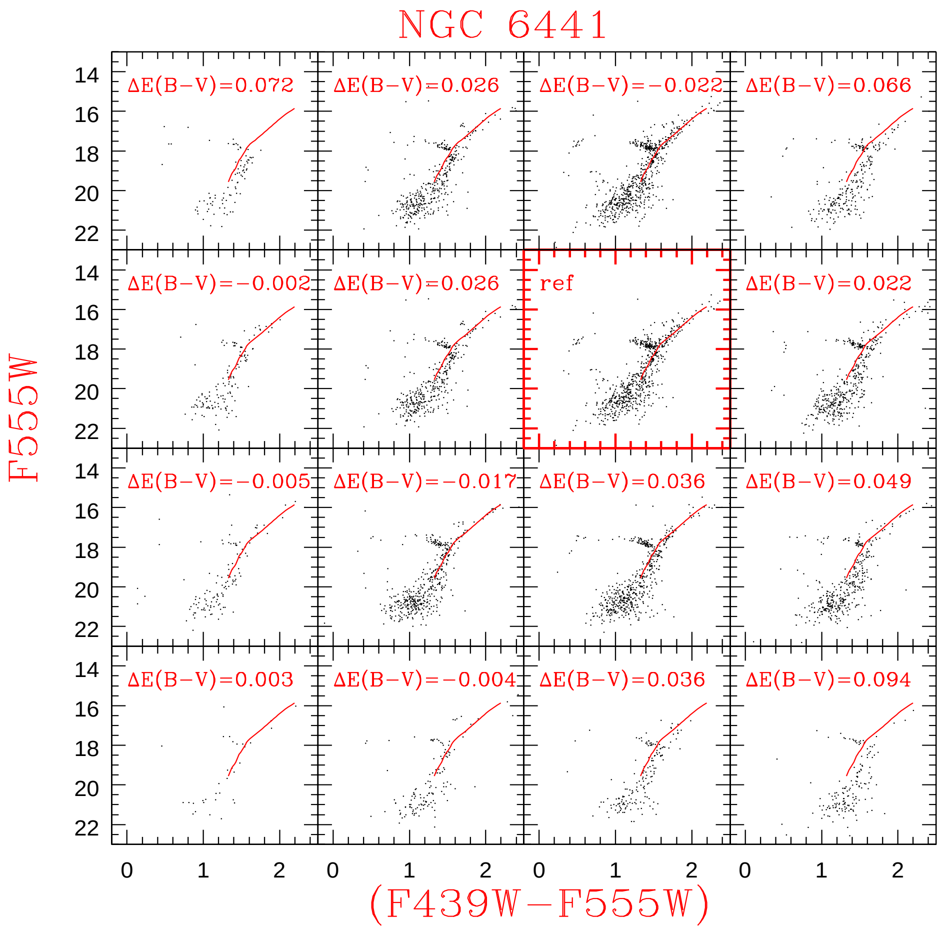

Figure 7.12: As in 7.11, but for NGC 6441.

7.6.2 Radiative levitation

Grundahl et al. [1998] discovered in their study of the Galactic GC M13 (based on Strömgren photometry) the existence of an anomalous discontinuity (jump) in its HB at $T_{\rm eff} \sim 11,500$K. The result on M13 was soon after confirmed and extended to a larger sample of clusters by Grundahl et al. [1999]: all clusters with HB extending beyond $T_{\rm eff} \sim 11,500$K show the presence of Grundahl's jump. More recently Momany et al. [2002], Momany et al. [2004] showed that this jump is also visible in the near-UV broad-band CMDs. Grundahl et al. [1999], on the basis of some empirical findings and theoretical evidence, developed an interpretative framework able to provide an explanation for the occurrence of the HB jump in the Strömgren photometric bands: the high efficiency of radiative levitation for $T_{\rm eff} \geq 11,500$K, by changing the abundances of elements, modifies the element ratio in the stellar atmospheres and, in turn, the spectral distribution of the flux with respect to the normal atmosphere of cooler stars. More in detail, HB stars hotter than 11,500K would appear brighter in the *u* Strömgren band (and *U* Johnson band) than predicted by canonical stellar models computed by neglecting th occurrence of this process. It is worthwhile to note that, due to the lack of adequate model atmosphere computations, Grundahl et al. [1999] supported their proposed theoretical scenario by comparing the observed flux distribution with model atmospheres corresponding to a solar - or larger - metallicity, i.e. assuming that all heavy elements have been enhanced by radiative levitation maintaining the solar element ratios. However, this zero-order approximation appears at odds with both spectroscopic measurements (Behr et al. [1999], Fabbian et al. [2005]) and theoretical expectations (Michaud et al. [1983], Hui-Bon-Hoa et al. [2000]).

Fig. 7.13 shows the (F336W-F555W,F336W) CMDs for NGC 6388 and NGC 6441. The solid lines represent the location of the theoretical ZAHBs. The distance modulus and reddening have been arbitrarily fixed in order to best fit the red portion of the HB. The two arrows show the start and the end temperature of the Grundahl's jump, respectively at 11,500K and 23,000K. There is a correspondence between the Grundahl's jump and the morphology of the HB of NGC 6388 and NGC 6441. However, it is also worth noting that the jump seems to begin at a lower T_{eff} with respect to $T_{\rm eff} \sim 11,500$K that characterizes the 'canonical' Grundahl's jump.

In the following I will address the important question on whether the occurrence of a tilted HB can be a consequence of the metal levitation, and, if so, whether the levitation can account also for the presence of the tilt in the optical bands. The radiative levitation has no significant effects in the optical bands in Grundahl et al. (1999) clusters which show the jump. However, the quite large metallicity of NGC 6388 and NGC 6441 could affect the efficiency of the various physical processes at work in the stellar atmosphere and envelope, such as diffusion, radiative levitation, mass loss (Vink & Cassisi 2002), and therefore create visible effects also in the optical bands.

Due to the strong similarity between the u-jump in intermediate-metallicity clusters and the jump observed in the two clusters NGC 6388 and NGC 6441, some numerical experiments were performed (Castelli, priv. comm.) in order to check whether the occurrence of radiative levitation in the atmosphere of HB stars could help to reconcile - at least partially - the observed HB morphology with theoretical evolutionary predictions.

By using the ATLAS12 code (Kurucz 2005) which computes model atmospheres for individual abundances, some atmospheric models, with solar

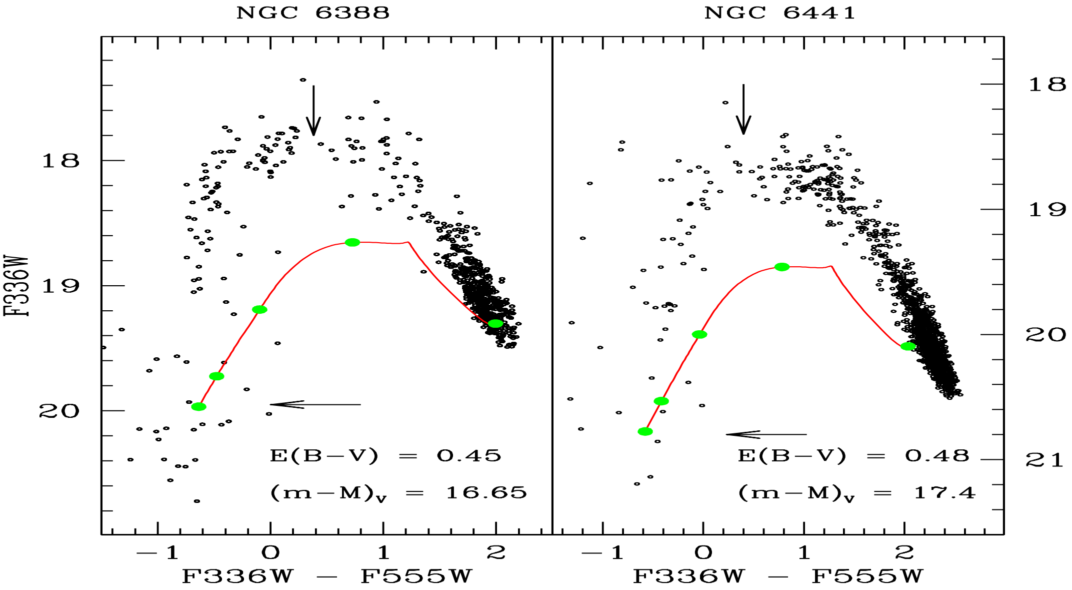

Figure 7.13: Left panel: the (F336W, F336W-F555W) CMD for the HB region of NGC 6388. The solid line shows the location of the same theoretical ZAHBs adopted in previous figures. The adopted values for the distance modulus and reddening are labeled. The two arrows mark the start and the end temperature of the Grundahl jump, respectively 11,500K and 23,000K. Right panel: as left panel but for NGC 6441. The fat dots on the ZAHB mark step of 5000 K.

Photometric filter	Δmag
u Strömgren	-0.08
v Strömgren	-0.05
b Strömgren	-0.05
y Strömgren	-0.04
F336W	-0.07
F439W	-0.05
F555W	-0.04

Table 7.4: The brightness difference predicted by a model atmosphere computed by accounting for the effects of radiative levitation with respect to a canonical model, for different photometric bands.

He/H ratio, [Fe/H]=-0.5 and scaled solar distribution for all the heavy elements, were computed (Castelli, private communication) In addition, model atmospheres were computed by adopting the same physical assumptions but by accounting for an overabundance for those elements which are known to be affected by radiative levitation. Namely, an overabundance of +0.5 relative to solar values for P, Ti, V, Cr, Mn and Fe[4] was assumed. The corresponding energy distributions from 2000 Å to 8000 Å, and the colors in different photometric bands were then computed. Tab. 7.4 gives, for a number of photometric bands, the difference in magnitude between the flux predicted by a canonical ATLAS9 model atmosphere computed with $T_{\rm eff}$ =12000 K, $\log g = 4.5$, microturbulence velocity ξ=2km s^{-1}, [Fe/H]= -0.5, scaled solar distribution for all heavy elements and the flux predicted by the ATLAS12 model computed with the same parameters but different abundances for the above quoted elements.

The results listed in Tab. 7.4 are interesting for several reasons:

- Accounting for the enhancement of the heavy elements which are more affected by the occurrence of radiative levitation makes the stellar models brighter than in the case this effect is neglected. This result confirms, on more solid basis, the scenario suggested by Grundahl et al. (1999).

---

[4] We note that both the theoretical and observational scenario as far as it concerns the efficiency of radiative levitation of the various chemical species are not yet well settled. Some empirical evidence (see for instance Behr et al. 2003) suggests that other additional chemical elements - such as Nickel - could be affected by radiative levitation. In view of this occurrence, this investigation has to be considered as an exploratory analysis on this issue. More accurate and extended grids of model atmospheres and evolutionary models accounting for this non-canonical process are mandatory.

- The effect is of the order of −0.08 magnitudes in the *u* Stromgren band, and of the order of −0.04 magnitudes in the HST F555W band, so it appears significantly lower than predicted by Grundahl et al. (1999). Also optical bands are affected by the levitation, though at a lower extent than UV bands.

These results should be confirmed by a more detailed investigation which is beyond the purposes of the present work.

7.7 A possible solution for the enigma

An interesting scenario, which could help solving the puzzle of the extended and tilted HB of NGC 6388 and NGC 6441, has recently emerged from some quite unexpected results that other authors obtained for the Galactic GC ω Cen. Bedin et al. [2004] showed that the main sequence of ω Cen (see Fig.7.7) is splitted into two sequences, and that this double MS is an ubiquitous feature, spread all over the cluster. Piotto et al. [2005], by using high-resolution spectra, showed that the bluer MS is more metal-rich than the red one, at odds with any expectation based on stellar evolution theory. The only possibility to account for a bluer and more metal rich secondary MS (it contains about 25% of ω Cen MS stars) is to assume (as already suspected by Bedin et al.[2004]) that it corresponds to a highly helium enhanced (Y=0.38) stellar population. Such a population must necessarily be a second generation of stars formed from material polluted by intermediate-mass AGB stars, and/or type II supernovae, and/or massive rotating stars (see discussion in Piotto et al. [2005]. Since He-rich stars have a lower turn-off mass at a given age, they will populate the blue side of the HB during the He-burning phase, and they will also be more luminous because of the higher energy produced by the hydrogen-burning shell. Both effects would produce a bluer and brighter HB, exactly as observed in NGC 6388 and NGC 6441. The HB of ω Cen is too complicated (because of the large spread in metallicity and age) to clearly distinguish the effect of He enhancement in a minor component of its stellar population from the more prominent effects due to age and metal content. Moreover, ω Cen may well be an extreme example in which ejecta by a first generation of massive stars can be kept inside a Galactic GC, because of its mass. Indeed, ω Cen is the most massive GC in our Galaxy, and it might well have been much more massive in the past, as, because of its orbit, it must have lost a huge amount of mass due to tidal shocks (mainly passing through the bulge). Interestingly enough, NGC 6388 and NGC 6441 are among the most massive GCs and, because of their location inside the Galactic bulge, they must have been rather more massive in

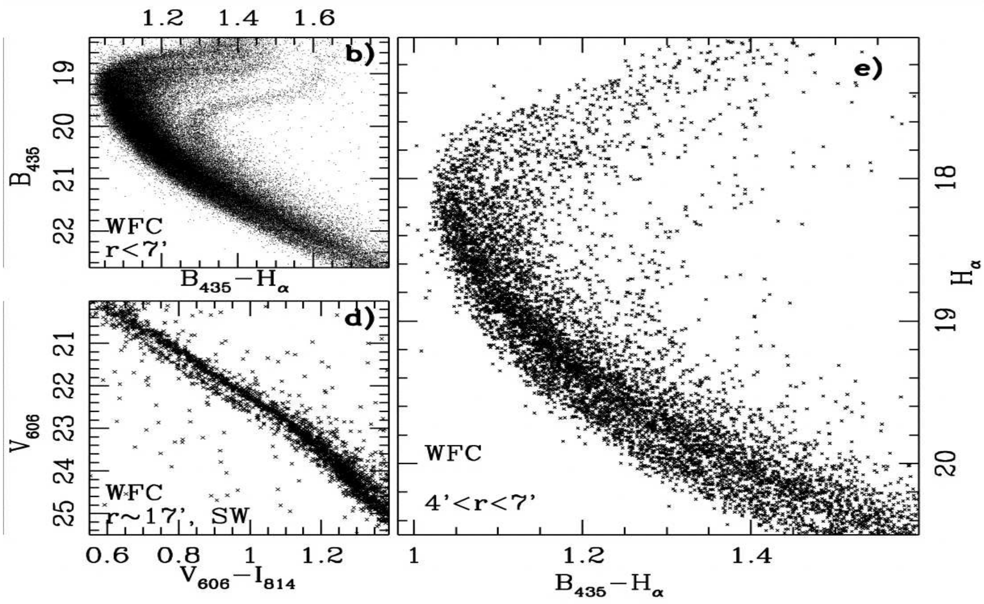

Figure 7.14: From Bedin et al. [2004]: the two Main Sequences are evident in the right and in the bottom left panels; also a double Sub Giants Branch is visible in the top left panel.

the past (Ree et al. [2002]), in order to have managed to survive till now. Indeed, according to Gnedin & Ostriker [1997], both clusters have a disruption time slightly shorter than an Hubble time, which means that what we see at the present time might be two remnants of much bigger stellar systems.

It is therefore rather tempting to associate their anomalously blue, and anomalously tilted HB to a second generation of stars, strongly He-enriched by pollution from massive stars of the first star formation burst. This scenario has been suggested also by Moehler & Sweigart [2006] and is completely different from the already discarded suggestion by Sweigart and Catelan [1998], i.e. that the HB morphology of NGC 6388 and NGC 6441 is due to a whole cluster of He enriched stars. Sweigart and Catelan [1998] suggested that “all” of the stars in these two clusters are He-rich. Here the hypothesis is that a minority of the stellar population of NGC 6388 and NGC 6441 is He-enriched. Indeed, in Sec.7.3 I showed that only 11% of the HB stars of NGC 6441 and only 17% of the HB stars in NGC 6388 populate the anomalous blue HB. From evolutionary computations (see below), it was verified that very hot (i.e. $T_{\rm eff} > 20,000$ K) HB stellar structures with a He-enhanced chemical composition have a longer lifetime for the core He-burning phase with respect to stellar structures characterized by a “normal” initial He abundance at the same $T_{\rm eff}$ in the ZAHB. Such an occurrence is due to the smaller He-core mass and, in turn, lower surface luminosity which characterizes these He-enhanced, Hot-HB structures, that do not have a hidrogenum shell burning. At $T_{\rm eff} \approx 23,000$ K, He-enhanced HB stars with Y=0.40 have core He-burning lifetime about 15% longer with respect to structures with Y=0.256. In addition, one has to bear in mind that, regardless of their initial He content, hot HB stars have evolutionary lifetimes longer than HB structures populating the red portion of the HB. The difference is - on average - of the order of 20% (see Castellani et al.[1993]). When accounting for these evolutionary effects, it turns out that, in the hypothesis that all the blue HB stars belong to the He-enhanced stellar population, such a He-rich stellar component has to contribute to $\approx 8\%$ and $\approx 13\%$ to the total stellar population in NGC 6441 and NGC 6388, respectively.

In order to verify the possibility that the peculiar HB morphology could be explained by accounting for the presence in the target clusters of a He-rich stellar population, additional sets of low-mass, He-burning models for suitable choices of the initial He content were calculated (Cassisi, priv. comm.). More in detail, the HB models were calculated for a metallicity Z=0.008 and initial He contents equal to Y=0.30 and 0.40. The mass of the RGB progenitors ($\sim 0.7 M_{\odot}$) has been selected in order to fulfill the condition that their age at the RGB tip is equal to about 13Gyr. It is worth noticing that these models are fully consistent with the other ones computed by adopting Y=0.256, as far as both the physical input and numerical assumptions are concerned. The stellar models have been transferred from the theoretical plane to the various observational ones by using the same set of color-$T_{\rm eff}$ relations adopted for the Y=0.256 models.

In Figs. 7.15 and 7.16, I show a comparison between the observed CMDs and the theoretical models computed for the various He contents, adopting the same reddenings and distance moduli as in Sec.7.4.2. These reddenings and distance moduli have been fixed by imposing that the canonical models overlap the red clump of the HB in the optical bands. As already discussed in Sec.7.4.2, the canonical models are not able to reproduce the blue HB. On the contrary, one can easily see that the ZAHB models corresponding to Y=0.40 are in good agreement with the observed distribution of blue HB stars of NGC 6388 in all of the CMDs (Fig.7.15). This agree with the results of Moehler & Sweigart [2006] who estimate Y≈0.32 at about 10000 K from spectroscopic analysis. The same kind of comparison, but for the case of NGC 6441 is performed in Fig. 7.16. In this case, it is evident that the Y=0.40 ZAHB is slightly brighter than the observed distribution of blue HB stars. By the comparison between empirical data and the ZAHBs computed for various initial He contents, it appears that it is possible to reproduce the brightness of the blue HB star population by assuming for it a He content of the order of $Y \approx 0.35$, slightly smaller than in NGC 6388. This fact is consistent with the observational evidence that the blue HB is less extended in NGC 6441 than in NGC 6388.

The presence of two distinct stellar populations characterized by two different initial He contents, can help in explaining the brightness difference between the red portion of the HB and the blue component. However, in order to explain the tilted morphology of the whole HB sequence one should also account for the presence of a spread in the He content at the level of about $\Delta Y \approx 0.05 \div 0.06$ (see also Moehler & Sweigart 2006). Furthermore the presence of a moderate spread ($\Delta Y \approx 0.02 - 0.03$) in the He abundance around the canonical value ($Y \sim 0.26$) among the red clump stars, by affecting their intrinsic luminosity, could help to explain the peculiar tilted distribution of the red HB clump.

The previous analysis has shown that it would be possible to explain the different observational peculiarities of the HBs in NGC 6388 and NGC 6441 by accounting for the presence in both clusters of distinct stellar populations characterized by two different - with some amount of spread - initial He contents. At the beginning of this section, I noticed that the most clear, empirical support to the existence in a globular cluster of multiple stellar populations with different He content is the splitting of the Main Sequence observed in the cluster ω Cen. Therefore, one could argue if the same circumstantial evidence could be observed in the two target clusters, but this cannot be easily achieved for the following reasons: 1) the two clusters are affected by a sizeable amount of differential reddening, 2) the full interpretation of the HB morphology would require the presence of some amount of spread in the initial He content between the different stellar populations. Both processes affects the CMD location of main Sequence stars with the global effect of hampering the possibility to detect any splitting of the Main Sequence locus.

7.8 The integrated spectra

NGC 6388 and NGC 6441 has been observed not only from the photometric point of view, but also by means of spectroscopy. Rich et al. [1993] obtained IUE spectra founding that both clusters show an UV excess, weak for NGC 6388 and mild for NGC 6441. Schiavon et al. [2005] observed the two clusters in the range 3350-6430 Å with the Blanco Telescope at Cerro Tololo during a survey of spectra of Galactic globular clusters. Having the photometry, I constructed therefore the integrated spectrum for both clus-

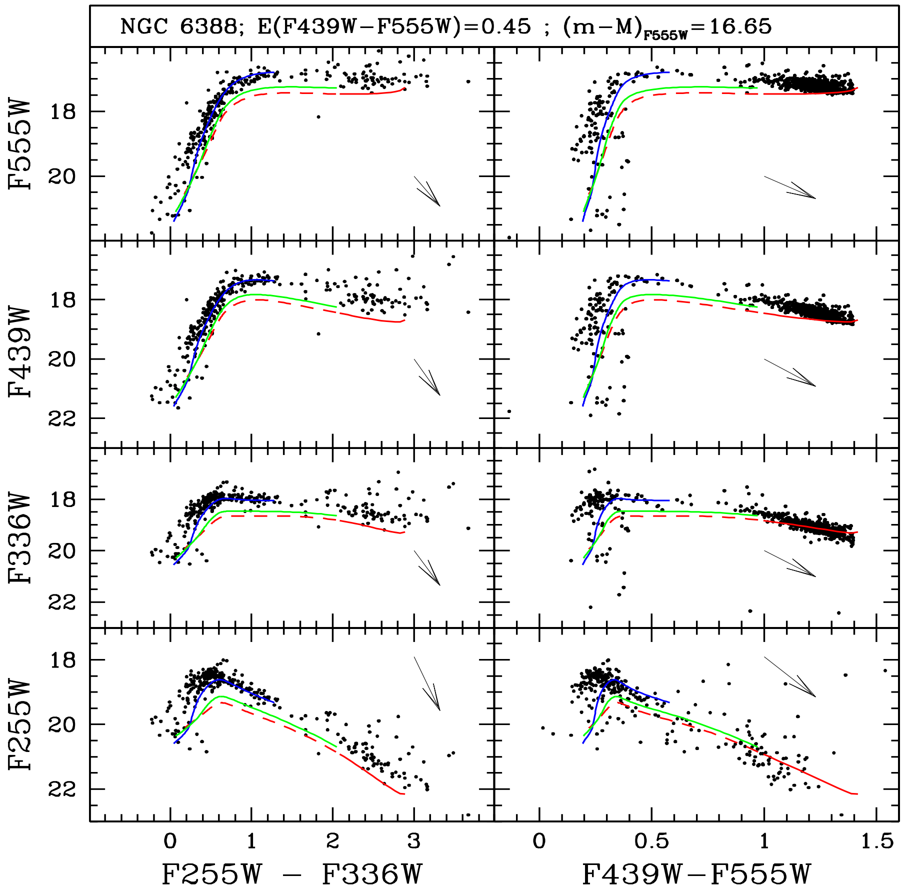

Figure 7.15: The CMDs of the HB region in the different photometric planes are compared with the theoretical models for a canonical Y=0.256 (dashed black line), for Y=0.30 (dotted green line), and for Y=0.40 (continuous blue line). Only models with strong He enhancement can reproduce the blue part of the HB. The arrows represent the reddening vector in the different photometric planes.

ters to check if the procedure I adopted for the bulge is valid. The Pickles library provides spectra at solar metallicity, a value too high also for clusters as metal-rich as NGC 6388 and NGC 6441, and some metal-poor and metal-rich spectra, but the coverage in temperature and luminosity class for these stars is not large, such that the objects with the proper metallicity do not cover all the color magnitude diagram. As shown in Sec. 6.2.1, the Pickles and the BaSeL libraries agree quite well. Thus, to construct the spectra for the globular clusters I used the BaSeL spectra, selected for the metallicity

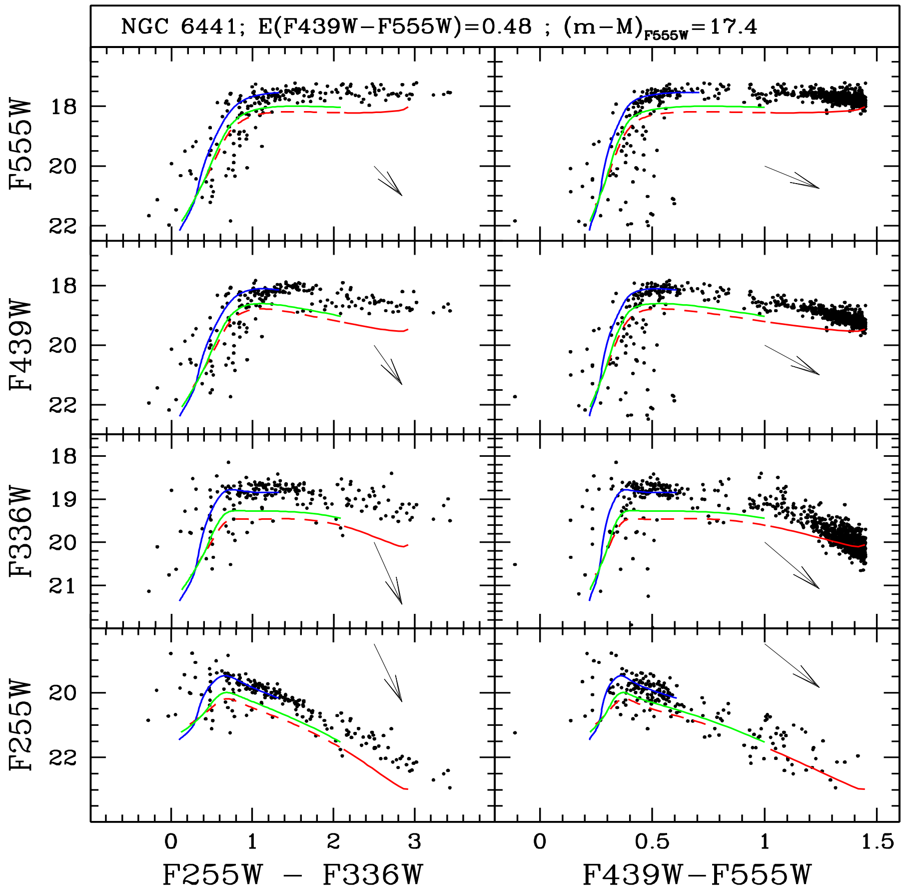

Figure 7.16: As in Fig.7.15 but for NGC 6441

appropriate for the clusters. Since obviously there are no models with the exact metallicity of the clusters I chose the two closest values. NGC 6388 has [Fe/H]=-0.60 and NGC 6441 has [Fe/H]=-0.53.I therefore selected the spectra models at $[M/H]=-1.0$ and -0.5. I run the procedure exactly as I did in the case of the bulge integrated spectrum (see Sec. 6.2): I plotted on the CMD the grid of temperature and surface gravity of the BaSeL models (see an example for NGC 6388 in Fig. 7.17), and I chose the boxes on the basis of the grid. I calculated the mean magnitude of the stars inside each box and the weight associated to each box, and I summed the spectra taking into account the weigths given by the CMD. Also in this case I considered only sdB and HB stars and not post-HB and post-AGB stars.

I compared the obtained integrated spectra with those provided by Schiavon et al. [2003] in the optical, (see Fig. 7.18) and with those observed by

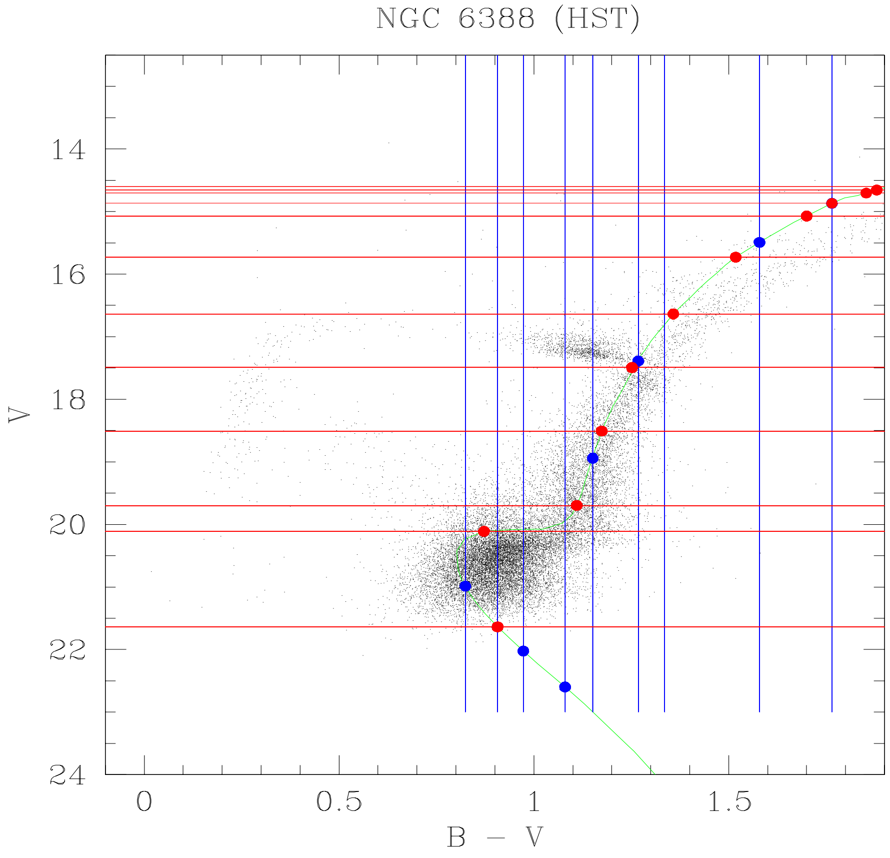

Figure 7.17: Overplot of the grid in temperature and surface gravity of the BaSeL models on the color magnitude diagram of NGC 6388.

Rich. et al. [1993] in the UV (see Fig. 7.19). Schiavon spectra were not corrected by reddening. Thus I applied to the spectra the reddening law of Savage & Mathis [1979] to correct this effect (see also sec.5.3). To match the observations and the integrated spectra I had to apply a value of E(B-V)=0.30 for NGC 6388 and 0.40 for NGC 6441, much smaller than the value (0.45 and 0.48 respectively) I used on the photometry. This could be caused by the fact that Savage & Mathis law is not very accurate or, since these two clusters belong to the bulge, it could be another hint that the reddening law toward the Galactic bulge is different from the local one (Udalski et al. 2003). Once corrected for reddening, the agreement between observed and integrated spectrum seems to be good.

Fig. 7.19 shows the comparison in the UV range between observed and integrated spectrum and the spectrum of a single stellar population at [M/H]=-0.1 as well. While in the "redder" part the spectra agree, in the bluer there is discrepancy between observations and both integrated spectrum and single stellar population spectrum. The observations show a small increase of the flux similar to the UV excess observed in the ellipticals.

In general the procedure to construct the integrated spectrum following the method of Santhos et al. [1995] works quite well. Both in the bulge and in the clusters though the integrated spectrum shows no or only a little UV excess, in disagreement with the IUE observations for the globular clusters. Since in both cases I did not include post-HB and post-AGB stars, this could suggest a more important role of these stars in the UV excess.

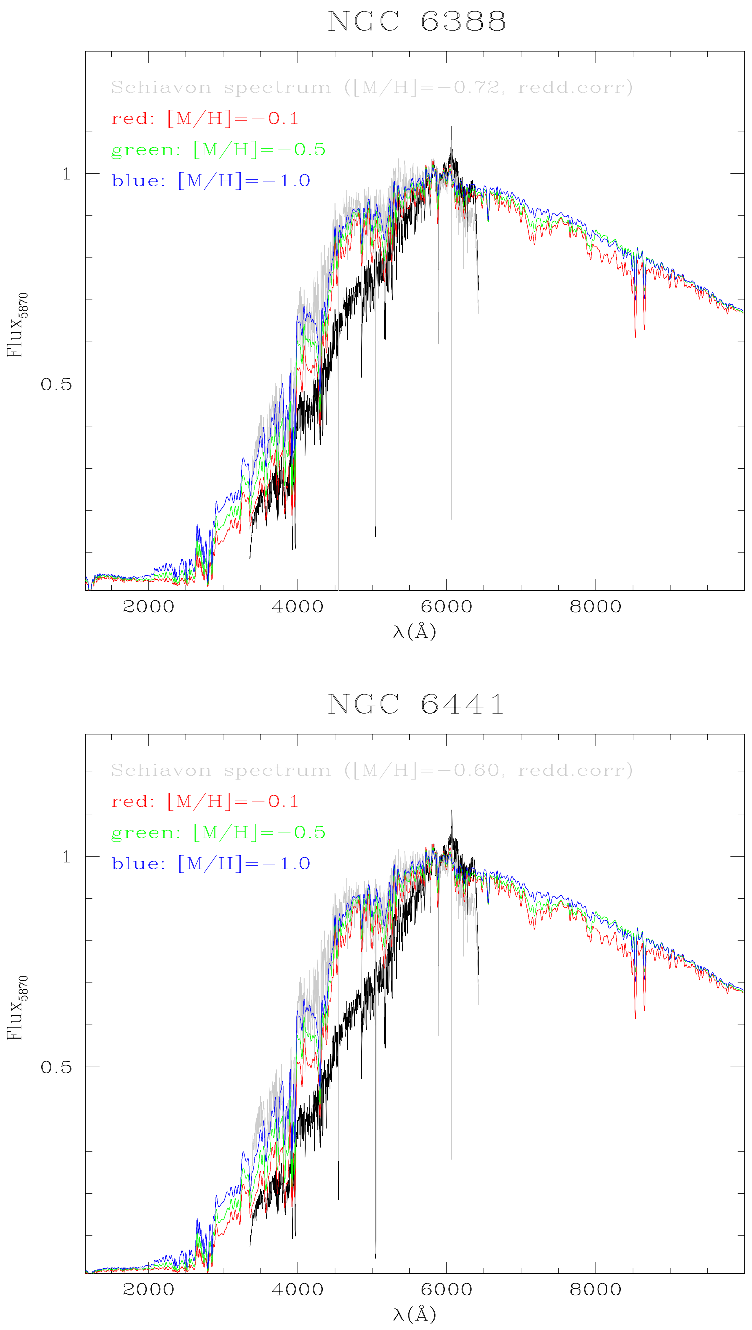

Figure 7.18: Integrated spectra of the Galactic globular clusters NGC 6388 (top panel) and NGC 6441 (bottom panel) in the optical wavelength range. The spectrum observed by Schiavon et al. [2003] is plotted in black, while the reddening corrected is plotted in grey. The constructed integrated spectra of the two cluster are plotted in red, green and blue with metallicity as labeled.

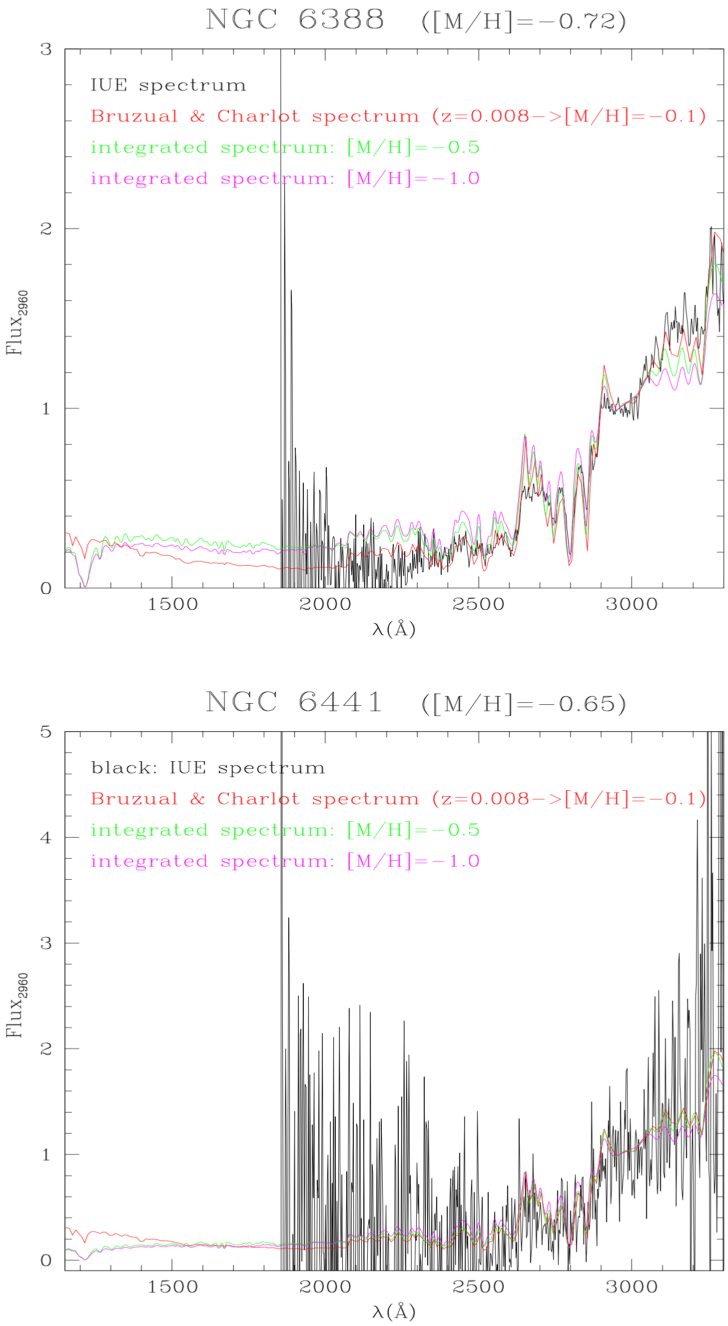

Figure 7.19: Integrated spectra of the Galactic globular clusters NGC 6388 (top panel) and NGC 6441 (bottom panel) in the UV range. The spectrum observed by Rich et al. [1993] is plotted in black. The constructed integrated spectra of the two cluster are plotted in green and magenta with metallicity as labeled. The spectrum of a single stellar population (Bruzual & Charlot [2003]) with metallicity z=0.008 is also plotted.

Chapter 8

Summary and conclusions

The aim of this thesis was to verify the role of Extreme Horizontal Branch stars in the UV excess observed in elliptical galaxies and bulges of spiral galaxies using the bulge of our Galaxy as a nearby study case.

Recent photometric observations (Zoccali et al. [2003]) of a bulge field in Baade's Window drew attention to possible subdwarf B (sdB) star candidates in this region, but spectroscopic observations were required to verify their evolutionary status. Follow-up spectroscopic data were obtained with FORS2 at the VLT. The comparison of these spectra with model spectra allowed me to obtain the physical parameters of these stars, i.e. temperatures, surface gravities, and helium abundances. This way I verified that most of the candidates are indeed hot stars, with high gravities and, except in one case, low helium abundances. The comparison of these parameters with evolutionary tracks (zero-age horizontal branch and terminal-age horizontal branch tracks for bulge metallicity) confirmed their evolutionary status as Extreme Horizontal Branch stars. The analysis of the radial velocities and the distances was used to verify their membership: while most of them belong to the bulge, some are instead disk members. In total, I found that about 55% of the candidates are indeed EHB stars in the Galactic bulge.

With the aim of looking for sdB candidates in other bulge fields and thereby checking that the examined field was not peculiar, I reduced photometric data retrieved from the ESO Imaging Survey (EIS) archive. Indeed I found sdB candidates also in these bulge fields, but in much smaller numbers compared to the sample found from Zoccali et al. [2003]. This effect is probably due to the fact that these fields are located at higher galactic latitudes, thus sampling a smaller volume of the bulge.

Also EIS photometric data for two disk fields were analyzed, in order to statistically subtract the disk component from the color magnitude diagram of the bulge. Both disk fields and the Zoccali et al. (2003) bulge field contain a globular cluster. The correction for the globular cluster population was performed considering only the stars in a region outside the tidal radius of the cluster. The subtraction of the disk instead was much more difficult than originally thought: to do the statistical subtraction, it is necessary to normalize the number of the stars in the disk field and in the bulge field (since they are located at different galactic coordinates and therefore sampling different disk regions) by comparing the number of stars on the bright blue main sequence, which is typical of the disk population and is not present in the bulge. It was not possible to use this approach since the blue main sequence shows different slopes in different fields, even after the reddening correction. This problem could be related to anomalous interstellar extinction toward the Galactic center. Unfortunately the degree of this anomaly varies quite considerably from one line of sight to another (Udalski, priv.comm. and Udalski et al.[2003]) and is not yet very well known. The statistical subtraction was therefore performed adopting a synthetic color magnitude diagram of the disk created by S. Ragaini (priv. comm., PhD.Thesis) at the University of Padova, using the Padova Galaxy Model (Bertelli et al. [1995]). The subtraction was effective, even though some spurious stars remained.

Adopting the method of Santos et al. [1995], I constructed the integrated spectrum, associating to stars in the color-magnitude diagram an appropriate library spectrum. I did not consider the spurious stars remaining after the disk correction and I did not include stars located in the bright blue region of the color-magnitude diagram, where post-HB and post-AGB stars should be located, because it is not possible to distinguish them from remaining disk main sequence stars. In addition the scenarios for the explanation of the UV excess observed in elliptical galaxies predict that the main contribution comes from the EHB stars.

I carried out the procedure using both observed (Pickles [1998]) and synthetic (Lejeune et al. [1997]) spectral libraries, achieving very similar results. The bulge integrated spectra obtained this way agree very well with the spectral energy distribution (SED) for a simple stellar population (SSP) of 11 Gyr as calculated by Bruzual & Charlot [2003]. The best agreement is for a SSP with metallicity Z=0.008. In the UV part of the spectrum, however, the integrated spectra differ from the SSP one, since the SSP model predicts more UV flux than calculated from the observed color-magnitude diagrams. This difference is probably due to the inclusion of post-HB and post-AGB stars in the SSP, which were omitted from the integrated spectra.

However, the EHB stars I found are not the only ones detected in the bulge, since they are evident also in the color-magnitude diagram of two Galactic globular clusters, NGC 6388 and NGC 6441. Despite their high metallicities both clusters show extended blue horizontal branches. The spectra of both clusters have been observed in the optical range by Schiavon et al. [2005] and also in the UV from Rich et al. [1993]. To check the procedure described above I constructed the integrated spectra for both clusters and I compared them with the observed spectra and also with an SED of a simple stellar population: in the optical range there is a fair agreement, while in the UV neither the integrated spectrum nor the SED manage to reproduce the observed spectrum. Both clusters are, however, quite peculiar, having unexpected EHB star populations, tilted horizontal branches and unusual populations of variables. All these facts could be explained with the presence of more than one population with different He abundance, implying the occurrence of at least two star formation episodes in both clusters.

In conclusion, the bulge of our Galaxy probably shows only a weak UV excess. This claim is neither in contradiction with nearby observations, as in M31, a spiral galaxy very similar to the Milky Way, but more massive, showing instead a stronger UV excess, nor with observations of more distant galaxies. In fact the UV excess can vary considerably from object to object and shows no dependence on physical parameters like metallicity and velocity dispersion, as explained by Rich et al. [2005].

Future developments of this work are the reduction and analysis of new WFI data in the U band, which have become available only now. Hopefully these new observations will be very helpful for several reasons:

- it will be possible to construct two color diagrams, which will allow a better reddening correction;
- the U band is certainly more suited than V and I bands to observe hot stars and it will permit a better sdB selection in the color-magnitude diagram;
- the difference of epoch between old and new observations is about 6 years so it will be possible to calculate the proper motions of the stars and therefore to distinguish better between the bulge and the disk populations;
- once the correction for the disk population has been improved, the inclusion in the integrated spectrum of any remaining post-HB and post-AGB could verify their importance in the UV part of the spectrum.

Moreover it is interesting to note that in both NGC 6388 and NGC 6441, the horizontal branch reaches very high temperatures, where it is possible to detect Blue Hook stars, while in the bulge fields these extremely hot stars are not seen. Deeper observations would be helpful to check if also the bulge contains these peculiar stars.

Bibliography

Allard, F. & Hauschildt, P. H. 1995, ApJ, 445, 433

Altmann, M., Edelmann, H., & de Boer, K. S. 2004, A&A, 414, 181

Appenzeller, I., Fricke, K., Furtig, W., et al. 1998, The Messenger, 94, 1

Ažusienis, A. & Straižys, V. 1969, Soviet Astronomy, 13, 316

Baugh, C. M., Cole, S., & Frenk, C. S. 1996, MNRAS, 283, 1361

Bedin, L. R., Piotto, G., Anderson, J., et al. 2004, ApJ, 605, L125

Bedin, L. R., Piotto, G., Zoccali, M., et al. 2000, A&A, 363, 159

Behr, B. B., Cohen, J. G., McCarthy, J. K., & Djorgovski, S. G. 1999, ApJ, 517, L135

Bergeron, P., Saffer, R. A., & Liebert, J. 1992, ApJ, 394, 228

Bertelli, G., Bressan, A., Chiosi, C., Ng, Y. K., & Ortolani, S. 1995, A&A, 301, 381

Bertelli, G., Nasi, E., Girardi, L., et al. 2003, AJ, 125, 770

Bertola, F., Capaccioli, M., Holm, A. V., & Oke, J. B. 1980, ApJ, 237, L65

Bessell, M. S. 1979, PASP, 91, 589

Bessell, M. S. & Brett, J. M. 1988, PASP, 100, 1134

Bessell, M. S., Castelli, F., & Plez, B. 1998, A&A, 333, 231

Blum, R. D., Carr, J. S., Sellgren, K., & Terndrup, D. M. 1995, ApJ, 449, 623

Brown, T. M., Ferguson, H. C., Davidsen, A. F., & Dorman, B. 1997, ApJ, 482, 685

Brown, T. M., Ferguson, H. C., Smith, E., et al. 2003, ApJ, 584, L69

Brown, T. M., Sweigart, A. V., Lanz, T., Landsman, W. B., & Hubeny, I. 2001, ApJ, 562, 368

Bruzual, G. & Charlot, S. 2003, MNRAS, 344, 1000

Burstein, D., Bertola, F., Buson, L. M., Faber, S. M., & Lauer, T. R. 1988, ApJ, 328, 440

Buser, R. 1978, A&A, 62, 425

Cassisi, S., Schlattl, H., Salaris, M., & Weiss, A. 2003, ApJ, 582, L43

Castellani, M. & Castellani, V. 1993, ApJ, 407, 649

Castellani, M., Castellani, V., & Prada Moroni, P. G. 2006, A&A, 457, 569

Catelan, M. 2004, in ASP Conf. Ser. 310: IAU Colloq. 193: Variable Stars in the Local Group, ed. D. W. Kurtz & K. R. Pollard, 113–+

Clementini, G., Gratton, R. G., Bragaglia, A., et al. 2005, ApJ, 630, L145

Code, A. D. 1969, PASP, 81, 475

Craig, N., Abbott, M., Finley, D., et al. 1997, ApJS, 113, 131

D'Cruz, N. L., Dorman, B., Rood, R. T., & O'Connell, R. W. 1996, ApJ, 466, 359

D'Cruz, N. L., O'Connell, R. W., Rood, R. T., et al. 2000, ApJ, 530, 352

Deharveng, J. M., Joubert, M., Donas, J., & Monnet, G. 1982, A&A, 106, 16

Dolphin, A. E. 2000, PASP, 112, 1397

Dorman, B., O'Connell, R. W., & Rood, R. T. 1995, ApJ, 442, 105

Dwek, E., Arendt, R. G., Hauser, M. G., et al. 1995, ApJ, 445, 716

Eggen, O. J., Lynden-Bell, D., & Sandage, A. R. 1962, ApJ, 136, 748

Fabbian, D., Recio-Blanco, A., Gratton, R. G., & Piotto, G. 2005, A&A, 434, 235

Ferguson, H. C., Davidsen, A. F., Kriss, G. A., et al. 1991, ApJ, 382, L69

Fitzgerald, M. P. 1970, A&A, 4, 234

Fluks, M. A., Plez, B., The, P. S., et al. 1994, A&AS, 105, 311

Fulbright, J. P., McWilliam, A., & Rich, R. M. 2006, ApJ, 636, 821

Gnedin, O. Y. & Ostriker, J. P. 1997, ApJ, 474, 223

González Delgado, R. M. & Leitherer, C. 1999, ApJS, 125, 479

Gratton, R., Sneden, C., & Carretta, E. 2004, ARA&A, 42, 385

Gratton, R. G., Lucatello, S., Bragaglia, A., et al. 2006, A&A, 455, 271

Gray, R. O. & Corbally, C. J. 1994, AJ, 107, 742

Greggio, L. & Renzini, A. 1990, ApJ, 364, 35

Grundahl, F., Catelan, M., Landsman, W. B., Stetson, P. B., & Andersen, M. I. 1999, ApJ, 524, 242

Grundahl, F., Vandenberg, D. A., & Andersen, M. I. 1998, ApJ, 500, L179+

Gummersbach, C. 1998, PhD thesis, PhD Thesis, Landessternwarte Heidelberg/Königstuhl (1998).

Gunn, J. E. & Stryker, L. L. 1983, ApJS, 52, 121

Hamuy, M., Walker, A. R., Suntzeff, N. B., et al. 1995, VizieR Online Data Catalog, 2179, 0

Han, Z., Podsiadlowski, P., Maxted, P. F. L., & Marsh, T. R. 2003, MNRAS, 341, 669

Harris, W. E. 1996, AJ, 112, 1487

Heber, U. 1986, A&A, 155, 33

Heber, U., Moehler, S., Napiwotzki, R., Thejll, P., & Green, E. M. 2002, A&A, 383, 938

Hills, J. G. 1971, A&A, 12, 1

Holtzman, J. A., Burrows, C. J., Casertano, S., et al. 1995, PASP, 107, 1065

Horne, K. 1986, PASP, 98, 609

Hui-Bon-Hoa, A., LeBlanc, F., & Hauschildt, P. H. 2000, ApJ, 535, L43

Ibata, R. A. & Gilmore, G. F. 1995, MNRAS, 275, 605

Kauffmann, G. 1996, MNRAS, 281, 487

King, I. R., Deharveng, J. M., Albrecht, R., et al. 1992, ApJ, 397, L35

Kurucz, R. L. 1993, VizieR Online Data Catalog, 6039, 0

Landolt, A. U. 1992, AJ, 104, 340

Larsen, J. A. & Humphreys, R. M. 2003, AJ, 125, 1958

Lauer, T. R., Faber, S. M., Ajhar, E. A., Grillmair, C. J., & Scowen, P. A. 1998, AJ, 116, 2263

Le Borgne, J.-F., Bruzual, G., Pelló, R., et al. 2003, A&A, 402, 433

Leitherer, C., Kinney, E., Baum, S., & Clampin, M. ????

Lejeune, T., Cuisinier, F., & Buser, R. 1997, A&AS, 125, 229

Lejeune, T., Cuisinier, F., & Buser, R. 1998, A&AS, 130, 65

Lewis, J. R. & Freeman, K. C. 1989, AJ, 97, 139

Lisker, T., Heber, U., Napiwotzki, R., et al. 2004, Ap&SS, 291, 351

López-Corredoira, M., Cabrera-Lavers, A., & Gerhard, O. E. 2005, A&A, 439, 107

López-Corredoira, M., Cabrera-Lavers, A., Gerhard, O. E., & Garzón, F. 2004, A&A, 421, 953

López-Corredoira, M., Hammersley, P. L., Garzón, F., et al. 2001, A&A, 373, 139

López-Corredoira, M., Hammersley, P. L., Garzón, F., Simonneau, E., & Mahoney, T. J. 2000, MNRAS, 313, 392

Maoz, D., Filippenko, A. V., Ho, L. C., et al. 1996, ApJS, 107, 215

McWilliam, A. & Rich, R. M. 1994, ApJS, 91, 749

Meyer, M. R., Edwards, S., Hinkle, K. H., & Strom, S. E. 1998, ApJ, 508, 397

Michaud, G., Vauclair, G., & Vauclair, S. 1983, ApJ, 267, 256

Minniti, D. 1996, ApJ, 459, 579

Moehler, S. 2001, PASP, 113, 1162

Moehler, S. & Sweigart, A. V. 2006a, A&A, 455, 943

Moehler, S. & Sweigart, A. V. 2006b, Baltic Astronomy, 15, 41

Moehler, S., Sweigart, A. V., Landsman, W. B., & Dreizler, S. 2002, A&A, 395, 37

Moehler, S., Sweigart, A. V., Landsman, W. B., Hammer, N. J., & Dreizler, S. 2004, A&A, 415, 313

Momany, Y., Bedin, L. R., Cassisi, S., et al. 2004, A&A, 420, 605

Momany, Y., Piotto, G., Recio-Blanco, A., et al. 2002, ApJ, 576, L65

Montes, D., Ramsey, L. W., & Welty, A. D. 1999, ApJS, 123, 283

Murphy, T. & Meiksin, A. 2004, MNRAS, 351, 1430

Napiwotzki, R. 1997, A&A, 322, 256

Napiwotzki, R., Green, P. J., & Saffer, R. A. 1999, ApJ, 517, 399

Norris, J. 1986, ApJS, 61, 667

O'Connell, R. W. 1999, ARA&A, 37, 603

O'Connell, R. W., Thuan, T. X., & Puschell, J. J. 1986, ApJ, 303, L37

Ojha, D. K. 2001, MNRAS, 322, 426

Oke, J. B. 1990, AJ, 99, 1621

Oke, J. B., Bertola, F., & Capaccioli, M. 1981, ApJ, 243, 453

Origlia, L. & Leitherer, C. 2000, AJ, 119, 2018

Ortolani, S., Renzini, A., Gilmozzi, R., et al. 1995, Nature, 377, 701

Paczynski, B. 1986a, ApJ, 301, 503

Paczynski, B. 1986b, ApJ, 304, 1

Peterson, R. C., Terndrup, D. M., Sadler, E. M., & Walker, A. R. 2001, ApJ, 547, 240

Pickles, A. J. 1998, PASP, 110, 863

Pietrinferni, A., Cassisi, S., Salaris, M., & Castelli, F. 2006, ApJ, 642, 797

Piotto, G., King, I. R., Djorgovski, S. G., et al. 2002, A&A, 391, 945

Piotto, G., Sosin, C., Djorgovski, S., et al. 1997, The Combination of Theory, Observations, and Simulation for the Dynamics of Stars and Star Clusters in the Galaxy, 23rd meeting of the IAU, Joint Discussion 15, 25 August 1997, Kyoto, Japan, meeting abstract., 15

Piotto, G., Villanova, S., Bedin, L. R., et al. 2005, ApJ, 621, 777

Pych, W. 2004, PASP, 116, 148

Raimondo, G., Castellani, V., Cassisi, S., Brocato, E., & Piotto, G. 2002, ApJ, 569, 975

Recio-Blanco, A., Piotto, G., Aparicio, A., & Renzini, A. 2002, ApJ, 572, L71

Ree, C. H., Yoon, S.-J., Rey, S.-C., & Lee, Y.-W. 2002, in ASP Conf. Ser. 265: Omega Centauri, A Unique Window into Astrophysics, ed. F. van Leeuwen, J. D. Hughes, & G. Piotto, 101–+

Renzini, A. 1991, in NATO ASIC Proc. 348: Observational Tests of Cosmological Inflation, ed. T. Shanks, A. J. Banday, & R. S. Ellis, 131–+

Rich, R. M. 1988, AJ, 95, 828

Rich, R. M., Minniti, D., & Liebert, J. 1993, ApJ, 406, 489

Rich, R. M. & Origlia, L. 2005, ApJ, 634, 1293

Rich, R. M., Ortolani, S., Bica, E., & Barbuy, B. 1998, AJ, 116, 1295

Rich, R. M., Salim, S., Brinchmann, J., et al. 2005, ApJ, 619, L107

Rich, R. M., Sosin, C., Djorgovski, S. G., et al. 1997, ApJ, 484, L25+

Ridgway, S. T., Joyce, R. R., White, N. M., & Wing, R. F. 1980, ApJ, 235, 126

Robin, A. C., Reylé, C., Derrière, S., & Picaud, S. 2003, A&A, 409, 523

Rosenberg, A., Piotto, G., Saviane, I., & Aparicio, A. 2000, A&AS, 144, 5

Saffer, R. A., Bergeron, P., Koester, D., & Liebert, J. 1994, ApJ, 432, 351

Santos, Jr., J. F. C., Bica, E., & Dottori, H. 1990, PASP, 102, 454

Santos, Jr., J. F. C., Bica, E., Dottori, H., Ortolani, S., & Barbuy, B. 1995a, A&A, 303, 753

Santos, Jr., J. F. C., Bica, E., Dottori, H., Ortolani, S., & Barbuy, B. 1995b, A&A, 303, 753

Savage, B. D. & Mathis, J. S. 1979, ARA&A, 17, 73

Schiavon, R. P., Rose, J. A., Courteau, S., & MacArthur, L. A. 2005, ApJS, 160, 163

Schlegel, D. J., Finkbeiner, D. P., & Davis, M. 1998, ApJ, 500, 525

Schmidt-Kaler, T. 1982, Landolt-Brstein, Neue Serie, Gruppe VI, Bd. 2b, Schaifers K., Voigt H.H. (eds.). Springer, Berlin Heidelberg New York,

Silbermann, N. A., Harding, P., Madore, B. F., et al. 1996, ApJ, 470, 1

Silva, D. R. & Cornell, M. E. 1992, ApJS, 81, 865

Sosin, C., Dorman, B., Djorgovski, S. G., et al. 1997, ApJ, 480, L35+

Stanek, K. Z., Mateo, M., Udalski, A., et al. 1994, ApJ, 429, L73

Stetson, P. B. 1987, PASP, 99, 191

Stetson, P. B. 1994, PASP, 106, 250

Stetson, P. B. 2000, PASP, 112, 925

Straižys, V., Lazauskaite, R., & Valiauga, G. 2002, Baltic Astronomy, 11, 341

Sumi, T., Wu, X., Udalski, A., et al. 2004, MNRAS, 348, 1439

Sviderskiene, Z. 1988, Vilnius Astronomijos Observatorijos Biuletenis, 80, 3

Sweigart, A. V. 1997a, ApJ, 474, L23+

Sweigart, A. V. 1997b, in The Third Conference on Faint Blue Stars, ed. A. G. D. Philip, J. Liebert, R. Saffer, & D. S. Hayes, 3–+

Sweigart, A. V. & Catelan, M. 1998, ApJ, 501, L63+

Tantalo, R., Chiosi, C., Bressan, A., & Fagotto, F. 1996, A&A, 311, 361

Terndrup, D. M., Sadler, E. M., & Rich, R. M. 1995, AJ, 110, 1774

Tiede, G. P. & Terndrup, D. M. 1999, AJ, 118, 895

Tinsley, B. M. 1971, A&A, 15, 403

Tug, H. 1977, The Messenger, 11, 7

Udalski, A. 2003, ApJ, 590, 284

Udalski, A., Szymanski, M., Kubiak, M., et al. 2002, Acta Astronomica, 52, 217

Udalski, A., Szymanski, M., Stanek, K. Z., et al. 1994, Acta Astronomica, 44, 165

Vallenari, A., Bertelli, G., & Schmidtobreick, L. 2000, A&A, 361, 73

Vallenari, A., Pasetto, S., Bertelli, G., et al. 2006, A&A, 451, 125

Villeneuve, B., Wesemael, F., Fontaine, G., Carignan, C., & Green, R. F. 1995, ApJ, 446, 646

Wallace, L., Meyer, M. R., Hinkle, K., & Edwards, S. 2000, ApJ, 535, 325

Werner, K. & Dreizler, S. 1999, J. Comp. Appl. Math. 109, ed H. Riffert, & K. Werner (Elsevier Press, Amsterdam)

Westera, P., Lejeune, T., Buser, R., Cuisinier, F., & Bruzual, G. 2002, A&A, 381, 524

Wyse, R. F. G. & Gilmore, G. 1992, AJ, 104, 144

Wyse, R. F. G., Gilmore, G., & Franx, M. 1997, ARA&A, 35, 637

Yi, S., Demarque, P., & Kim, Y.-C. 1997, ApJ, 482, 677

Yi, S., Lee, Y.-W., Woo, J.-H., et al. 1999, ApJ, 513, 128

Zhao, H., Spergel, D. N., & Rich, R. M. 1995, ApJ, 440, L13

Zoccali, M., Lecureur, A., Barbuy, B., et al. 2006, A&A, 457, L1

Zoccali, M., Renzini, A., Ortolani, S., et al. 2003, A&A, 399, 931

Acknowledgments

First of all I want to thank my supervisor Sabine Moehler for all the things she teached me in these three years, but also because she was very patient, she pushed me when I was too slow and gave me time when I needed it, she was understanding in the hard times. I think she is one of the best supervisors a PhD student can have and I hope to become an astronomer as good as her.

Thanks also Detlev Koester for the help every time I needed it and for his sense of humor.

Thanks to Holger, who kept me company drinking coffee and trying to cheer me up when I was sad, and also because basically he undertook the role of my personal secretary, without him I would not have survived in these three years.

Thanks to Elke, Danica, Bjorn, Tim, Sascha1 and Sascha2 and all friends in Italy and in all the rest of the world.

And Vielen Danke to Frau Kuhr, because somehow she managed always to understand what I wanted.

Thanks to Giampaolo Piotto and Santino Cassisi, because they did not forget me and for the wonderful work with the globular clusters; to Uli Heber for the sdBs spectra library; to Manuela Zoccali for the photometric data; to Giuseppe Bono for the helpful comments on the thesis.

I acknowledge the Deutsche Forschungsgemeinschaft via grant Mo 602/8 for the financial support.